



N7575684

**EFFECT OF AFTERBODY SHAPE, NOZZLE TYPE,
AND ENGINE LATERAL SPACING ON THE
INSTALLED PERFORMANCE OF A TWIN-JET
AFTERBODY MODEL**

~~CONFIDENTIAL~~

1. Report No. NASA TM X-1855	2. Government Accession No.	3. Recipient's Catalog No.	
4. Title and Subtitle EFFECT OF AFTERBODY SHAPE, NOZZLE TYPE, AND ENGINE LATERAL SPACING ON THE INSTALLED PERFORMANCE OF A TWIN-JET AFTERBODY MODEL 16		5. Report Date September 1969 ¹	
		6. Performing Organization Code	
7. Author(s) Charles E. Mercer and Bobby L. Berrier		8. Performing Organization Report No. L-6708	
9. Performing Organization Name and Address NASA Langley Research Center Hampton, Va. 23365		10. Work Unit No. 126-63-11-22-23	
		11. Contract or Grant No.	
12. Sponsoring Agency Name and Address National Aeronautics and Space Administration Washington, D.C. 20546		13. Type of Report and Period Covered Technical Memorandum	
		14. Sponsoring Agency Code	
15. Supplementary Notes			
16. Abstract An investigation has been conducted in the Langley 16-foot transonic tunnel and the Langley 4- by 4-foot supersonic pressure tunnel to determine the installed performance of a generalized twin-jet afterbody-exhaust nozzle model. The model was tested statically and at Mach numbers from 0.6 to 1.3 and 2.2. The effects of exhaust nozzle design, nozzle operation, lateral spacing on afterbody and nozzle thrust-minus-drag performance, and the effects of afterbody geometric shaping on exhaust nozzle per- formance are included. ----- -----			
17. Key Words Suggested by Author(s) Nozzles Engine lateral spacing Afterbody shape		UNLIMITED F- 8/75	
19. Security Classif. (of this report) Confidential - Group 3	20. Security Classif. (of this page) Unclassified	21. No. of Pages 162	22. Price

REPRODUCED BY
NATIONAL TECHNICAL
INFORMATION SERVICE
U.S. DEPARTMENT OF COMMERCE
SPRINGFIELD, VA. 22161

**EFFECT OF AFTERBODY SHAPE, NOZZLE TYPE, AND
ENGINE LATERAL SPACING ON THE INSTALLED PERFORMANCE
OF A TWIN-JET AFTERBODY MODEL ***

By Charles E. Mercer and Bobby L. Berrier
Langley Research Center

SUMMARY

An investigation has been conducted in the Langley 16-foot transonic tunnel and in the Langley 4- by 4-foot supersonic pressure tunnel of the installed performance of a generalized twin-jet afterbody-exhaust nozzle model. The model was tested statically and at Mach numbers from 0.6 to 1.3 and 2.2. High-pressure compressed air provided primary exhaust gases at total-pressure ratios up to 22. The effects of exhaust nozzle design, nozzle operation, lateral spacing on afterbody and nozzle thrust-minus-drag performance, and the effects of afterbody geometric shaping on exhaust nozzle performance were obtained.

The results show that an iris-convergent nozzle generally had the highest installed performance for all afterbodies at subsonic Mach numbers, whereas no single nozzle type exhibited consistently better performance when integrated with the different afterbodies at supersonic speeds. However, a convergent-divergent-iris nozzle generally showed competitive performance when compared with the other nozzles. The generalized clean external contoured afterbody with minimum lateral engine spacing had the best performance for nearly all test conditions. The afterbody similar to a twin-jet fighter-type airplane having a long engine interfairing and long stabilizer actuator fairings had the lowest performance at military (dry) and partial afterburning power settings but was competitive with other afterbodies at maximum afterburning power setting. Increasing engine lateral spacing along with maximum cross-sectional area generally increases afterbody drag, slightly increases thrust minus nozzle drag, and decreases thrust minus afterbody and nozzle drag.

INTRODUCTION

Recent research with powered models of aircraft having twin engines mounted in the aft end of the fuselage has shown performance losses associated with this type of

*Title, Unclassified.

installation. (See refs. 1 to 3.) Such losses appear because of increased afterbody drag due to unfavorable jet effects, increased nozzle drag due to unfavorable afterbody flow field, or nozzle internal losses due to unfavorable afterbody flow field (especially blow-in-door and plug nozzles). As shown in reference 4 for a fixed afterbody design having an unfavorable flow field, changes in nozzle geometry resulted in small variations in thrust-minus-drag performance; whereas reference 5 shows that airframe geometry alterations resulted in large gains in gross thrust-minus-drag performance. It is obvious that early in the design stages of a twin-engine fighter aircraft, a thorough study should be made of the complete airplane configuration including the powerplant installation with emphasis on nozzle design, proper installation, and accurate performance estimates. Since nozzle-airframe interaction is generally too complex for theoretical analysis, experimental work must be done to determine interference forces and absolute performance levels.

The purpose of the present paper is to present the results of an investigation of the performance of five related generalized twin-jet airplane afterbodies in combination with four types of engine exhaust nozzles installed on the Langley two-balance air-powered model. Objectives of the investigation were to determine the effects of exhaust nozzle design, nozzle operation, and lateral spacing on the thrust minus afterbody and nozzle drag performance, and the effects of afterbody shape on exhaust-nozzle performance.

These investigations were conducted in the Langley 16-foot transonic tunnel and the Langley 4- by 4-foot supersonic pressure tunnel at static conditions and at Mach numbers of 0.6 to 1.3 and 2.2. The jet total-pressure ratio was varied from 1 (jet-off) to about 22 depending on the Mach number. The engine primary flow was simulated with compressed air and the nozzle secondary mass flow was zero during the entire investigation.

SYMBOLS

A	cross-sectional area, meters ²
A_e	nozzle exit area, meters ²
A_{eng}	engine maximum cross-sectional area at upstream end of nozzle, meters ²
A_{max}	maximum cross-sectional area of afterbody, meters ²
A_s	exit area of plug nozzle shroud, meters ²
A_{seal}	cross-sectional area enclosed by seal at seal station, meters ²

A_t	nozzle throat area (one engine), meters ²
$A_{t,t}$	total nozzle throat area (two engines), meters ²
$C_{A,a}$	axial-force coefficient on afterbody including base annuli, $\frac{F_{A,a}}{q_\infty A_{\max}}$
$C_{A,c}$	drag coefficient obtained from integration of pressures on faired end caps replacing nozzles, $\sum_{N=0}^{N=41} -C_p \frac{A}{A_{\max}}$
$C_{A,f}$	skin-friction axial-force coefficient
C_p	local pressure coefficient, $\frac{p_L - p_\infty}{q_\infty}$
d_e	diameter of nozzle exit, meters
d_{eng}	diameter of engine at engine maximum cross section, meters
d_s	diameter of shroud exit (plug nozzle), meters
d_t	diameter of nozzle throat, meters
$F_{A,a}$	axial force (drag) on afterbody including base annuli, newtons
$F_{A,n}$	axial force on nozzle (external drag), newtons
$F_{A,t}$	total axial force of afterbody plus nozzles (external drag), newtons
$F_{\text{bal},a}$	afterbody axial-force balance reading, newtons
$F_{\text{bal},j}$	thrust minus axial-force balance reading, newtons
F_i	ideal primary thrust for complete isentropic expansion of primary mass flow, $\dot{m} \sqrt{2R \frac{\gamma}{\gamma-1} T_{t,j} \left[1 - \left(\frac{p_\infty}{p_{t,j}} \right)^{\frac{\gamma-1}{\gamma}} \right]}, \text{ newtons}$
F_j	internal nozzle gross thrust, newtons

$F_j - F_{A,n}$	gross thrust minus external axial force of nozzles, newtons
$F_j - F_{A,t}$	gross thrust minus axial force of afterbody-nozzle combination, newtons
h	body height at maximum cross section, meters
l	model length, meters
l_n	exposed length of nozzle, meters
l_3	length of model to end of afterbody, meters
M	free-stream Mach number
\dot{m}	measured mass-flow rate
N	integer
$P_{e,s}$	local static pressure at external surface of seal, newtons/meter ²
$P_{i,s}$	local static pressure at internal surface, newtons/meter ²
P_l	local static pressure, newtons/meter ²
$P_{t,j}$	jet total pressure, newtons/meter ²
P_∞	free-stream static pressure, newtons/meter ²
q_∞	free-stream dynamic pressure, newtons/meter ²
R	gas constant, newton-meters/kilogram-degree Kelvin
r	radius, meters
s	spacing distance between engine center lines, meters
s/d_{eng}	lateral spacing ratio based on engine diameter
$T_{t,j}$	jet stagnation temperature, degrees Kelvin

w	body width at maximum cross section, meters
x_0	longitudinal distance from model nose (station 0), positive rearward, meters
x	longitudinal distance from model station 129.73, positive rearward, meters
z	vertical distance from horizontal reference plane, positive upward, meters
β	boattail angle, degrees
γ	ratio of specific heats
ϕ	radial angle of pressure orifice rows on end caps, degrees

A bar over a symbol indicates an average value.

APPARATUS AND METHODS

Wind Tunnels

The investigation was conducted in the Langley 16-foot transonic tunnel and the Langley 4- by 4-foot supersonic pressure tunnel. The Langley 16-foot transonic tunnel is an atmospheric wind tunnel with a slotted octagonal test section having a continuously variable speed range from a Mach number of 0.20 to 1.30. The Langley 4- by 4-foot supersonic pressure tunnel is a single-return, continuous wind tunnel with a stagnation pressure range of $2.758 \times 10^4 \text{ N/m}^2$ to $2.0684 \times 10^5 \text{ N/m}^2$ and a stagnation temperature range of 316.7° K to 322.2° K . By use of interchangeable nozzle blocks, the Mach number can be varied from 1.25 to 2.60.

Model

The basic test rig for this investigation was a twin-jet, two-balance air-nacelle model shown in the photograph (fig. 1) mounted in the test section of the Langley 16-foot transonic wind tunnel. The twin-jet model with the exhaust nozzles replaced with streamlined fairings (end caps) is shown in the photographs of figure 2 with two different afterbodies.

A sketch of the twin-jet, two-balance model is presented in figure 3(a) and important geometric parameters are given in figure 3(b). The metric afterbody starts at the model parting line which is located at model seal station 83.502. A flexible teflon strip inserted into slots machined into the metric and nonmetric portions of the model was

used as a seal. (See fig. 3(c).) In this investigation, a two-balance arrangement was used as shown in figure 3(c): one balance measured the gross thrust and external drag forces and the other balance measured only the external drag forces of the afterbody.

The engine primary flow was simulated with a high-pressure compressed-air system similar to that described in reference 6. Nozzle secondary mass flow was zero for all cases, the nozzle internal geometry being designed accordingly.

The available literature on the effect of jet exhaust interference has indicated that the jet plume shape has the primary effect on nozzle external boattail drag. The initial plume shape is primarily determined by jet static-pressure ratio, ratio of specific heats of the exhaust fluid, nozzle internal-divergence angle, and external Mach number. (See ref. 7.) Reference 7 indicates that for the range of pressure ratio of the present investigation, the difference in specific-heat ratio between air ($\gamma = 1.4$) and engine exhaust ($\gamma \approx 1.3$) would result in a very small difference in initial inclination angle of the jet boundary. Reference 8 emphasizes the possible importance of jet temperature and specific-heat ratio simulation when significant interference between the jet plume and airplane structure downstream of the nozzle exit exists. Since the afterbody configurations of this investigation had little structure downstream of the nozzle exits and the nozzles generally were not operating greatly underexpanded, it is believed that the relative interference levels of various configurations are valid. Any differences in interference effects due to improper jet simulation are probably small and unpublished data tends to substantiate this belief.

Since a large number of afterbody—exhaust-nozzle combinations were investigated, the configuration number has been coded to facilitate the comparison of different configurations on the data figures. The code consists of a three-number format where the first number indicates the afterbody type, the second number indicates the exhaust nozzle type, and the third number indicates the engine power setting. Photographs of the afterbodies and exhaust nozzles are shown in figure 3(d).

Details of the five afterbody arrangements investigated are given in figure 4. The normal cross-sectional area distributions of the five afterbodies are shown in figure 4(e). The afterbodies which represent several types of aircraft shapes are designated as follows:

Afterbody 1: Afterbody 1 is similar to a twin-jet fighter-type airplane which has a long engine interfairing and long horizontal stabilizer actuator fairings

Afterbody 2: Afterbody 2 is similar to afterbody 1, but has a short blunt engine interfairing and short stubby stabilizer actuator fairings

Afterbodies 3 to 5: Generalized afterbodies with clean external contours and with engine center lines spaced to represent various degrees of lateral spacing - 3 minimum, 4 intermediate, and 5 maximum.

Each of these afterbodies were integrated with four nozzles representing different exhaust-nozzle concepts. The geometric details of these nozzles are shown in figure 5. The basic nozzle concepts were:

Nozzle 1: Iris-convergent nozzle for which the primary leaves retract for afterburning

Nozzle 2: Convergent-divergent, variable-flap ejector-type nozzle

Nozzle 3: Plug nozzle with a 10° half-angle basic plug; plug collapses and shroud hinges out for afterburning

Nozzle 4: Blow-in-door ejector with iris-convergent primary.

Each of these nozzle types was investigated at power settings which are as follows:

- 0 Represents no power setting ($A_e = 0.0$)
- 1 Represents dry or military power
- 2 Represents partial afterburning
- 3 Represents maximum afterburning

In addition to the four basic nozzles, two reference blow-in-door nozzles (reference blow-in-door nozzle or nozzle 0) were investigated at power settings which represent approximately dry and maximum afterburning. (See figs. 5(f) and 5(g).) The nozzle shroud for the plug nozzle (nozzle 3) had a variable lip angle simulated with fixed hardware for each power setting; however, for the dry power condition, a floating flap shroud (nozzle 6) was also used with two afterbodies.

A new exhaust nozzle type, the convergent-divergent-iris (nozzle 5) was also investigated only in the maximum afterburning power setting. (See fig. 5(e).) The nozzle concept would have translating flaps which move along curved tracks at the rear of the afterburner shell. The internal contours are convergent in the nonafterburning position with smooth external boattail lines similar to those of nozzle 1 in the dry power setting. At afterburning positions, the shroud translates forward and the internal shape is convergent-divergent, the remaining external boattail area becoming small. This nozzle would probably be lighter and less complex than the typical variable-flap ejector nozzle.

The various afterbodies were also tested with streamlined fairings (nozzle 7, faired end caps, fig. 5(h)) in place of the exhaust nozzles to represent a closed body in which an afterbody reference drag level might be established.

Instrumentation

Thrust and drag forces on the metric portion of the model were obtained by means of two strain-gage balances. (See fig. 3(a).) A small-capacity six-component strain-gage balance is used to measure drag on the afterbody shell. (See fig. 3(c).) A large-capacity multicomponent strain-gage balance, which carried the small-capacity balance in tandem, is used to measure thrust of the nozzles minus total external afterbody and nozzle drag. Static pressures on the faired end caps at the orifice locations shown in figure 5(h) were measured by the use of electrical pressure transducers. External and internal static pressures were also measured at several locations on the periphery of the afterbody at the model station which separates the metric section from the nonmetric section (seal station). The jet total pressure and stagnation temperature were measured in both tailpipes at locations shown in figure 3(c). An electronic turbine flowmeter was used to obtain the mass-flow rate through the primary nozzles.

Data Reduction

Model and tunnel data were recorded by an automatic magnetic tape-recording system in the Langley 16-foot transonic tunnel and by a servo-punch card system in the Langley 4- by 4-foot supersonic pressure tunnel. These data were reduced to standard force and pressure coefficients. Pressure forces on the faired end caps were obtained by assigning each pressure orifice an incremental area projected on a plane normal to the model axis and numerically integrating the incremental forces. The support system used in this investigation has little or no interference effects (see ref. 6) and hence no correction to the data was made for strut interference.

The gross thrust minus afterbody and nozzle axial force was obtained directly from the thrust-minus-drag balance. (See fig. 3(c).) This term was computed as follows:

$$F_j - F_{A,t} = F_{bal,j} + (\bar{p}_{e,s} - p_{\infty})(A_{max} - A_{seal}) + (\bar{p}_{i,s} - p_{\infty})A_{seal}$$

The forces sensed by the balance and included in the axial-force term $F_{bal,j}$ are nozzle thrust, afterbody external and internal axial forces transferred to the thrust-minus-drag balance through the tandem drag balance, and internal and external axial forces on the nozzles.

Afterbody axial force was obtained directly from the tandem drag balance. (See fig. 3(c).) The afterbody axial force was computed as follows:

$$F_{A,a} = F_{bal,a} - (\bar{p}_{e,s} - p_{\infty})(A_{max} - A_{seal}) - (\bar{p}_{i,s} - p_{\infty})(A_{seal} - 2A_{eng})$$

Thrust minus nozzle drag performance is obtained by combining the two balance axial forces as follows:

$$F_j - F_{A,n} = F_{bal,j} + F_{bal,a} + (\bar{p}_{i,s} - p_{\infty})(2A_{eng})$$

Tests

Data were obtained at static conditions and at a Mach number range of 0.60 to 1.30 in the Langley 16-foot transonic tunnel and at a Mach number of 2.2 in the Langley 4- by 4-foot supersonic pressure tunnel. At all test conditions the model angle of attack was 0° . The average Reynolds number per meter varied from 11.15×10^6 at $M = 0.7$ to 12.14×10^6 at $M = 1.3$ and $M = 2.2$. Primary total-pressure ratio varied from 1.0 (jet off) to approximately 22.0, depending on Mach number. Nozzle secondary mass flow was zero throughout the entire investigation.

PRESENTATION OF DATA

The results of this investigation are presented in the following figures:

	Figure
Faired end-cap pressure coefficient distributions	6
Faired end-cap axial-force coefficient and afterbody axial-force coefficient variation with Mach number	7
Variation of skin-friction axial-force coefficient with Mach number for the various afterbodies	8
Variation of afterbody axial-force coefficient with primary total-pressure ratio for several nozzles:	
Afterbody 1	9
Afterbody 2	10
Afterbody 3	11
Afterbody 4	12
Afterbody 5	13
Static thrust performance for various nozzles installed on various afterbodies	14
Variation of thrust minus afterbody and nozzle axial-force performance with primary total-pressure ratios for several nozzles:	
Afterbody 1	15
Afterbody 2	16
Afterbody 3	17
Afterbody 4	18
Afterbody 5	19
Variation of thrust minus nozzle axial-force performance with primary total-pressure ratio for several nozzles:	
Afterbody 1	20
Afterbody 2	21
Afterbody 3	22

	Figure
Afterbody 4	23
Afterbody 5	24
Propulsive and aerodynamic performance variation with primary total- pressure ratio for the various afterbodies at $M = 2.2$:	
Convergent nozzle (nozzle 1)	25
Convergent-divergent nozzle (nozzle 2)	26
Plug nozzle (nozzle 3)	27
Blow-in-door ejector nozzle (nozzle 4)	28
Convergent-divergent-iris nozzle (nozzle 5)	29
Reference blow-in-door nozzle (nozzle 0)	30
Typical jet pressure ratio schedule of a turbofan-engine configuration for the Mach number range	31
Propulsive and aerodynamic performance for various configurations at scheduled conditions:	
Military power setting (setting 1)	32
Partial afterburning power setting (setting 2)	33
Maximum afterburning power setting (setting 3)	34
Effect of power setting on the installed performance of the various nozzles in combination with afterbodies 1 and 3	35
Effect of power setting on the installed performance of complex geometry afterbodies (afterbodies 1, 2, and 3) for several nozzles	36
Effect of nozzle spacing on installed performance for the various nozzles	37
Variation of installed performance of a plug nozzle having fixed or floating shroud tail flaps	38

RESULTS AND DISCUSSION

Faired End-Cap Results

Pressure measurements on the end caps provide information on local flow fields and possible effects on nozzle drag. Also the end caps could be used to establish reference afterbody drag with which to compare various nozzle-afterbody drag of other wind-tunnel force models.

Pressure coefficient distributions.- Figure 6 presents some representative pressure distributions on the faired end cap installed on the five twin-jet afterbodies. Pressure coefficients are shown for several radial rows at stations given in figure 5(h) and for several Mach numbers.

Pressure coefficients measured on the end caps installed on the long interfairing afterbody (afterbody 1) are generally negative except at $M = 0.70$ and $M = 0.90$ where

pressure recovery produced positive pressure coefficients near the end-cap tip. Pressures measured next to the engine interfairing (centerbody), $\phi = 270^\circ$ and $\phi = 315^\circ$, are generally lower than pressures measured away from the interfairing; thus, end-cap drag is increased and nozzle drag with actual nozzles installed is probably increased.

Pressure distributions obtained with the short interfairing afterbody (afterbody 2) generally follow the same trends as those obtained with afterbody 1 (long interfairings). However, the level of the pressure coefficient distributions at Mach numbers of 0.70 and 0.90 are higher than that shown in figure 6(a) for the long interfairing afterbody (afterbody 1), and thus the end caps should have less drag (same result should probably apply to nozzle drag) when installed on the short interfairing afterbody (afterbody 2). The detrimental effect on pressure of a surface adjacent to the end cap (or nozzle) shown for the long interfairing afterbody (afterbody 1) is also shown by the $\phi = 90^\circ$ row (next to actuator housing) pressure distribution obtained with the short interfairing afterbody (afterbody 2). Pressure measurements on this row, located next to a stabilizer actuator fairing are generally lower than measurements made on other rows.

Pressure distributions obtained on the end caps installed on the clean contour afterbodies (afterbodies 3, 4, and 5) follow the same trends as the pressure distributions obtained with the two complex afterbodies (afterbodies 1 and 2) on orifice rows which were not affected by surfaces adjacent to the end cap. The pressure distribution levels obtained with the clean contour afterbodies are generally higher at $M = 0.70$ and $M = 0.90$ than those obtained with the short interfairing afterbody (afterbody 2); thus, end-cap drag is lower and it might be expected that installed nozzle drag also would be lower. The differences in pressure coefficient distributions for different orifice rows are greatly reduced at a Mach number of 2.2 when compared with the differences shown at $M \approx 1.2$. In addition, the general pressure coefficient distribution levels are similar for all configurations at $M = 2.2$.

End-cap axial force. - The pressures measured on the end cap at locations shown in figure 5(h) were integrated over the end-cap projected area to obtain the end-cap axial force (drag). (See fig. 7.) Afterbody axial force (drag) measured by the tandem drag balance with end caps installed is also shown in figure 7. As was indicated by end-cap pressures, the clean contour afterbodies (afterbodies 3, 4, and 5) had lower end-cap drag than the complex afterbody configurations (afterbodies 1 and 2) at all Mach numbers. The end-cap drag obtained with the short interfairing afterbody (afterbody 2) was substantially lower than the end-cap drag obtained with the long interfairing afterbody (afterbody 1). Engine lateral spacing (fig. 7(b)) had little effect on end-cap drag except at low supersonic Mach numbers where the lowest end-cap drag was obtained with the wide spaced afterbody (afterbody 5). Perhaps the most significant result shown in figure 7 is the beneficial thrust forces ($-C_{A,c}$) obtained on the end caps for the clean contour afterbodies

(afterbodies 3, 4, and 5) and, although to a lesser degree, for the short interfairing afterbody (afterbody 2) at subsonic Mach numbers. This result suggests the possibility of obtaining beneficial thrust forces in the subsonic-speed regime on nozzle boattails, rather than detrimental drag forces, when a properly integrated afterbody-nozzle installation is achieved.

The short interfairing afterbody (afterbody 2) had the highest afterbody axial force (drag) of the complex afterbodies (afterbodies 1 and 2). It is interesting to note, that although the long interfairing afterbody (afterbody 1), for $M < 1.3$, had the lowest afterbody axial force (drag) of the configurations shown in figure 7(a), the highest end-cap drag was also obtained with this afterbody (long interfairings). The higher drag is probably a result of the low slopes on the afterbody; hence, most of the closure drag penalty occurs on the end caps (or nozzles). At Mach numbers above 0.8, increasing engine lateral spacing increases afterbody axial force (drag) as shown in figure 7(b). It should be noted that afterbody cross-sectional area also increased with spacing.

Propulsive and Aerodynamic Performance

Basic data. - Since there were no pressure measurements on the afterbodies in this investigation and in order that one might compare the axial force presented in this paper with the forces obtained by pressure measurements of a similar configuration, the skin friction over the afterbody portion would be required. A calculated skin-friction axial force for the various afterbodies is presented in figure 8 as a variation with Mach number. This force is obtained by using the Frankl and Voishel equation for compressible, turbulent flow on a flat plate as given in reference 9.

The thrust and drag data of this investigation are presented as a function of jet total-pressure ratio. Parameters presented are the afterbody axial-force or drag coefficient, the thrust minus afterbody and nozzle axial force (thrust minus total afterbody drag) performance, and the thrust minus nozzle axial-force (drag) performance. The subsonic and transonic Mach number variation is presented for one afterbody-nozzle combination and three nozzle throat sizes (power setting) per page. Therefore, the effects of Mach number, $p_{t,j}/p_{\infty}$, and power setting on the drag force and performance ratios can be readily observed. At the supersonic Mach number, $M = 2.2$, the jet total-pressure-ratio range was much greater, and thus requires separate plotting. All parameters are given for each nozzle type (maximum afterburning only) in combination with the different afterbodies. For the wider spacing afterbodies, very little data are presented because the tunnel starting loads (dynamics) on the model exceed the balance load limits.

The afterbody axial-force (drag) coefficients of the various exhaust nozzle-afterbody combinations are shown in figures 9 to 13 and 25 to 30. The static thrust performances for the various nozzles are presented in figure 14. An average thrust value is used for

each nozzle at each engine power setting and is represented by the single line fairing. Given in figures 15 to 30 are the thrust minus afterbody and nozzle axial-force (drag) performance and thrust minus nozzle axial-force (drag) performance.

The values of thrust minus nozzle drag performance exceed the ideal thrust for some of the afterbody-nozzle configurations (figs. 21 to 25) at subsonic Mach numbers and low pressure ratios. As mentioned previously a region of positive pressures would be located around the nozzles for several of the afterbodies (fig. 6). However, as was shown in figure 7(a), no such nozzle performance would be realized in combination with afterbody 1. Although each of the other afterbodies revealed this nozzle performance for some nozzles, only the "clean" afterbodies (afterbodies 3 to 5) remained consistent for more than two nozzles (for example, iris-convergent, convergent-divergent, and plug nozzle). As the throat diameter increased, the beneficial flow effects decreased, and only the thrust of the iris-convergent nozzle (nozzle 1) remained equal to or greater than ideal thrust for all power settings.

Comparative performance of afterbody-nozzle configurations at scheduled pressure ratios.— Although previous figures are a convenient way of presenting basic data, analysis with respect to comparison of performance of different nozzles on an afterbody, or a nozzle on different afterbodies, requires some form of cross plotting at selected jet total-pressure ratios. Here, for example, bar-graph comparisons (figs. 32 to 34) are presented at a schedule of $p_{t,j}/p_{\infty}$ as a function of M typical of a turbofan engine configuration (fig. 31). Although discussion for a particular schedule of $p_{t,j}/p_{\infty}$ as a function of M would generally be true for other schedules not too greatly different, the relative differences between configurations may vary. At subsonic Mach numbers and for all three power settings, the iris-convergent nozzle (nozzle 1) generally had the highest thrust minus afterbody and nozzle drag performance and thrust minus nozzle drag performance for any nozzle tested in combination with the five afterbody shapes (figs. 32 to 34, parts (a), (b), and (c)). At low supersonic Mach numbers and for the military (setting 1) and partial (setting 2) afterburning power settings, the blow-in-door nozzle (nozzle 4) gave better thrust minus afterbody plus nozzle drag performance. At low supersonic speeds and maximum afterburning power setting (setting 3), no single nozzle type gave the best performance when combined with any of the five afterbodies. The convergent-divergent-iris nozzle type (nozzle 5) generally showed competitive performance when compared with the other nozzles for the limited amount of data shown (three afterbodies at $M = 2.2$ and one afterbody at low supersonic speeds, see fig. 34, parts (d), (e), and (f)). This nozzle also offers savings in weight and complexity which further enhances its attractiveness.

Based on this information, the nozzle type which would give the better performance throughout the speed range would be one which was essentially an iris-convergent nozzle

at low pressure ratios and subsonic Mach numbers and a convergent-divergent nozzle in the afterburning case and supersonic Mach numbers (high pressure ratios), that is, one similar to the convergent-divergent-iris concept (nozzle 5). However, it should be pointed out that as a result of the short divergent section, expansion ratios are limited and large divergence losses may result at high power settings. In addition, power setting and expansion ratio are not independent and hence, at some conditions, large overexpansion or underexpansion losses may occur (for example, low pressure ratios at maximum power setting or high pressure ratios at dry power settings).

With few exceptions the blow-in-door ejector nozzle (nozzle 4) combined with the various afterbodies generally gave the lowest afterbody axial force at all Mach numbers. This condition is probably due to a pressure increase being fed upstream through the boundary layer as a result of a compression occurring ahead of the shroud inlet.

As mentioned previously in the discussion about the faired end-cap pressure and force data, the long interfairing afterbody (afterbody 1) generally had the lowest jet-off afterbody axial force for most conditions. Figures 32 to 34 also show the same result with the nozzles operating at a typical turbofan engine pressure ratio (afterbody 3 competitive at some conditions). However, combining the afterbody with the lowest afterbody drag (afterbody 1) with the nozzle which resulted in the least detrimental effect on afterbody drag, blow-in-door nozzle (nozzle 4), did not result in the optimum (thrust minus afterbody plus nozzle drag) afterbody-nozzle combination that might be expected. In fact, the long interfairing afterbody (afterbody 1) generally gave the lowest gross thrust minus afterbody and nozzle drag performance when combined with any nozzle type at Mach numbers up to 0.90 and power settings of military and partial afterburning. This low performance is a result of high nozzle drag as indicated by the low thrust minus nozzle drag performance in figures 32 to 34. (Some nozzle internal losses may also be included in this performance for the blow-in-door ejector and plug nozzles.) At maximum afterburning power setting or at supersonic Mach numbers, the performance of the long interfairing afterbody (afterbody 1) is generally below the performance of the closely spaced clean-contour afterbody (afterbody 3) but generally above the performance of the short interfairing afterbody (afterbody 2). This result again emphasizes that the total configuration (afterbody plus nozzles) must be integrated as a unit to achieve optimum airplane performance.

Effect of power setting. - The effect of power setting (throat and exit diameter) on the performance of four nozzle types in combination with the long interfairing afterbody and close-spaced, clean contour afterbody (afterbodies 1 and 3, respectively) is presented in figure 35. As nozzle throat size is increased, the gross thrust minus total afterbody drag performance increases as expected for most conditions because the drag becomes a smaller percentage of the increasing ideal thrust. This same trend would be expected for the thrust minus nozzle drag performance; however, for afterbody 3, values greater

than 1.0 were obtained because of the pressure recovery which actually caused thrust on the external surfaces of the nozzle at subsonic Mach numbers. This recovery was indicated by the pressure data shown in figure 6 for the faired end caps where positive pressure coefficients were obtained over much of the faired end cap.

As pointed out in the previous section, the iris-convergent nozzle (nozzle 1) generally was more efficient at subsonic speeds whereas no single nozzle was more efficient for all throat sizes at the higher speeds.

The afterbody drag was decreased as nozzle throat size increased for all configurations. This condition could probably be theorized as interference effects caused by a shorter nozzle boattail, a lower nozzle boattail angle, and effects of the jet exhaust plume, all of which affect the flow field around the afterbody.

The data of a reference blow-in-door nozzle (nozzle 0) are shown in figure 35 (at $A_{t,t}/A_{max} = 0.127$) in order to provide some tie-in of a flight-type nozzle (ref. 4) with the data of this report. The reference blow-in-door nozzle (nozzle 0) had fixed hardware (blow-in-doors fixed open for speeds up to 1.3 and doors fixed closed for $M = 2.2$; also the nozzle shroud exit diameter was fixed at an intermediate position of divergence for all speeds). Comparison of the reference nozzle (nozzle 0) with the floating blow-in-door nozzle (nozzle 4) shows that the reference nozzle had from 2 to 5 percent lower performance at speeds up to $M = 1.3$. Shown in figure 34(f) is the performance at $M = 2.2$ for the reference nozzle (nozzle 0) having the blow-in-doors fixed closed. This figure reveals that the free-floating blow-in-door nozzle (nozzle 4) had a lower performance than the fixed closed reference blow-in-door nozzle (nozzle 0) by about 1 percent in thrust minus afterbody and nozzle drag performance and about 3 percent in thrust minus nozzle drag performance. This loss is regarded as being due to faulty stops which allowed the shroud tail flaps to open more than desired at this speed and thus created nozzle overexpansion losses.

The effect of power setting (throat and exit diameter) on the installed performance of the afterbodies 1, 2, and 3 is presented in figure 36. Regardless of nozzle type, the thrust minus total afterbody drag performance and thrust minus nozzle drag performance of the closely spaced clean-contour afterbody (nozzle 3) were the highest; however, as the nozzle throat size is increased, the performances of the three afterbodies approach a common value. The apparent reason for this effect is that the external drag force is a smaller percentage of the total measurement, especially when the afterbody and nozzle drag is decreasing as the engine size increases. The long interfairing afterbody (afterbody 1) had the lowest performance at military and partial afterburning power settings, but at the maximum nozzle power setting (nozzle throat at maximum afterburning), its performance approached or exceeded the other afterbodies for most nozzles.

The afterbody axial force for the short interfairing afterbody (afterbody 2) was always the highest of the three afterbodies. This result is probably due to lower pressures on the afterbody portion of the model which would be expected as a result of the steeper slopes indicated by the area distributions shown in figure 4(e).

Effect of engine lateral spacing.- The effect of engine lateral spacing on gross thrust minus nozzle axial force, gross thrust minus afterbody and nozzle axial force, and afterbody axial force is shown in figure 37 for four nozzle types at selected Mach numbers and typical jet total-pressure ratios. With exception of $M = 1.3$, increasing engine lateral spacing generally increased gross thrust minus nozzle axial force for all four nozzle types as a result of decreased mutual jet interference and nozzle drag. At $M = 1.3$, gross thrust minus nozzle axial force decreased for the military power nozzle setting and generally increased for the maximum afterburning power nozzle setting with increasing engine lateral spacing. Mixed results were obtained at the partial afterburning power nozzle setting at $M = 1.3$.

Afterbody axial force (drag) increased substantially with increasing engine lateral spacing for all nozzle types. Since nozzle area or base area is constant for all afterbodies, the resultant afterbody closure area increases with increasing engine lateral spacing (increasing maximum cross-sectional area) and thus is the probable cause of the increase in afterbody axial force. This result is probably not valid if closure area does not increase (for example, two nacelles connected by a flat plate or a close approximation of such).

Increased engine lateral spacing substantially decreases gross thrust minus afterbody and nozzle axial force for all nozzle types and power settings, particularly at $M = 0.9$ and $M = 1.3$, as a result of increasing afterbody axial force (drag).

Plug nozzle performance with fixed end floating shroud flaps.- A comparison of the installed performance of plug nozzles having a shroud with fixed (nozzle 3) and floating (nozzle 6) tail flaps is presented in figure 38. The data show that the fixed-shroud plug nozzle (nozzle 3) had thrust minus nozzle drag performance which was generally 1 to 2 percent greater than the aerodynamically controlled floating flap shroud plug nozzle (nozzle 6). By comparing the data taken at static conditions (figs. 14(c) and 14(f)), the same difference in performance is noted. This condition indicates that the loss in nozzle efficiency is probably due to leakage through the flap linkage although no data are available to confirm this assumption.

CONCLUDING REMARKS

An investigation of the installed performance of a generalized twin-jet afterbody-exhaust nozzle model has been conducted in the Langley 16-foot transonic tunnel and the

Langley 4- by 4-foot supersonic pressure tunnel statically and at Mach numbers of 0.6 to 1.3 and 2.2. The effects of exhaust-nozzle design, nozzle operation, and lateral spacing on the gross thrust minus afterbody plus nozzle drag performance and the effects of afterbody geometric shaping on exhaust-nozzle performance are presented. An iris-convergent nozzle generally had the highest thrust minus total afterbody drag performance and thrust minus nozzle drag performance for all afterbodies at subsonic Mach numbers; whereas no single nozzle type gave the highest performance when integrated with the different afterbodies at supersonic speeds. However, a convergent-divergent-iris nozzle concept generally showed competitive performance when compared with other nozzles. An afterbody with the generalized clean external contours and with the engine center lines arranged to represent minimum amount of lateral spacing had the highest installed performance for nearly all test conditions. An afterbody similar to a twin-jet-fighter-type airplane with long engine interfairing and stabilizer actuator fairings extending downstream of the nozzles had the lowest performance at the lower power settings but was competitive at maximum afterburning power settings. Increasing engine lateral spacing along with maximum cross-sectional area (increasing closure area) generally increases afterbody drag force, slightly increases thrust minus nozzle drag force (decreases nozzle drag), and decreases thrust minus afterbody plus nozzle drag force.

Pressure instrumented faired end caps were tested on each afterbody to provide local flow-field information which would affect installed nozzle performance. Surfaces adjacent to the faired end caps (such as extended tail actuator fairings) generally decreases the end-cap pressure and thus increases the drag. As the adjacent surface area increases, the end-cap drag also increases. Study of the end-cap pressures infers that by proper tailoring of both afterbody and nozzle contours, beneficial thrust terms can be obtained on the nozzles at subsonic speeds. Afterbodies designed to reduce afterbody drag by providing low closure slopes on the afterbody may result in substantially increasing the end-cap drag at subsonic speeds. Although the drag of this type of afterbody may result in the lowest afterbody drag, it may not result in the optimum afterbody-nozzle combination. Thus, separately designed optimum afterbodies and optimum nozzles may not result in the optimum (lowest total drag) afterbody nozzle when combined and emphasizes the need for tests which include powered nozzles in an actual airplane flow field to determine the optimum configuration.

Langley Research Center,
National Aeronautics and Space Administration,
Langley Station, Hampton, Va., May 28, 1969,
126-63-11-22-23.

REFERENCES

1. Schmeer, James W.; Lauer, Rodney F., Jr.; and Berrier, Bobby L.: Performance of Blow-in-Door Ejector Nozzles Installed on a Twin-Jet Variable-Wing-Sweep Fighter Airplane Model. NASA TM X-1383, 1967.
2. Armstrong, R. S.; and Miller, S. R.: Subsonic Aerodynamic Performance of Nozzle Installations in Supersonic Airplanes. AIAA Paper No. 67-452, July 1967.
3. Re, Richard J.; Wilmoth, Richard G.; and Runckel, Jack F.: Investigation of Effects of Afterbody Closure and Jet Interference on the Drag of a Twin-Engine Tactical Fighter. NASA TM X-1382, 1967.
4. Mercer, Charles E.; Pendergraft, Odis C., Jr.; and Berrier, Bobby L.: Effect of Geometric Variations on Performance of a Twin-Jet Blow-In-Door Ejector Nozzle Installation. NASA TM X-1633, 1968.
5. Wilmoth, Richard G.; Norton, Harry T., Jr.; and Corson, Blake W., Jr.: Effect of Engine-Interfairing Modifications on the Performance of a Powered Twin-Jet Fighter-Airplane Model at Mach 1.20. NASA TM X-1534, 1968.
6. Berrier, Bobby Lee; and Wood, Frederick H., Jr.: Effect of Jet Velocity and Axial Location of Nozzle Exit on the Performance of a Twin-Jet Afterbody Model at Mach Numbers Up to 2.2. NASA TN D-5393, 1969.
7. Love, Eugene S.; Grigsby, Carl E.; Lee, Louise P.; and Woodling, Mildred J.: Experimental and Theoretical Studies of Axisymmetric Free Jets. NASA TR R-6, 1969. (Supersedes NACA RM L54L31 by Love and Grigsby; RM L55J14 by Love; RM L56G18 by Love, Woodling, and Lee; and TN 4195 by Love and Lee.)
8. Bonner, E.; and Nixon, J. A.: Wind Tunnel Testing Techniques for Integrated Airframe-Exhaust Nozzle Systems. Tech. Rep. AFFDL-TR-68-94, U.S. Air Force, July 1968.
9. Shapiro, Ascher H.: The Dynamics and Thermodynamics of Compressible Fluid Flow. The Ronald Press Co.
Vol. I, c.1953.
Vol. II, c.1954.

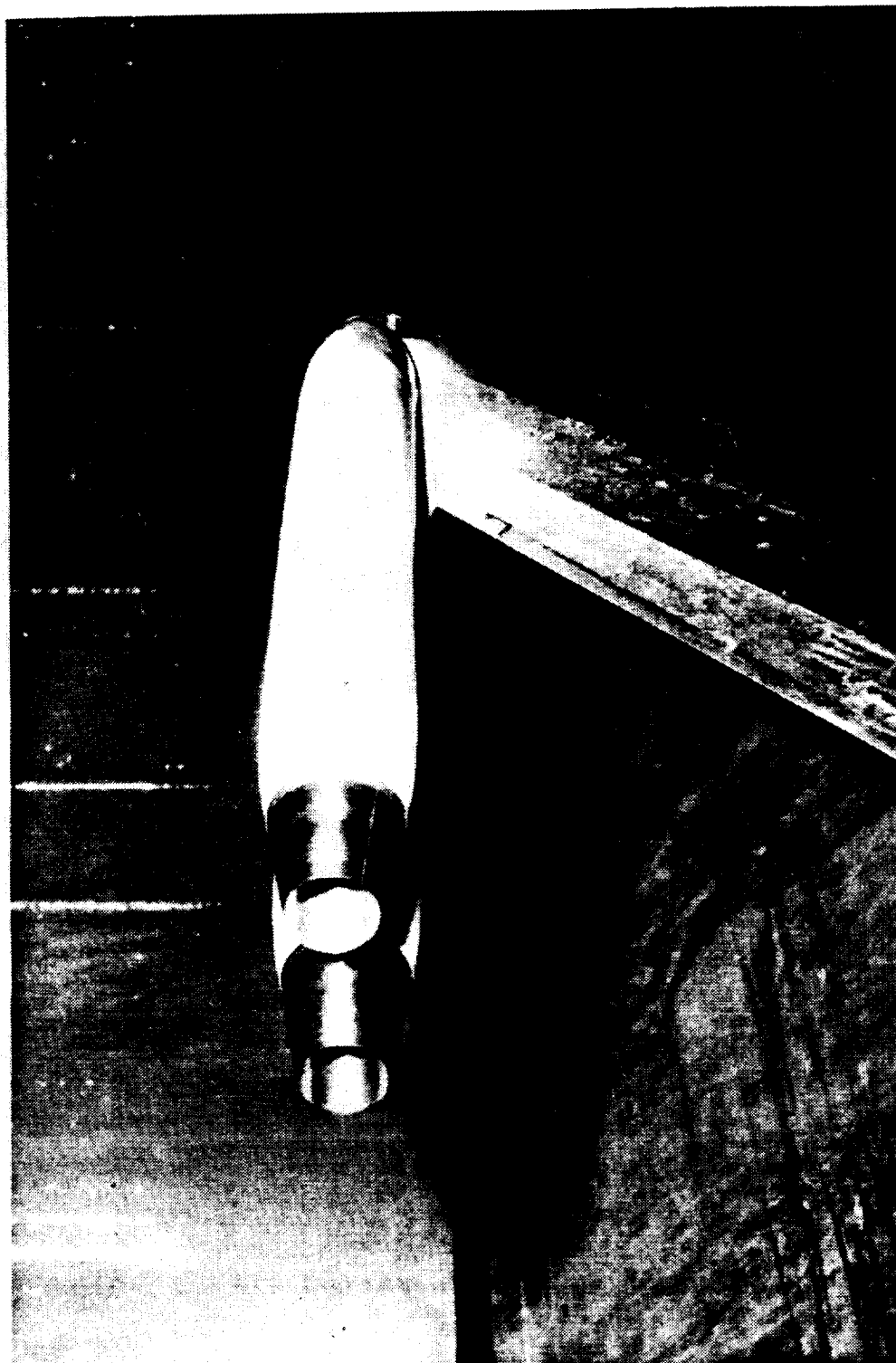
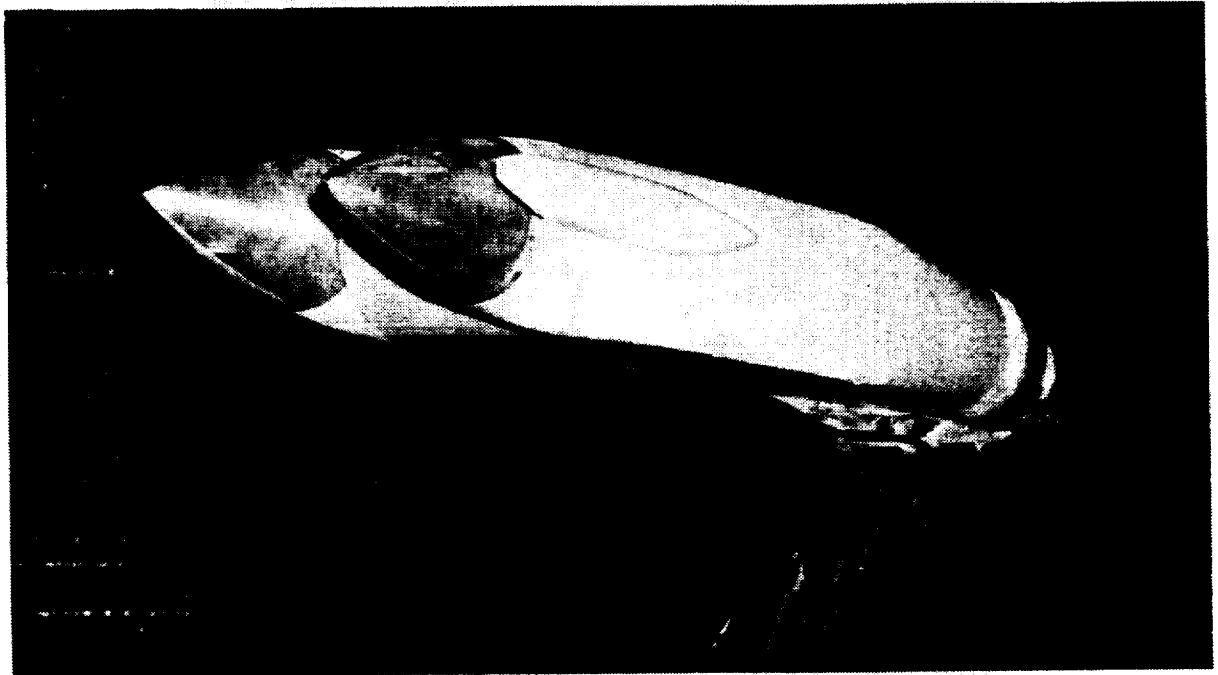
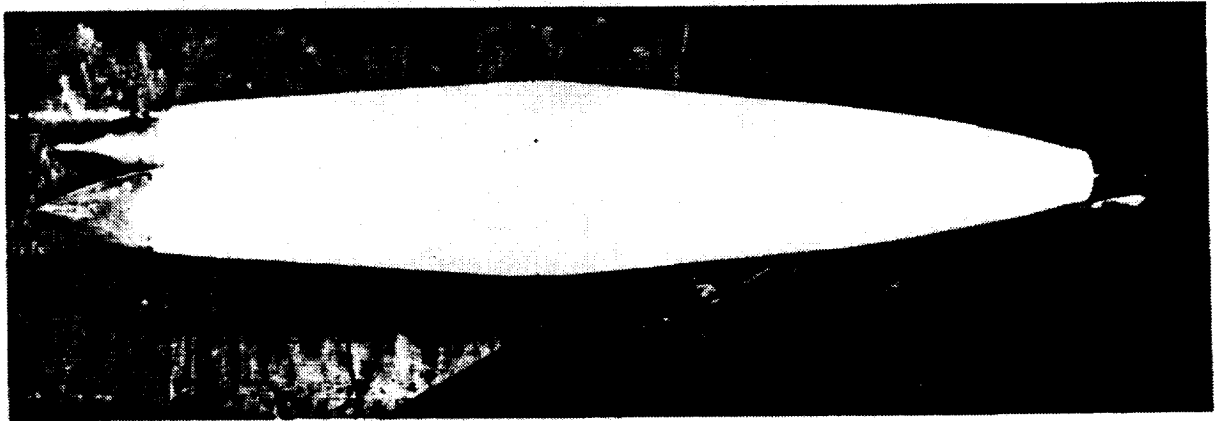


Figure 1.- Photograph of afterbody 4 with convergent-divergent nozzle (Configuration 421) mounted in the Langley 16-foot transonic tunnel. L-68-5442



(a) Afterbody 2.

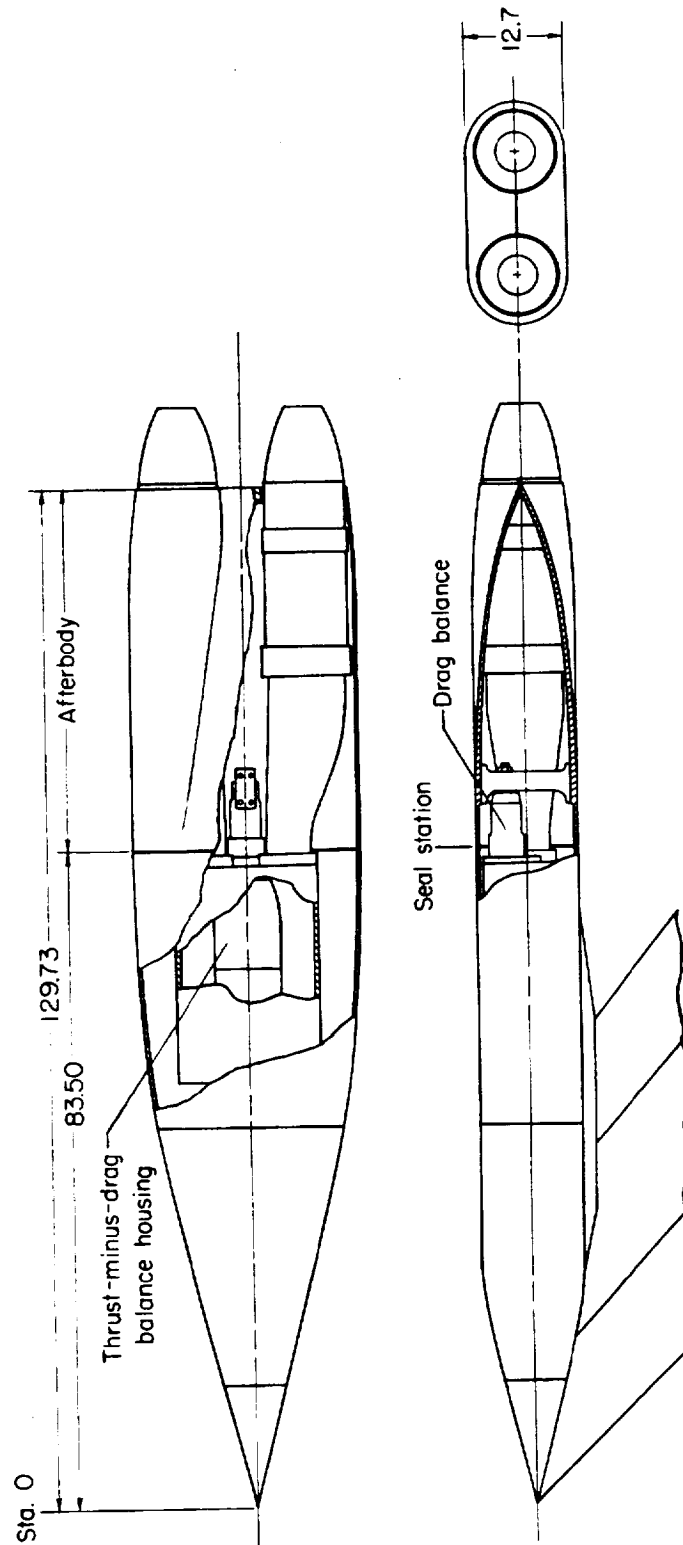
L-68-4129



(b) Afterbody 3.

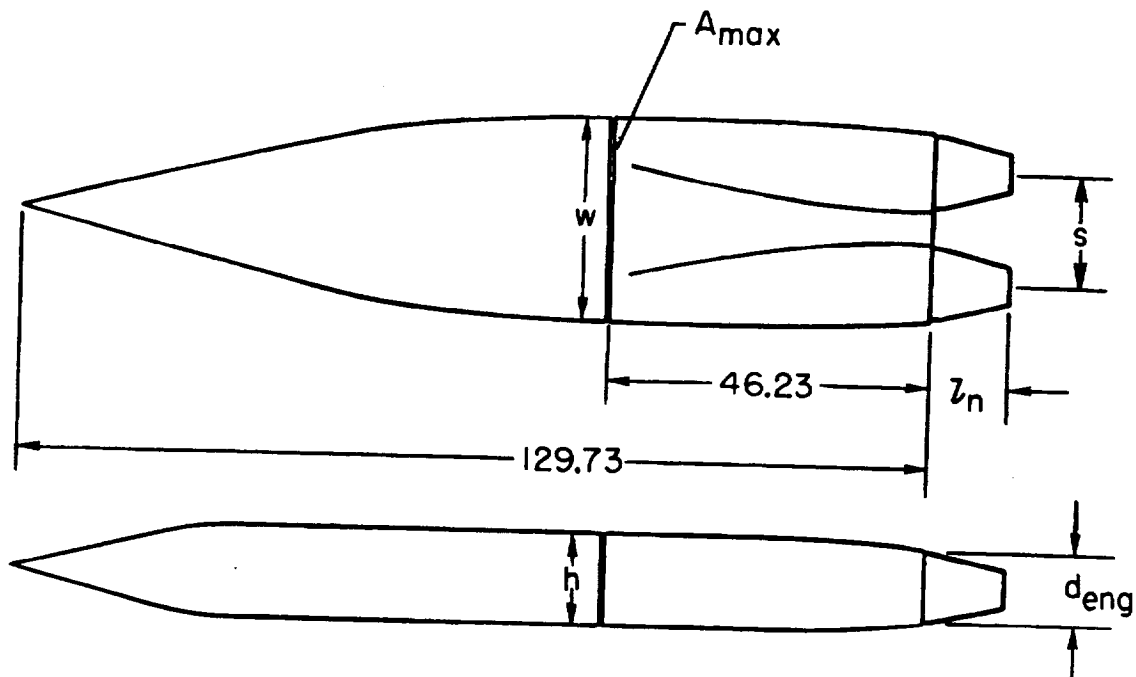
L-68-3761

Figure 2.- Photographs of two afterbodies with faired end caps mounted in the Langley 16-foot transonic tunnel.



(a) Sketch of twin-jet two-balance model.



Figure 3.- Sketches and photographs of twin-jet model and model components. All dimensions are in centimeters.



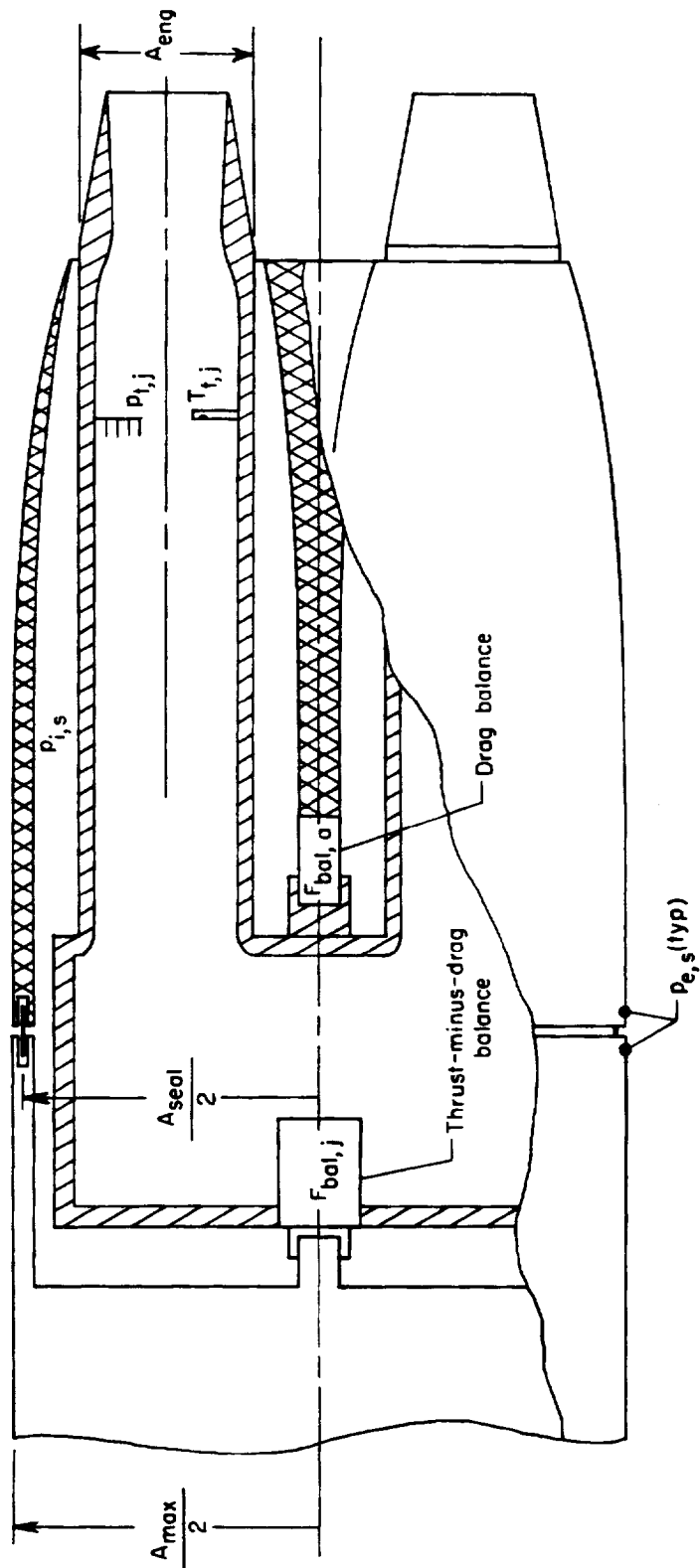
Parameter	Fuselage type				
	1	2	3	4	5
$A_{max} \text{ cm}^2$	320.92	320.92	320.92	326.73	417.06
$A_{max}/2A_{eng}$	2.05	2.05	2.05	2.09	2.66
w/h	2.00	2.00	2.00	2.24	2.80
s/d_{eng}	1.29	1.29	1.29	1.57	2.90
$A_{t,t}/A_{max}$					
Dry	.11	.11	.11	.11	.09
Partial	.19	.19	.19	.19	.15
Max	.26	.26	.26	.26	.20

(b) Geometric parameters.

Figure 3.- Continued.

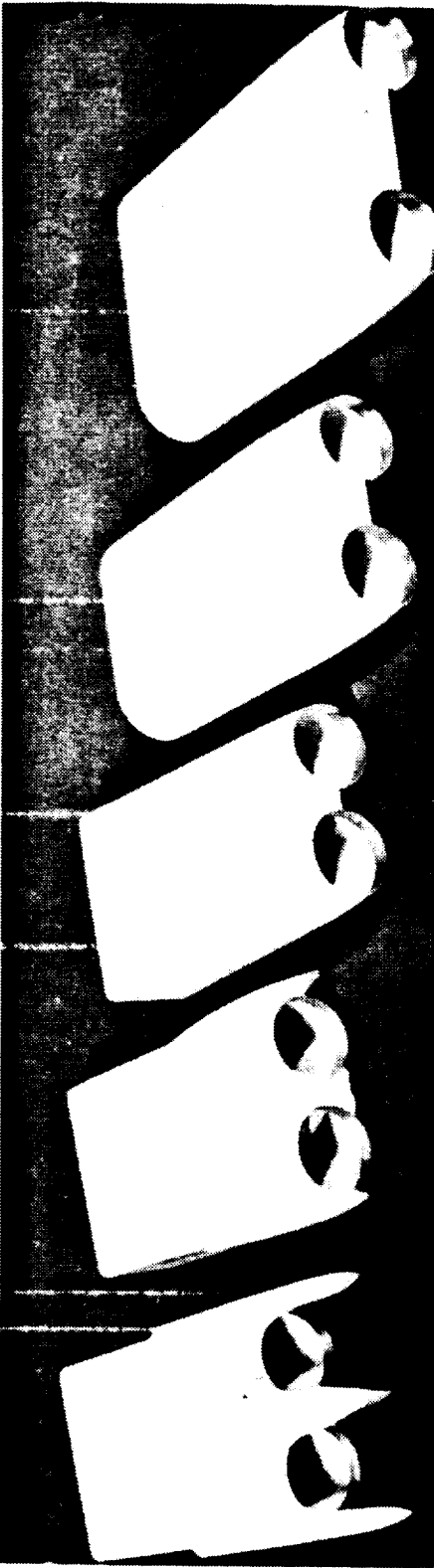
 Thrust-minus-drag balance
 Drag balance

p_{a0}

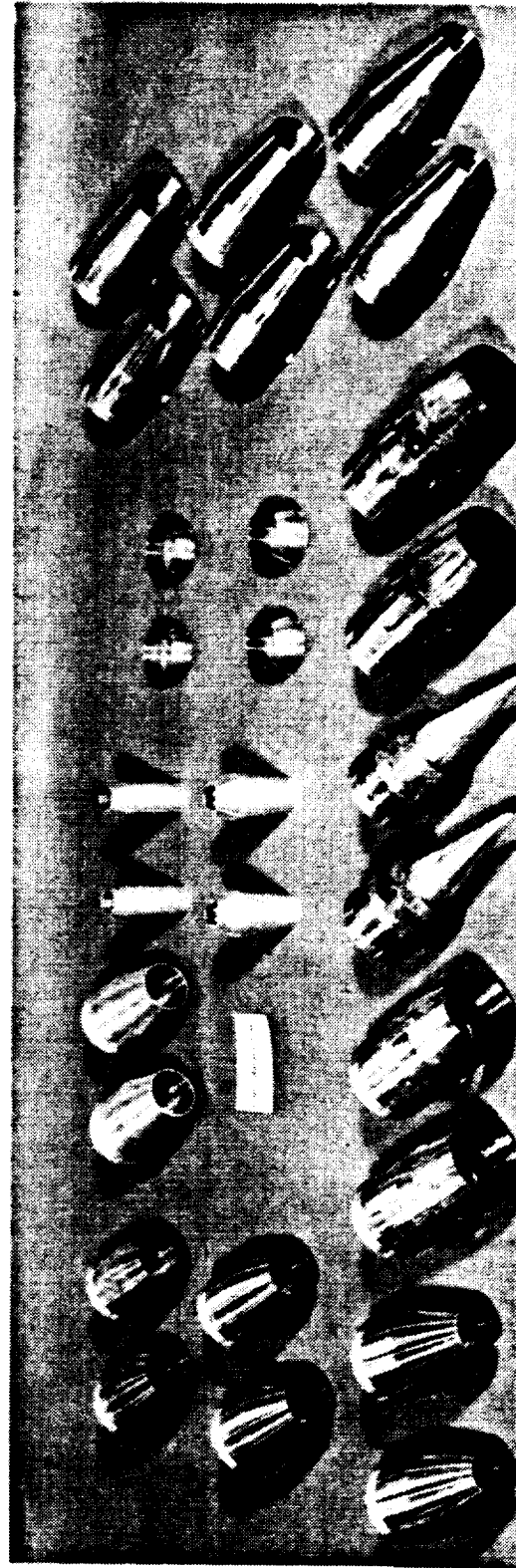


(c) Arrangement of the two force balances.

Figure 3.- Continued.



1 2 3 4 5
Afterbodies
L-68-3470

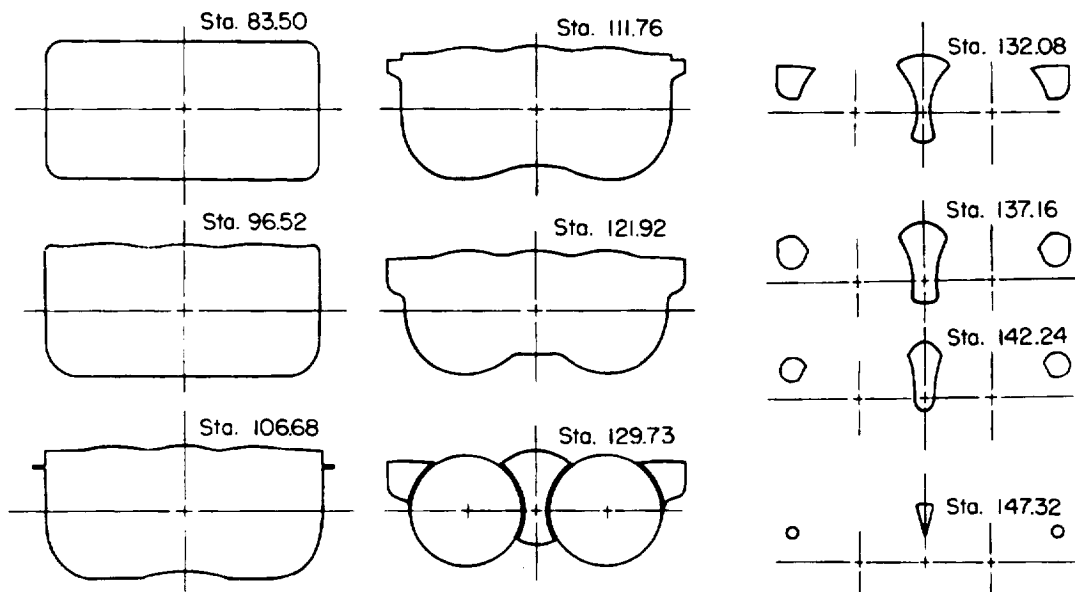
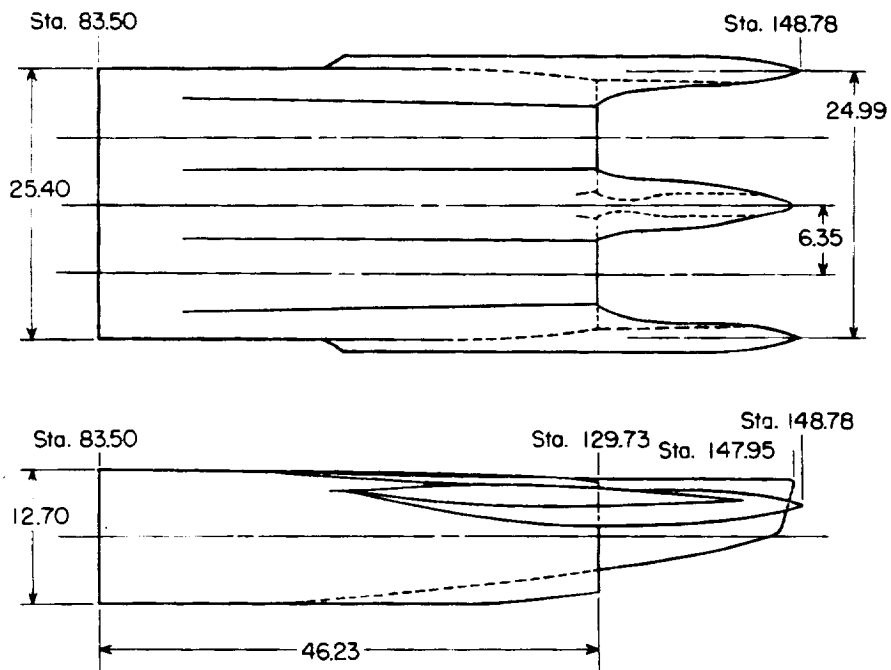


Iris-convergent Reference blow-in-door Plug Nozzles
Blow-in-door Convergent-divergent

(d) Model afterbodies and nozzles.

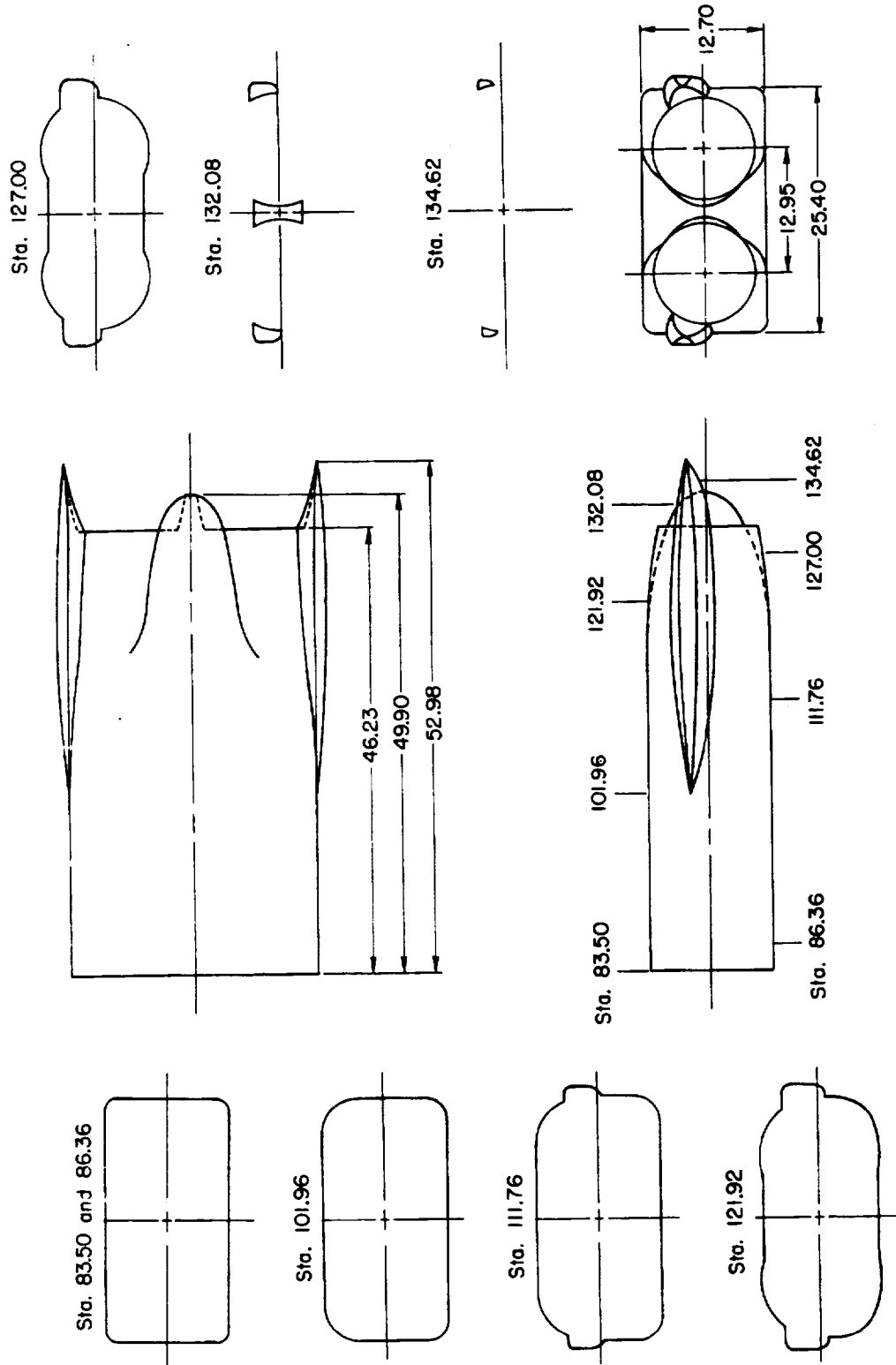
Figure 3.- Concluded.

L-68-3469

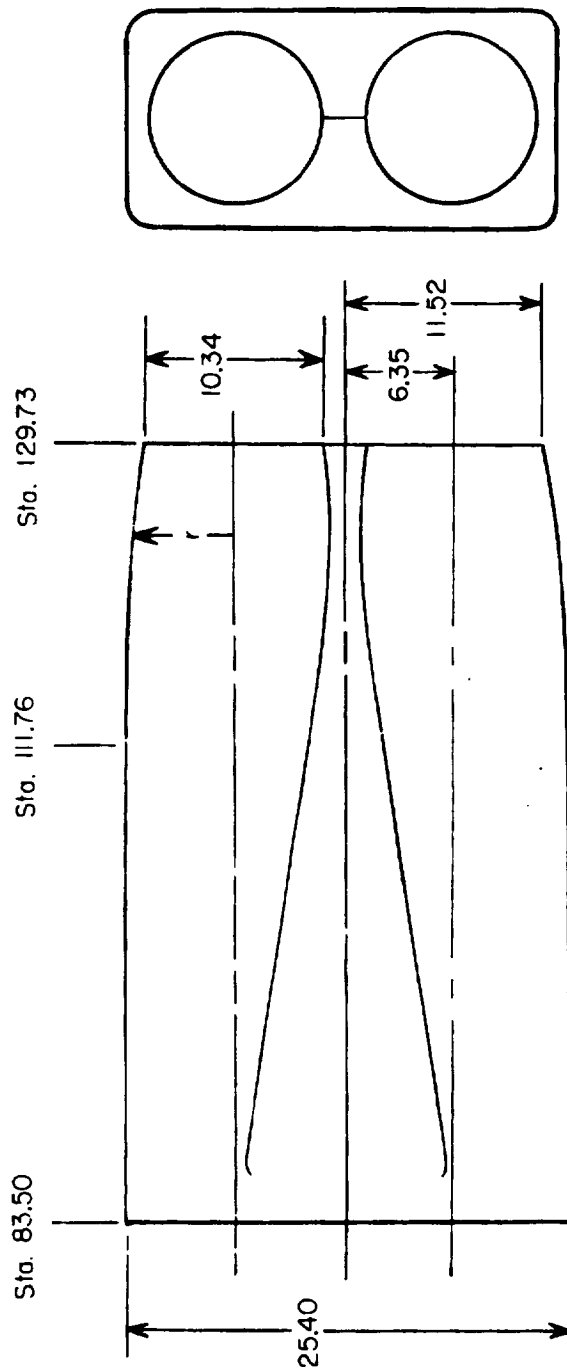


(a) Afterbody 1.

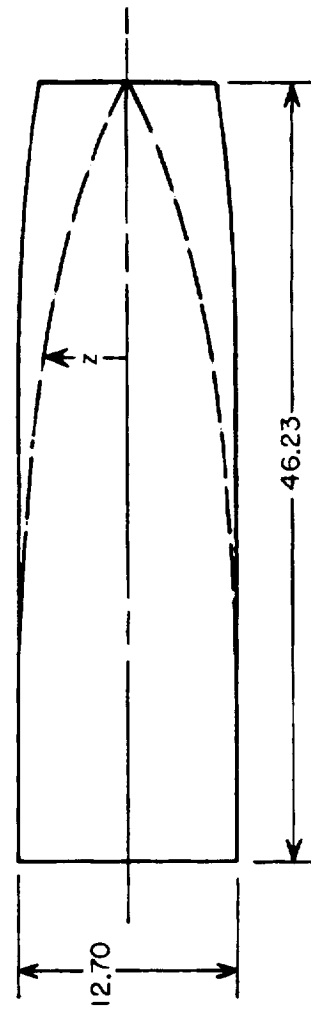
Figure 4.- Sketches of various afterbodies. All dimensions are in centimeters unless otherwise indicated.



(b) Afterbody 2.
Figure 4.- Continued.

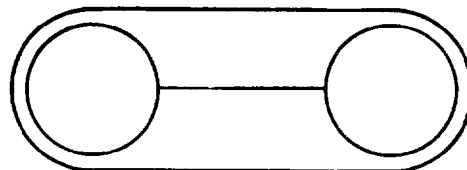
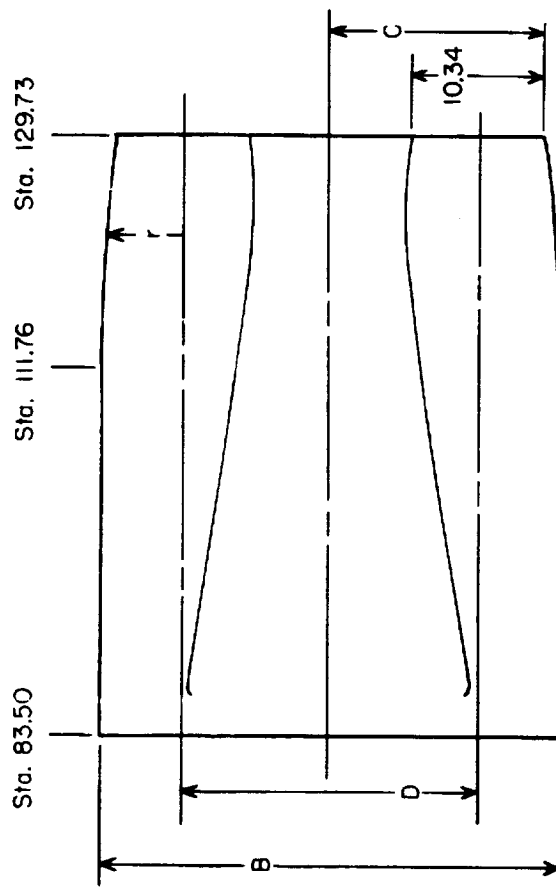


x_0	z	r
86.36	6.35	6.35
91.44	6.30	6.35
96.52	6.18	6.35
101.60	6.01	6.35
106.68	5.68	6.35
111.76	5.14	6.35
116.84	4.36	6.29
121.92	3.16	6.03
127.00	1.41	5.55
129.73	0	5.17



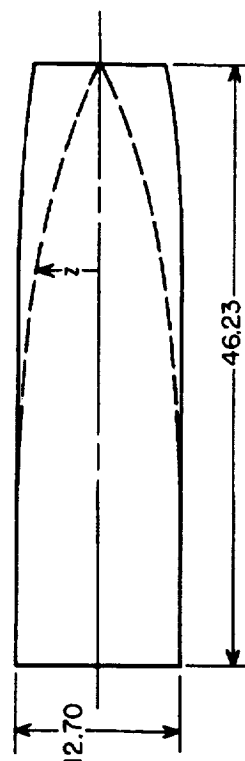
(c) Afterbody 3.

Figure 4.- Continued.

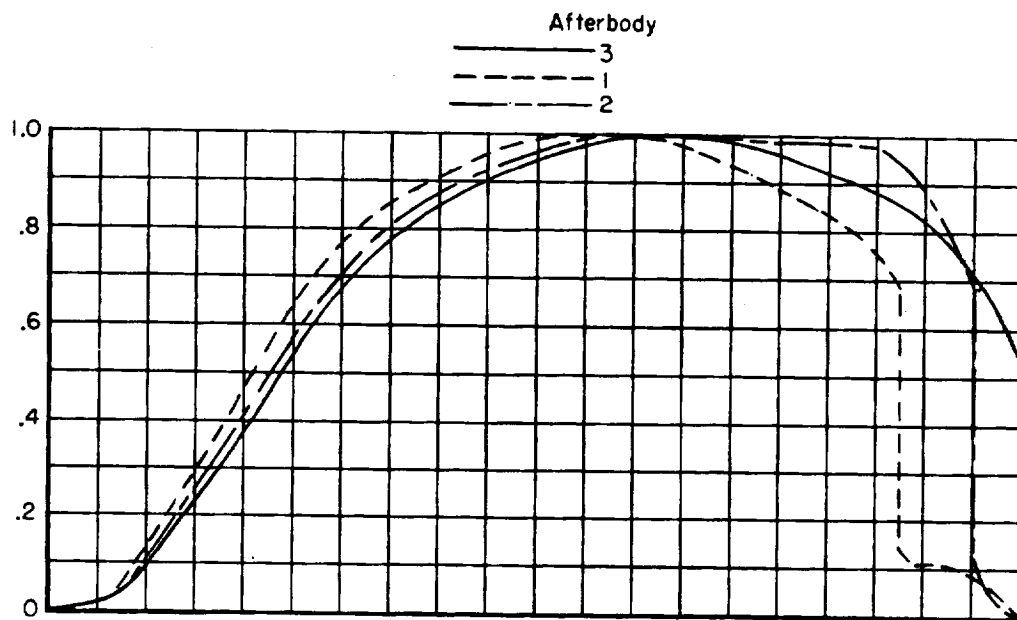


Afterbody	B	C	D
4	28.45	15.75	13.04
5	35.56	22.86	16.60

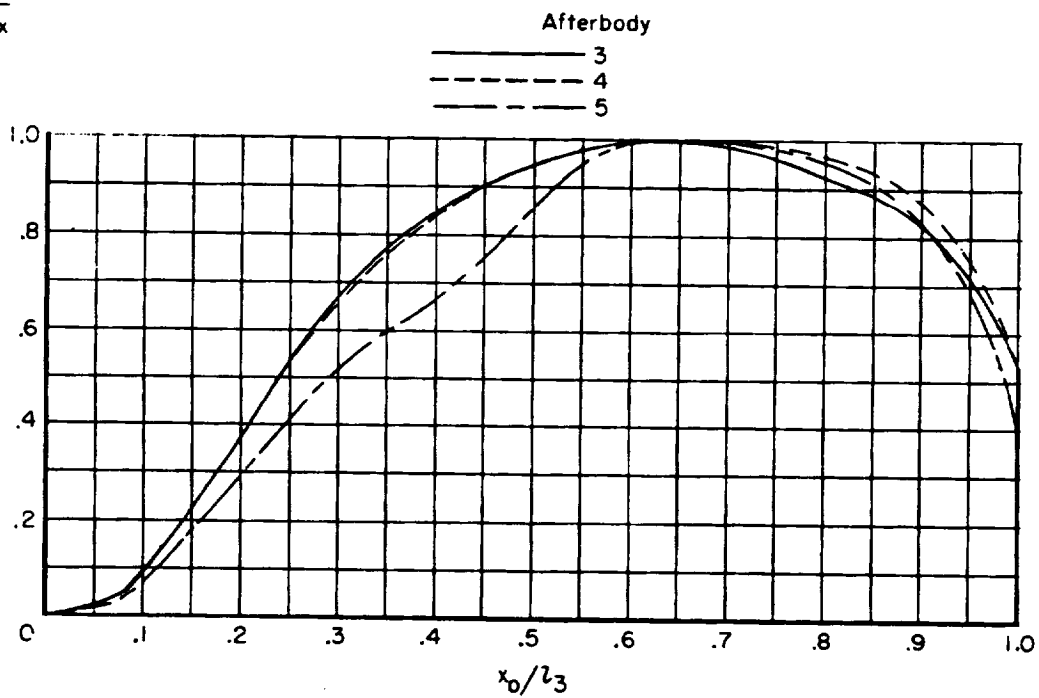
x_0	z	r
86.36	6.35	6.35
91.44	6.30	6.35
96.52	6.18	6.35
101.60	6.01	6.35
106.68	5.68	6.35
111.76	5.14	6.35
116.84	4.36	6.29
121.92	3.16	6.03
127.00	1.41	5.55
129.73	0	5.17



CONFIDENTIAL



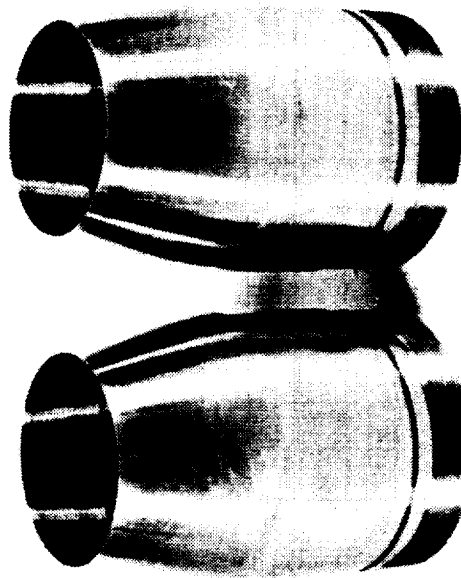
$\frac{A}{A_{max}}$



(e) Cross-sectional area distributions for the various fuselages. Nozzles excluded.

Figure 4.- Concluded.

CONFIDENTIAL

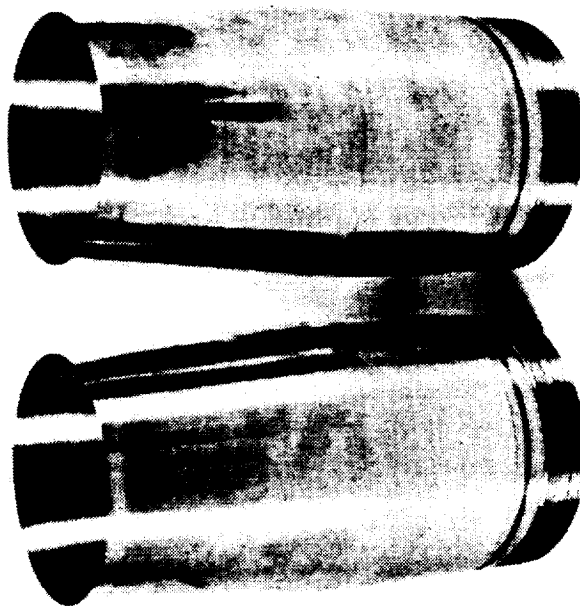
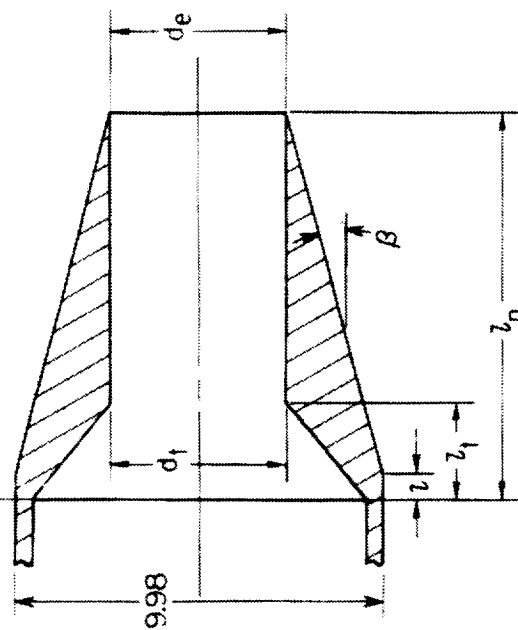


Power set	z_n	d_t	β , deg	z_n/d_{eng}	A_e/A_t	A_t
Dry	9.95	4.83	20.00	1.00	1.00	18.29
Partial	8.14	6.20	19.22	.82	1.00	30.17
Max	6.43	7.32	16.56	.64	1.00	42.03

(a) Iris-convergent nozzle. Nozzle 1.

Figure 5. Geometric parameters of various nozzle types. All dimensions are in centimeters.

Sta. 123.73

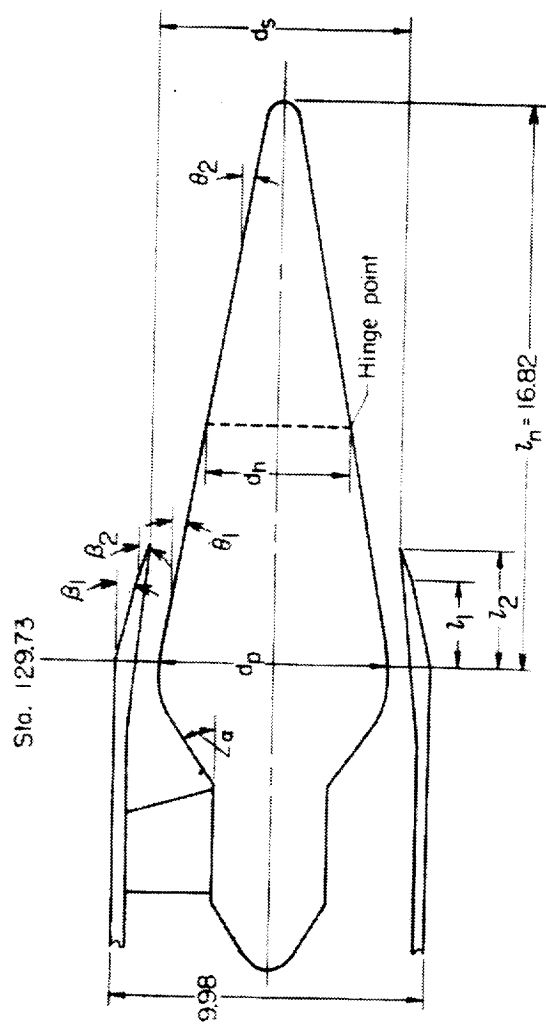


L 68-7663

Power set	z	z_1	z_n	β , deg	d_t	d_e	z_n/d_{eng}	A_e/A_t	A_t
Dry	0.71	2.86	10.95	14.0	4.83	4.83	1.10	1.00	18.29
Partial	1.16	3.27	11.16	8.8	6.20	6.86	1.12	1.22	30.17
Max	2.20	3.47	11.25	4.5	7.32	8.51	1.13	1.35	42.03

(b) Convergent-divergent nozzle. Nozzle 2.

Figure 5. Continued.



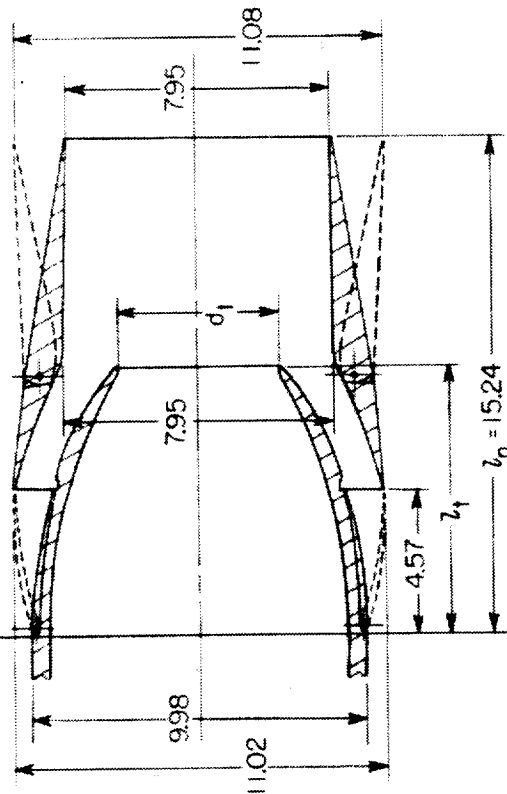
Power set	z_1	z_2	α	β_1	β_2	θ_1	θ_2	d_p	d_h	d_s	z_n/d_{eng}	A_e/A_t	A_1
Dry	2.86	3.98	34° 54'	13° 5'	19° 25'	10°	10°	7.27	—	7.82	1.68	2.63	18.29
Partial	2.87	4.04	22° 0'	7° 45'	13° 0'	5° 55'	10°	6.08	4.60	8.71	1.68	1.97	30.17
Max AB	2.85	4.05	11° 53'	0°	6° 15'	0° 42'	10°	4.78	4.60	9.63	1.68	1.73	42.03

L-68-7661

(c) Plug nozzle. Nozzle 3.

Figure 5.- Continued.

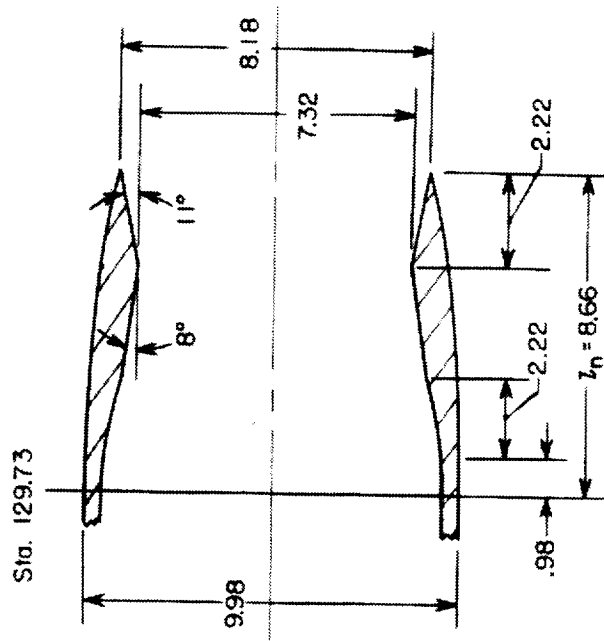
Sta. 129.73



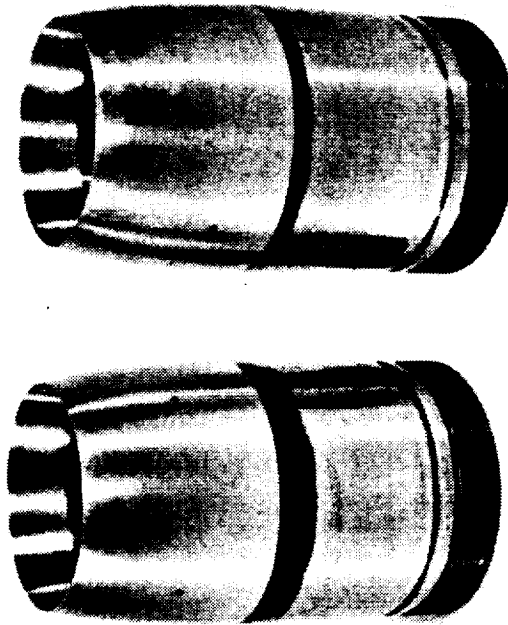
Power set	z_1	d_1	z_n/deg	A_e/A_t	A_t
Dry	8.28	4.83	1.53	2.71	18.29
Partial	7.47	6.20	1.53	—	30.17
Max AB	6.45	7.32	1.53	2.29	42.03

(d) Blow-in-door nozzle. Nozzle 4.

Figure 5.- Continued.



Power set	z_n	d_t	z_n/d_{eng}	A_e/A_t	A_t
Max	8.66	7.32	1.18	1.25	42.03

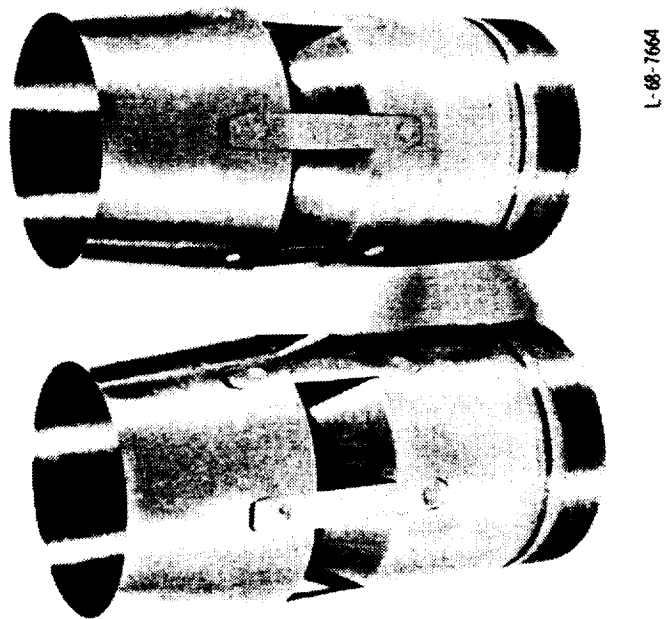


L-68-10 201

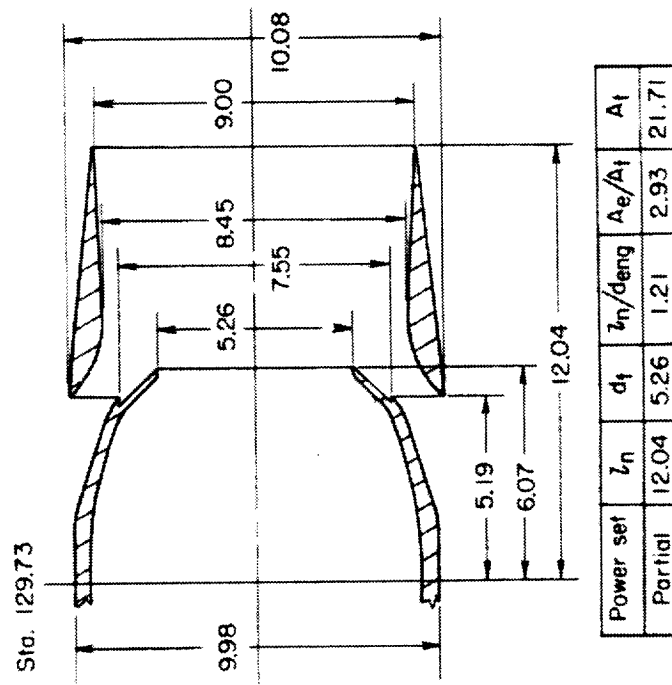
(e) Convergent-divergent iris nozzle. Nozzle 5.

Figure 5.- Continued.

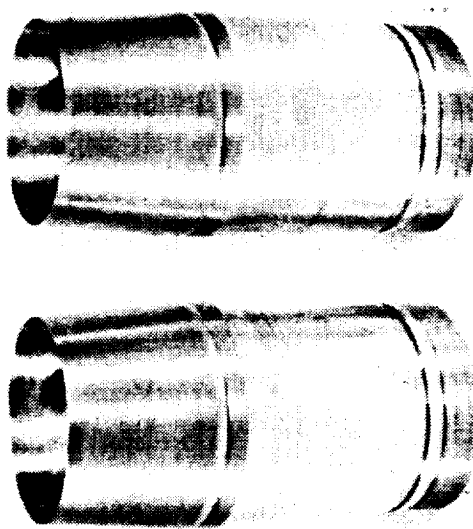
RESEARCH



L-68-7664



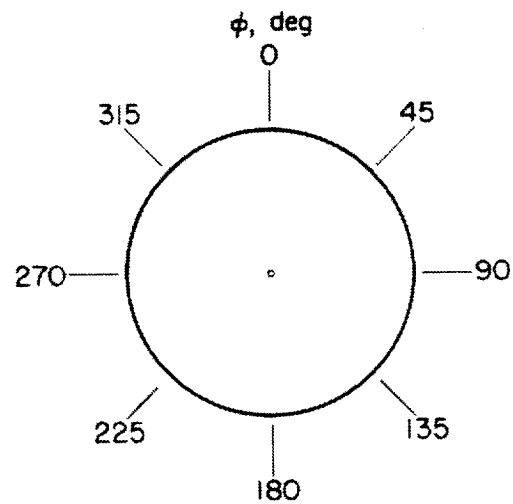
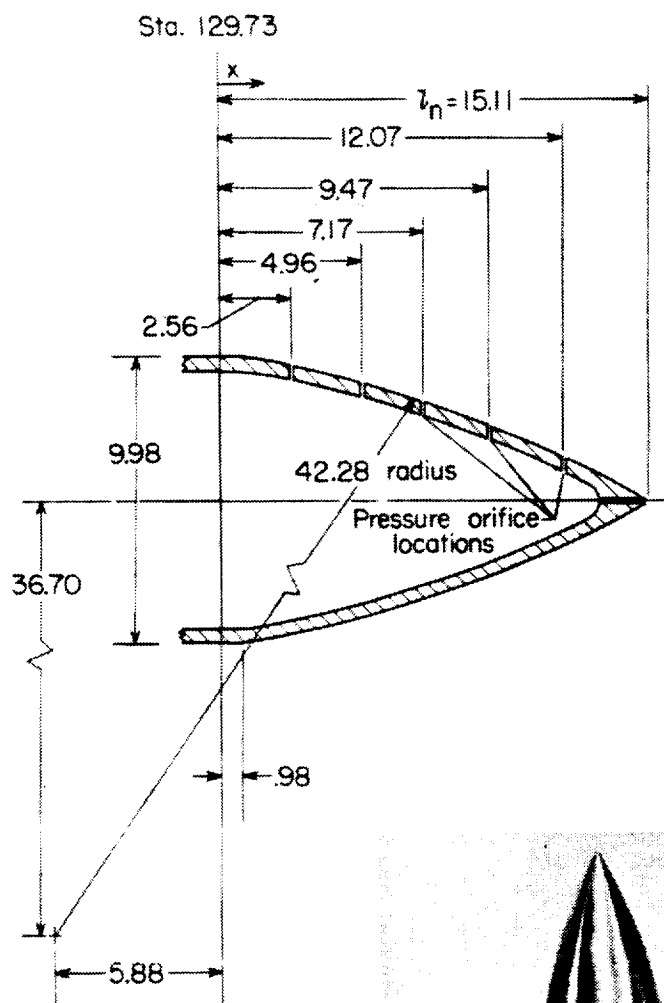
(f) Reference blow-in-door nozzle with doors fixed open. Nozzle 0.



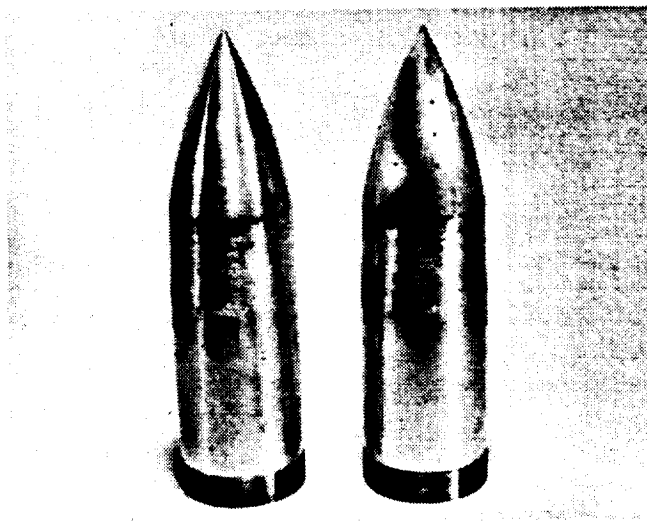
Power set	z_n	d_t	z_n/deng	A_e/A_t	A_t
Max	12.04	7.32	1.10	1.51	42.03

(g) Reference blow-in-door nozzle with doors fixed closed. Nozzle 0.

Figure 5.- Continued.



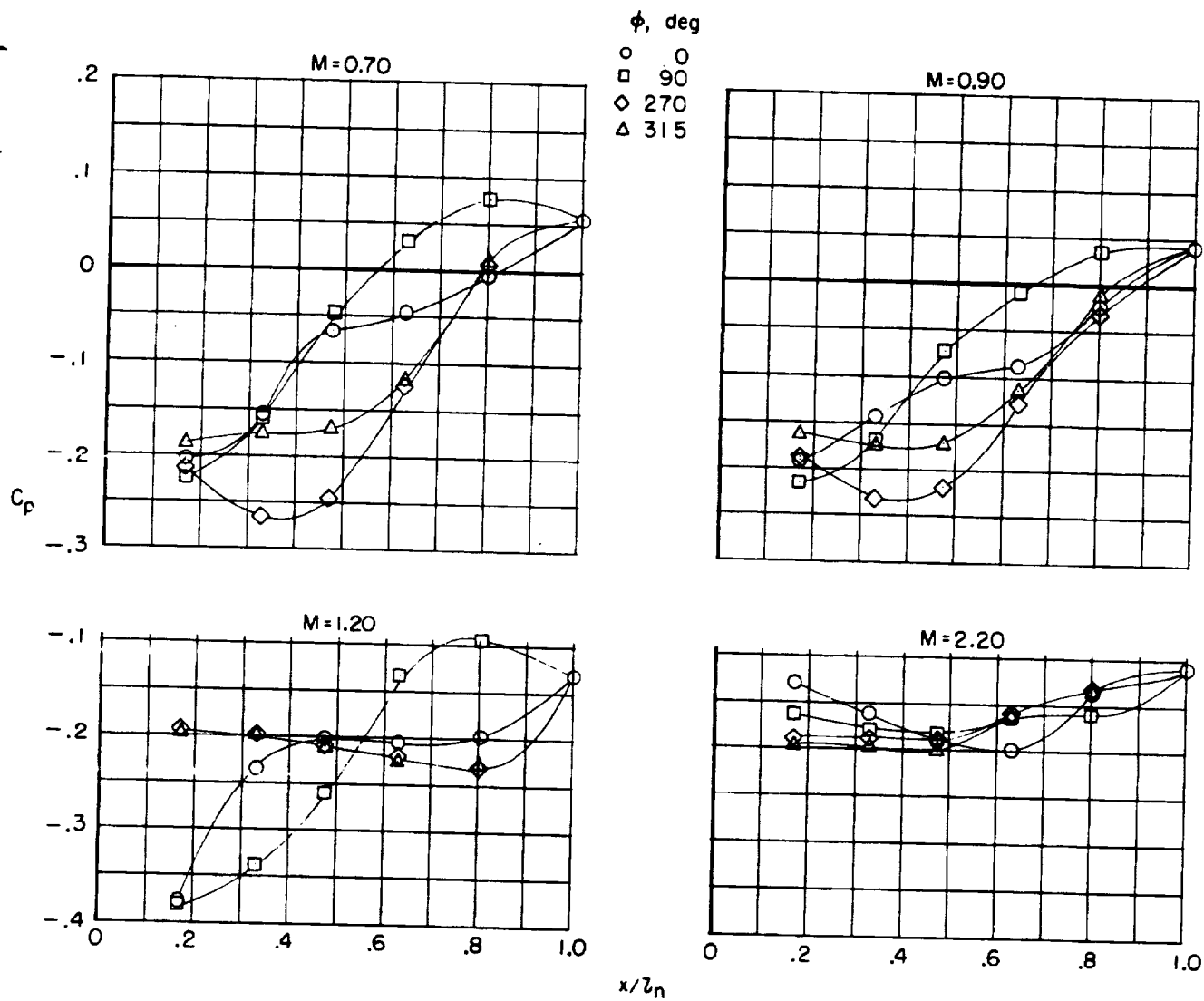
Right end cap looking upstream



(h) Faired end caps. Nozzle 7.

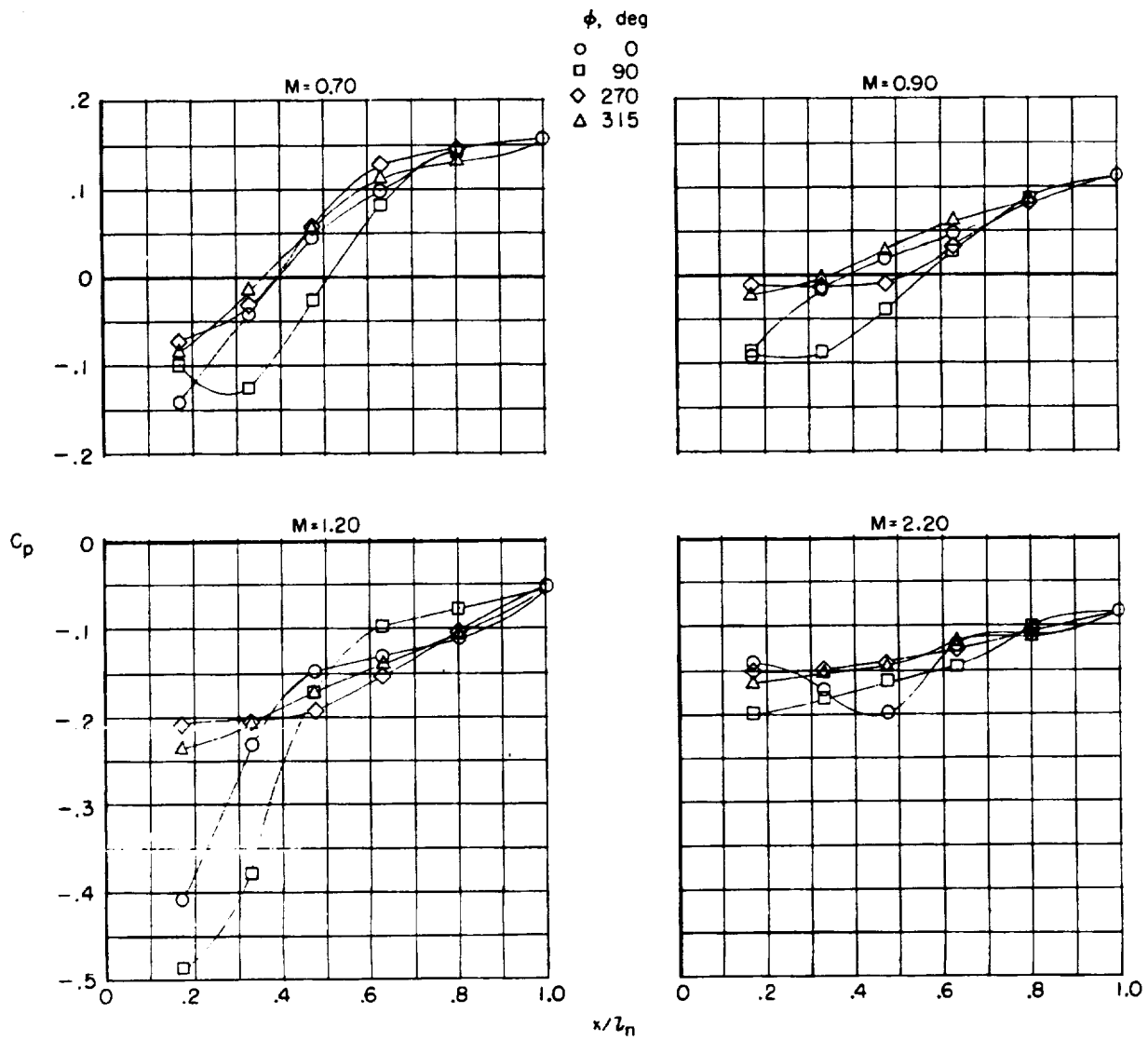
L-68-10 202

Figure 5.- Concluded.



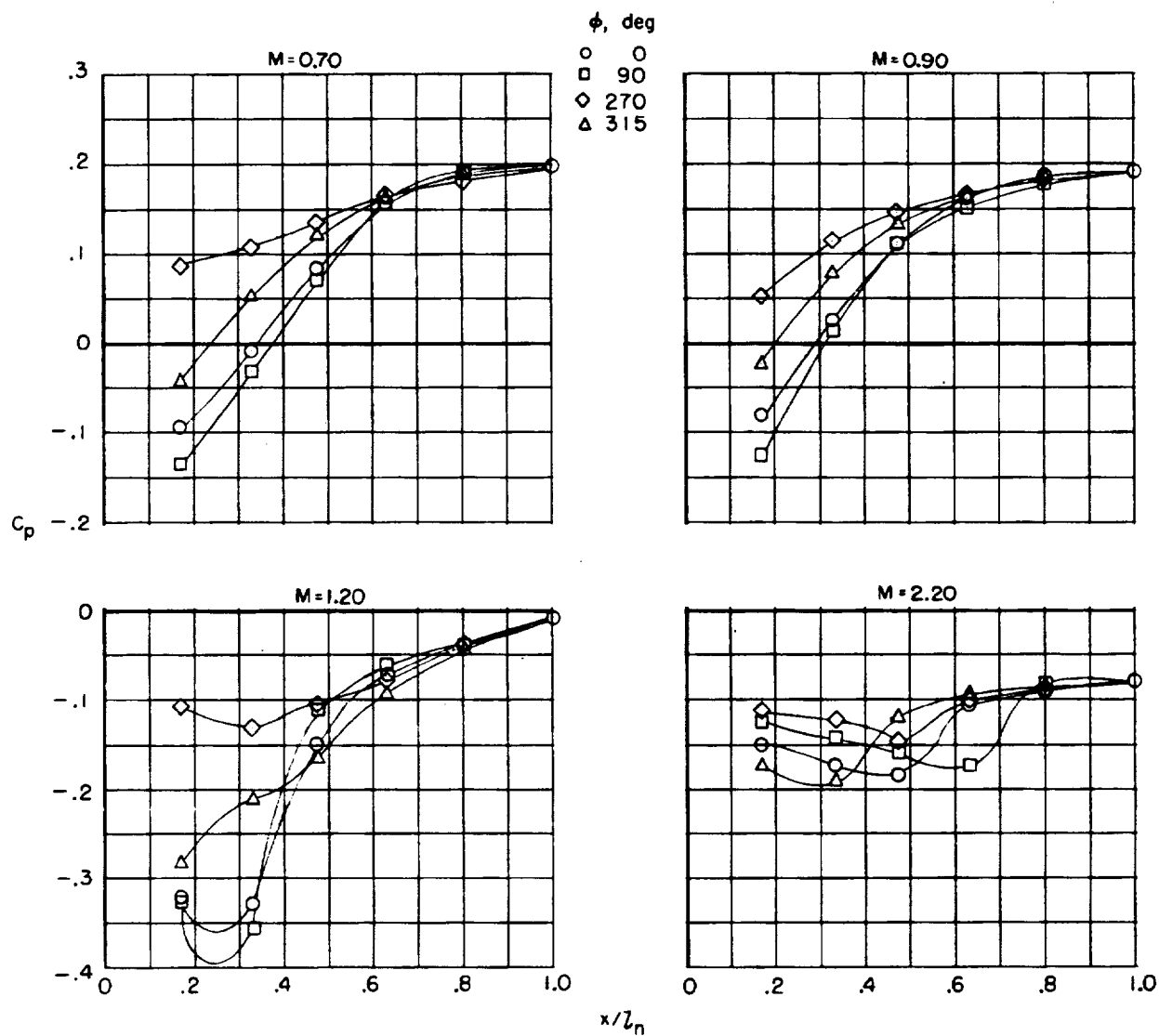
(a) Configuration 170.

Figure 6.- Typical pressure distributions on the faired end caps with the various afterbodies for several Mach numbers.



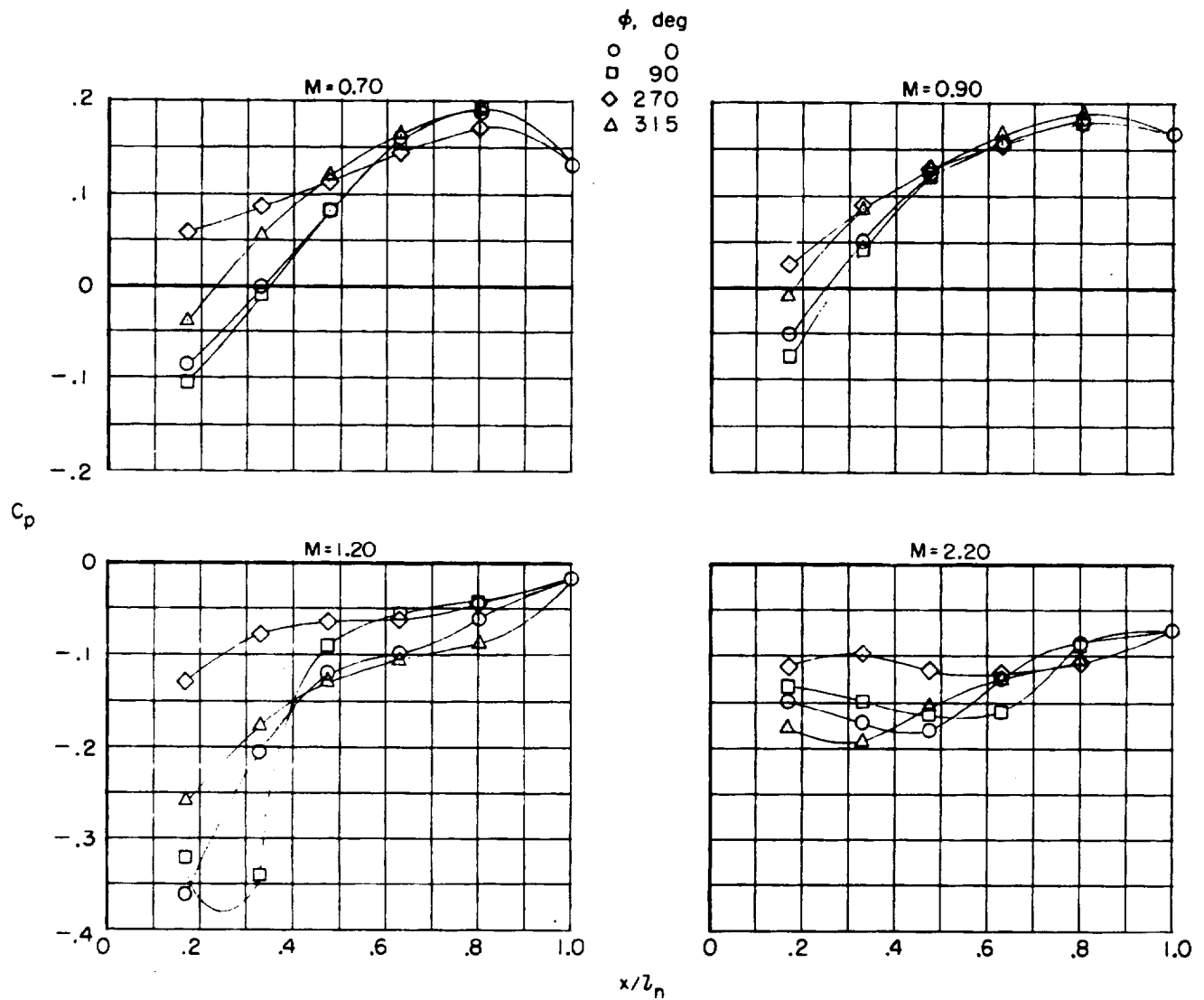
(b) Configuration 270.

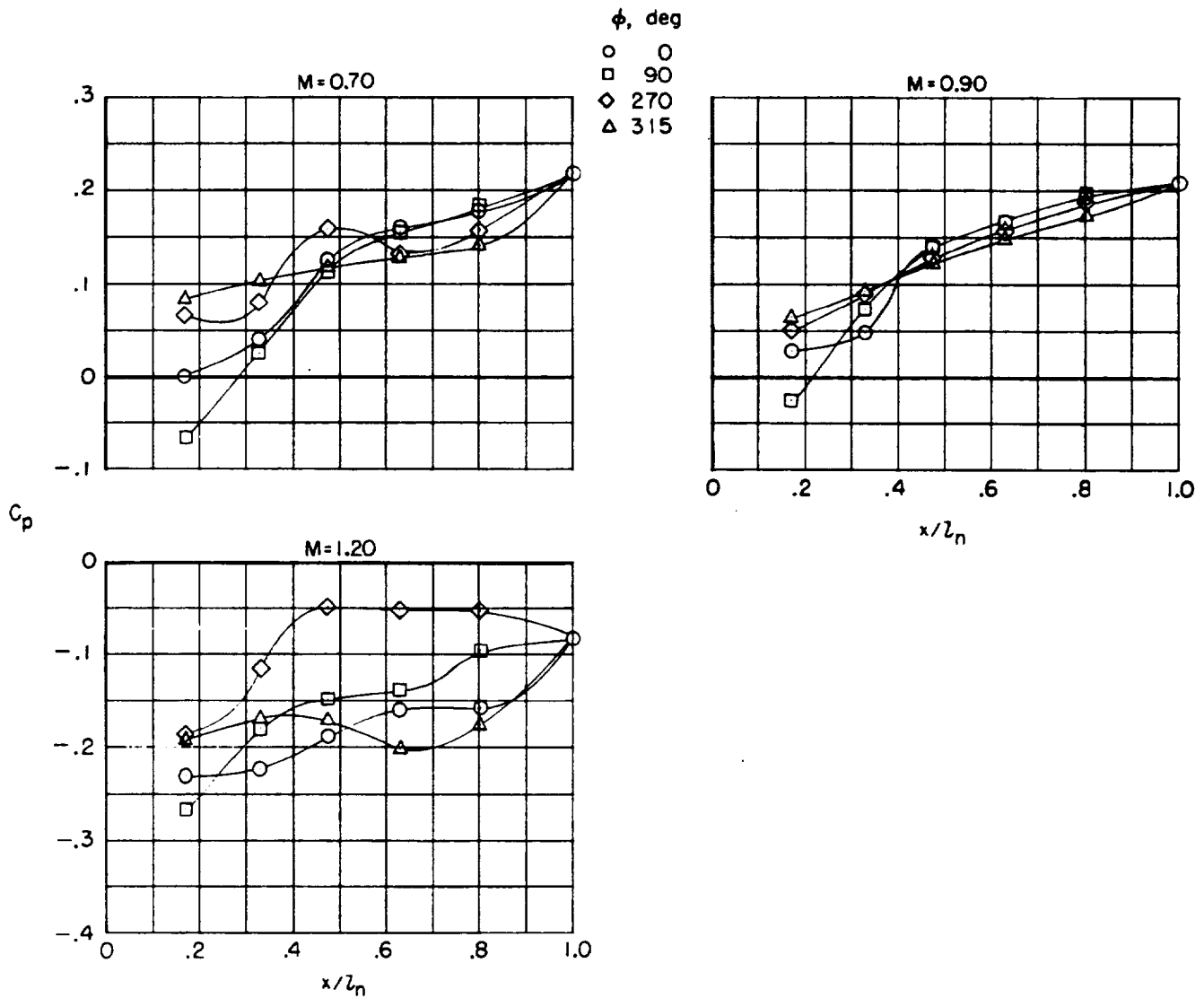
Figure 6.- Continued.



(c) Configuration 370.

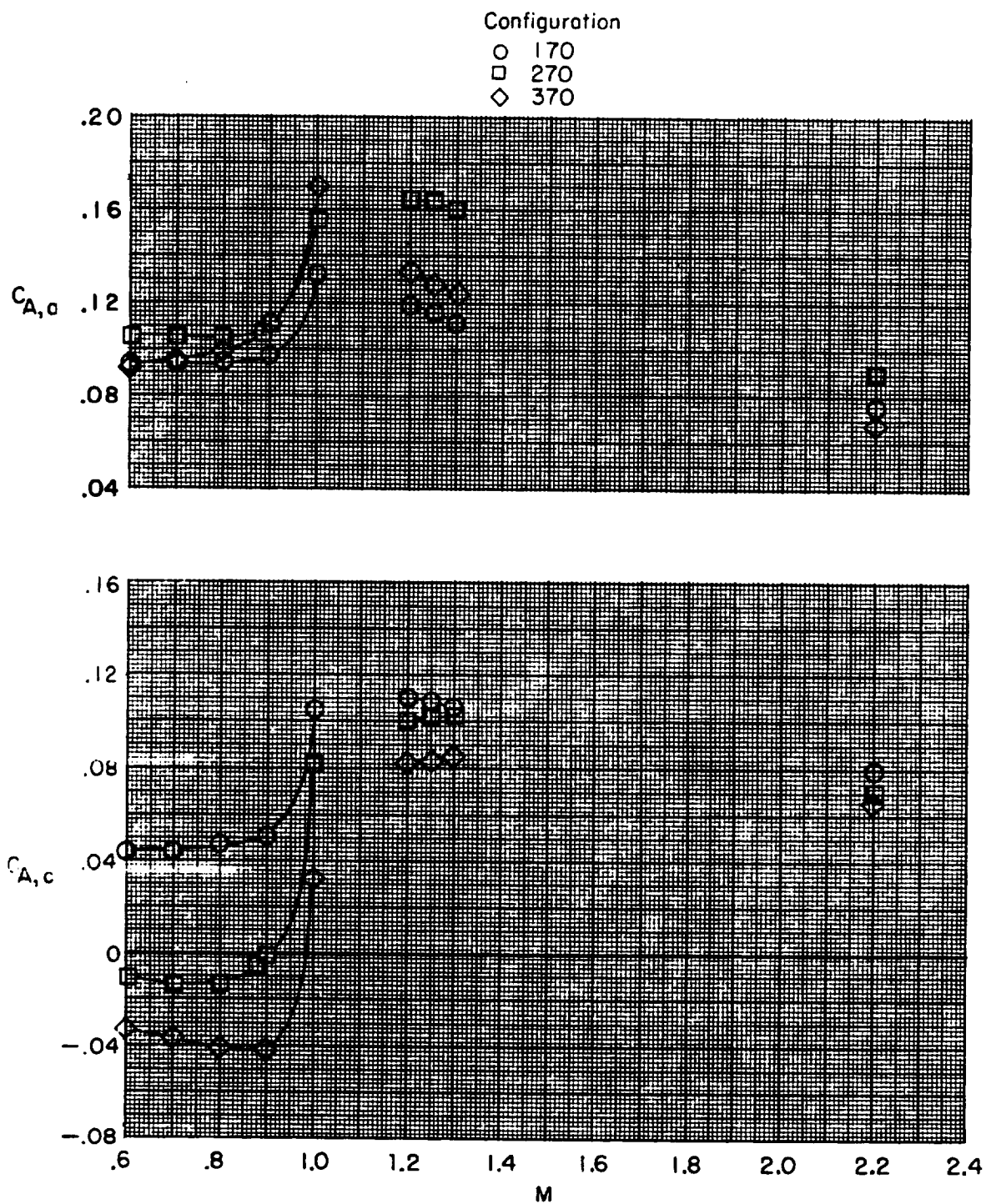
Figure 6.- Continued.





(e) Configuration 570.

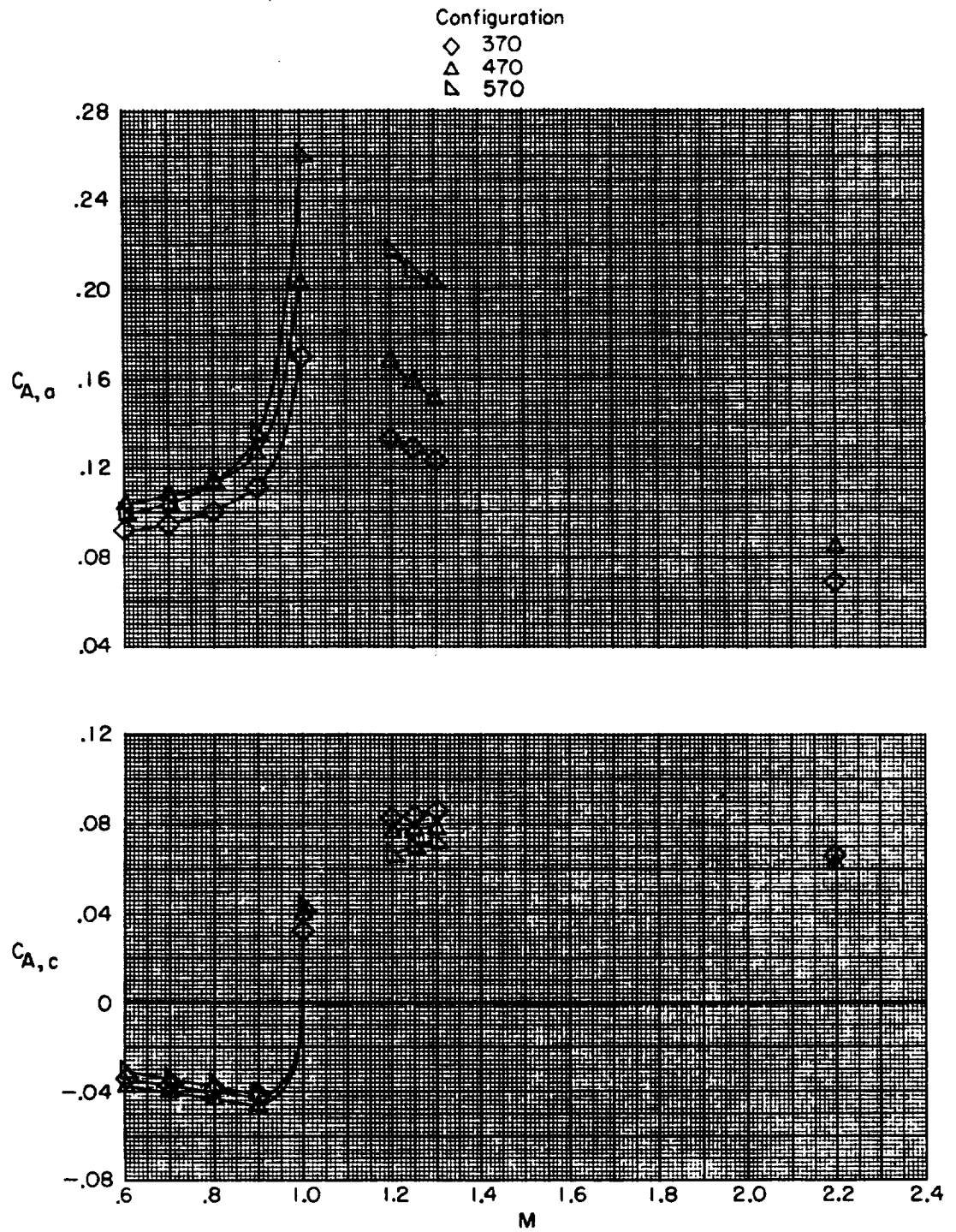
Figure 6.- Concluded.



(a) Complex geometry afterbodies.

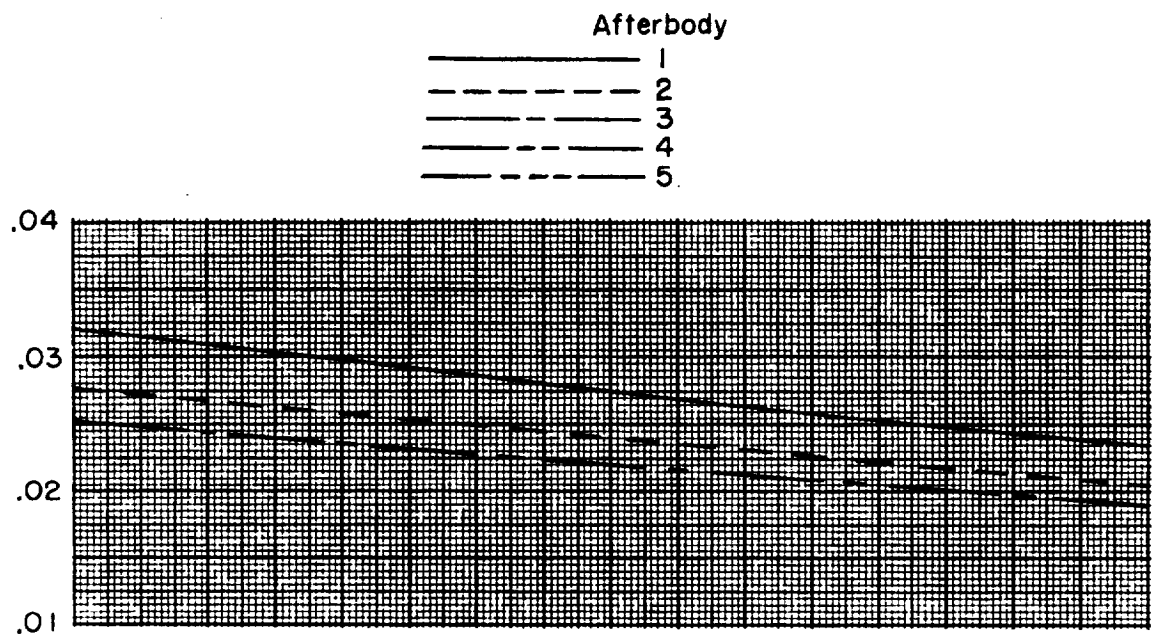
Figure 7.- Variation of afterbody and end-cap drag coefficient with Mach number for the various afterbodies. Nozzles replaced by faired end caps.

CONFIDENTIAL



(b) Lateral spacing afterbodies.

Figure 7.- Concluded.



$C_{A,f}$

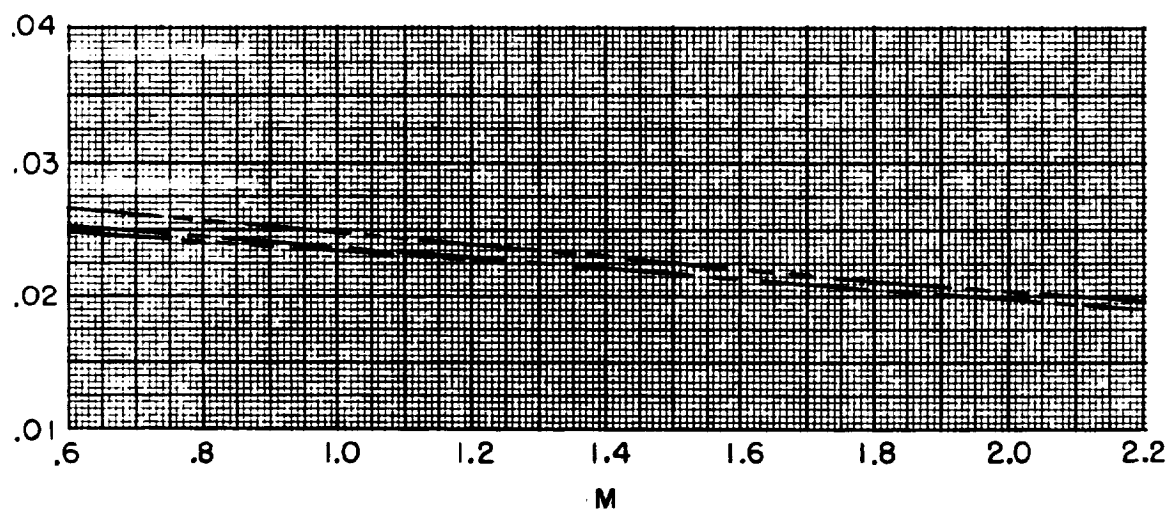
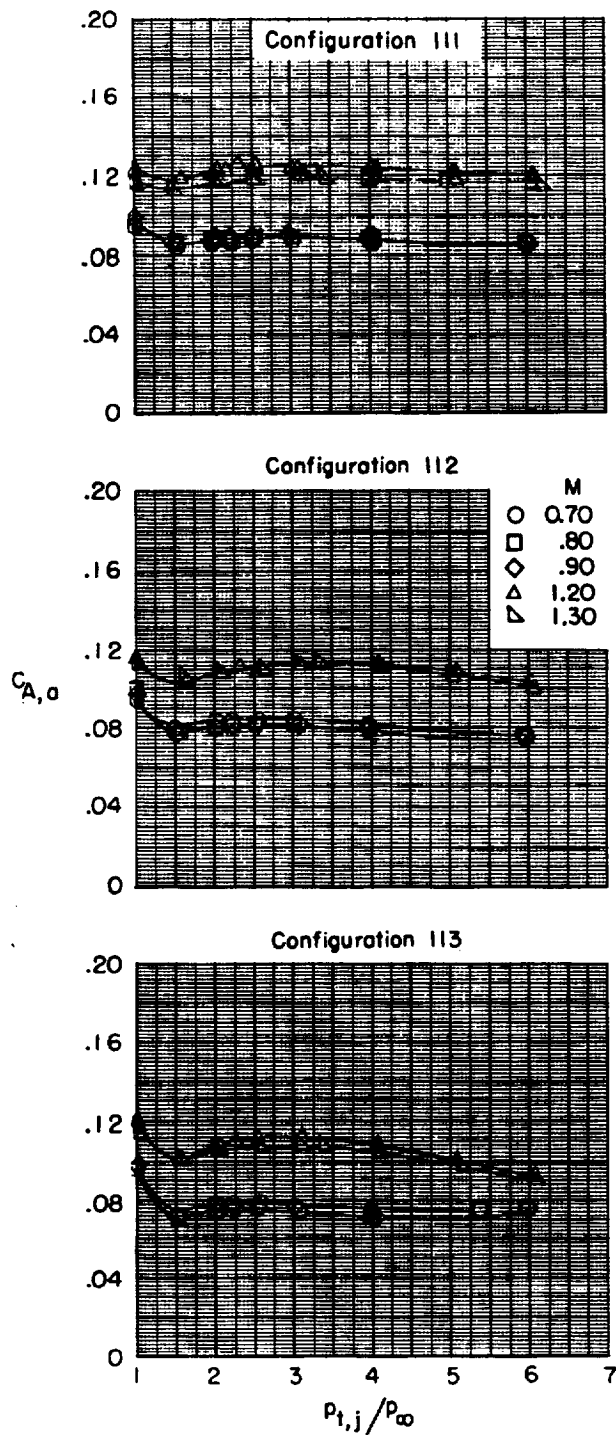
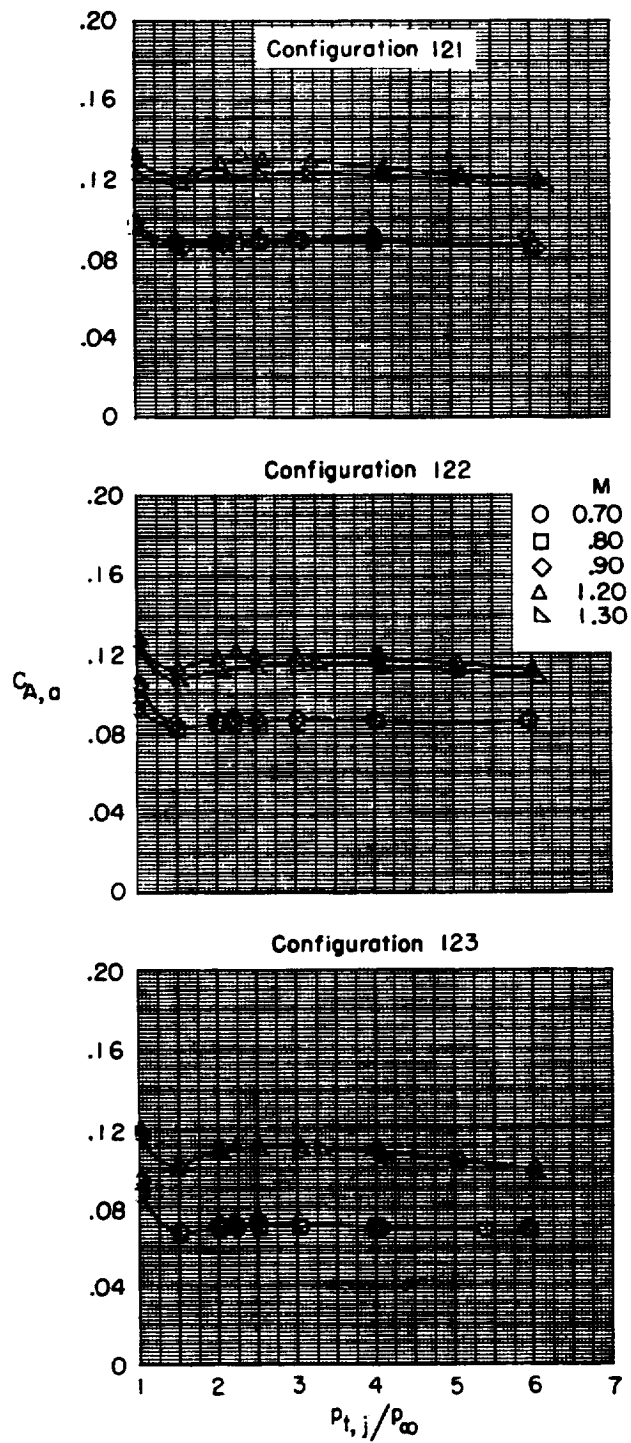


Figure 8.- Variation of calculated skin-friction drag coefficient with Mach number for the various afterbodies.



(a) Iris-convergent nozzles.

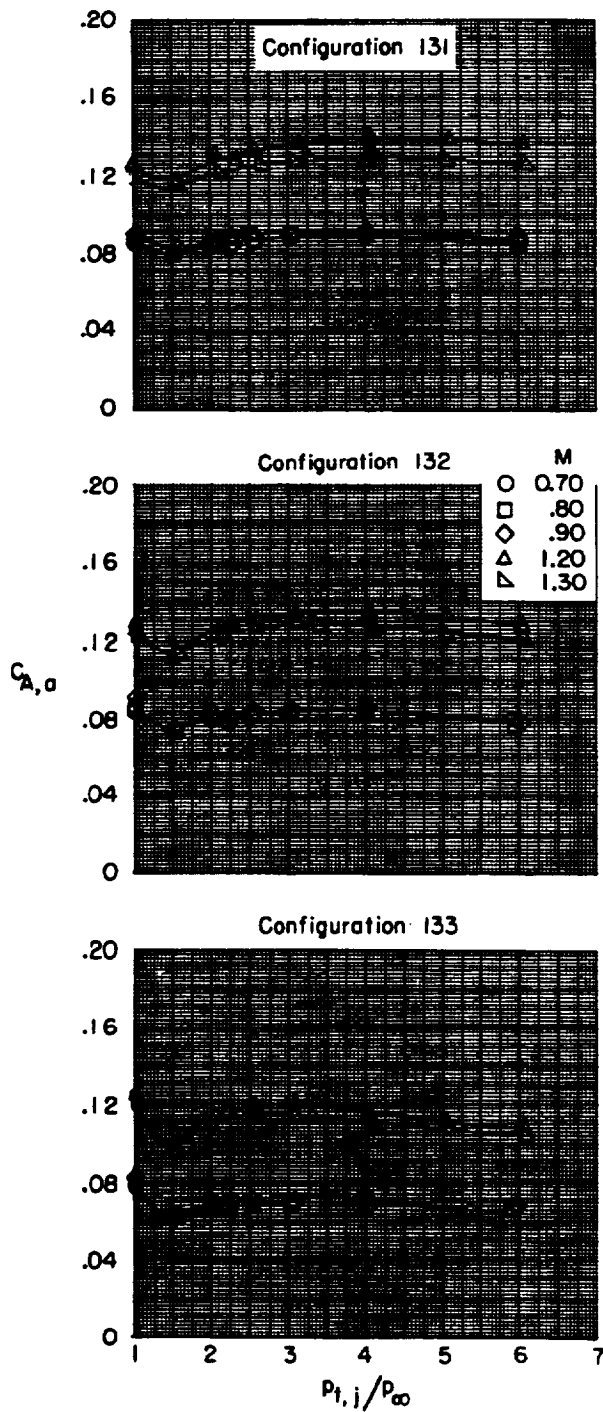
Figure 9.- Variation of afterbody axial-force coefficient with primary total-pressure ratio for afterbody 1.



(b) Convergent-divergent nozzles.

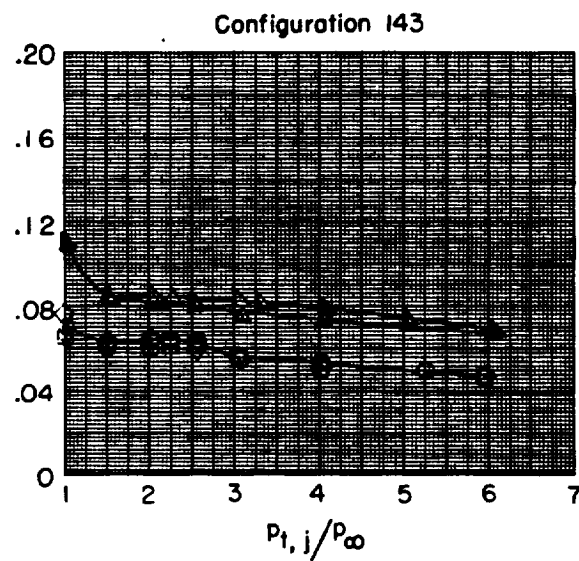
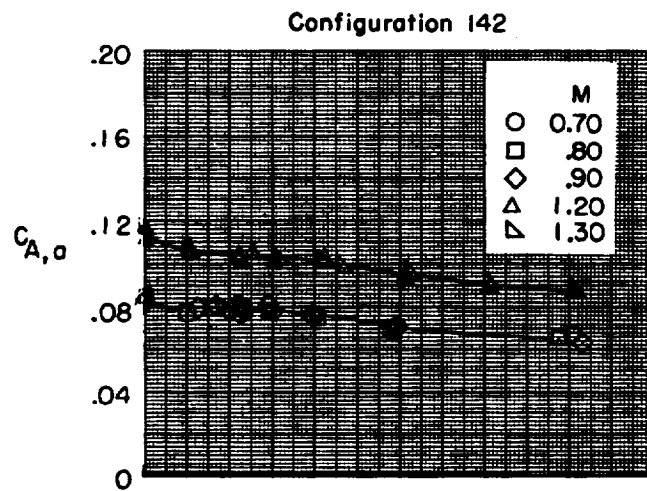
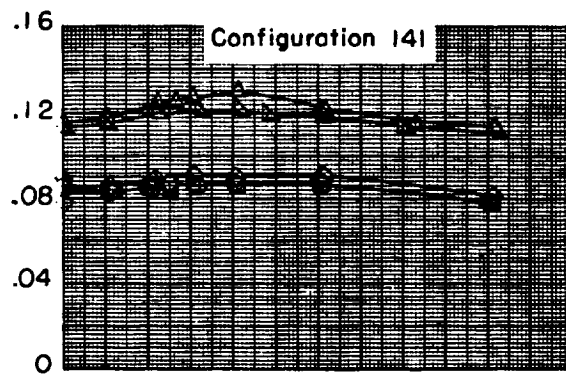
Figure 9.- Continued.

~~CONFIDENTIAL~~



(c) Plug nozzles.

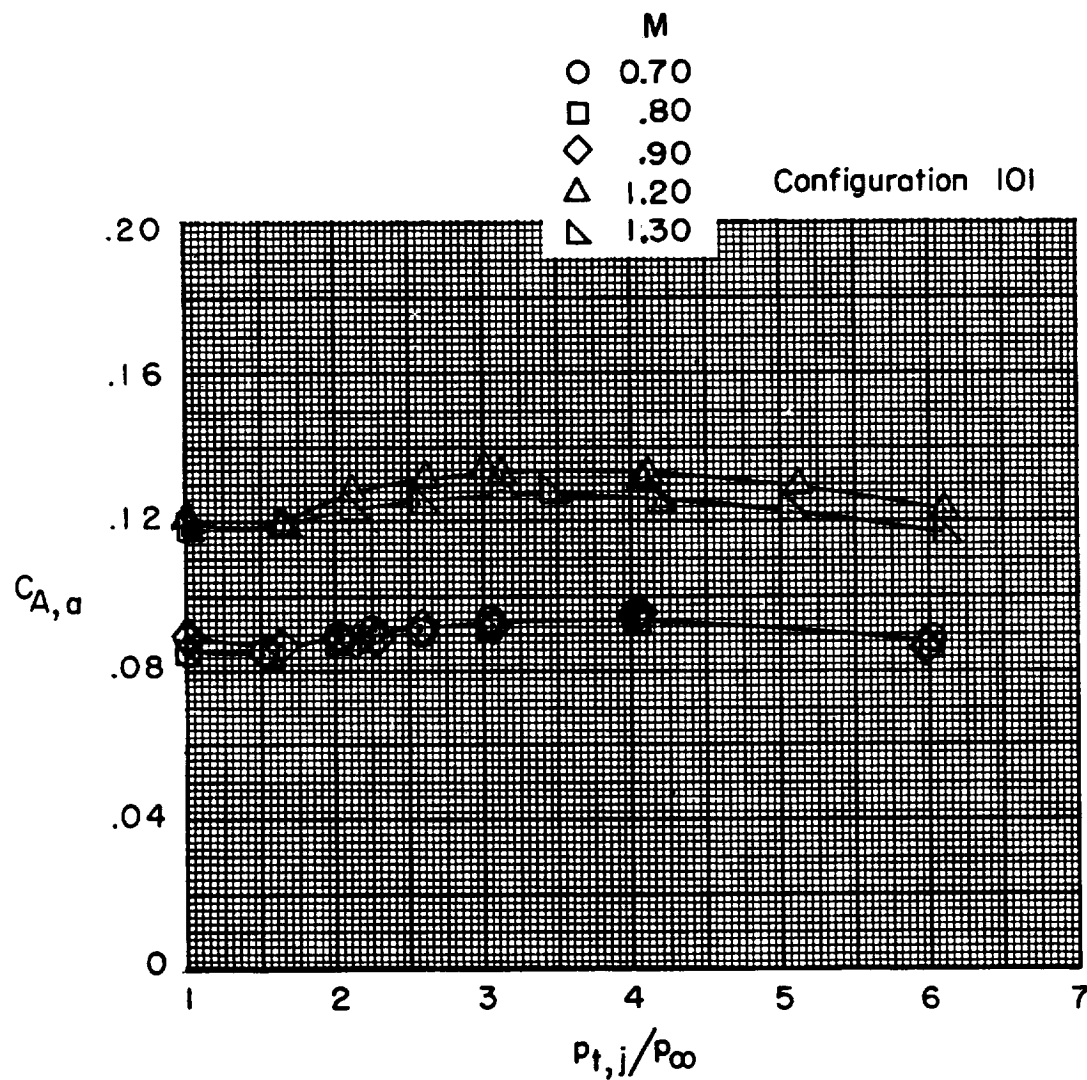
Figure 9.- Continued.



(d) Blow-in-door nozzles.

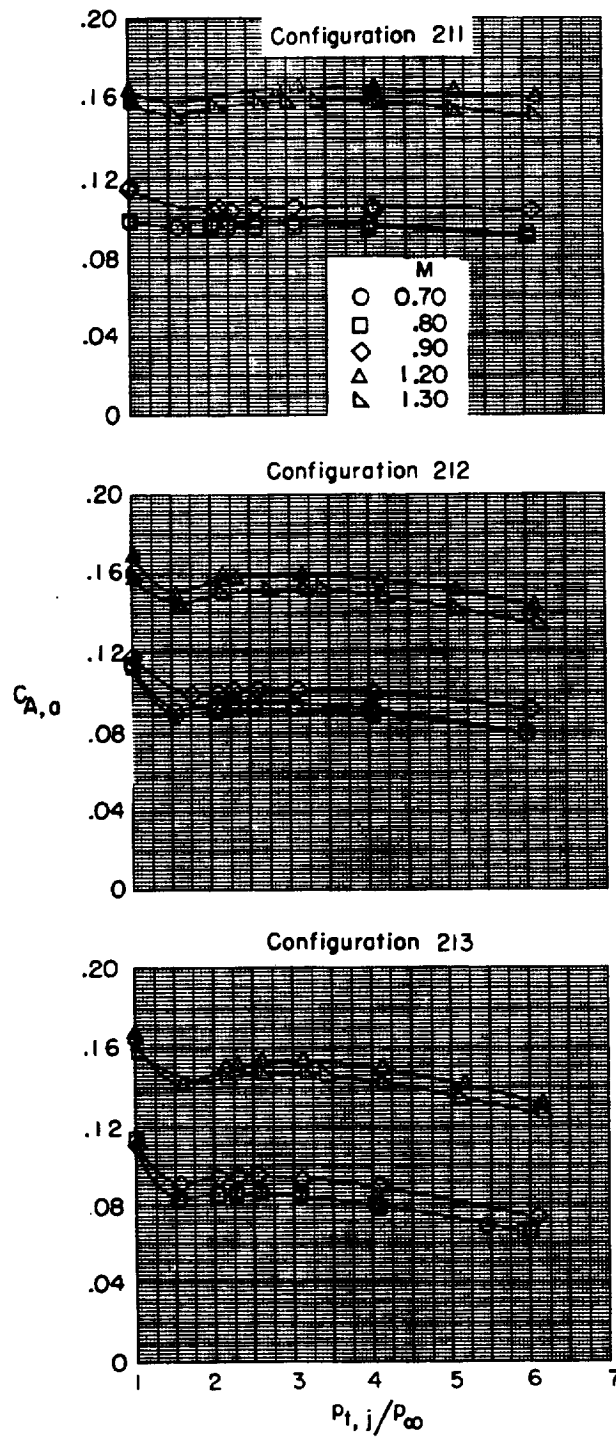
Figure 9.- Continued.

~~CONFIDENTIAL~~



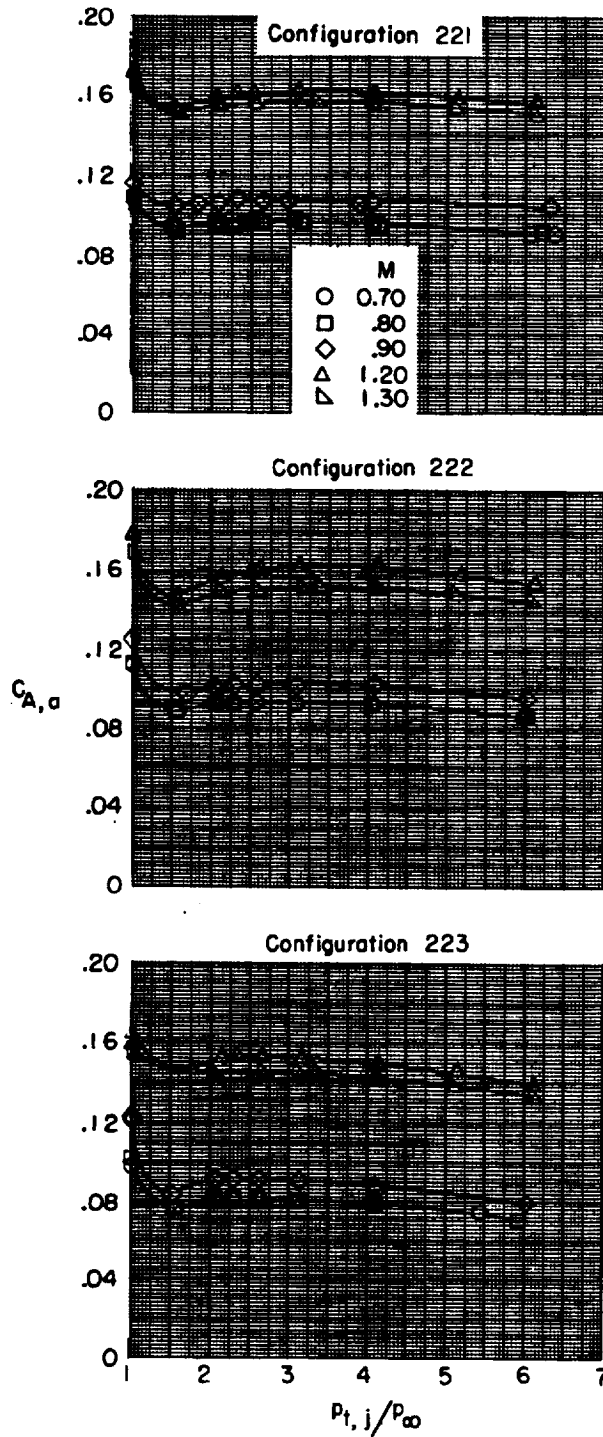
(e) Reference blow-in-door nozzles.

Figure 9.- Concluded.



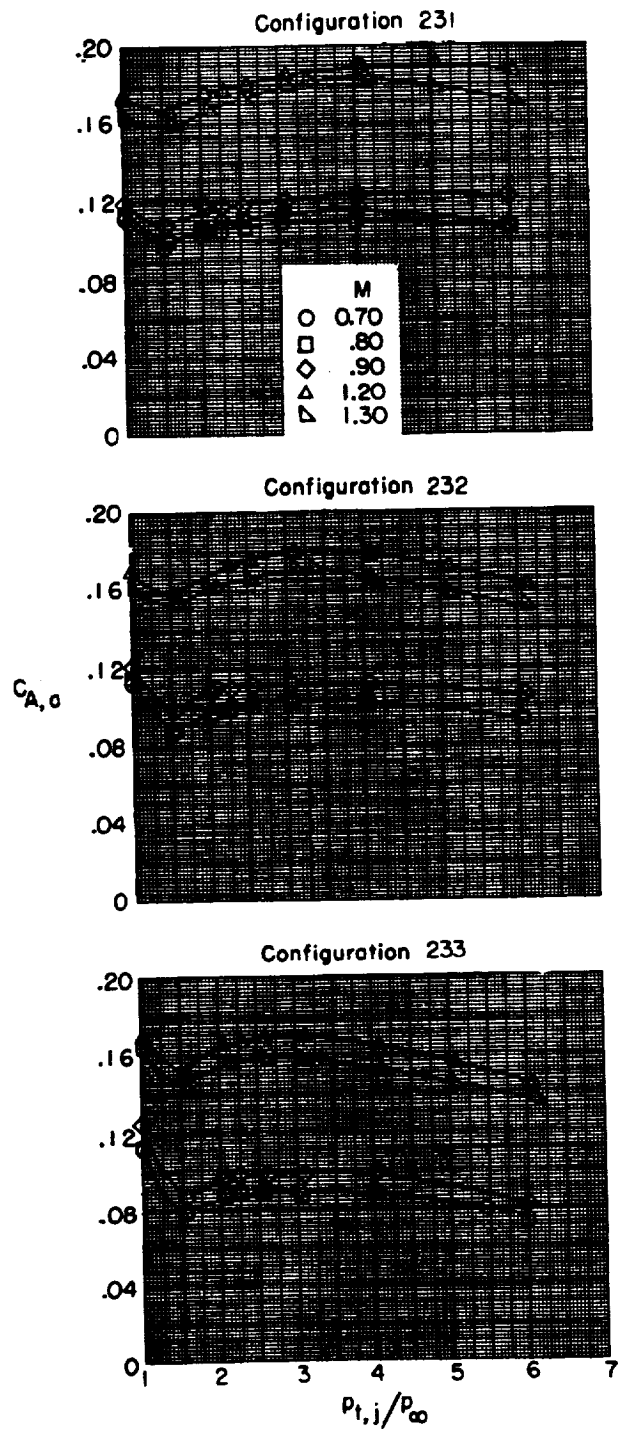
(a) Iris-convergent nozzles.

Figure 10.- Variation of afterbody axial-force coefficient with primary total-pressure ratio for afterbody 2.



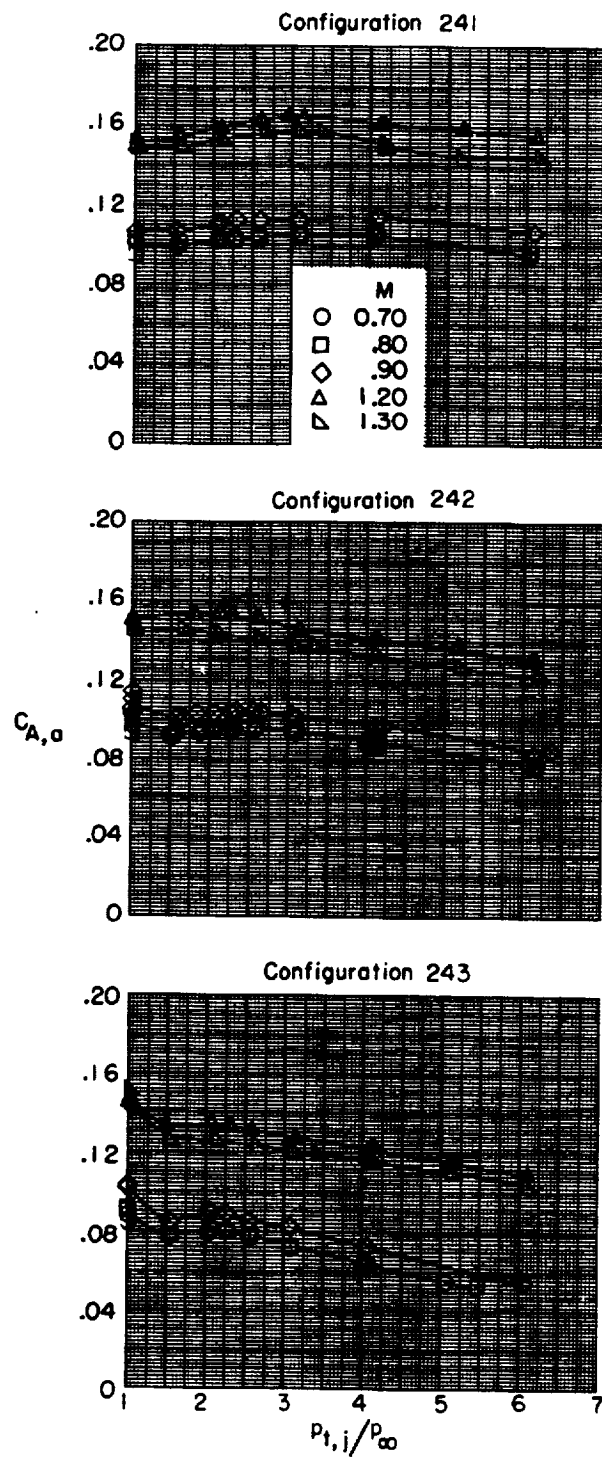
(b) Convergent-divergent nozzles.

Figure 10.- Continued.



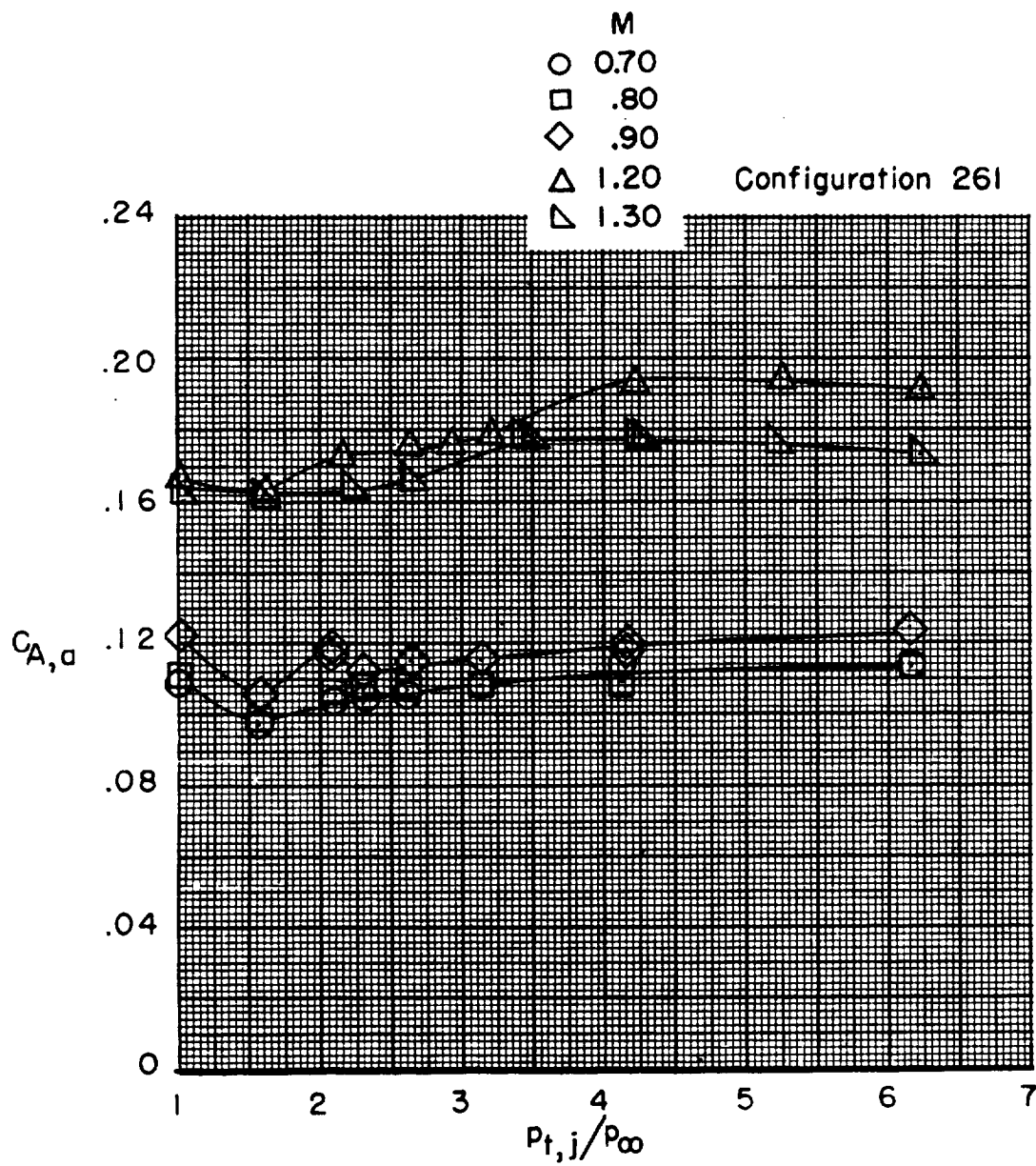
(c) Plug nozzles.

Figure 10.- Continued.



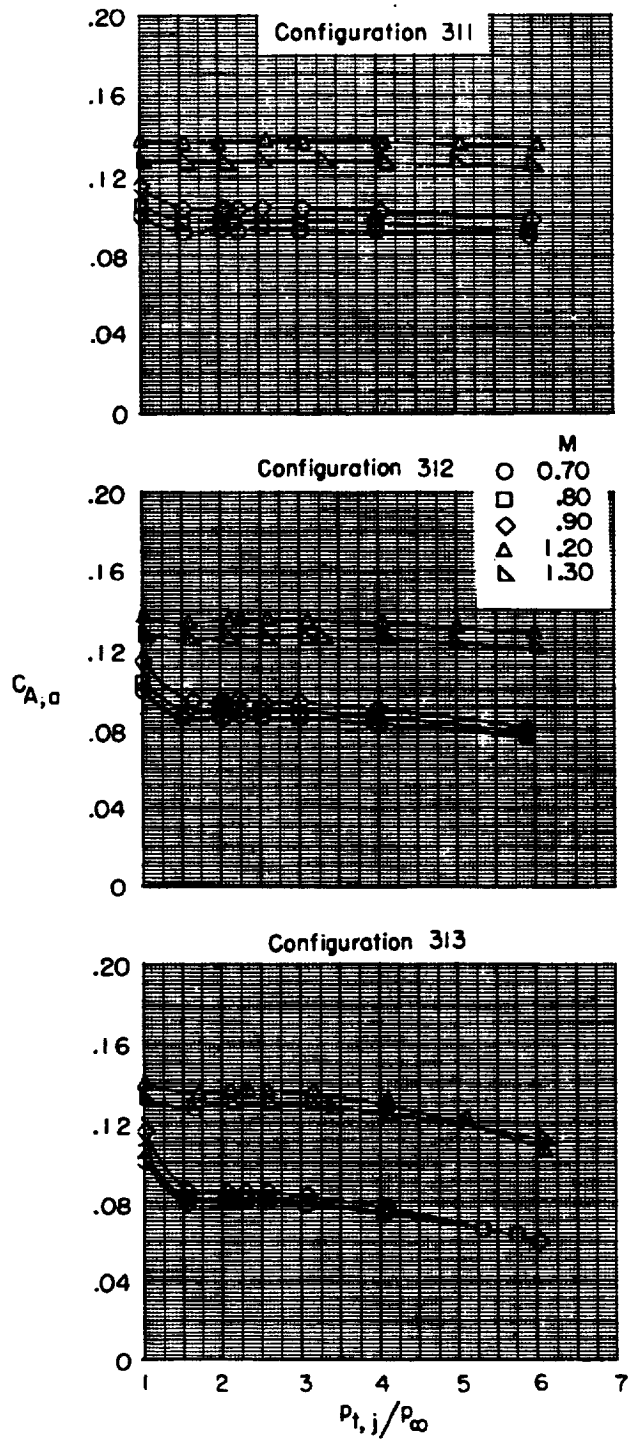
(d) Blow-in-door nozzles.

Figure 10.- Continued.



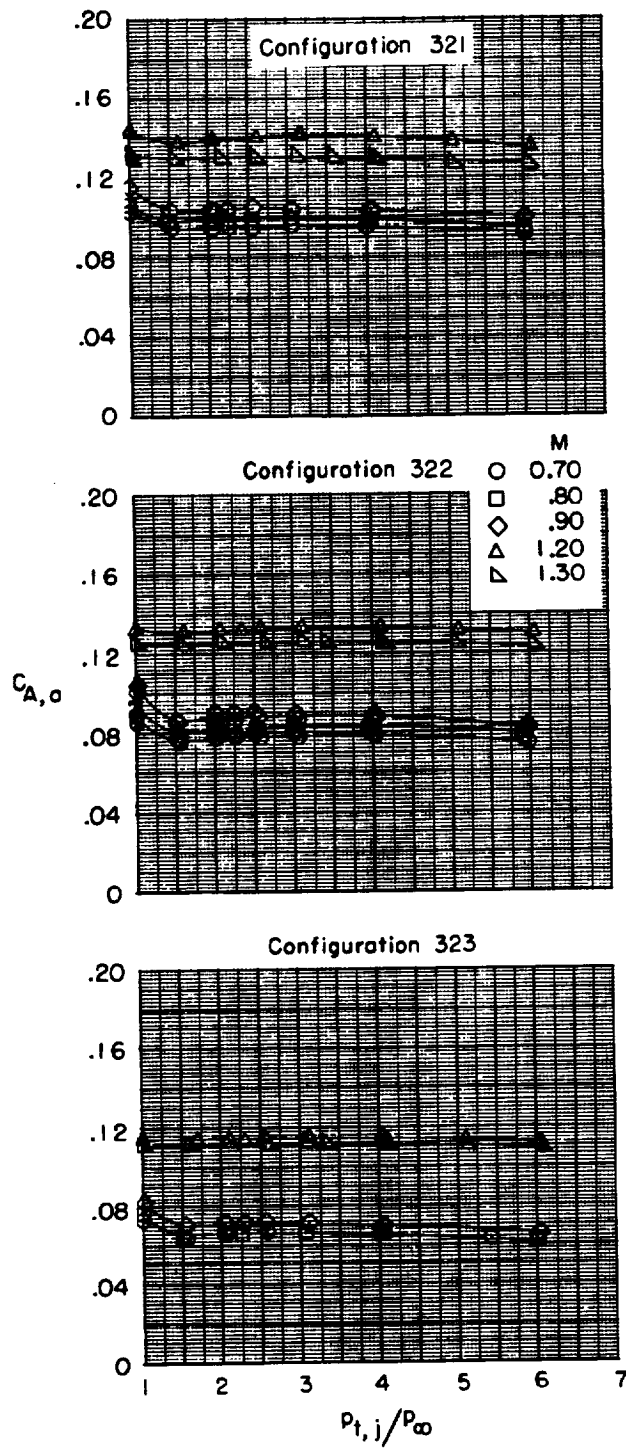
(e) Plug nozzles with floating tail flaps.

Figure 10.- Concluded.



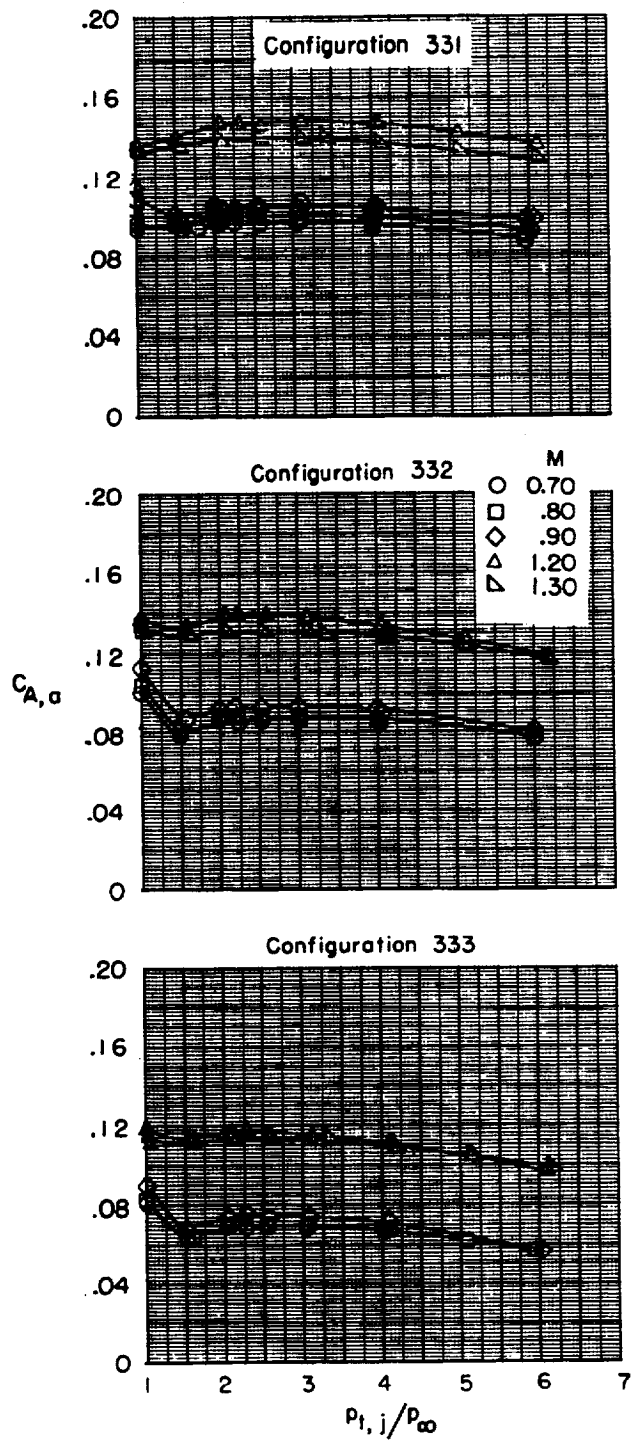
(a) Iris-convergent nozzles.

Figure 11.- Variation of afterbody axial-force coefficient with primary total-pressure ratio for afterbody 3.



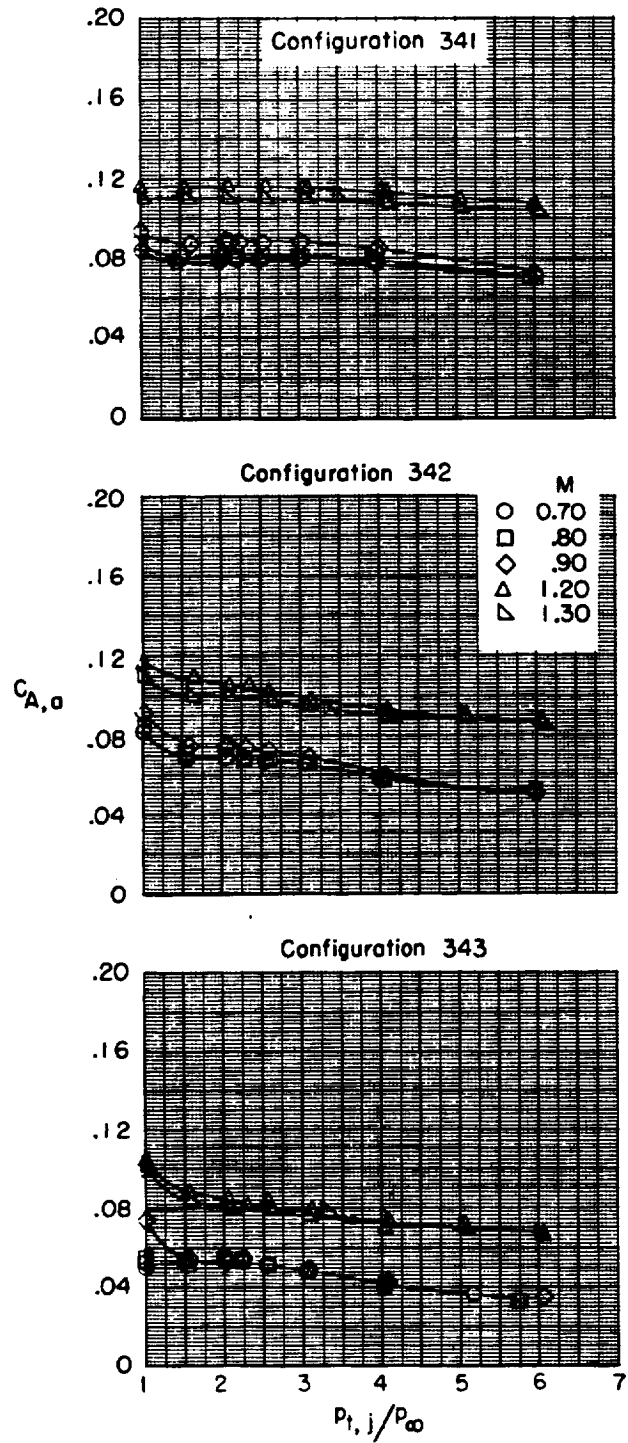
(b) Convergent-divergent nozzles.

Figure 11.- Continued.



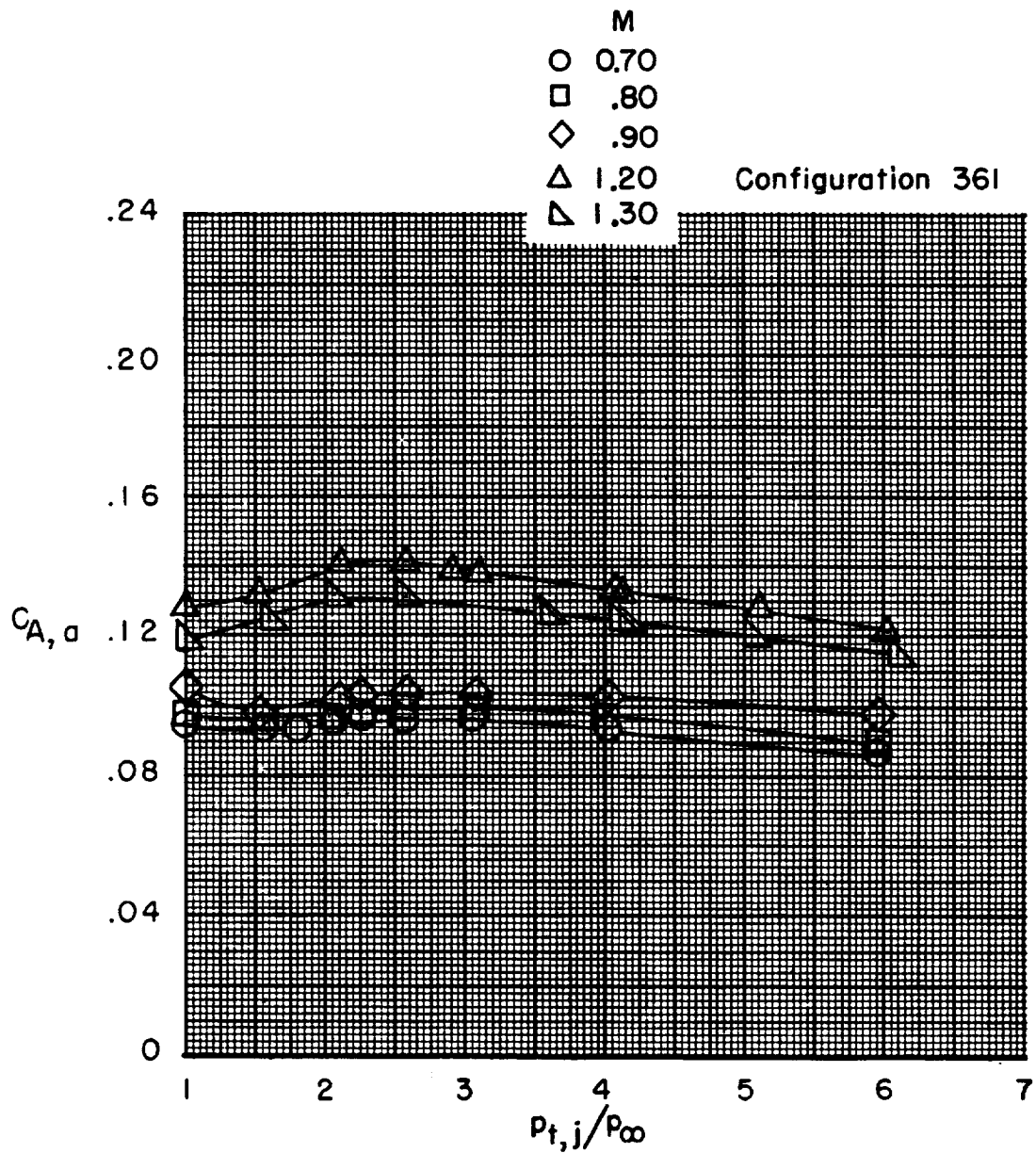
(c) Plug nozzles.

Figure 11.- Continued.



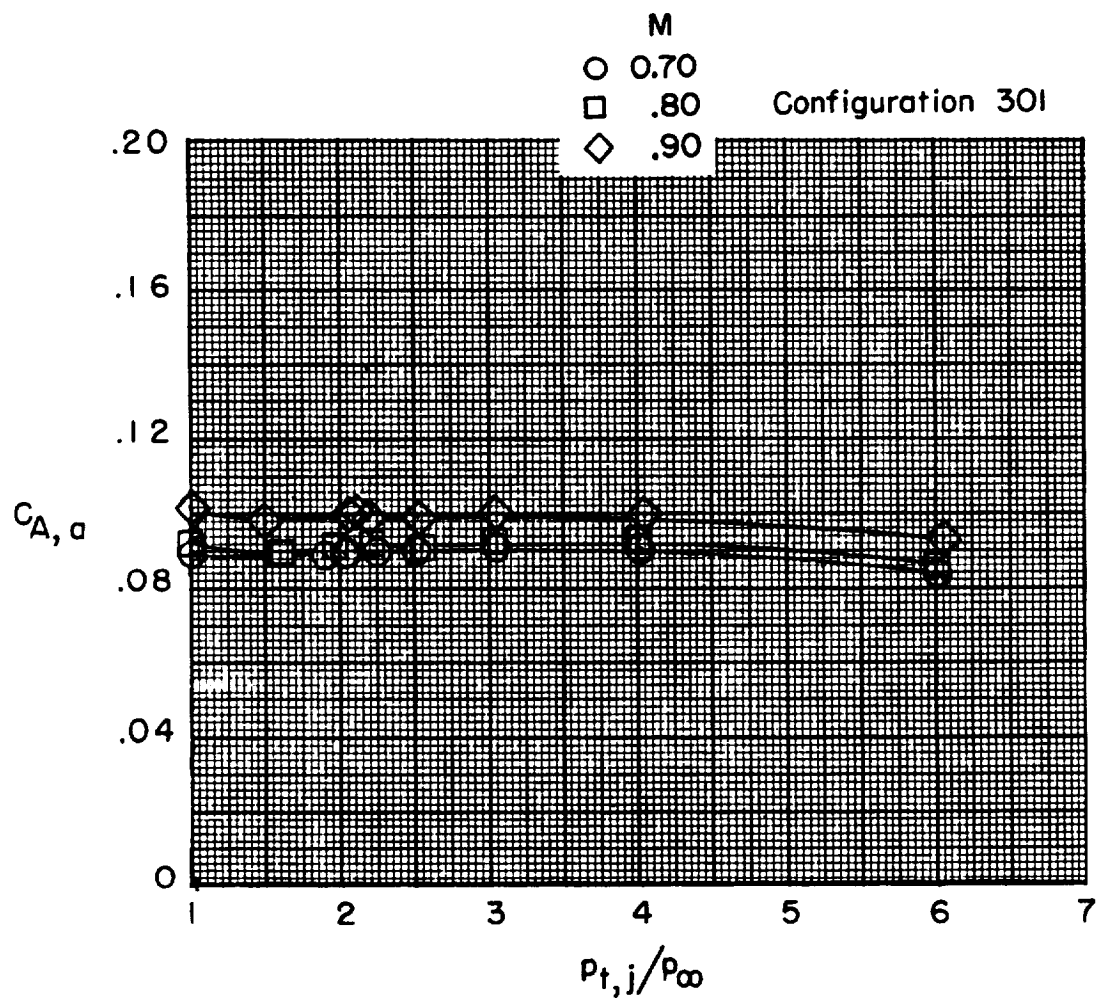
(d) Blow-in-door nozzles.

Figure 11.- Continued.



(e) Plug nozzles with floating tail flaps.

Figure 11.- Continued.



(f) Reference blow-in-door nozzles.

Figure 11.- Concluded.

CONFIDENTIAL

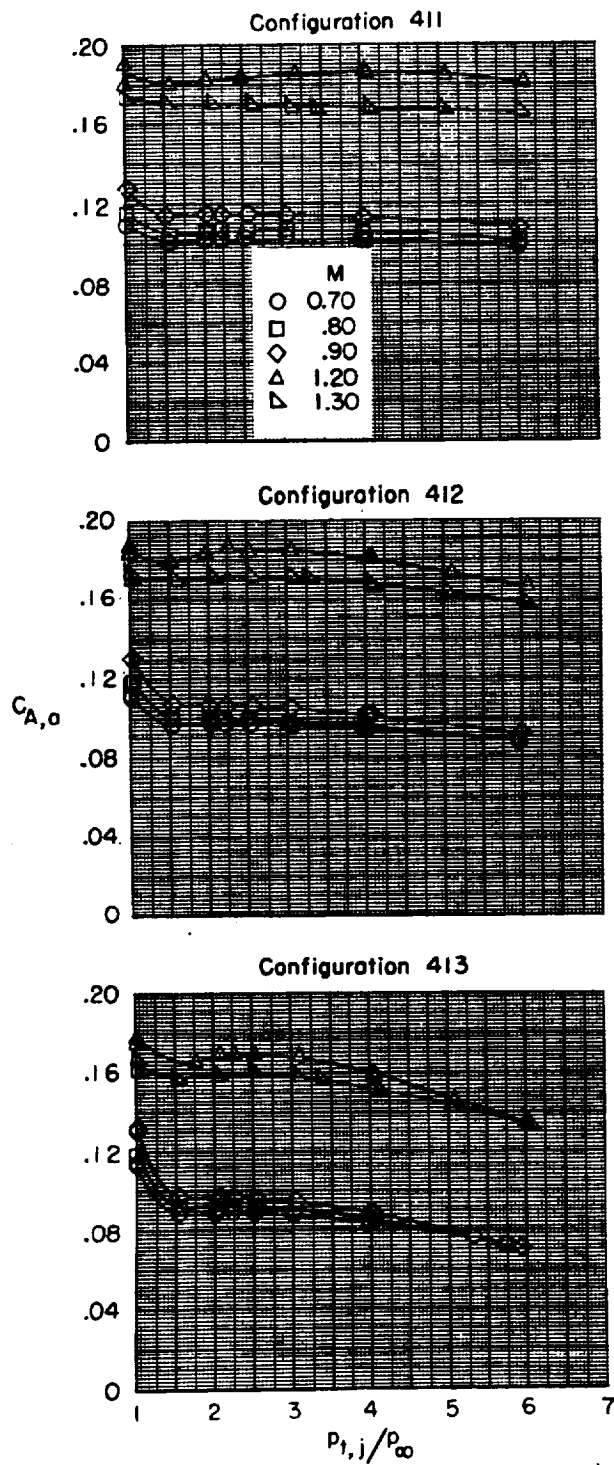
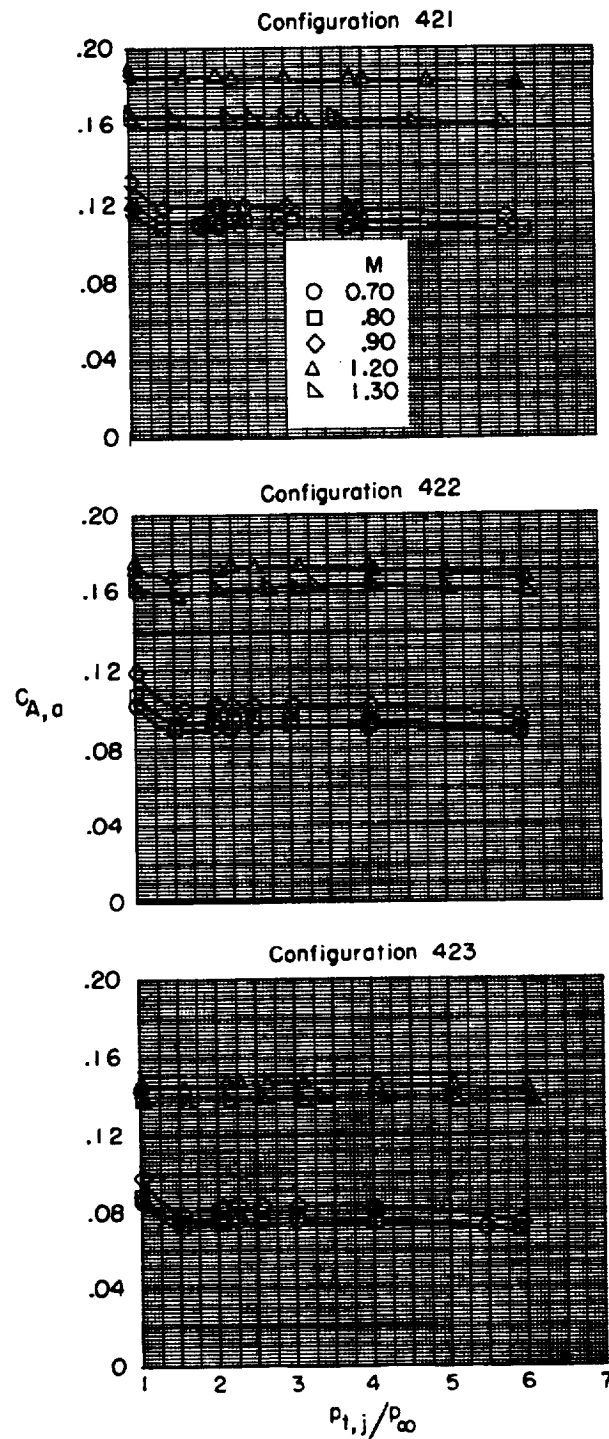
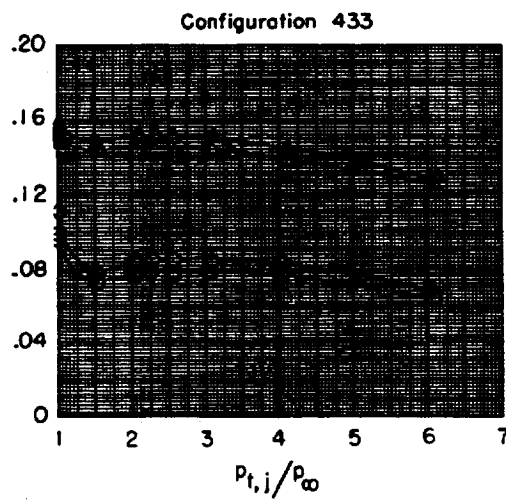
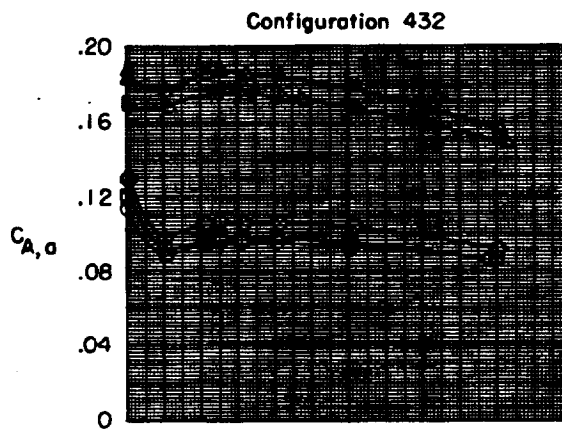
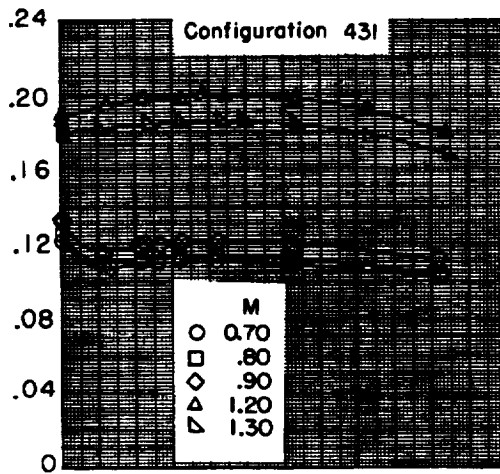


Figure 12.- Variation of afterbody axial-force coefficient with primary total-pressure ratio for afterbody 4.



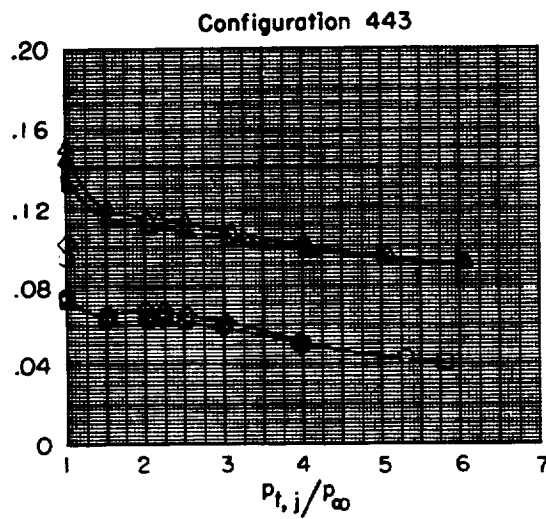
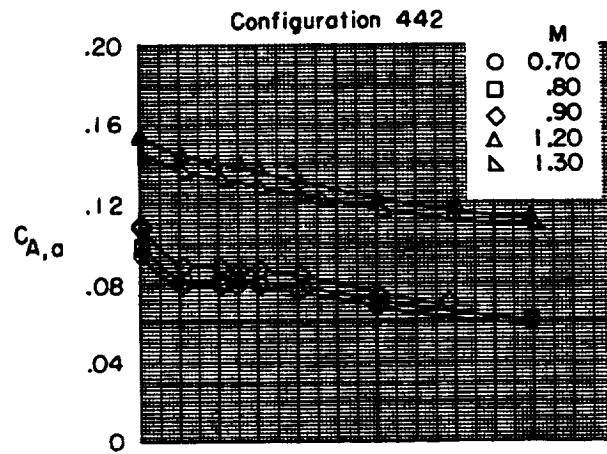
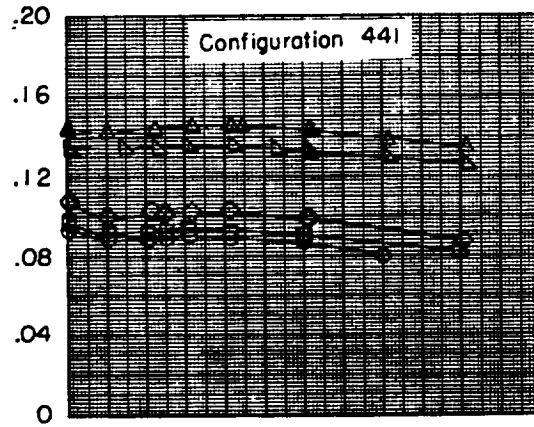
(b) Convergent-divergent nozzles.

Figure 12.- Continued.



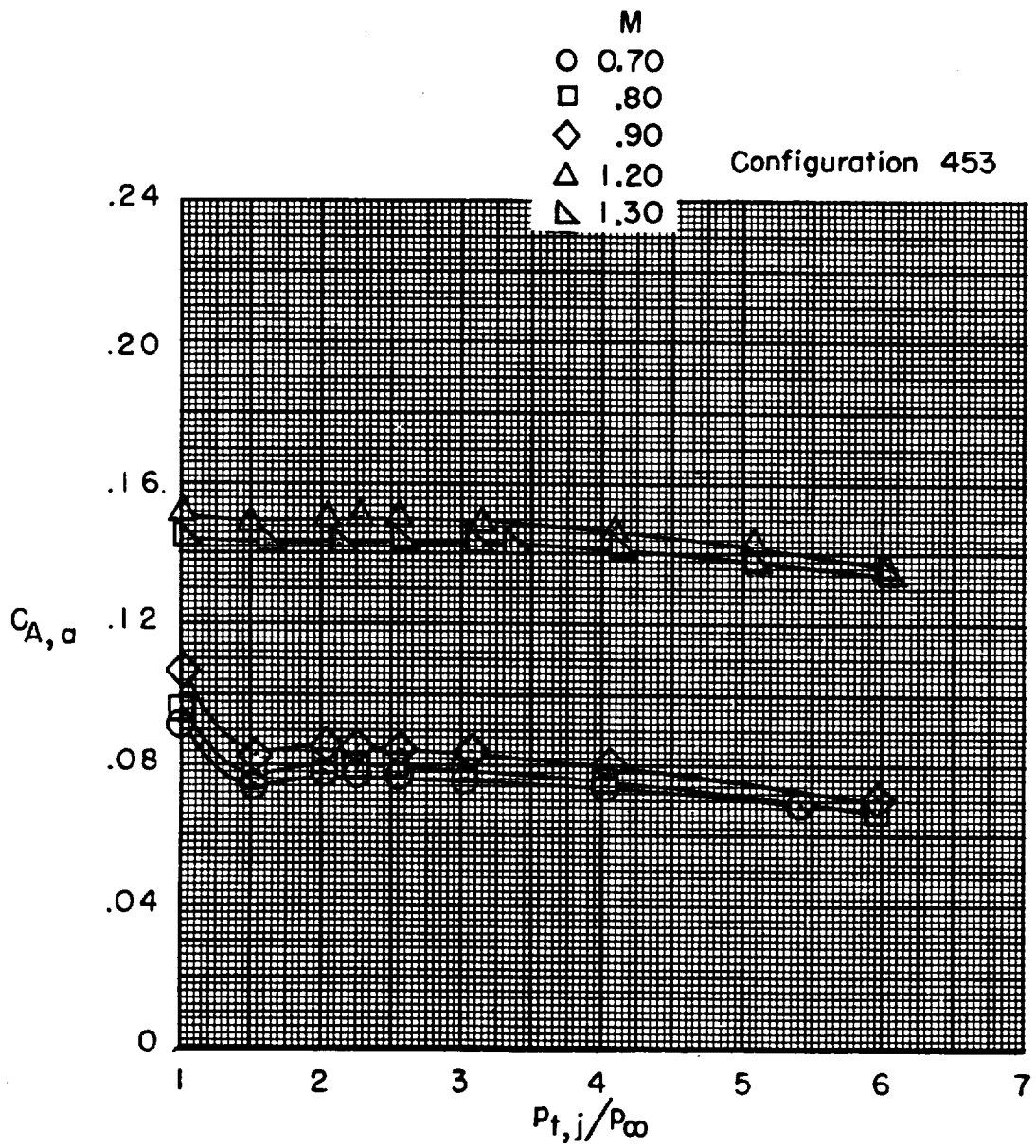
(c) Plug nozzles.

Figure 12.- Continued.



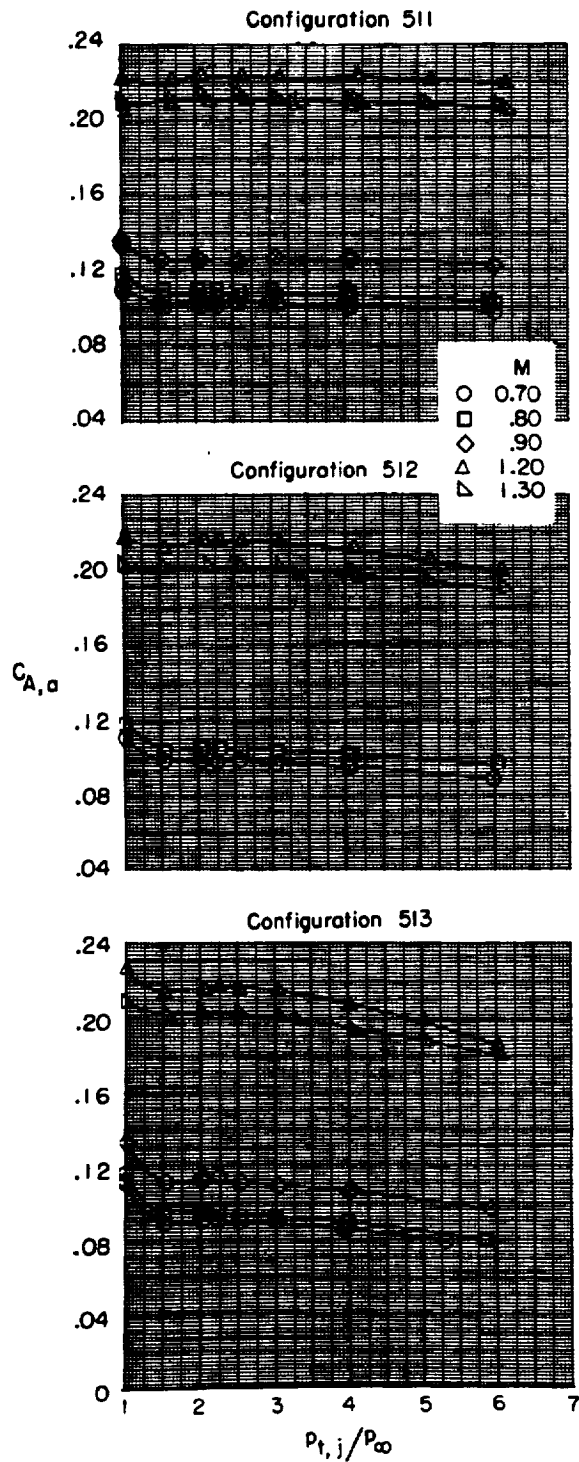
(d) Blow-in-door nozzles.

Figure 12.- Continued.



(e) Convergent-divergent nozzles with iris primary.

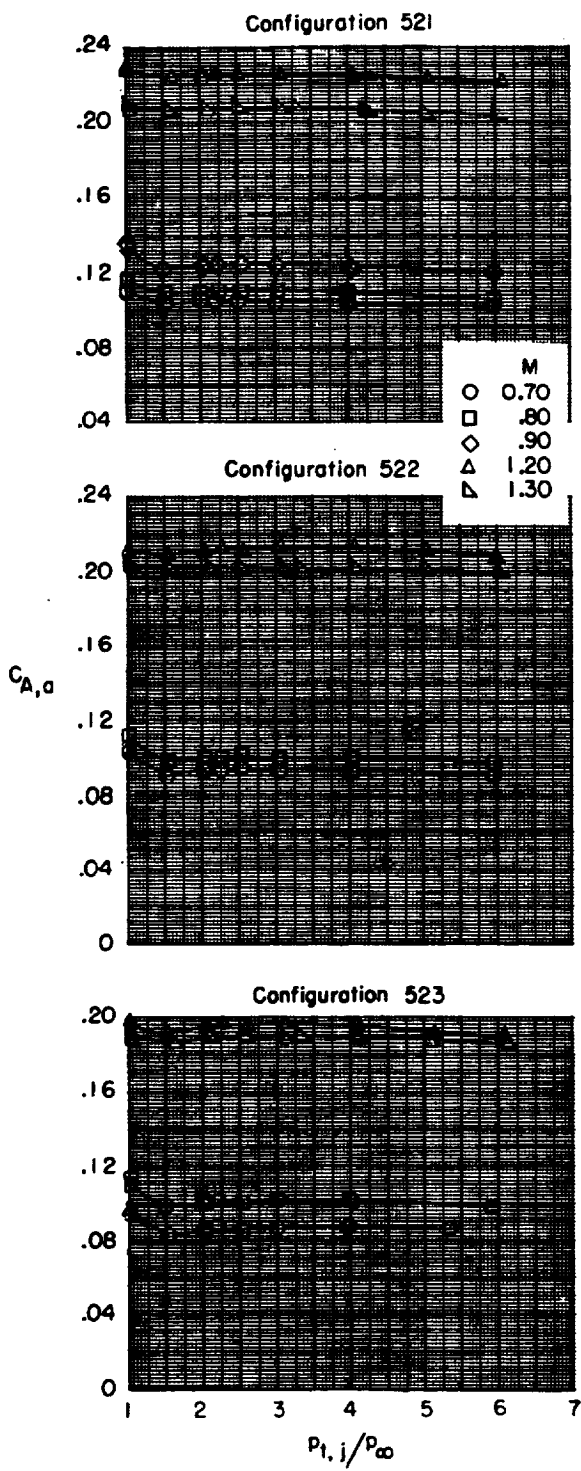
Figure 12.- Concluded.



(a) Iris-convergent nozzles.

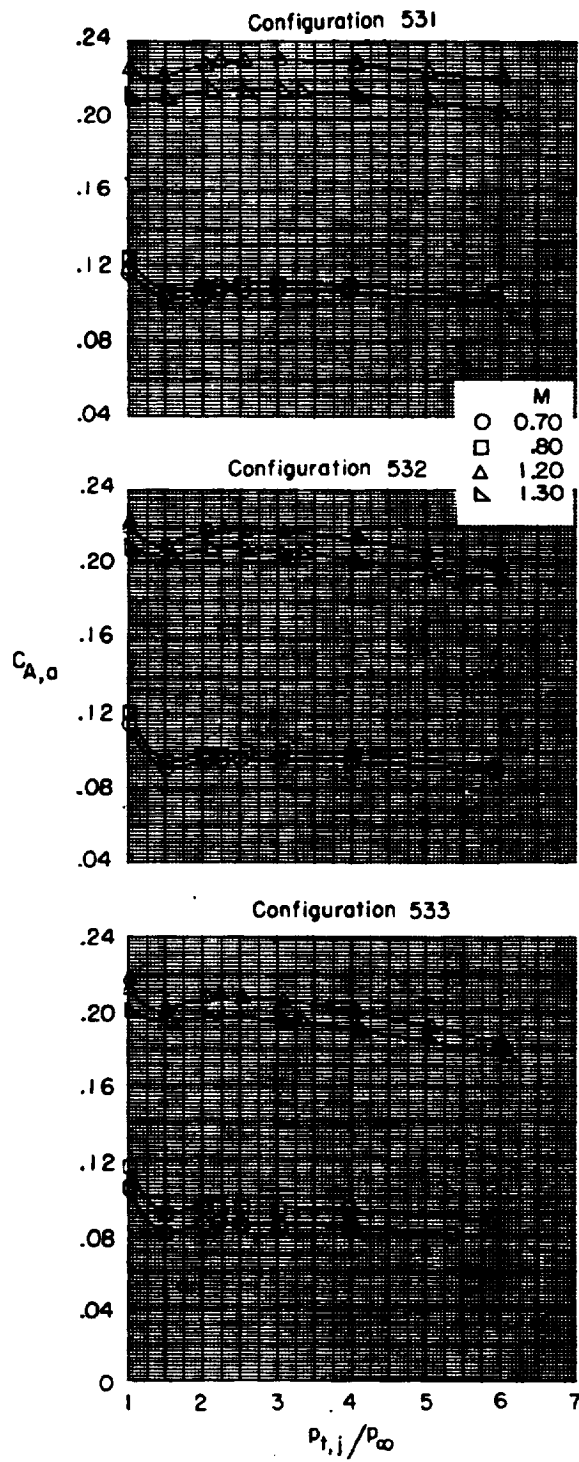
Figure 13.- Variation of afterbody axial-force coefficient with primary total-pressure ratio for afterbody 5.

CONFIDENTIAL



(b) Convergent-divergent nozzles.

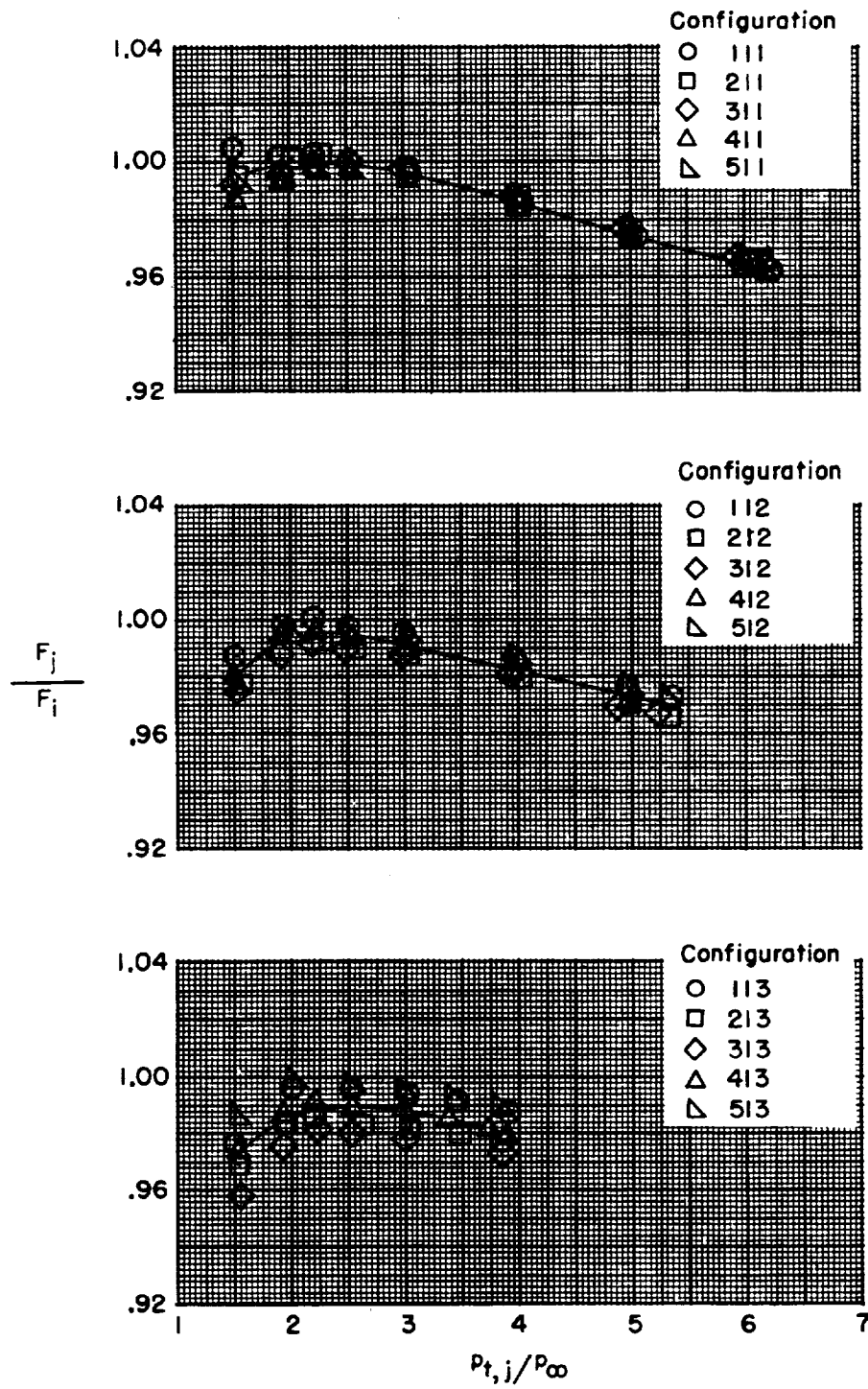
Figure 13.- Continued.



(c) Plug nozzles.

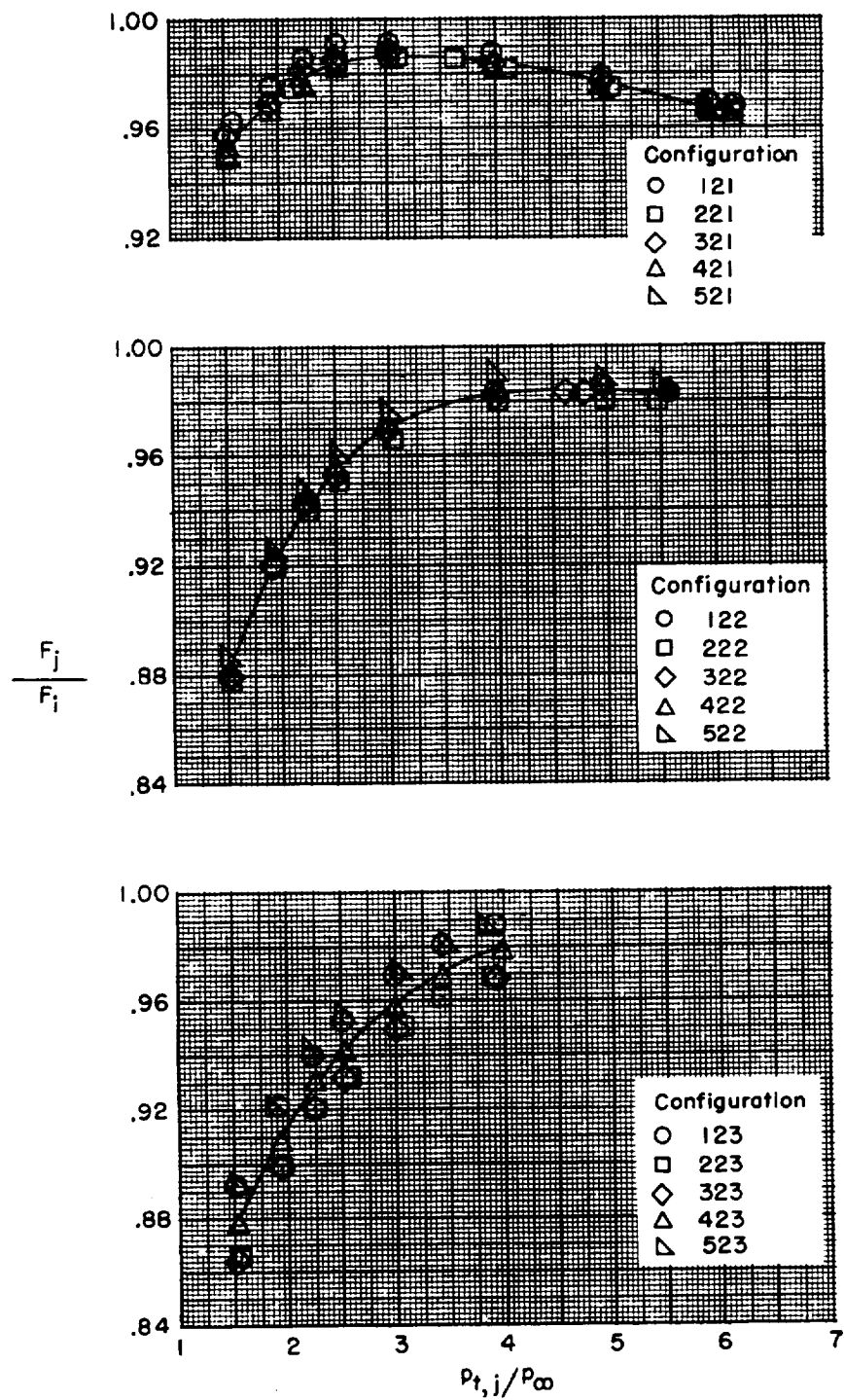
Figure 13.- Concluded.

CONFIDENTIAL



(a) Iris-convergent nozzles.

Figure 14.- Static thrust performance for the various afterbodies.



(b) Convergent-divergent nozzles.

Figure 14.- Continued.

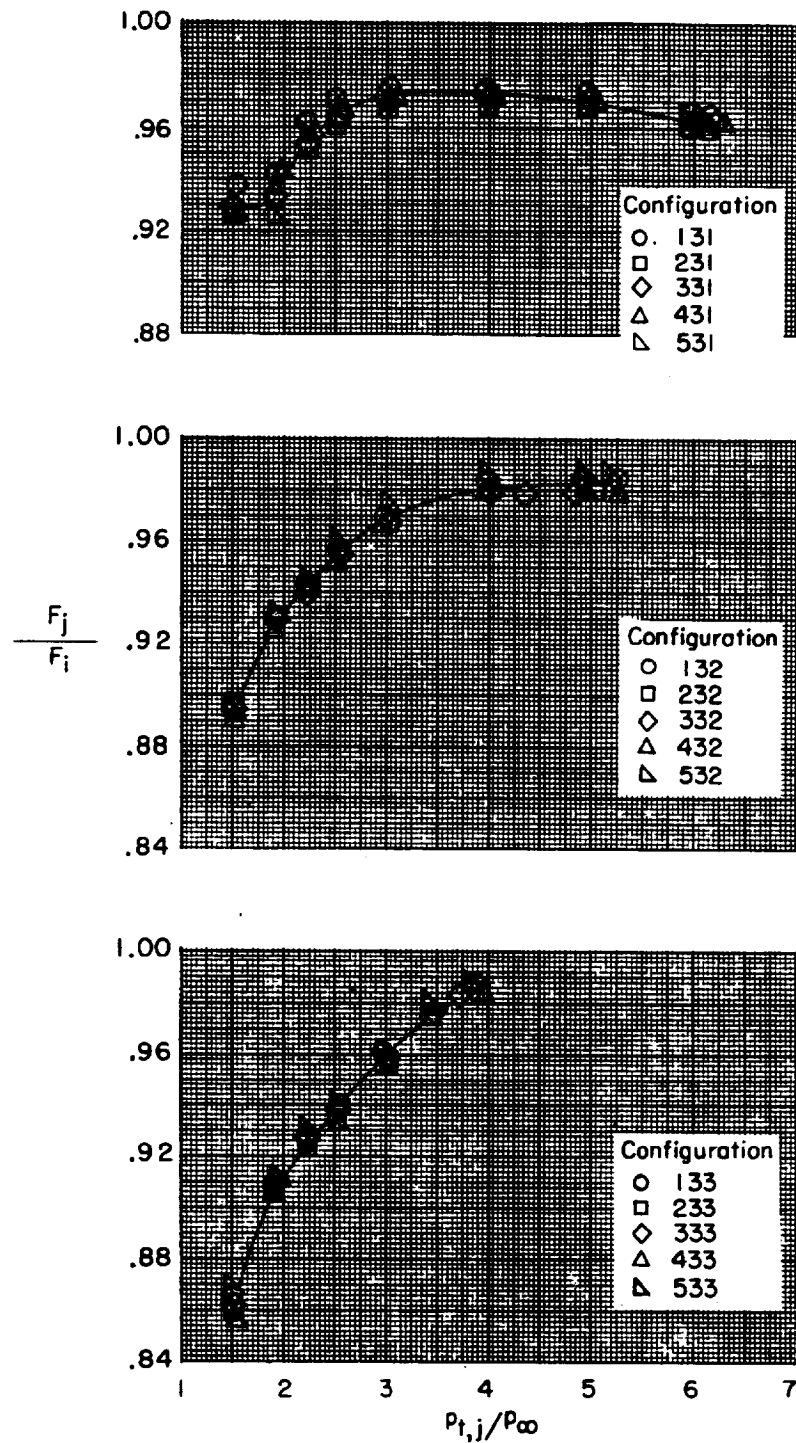
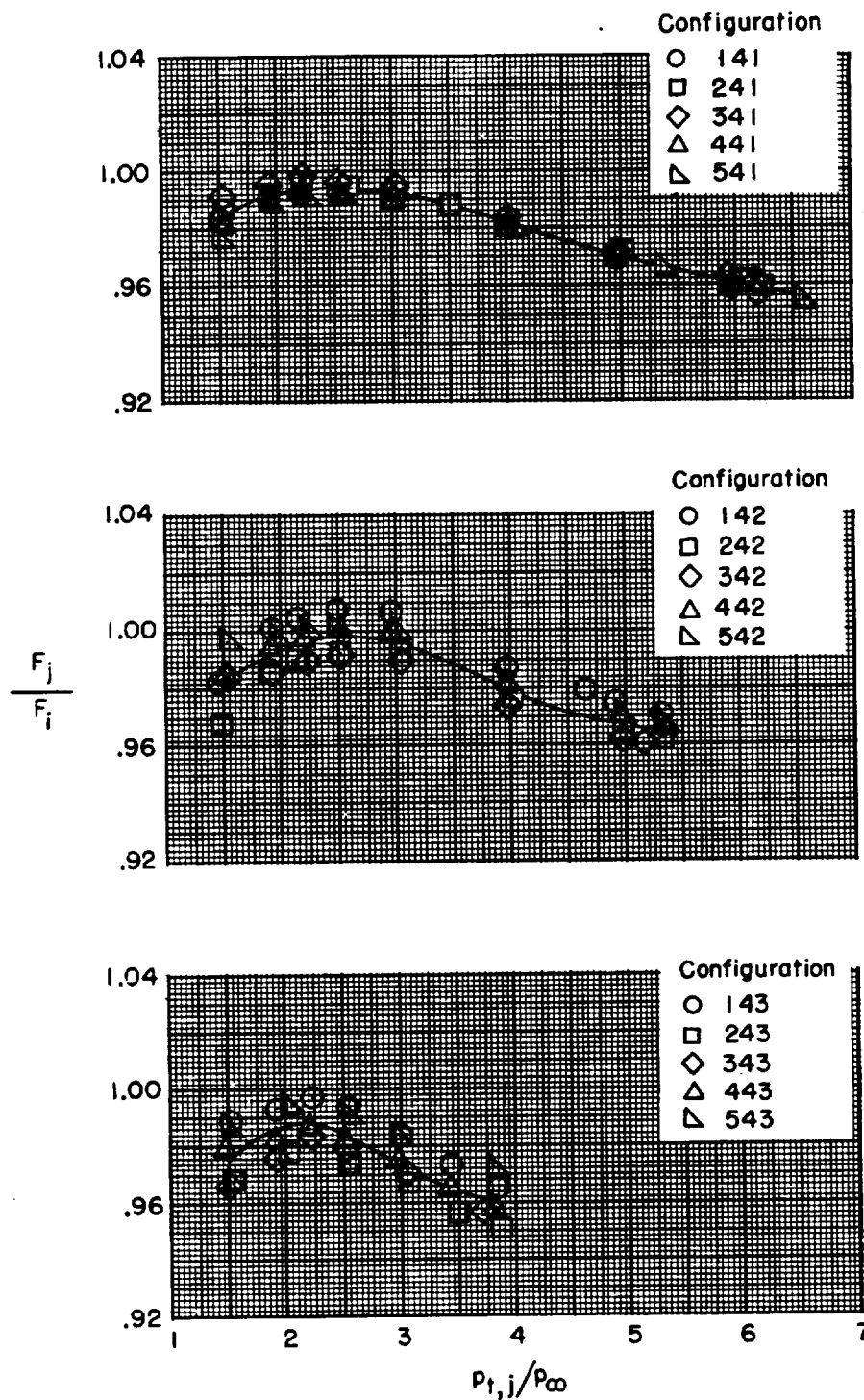


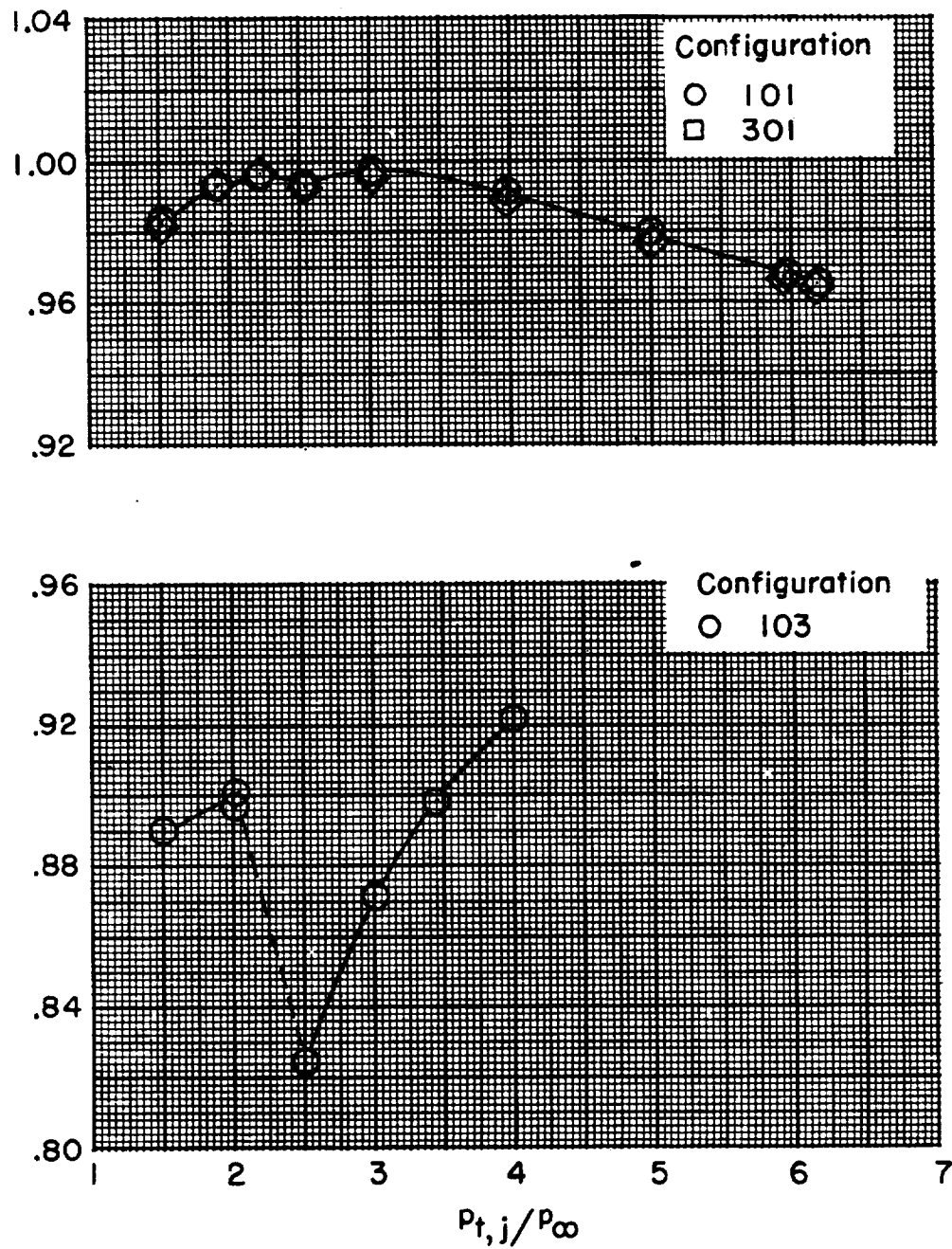
Figure 14.- Continued.



(d) Blow-in-door nozzles.

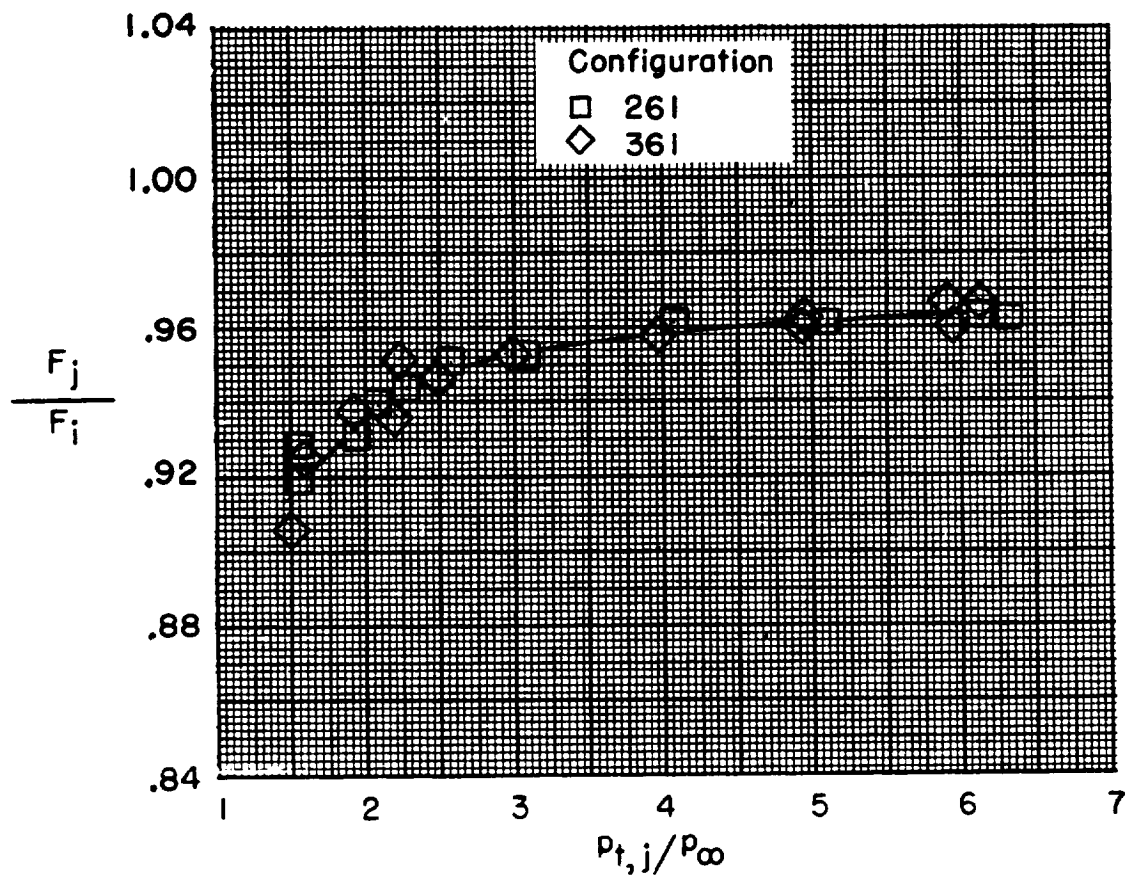
Figure 14.- Continued.

CONFIDENTIAL



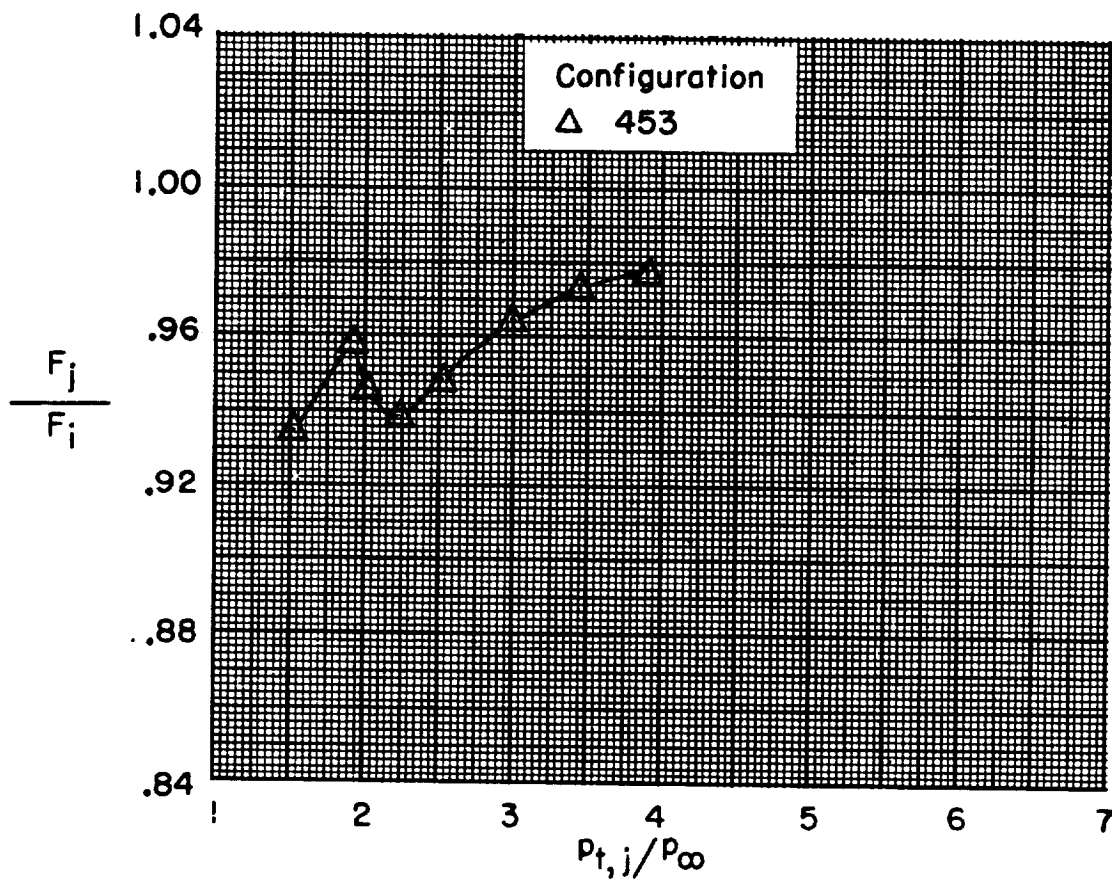
(e) Reference blow-in-door nozzles.

Figure 14.- Continued.



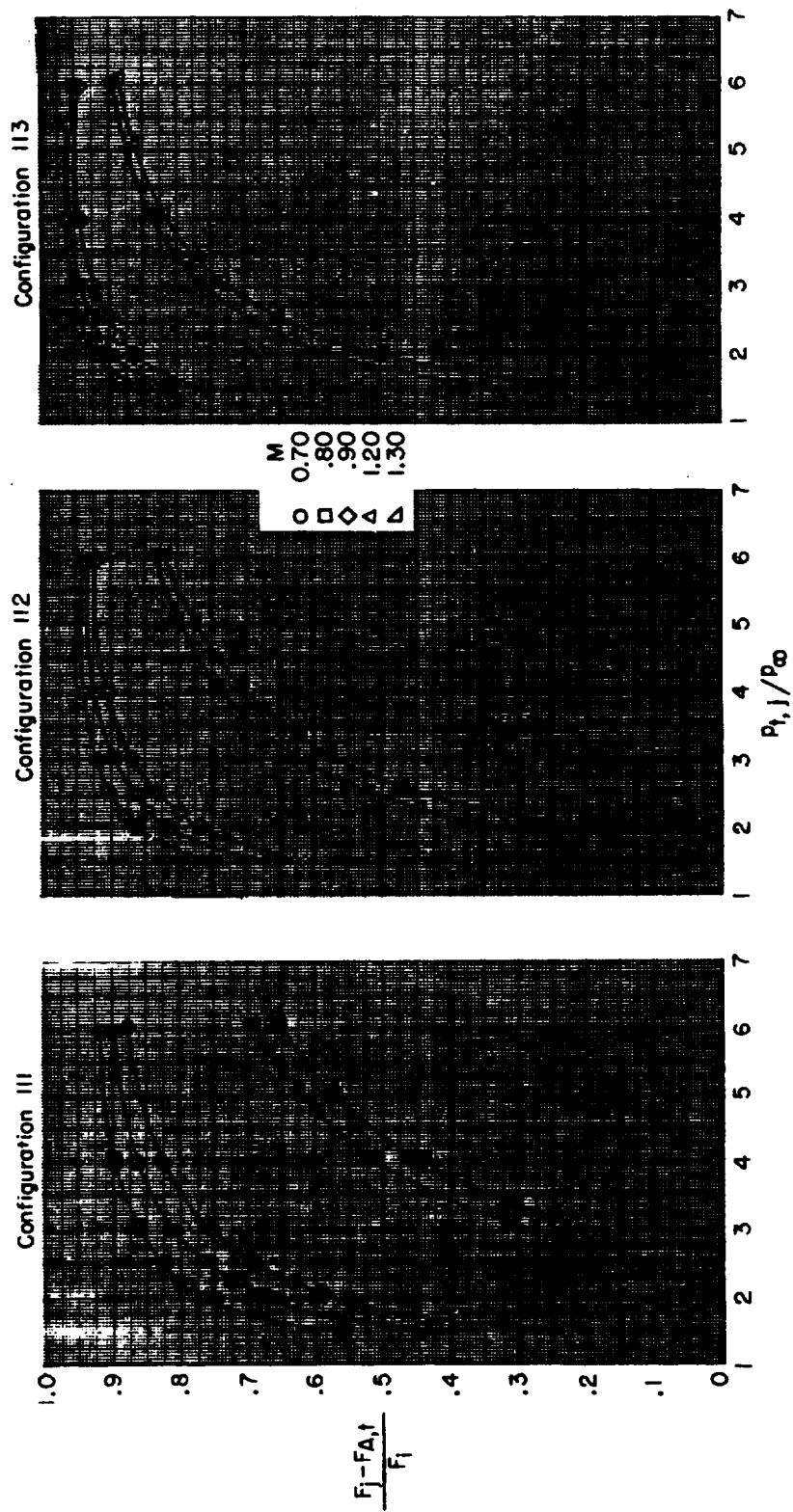
(f) Plug nozzles with floating tail flaps.

Figure 14.- Continued.



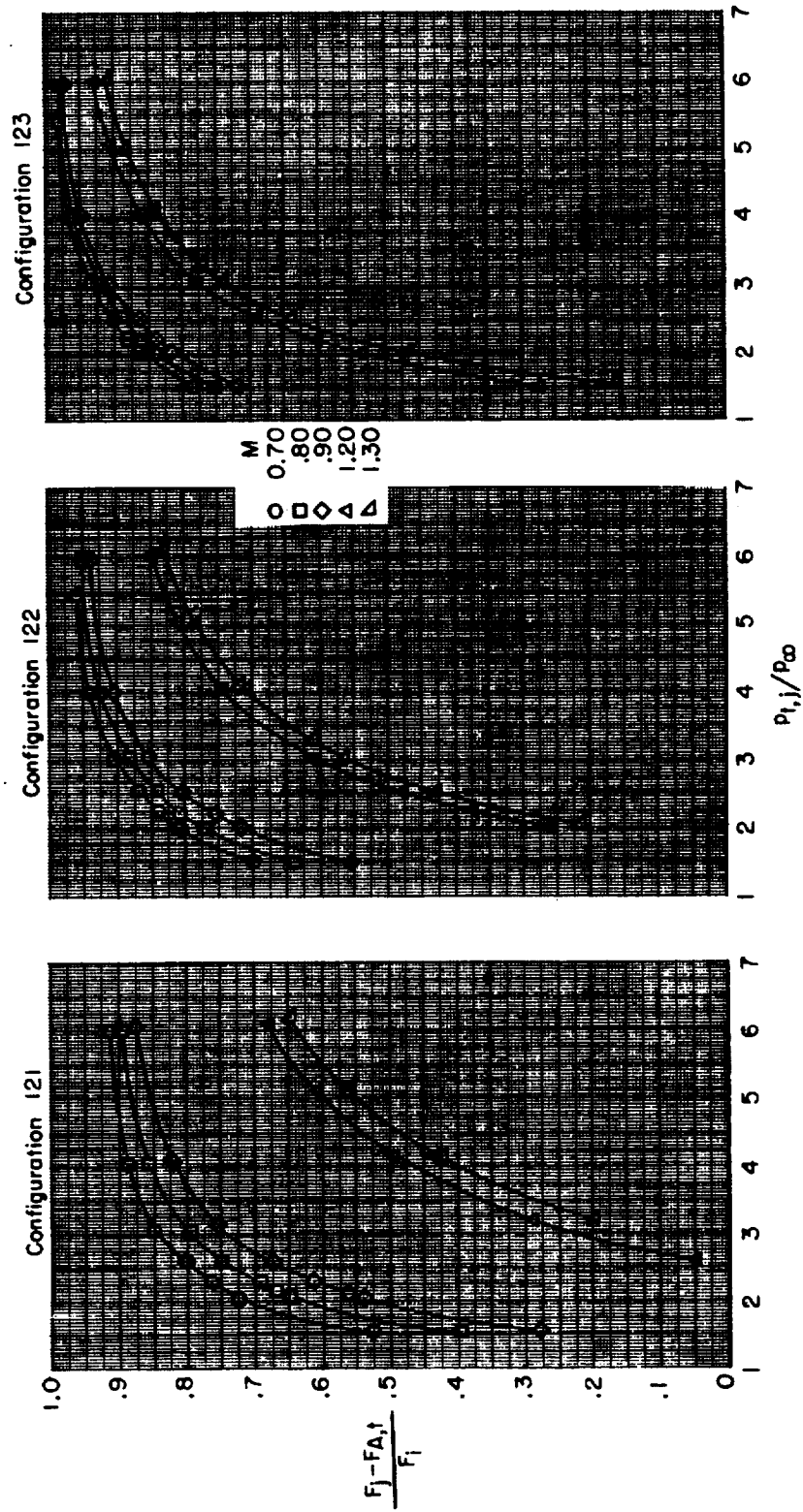
(g) Convergent-divergent-iris nozzles.

Figure 14.- Concluded.



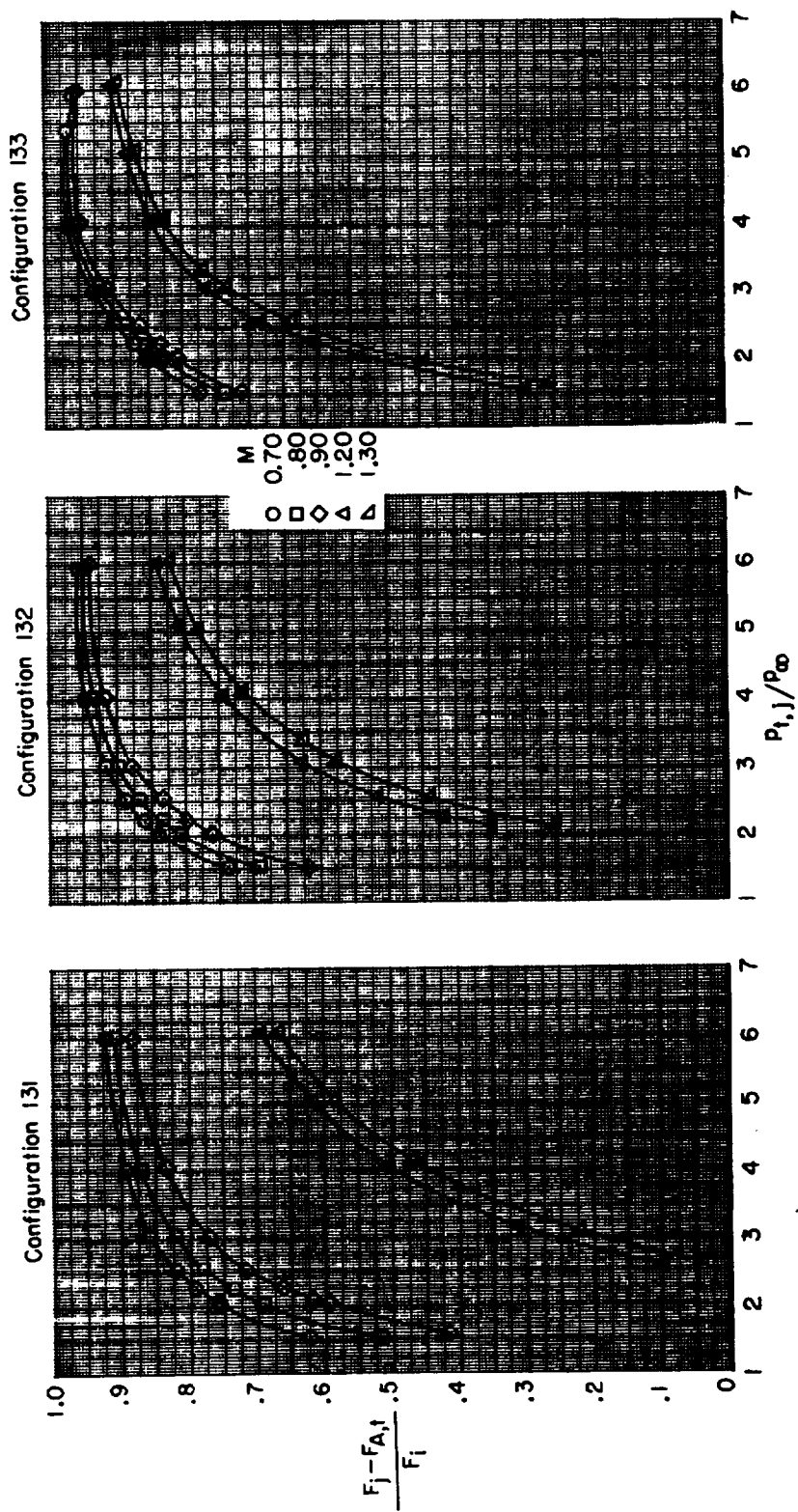
(a) Iris-convergent nozzles.

Figure 15.- Variation of gross thrust minus total afterbody axial-force performance with primary total-pressure ratio for afterbody 1.



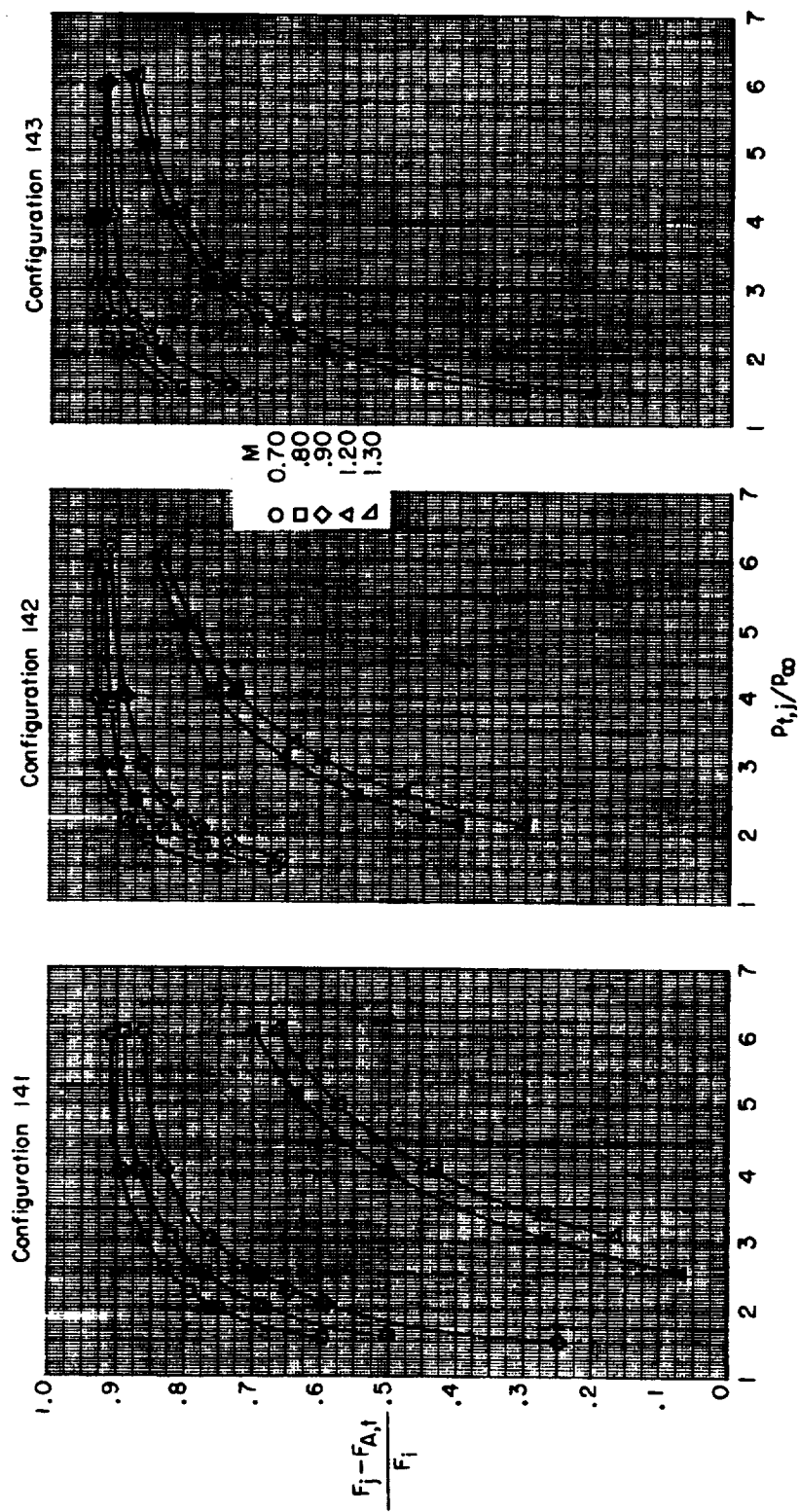
(b) Convergent-divergent nozzles.

Figure 15.- Continued.



(c) Plug nozzles with fixed tail flaps.

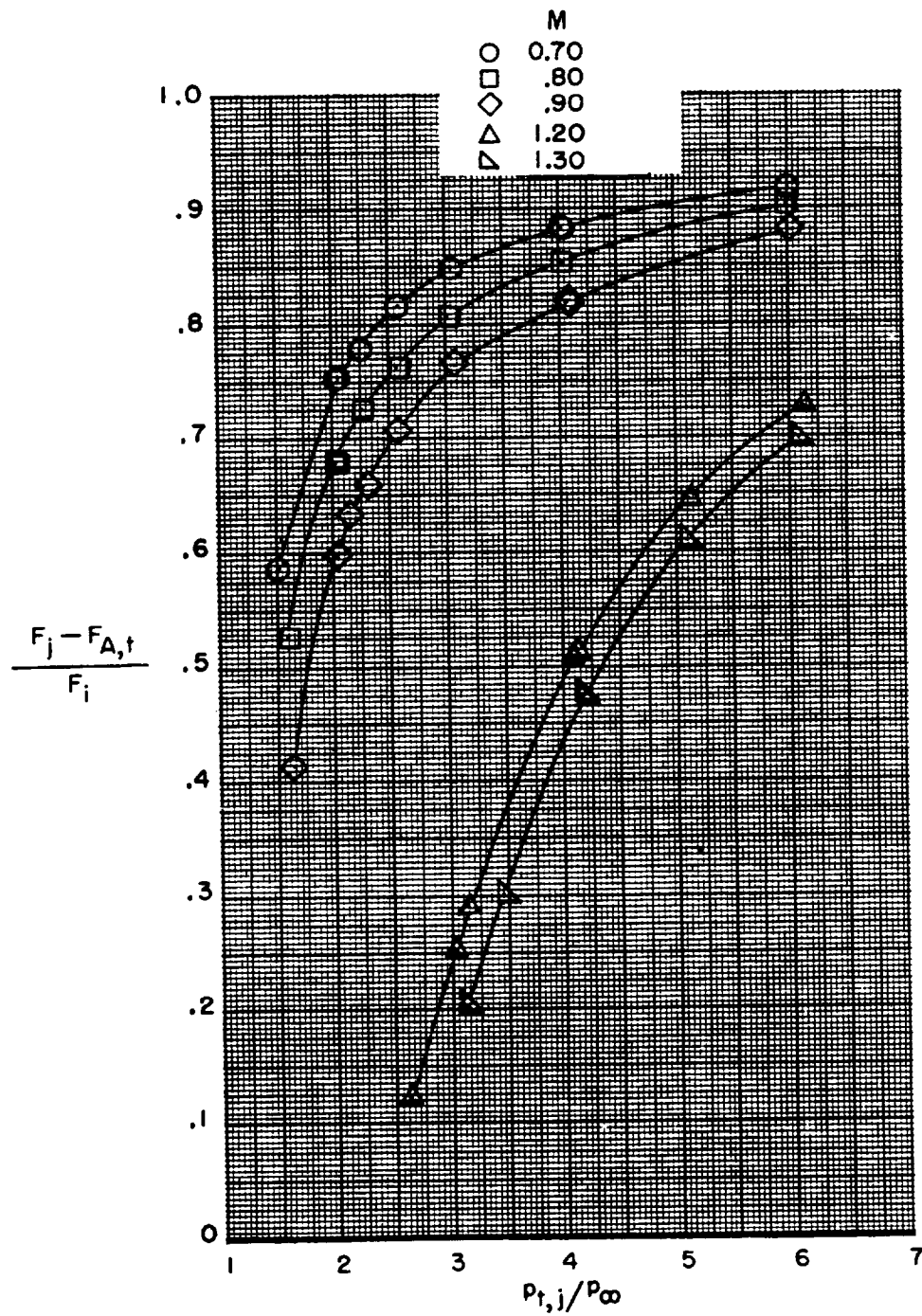
Figure 15.- Continued.



(d) Blow-in-door nozzles.

Figure 15.- Continued.

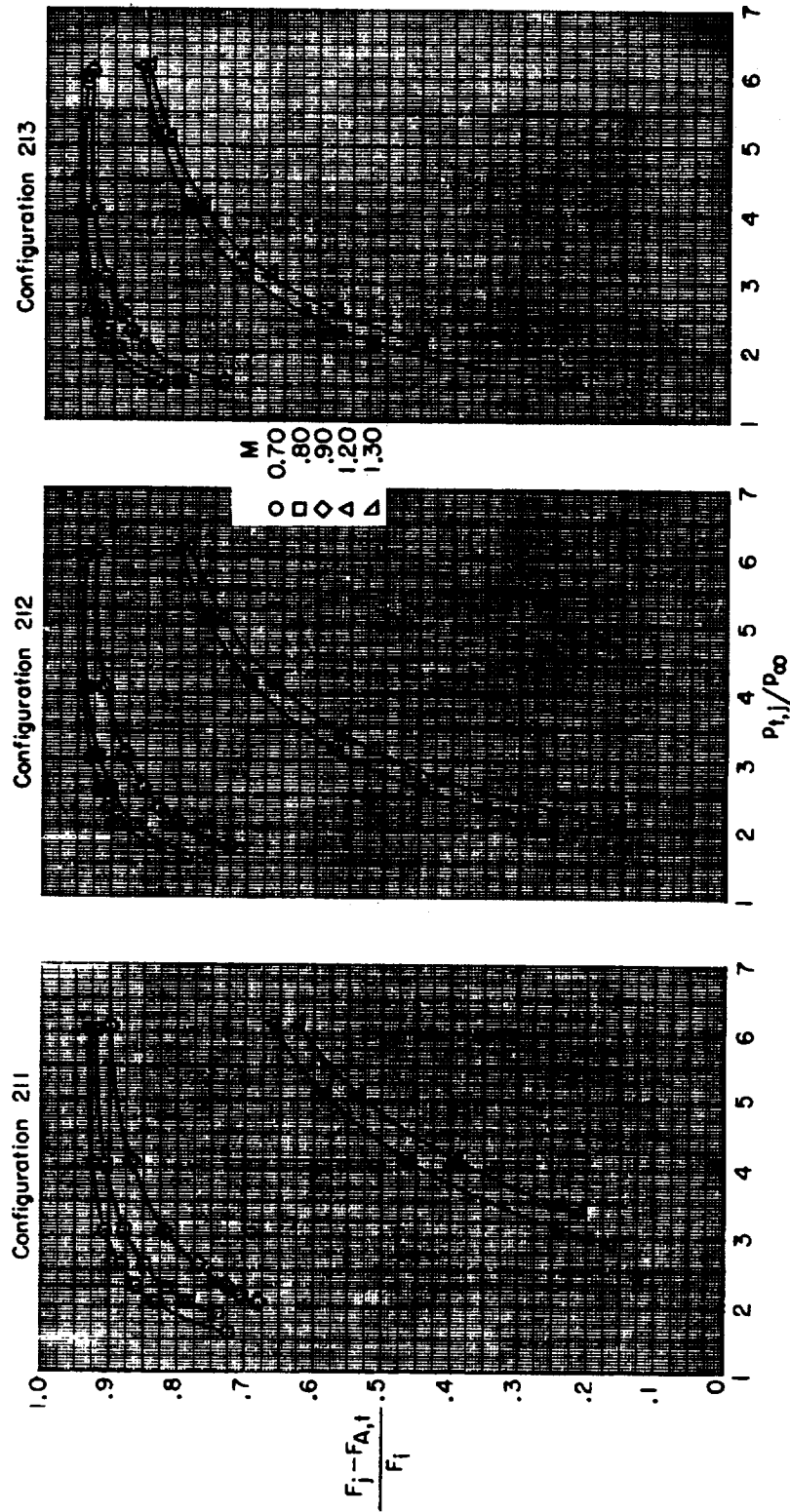
Configuration 101



(e) Reference blow-in-door nozzles.

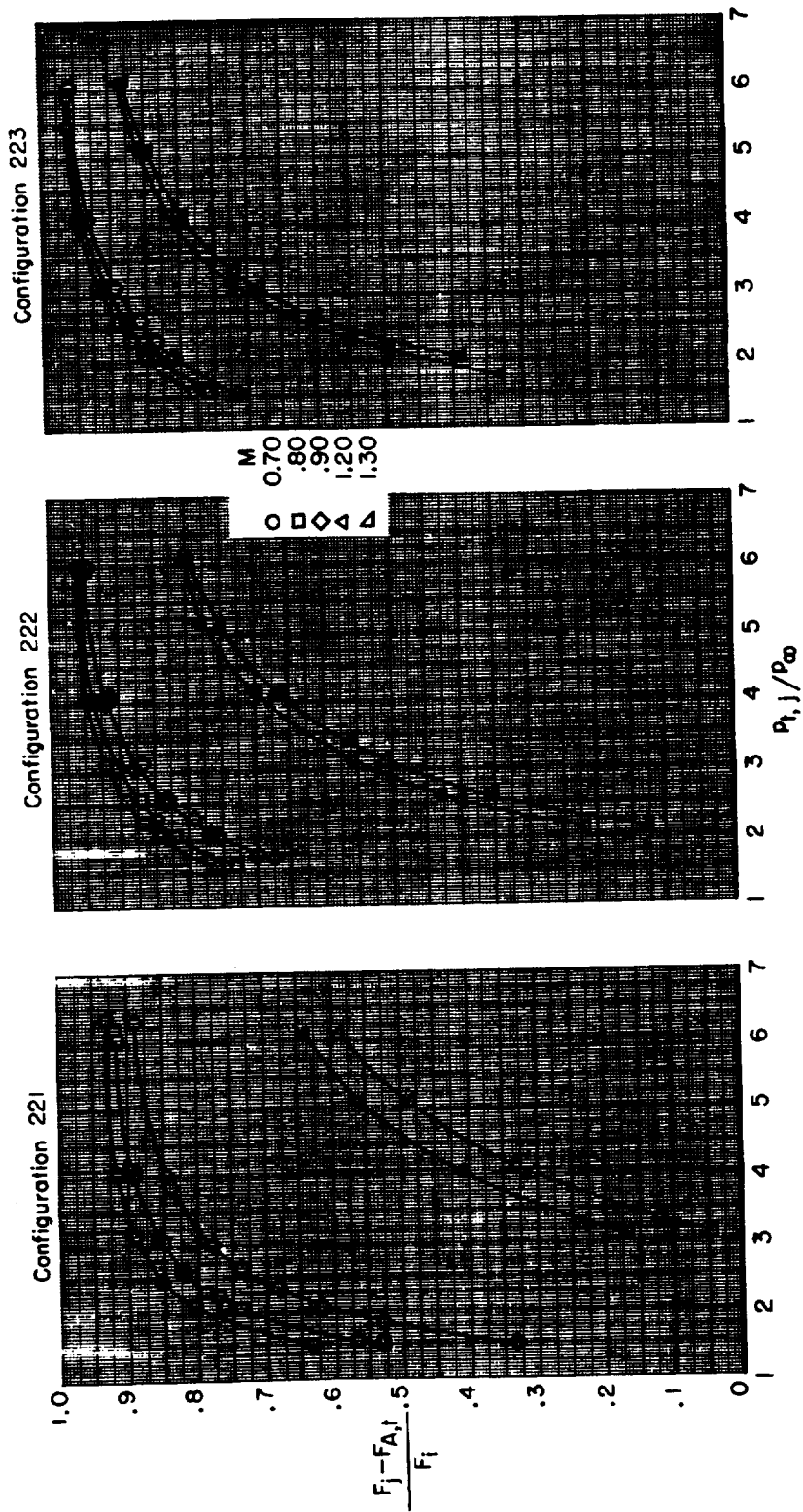
Figure 15.- Concluded.

CONFIDENTIAL



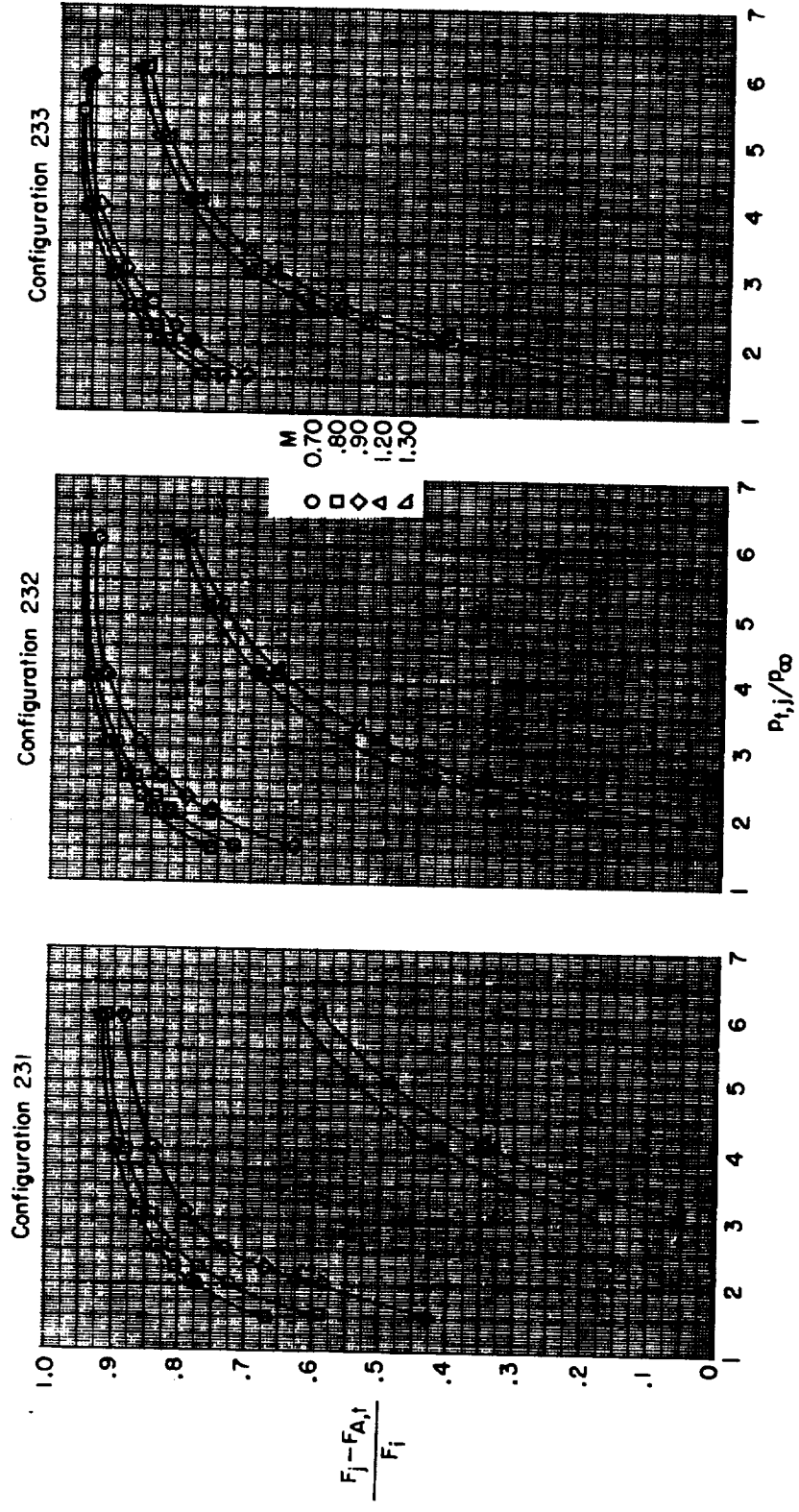
(a) Iris-convergent nozzles.

Figure 16.- Variation of gross thrust minus total afterbody axial-force performance with primary total-pressure ratio for afterbody 2.



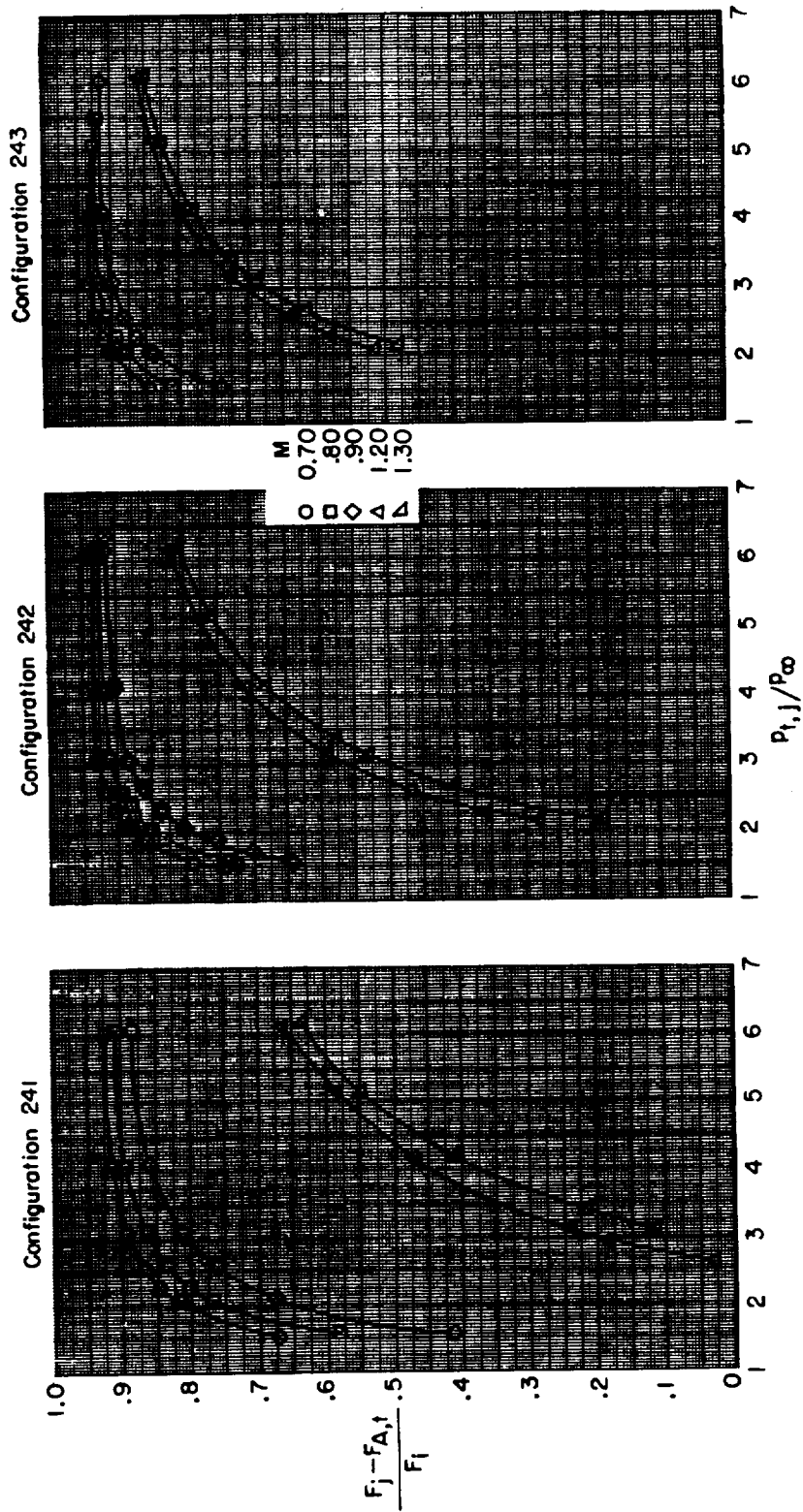
(b) Convergent-divergent nozzles.

Figure 16.- Continued.



(c) Plug nozzles with fixed tail flaps.

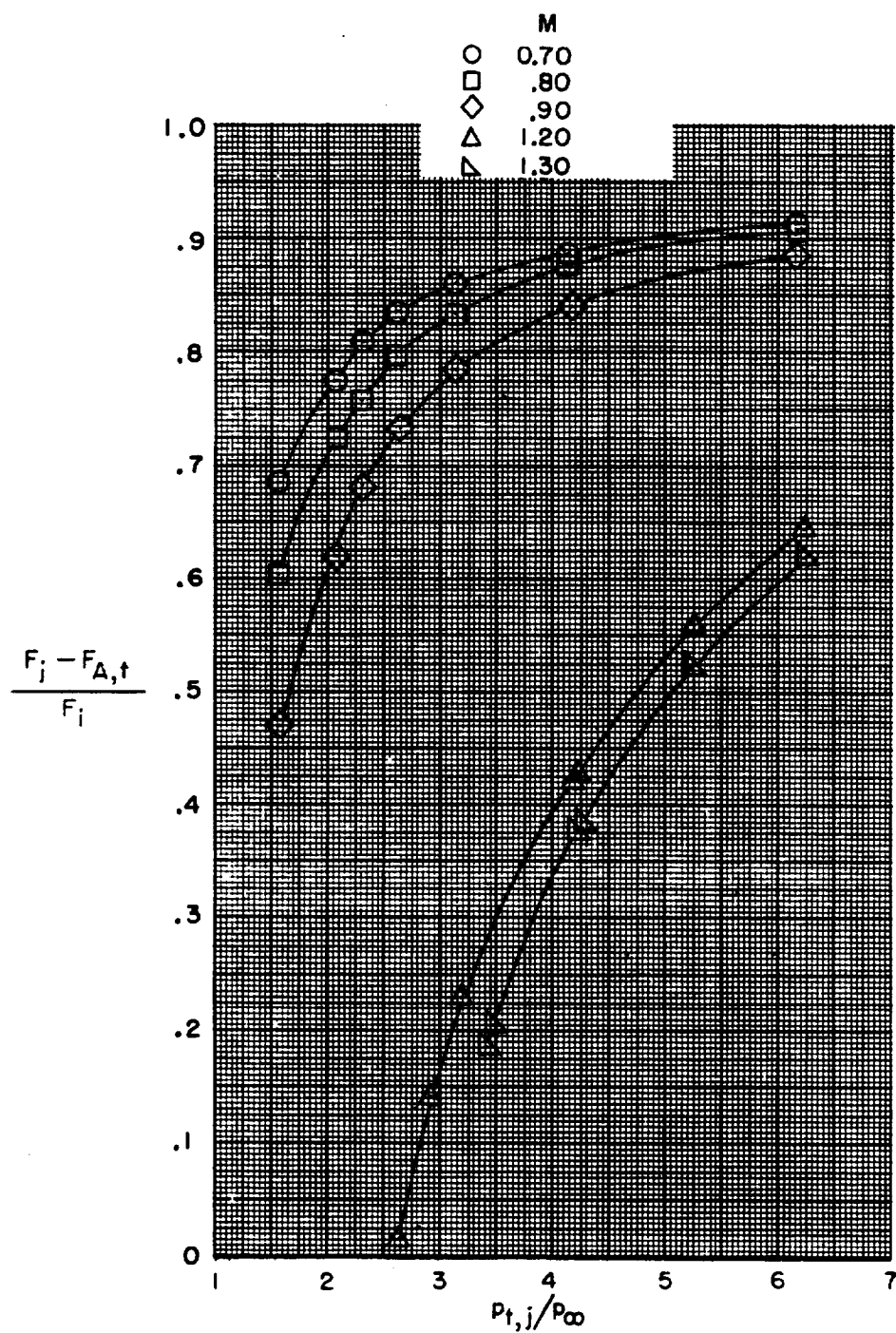
Figure 16.- Continued.



(d) Blow-in-door nozzles.

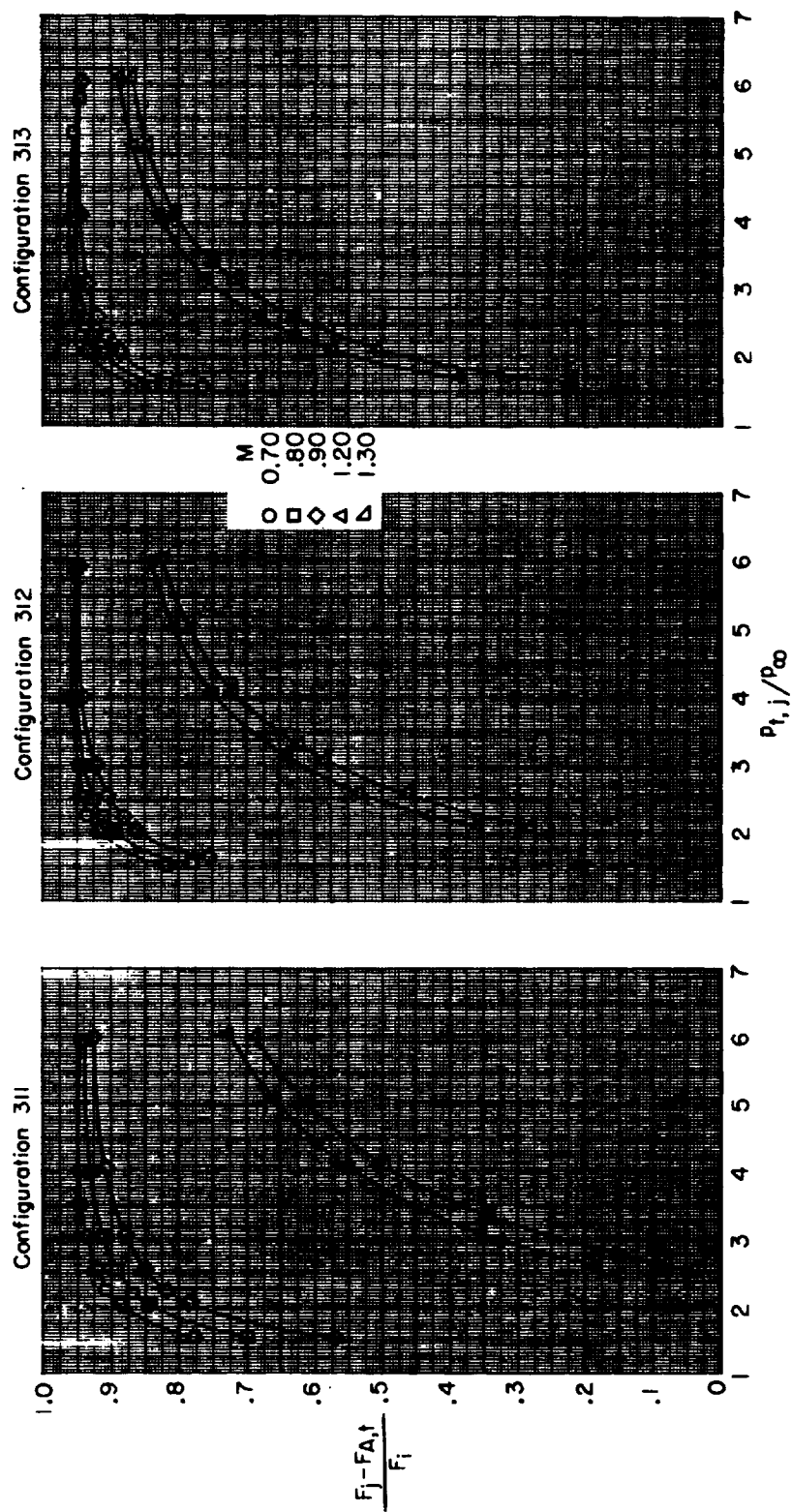
Figure 16.- Continued.

Configuration 26I



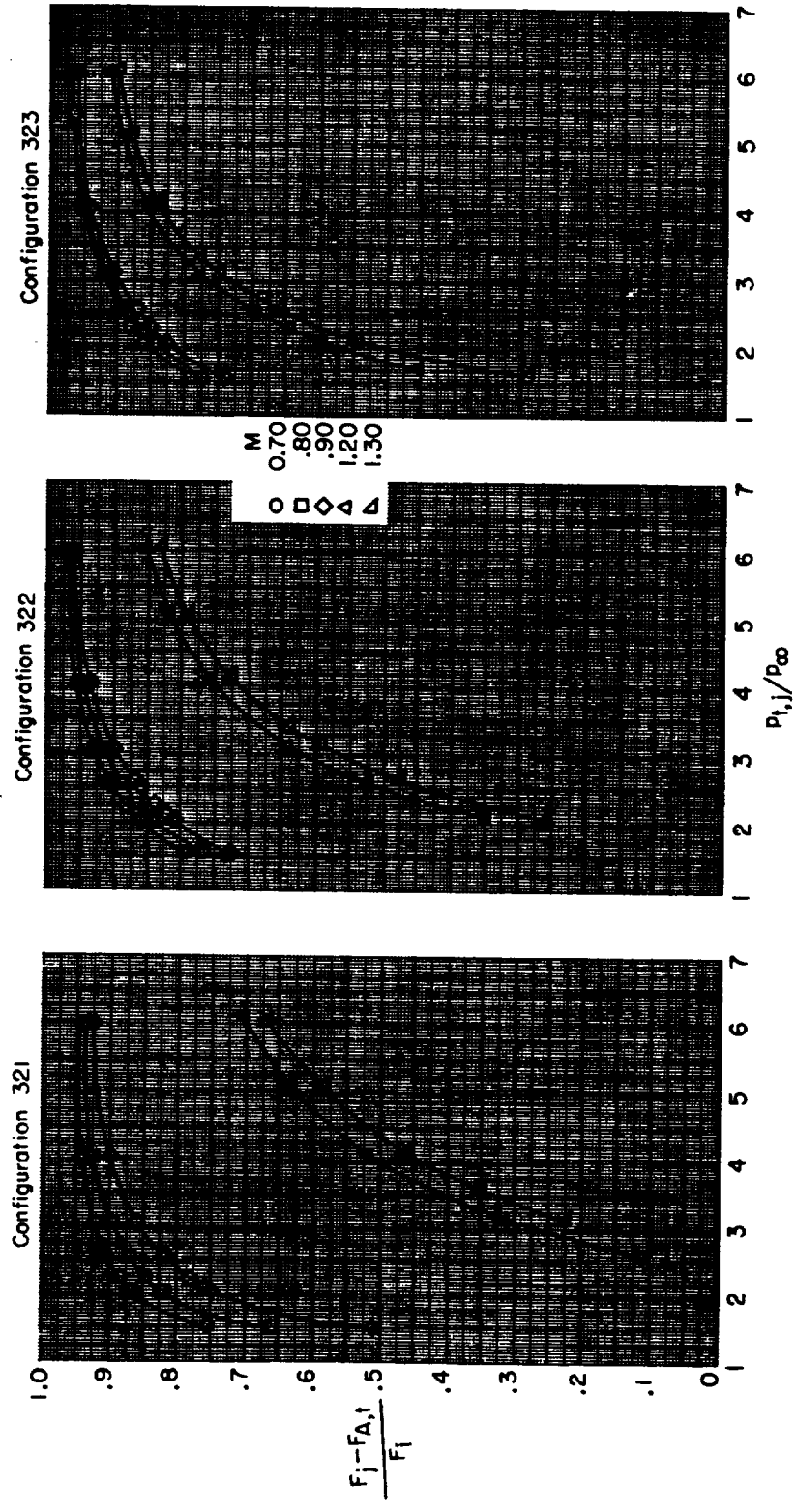
(e) Plug nozzles with floating tail flaps.

Figure 16.- Concluded.



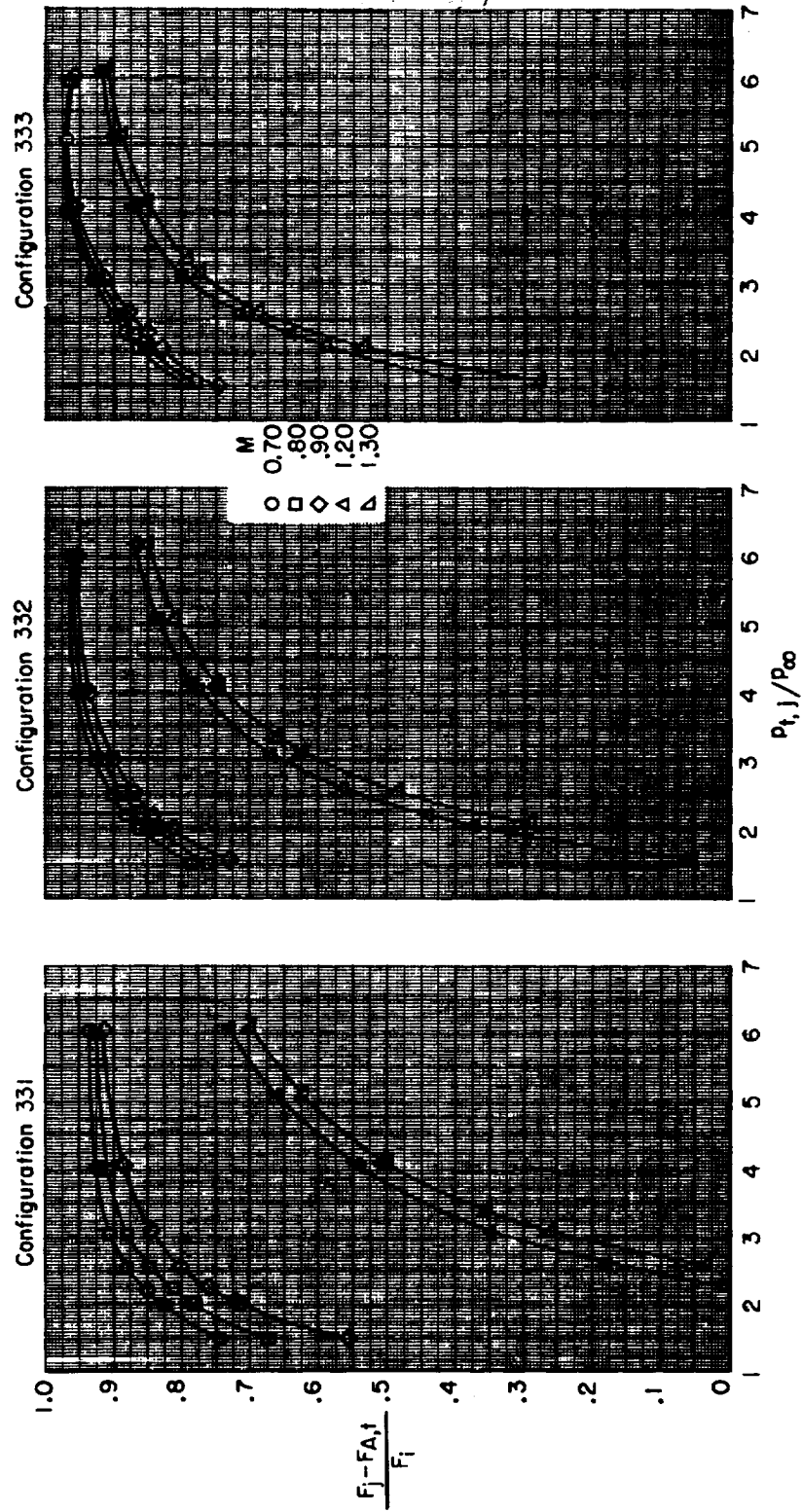
(a) Iris-convergent nozzles.

Figure 17.- Variation of gross thrust minus total afterbody axial-force performance with primary total-pressure ratio for afterbody 3.



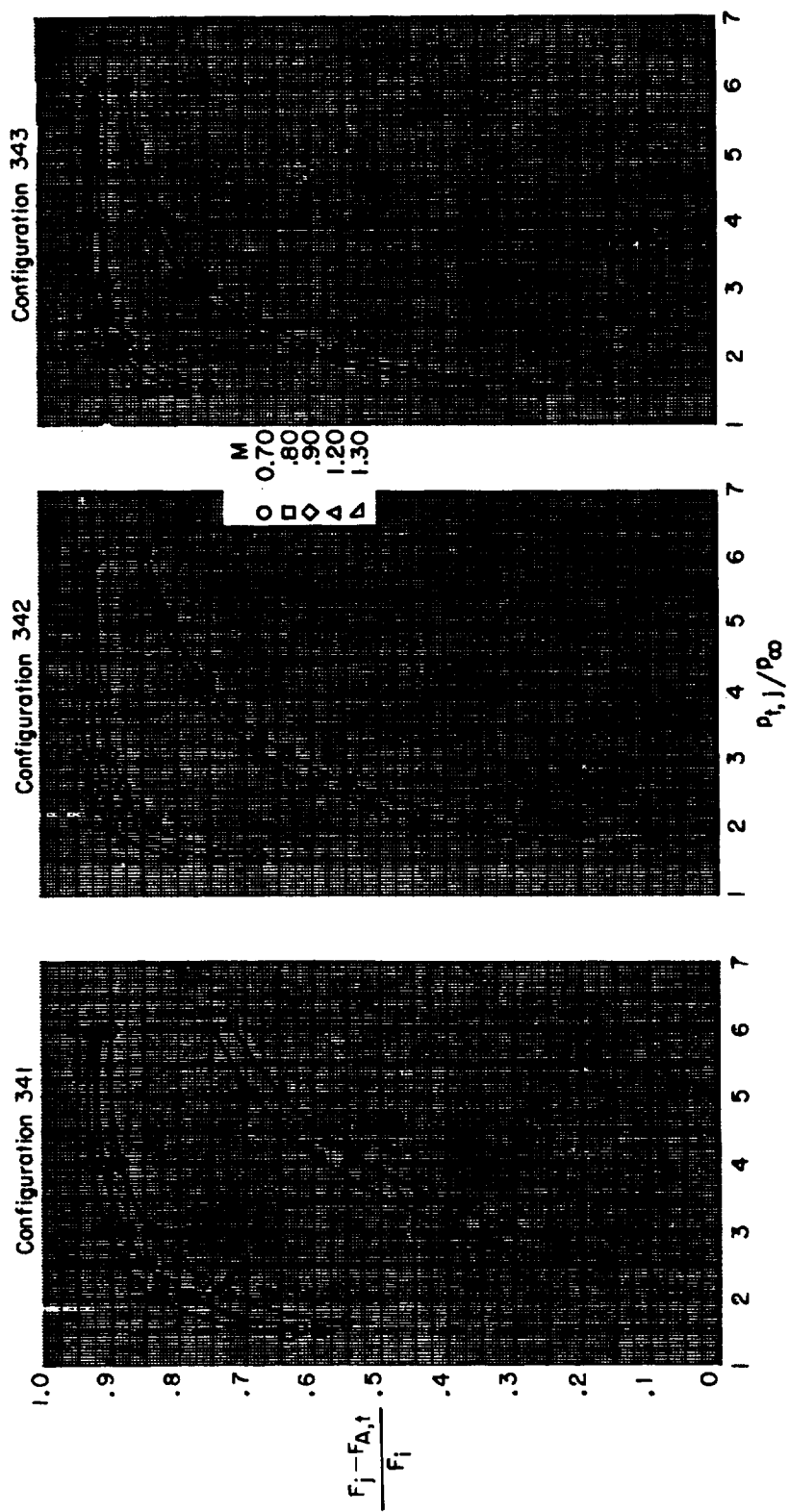
(b) Convergent-divergent nozzles.

Figure 17.- Continued.



(c) Plug nozzles with fixed tail flaps.

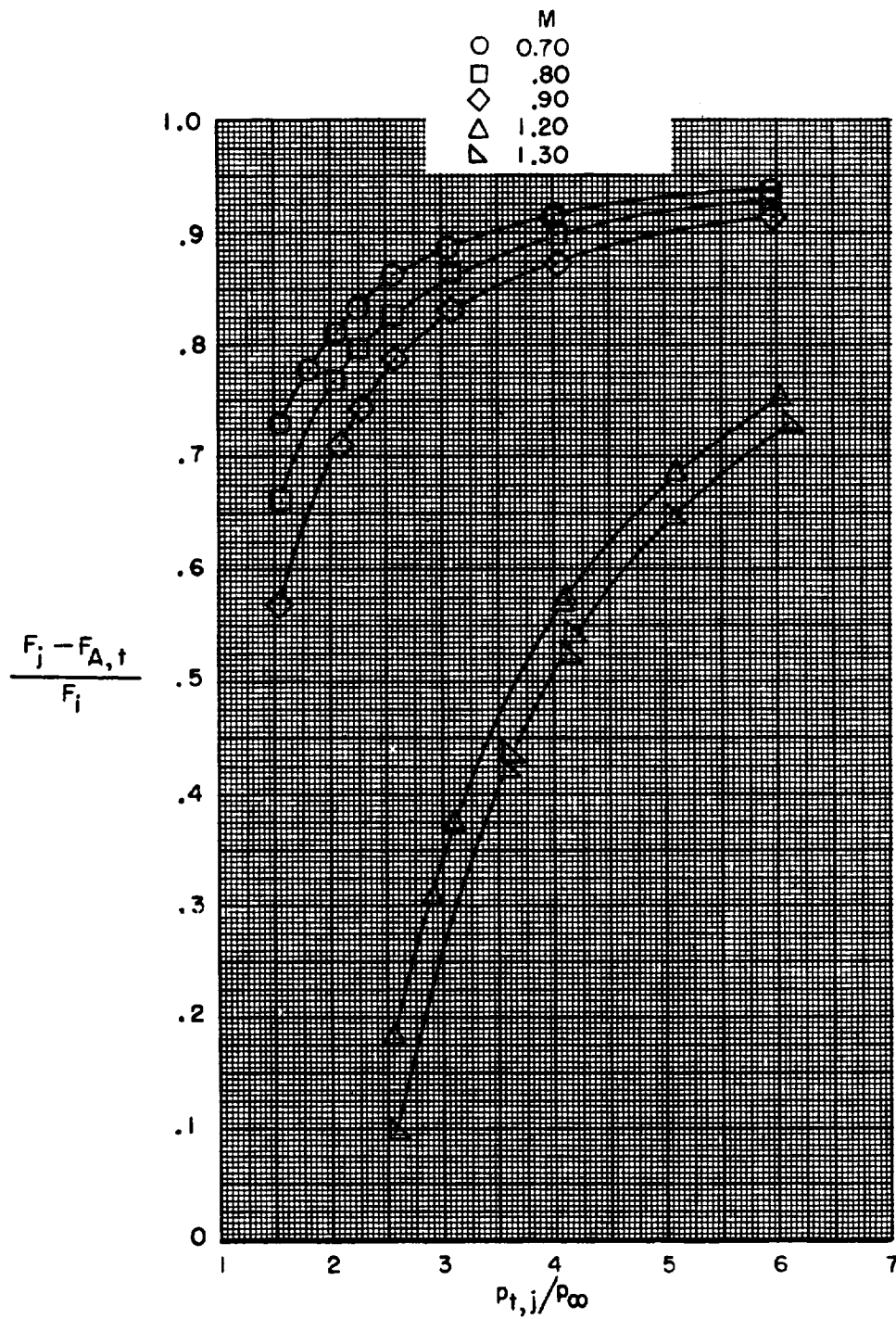
Figure 17.- Continued.



(d) Blow-in-door nozzles.

Figure 17.- Continued.

Configuration 361

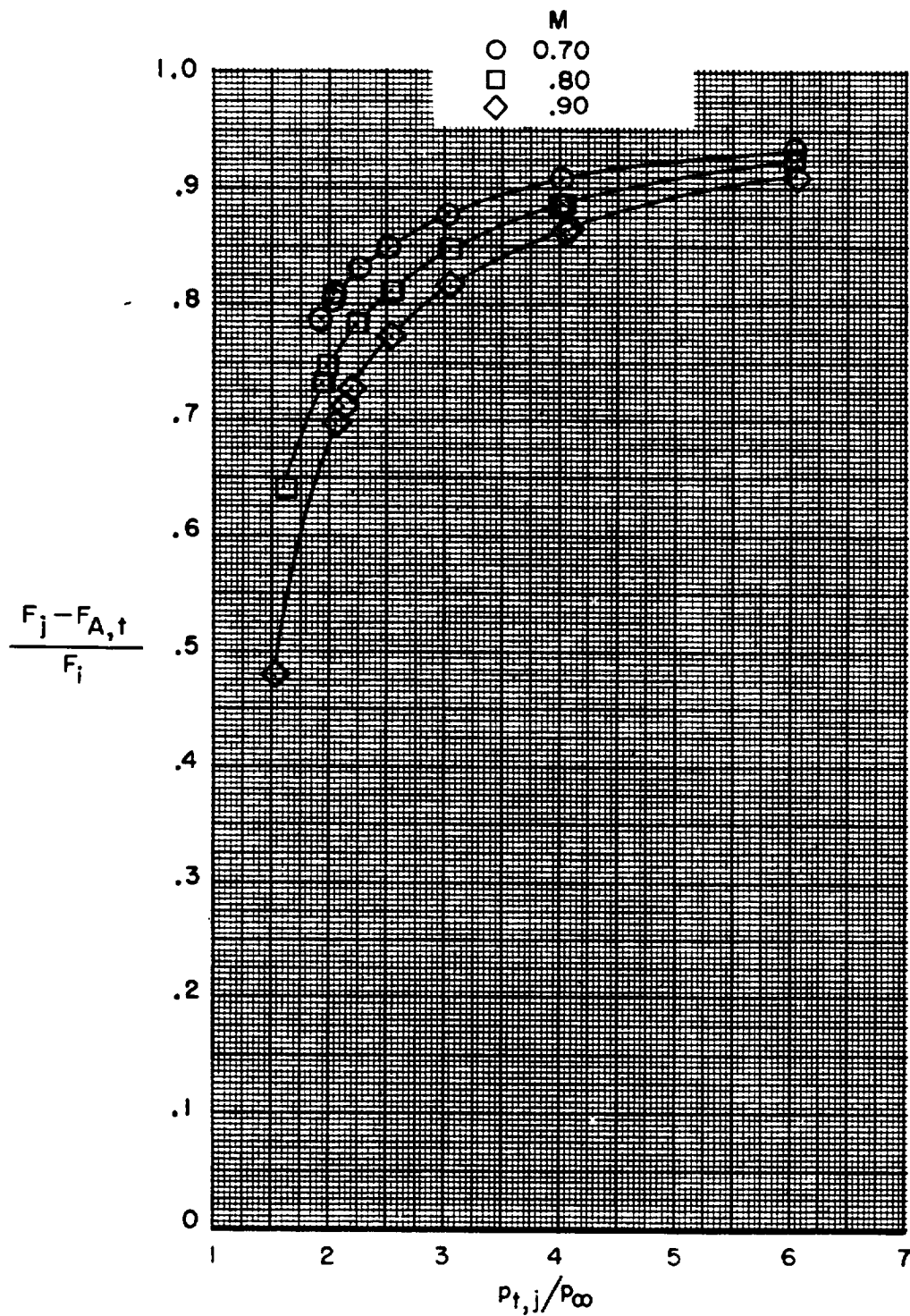


(e) Plug nozzles with floating tail flaps.

Figure 17.- Continued.

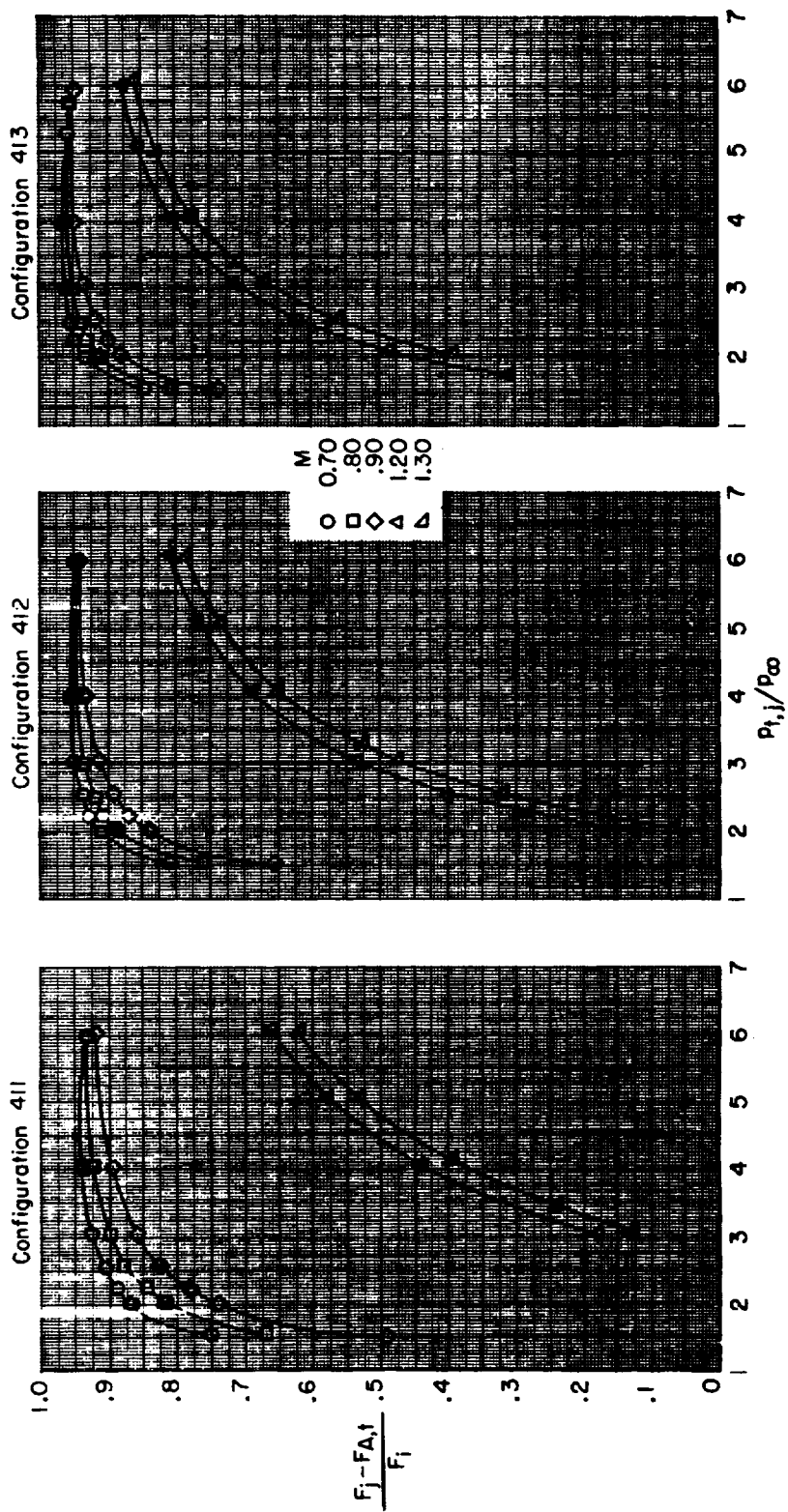
CONFIDENTIAL

Configuration 301



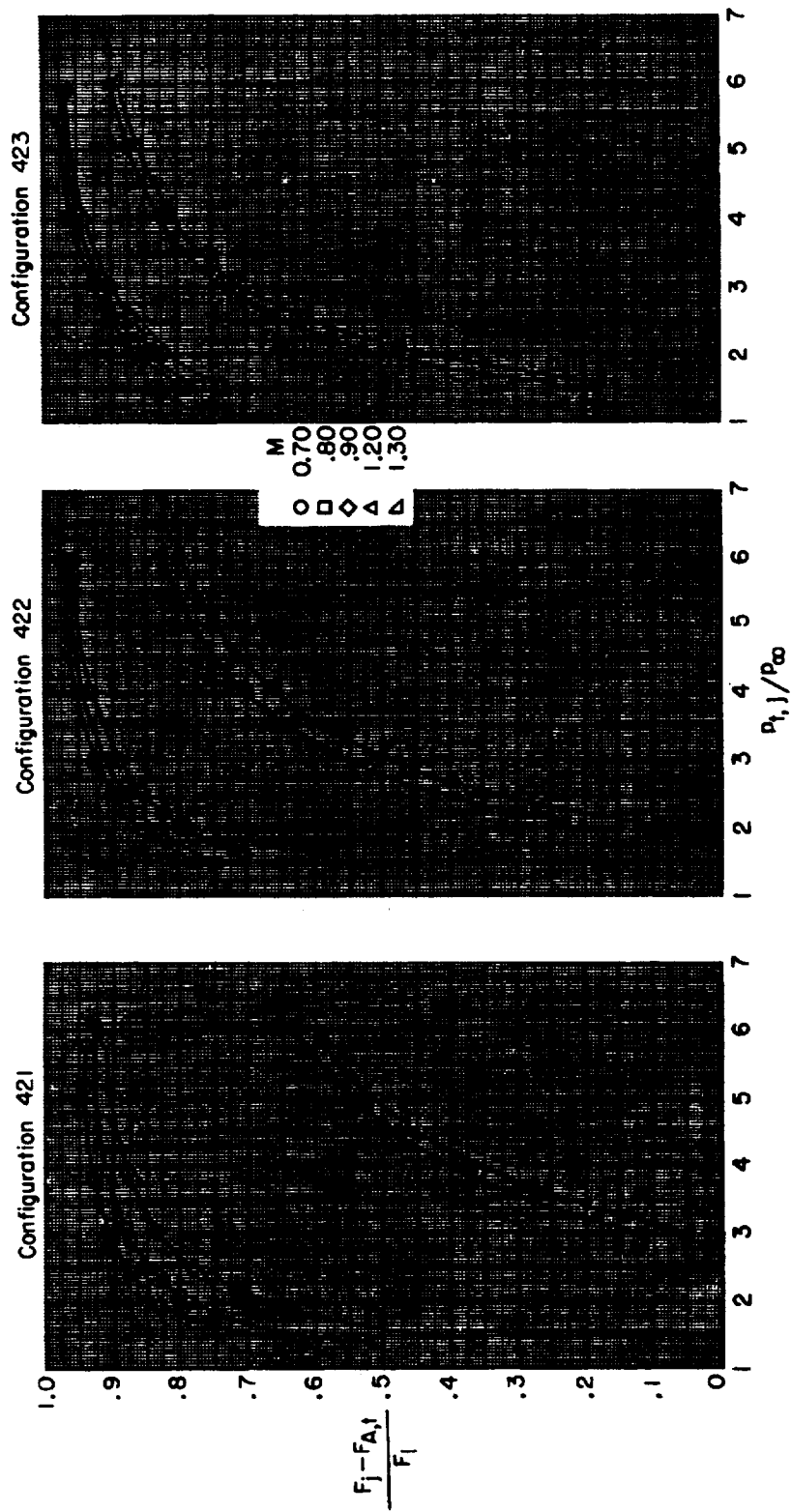
(f) Reference blow-in-door nozzles.

Figure 17.- Concluded.



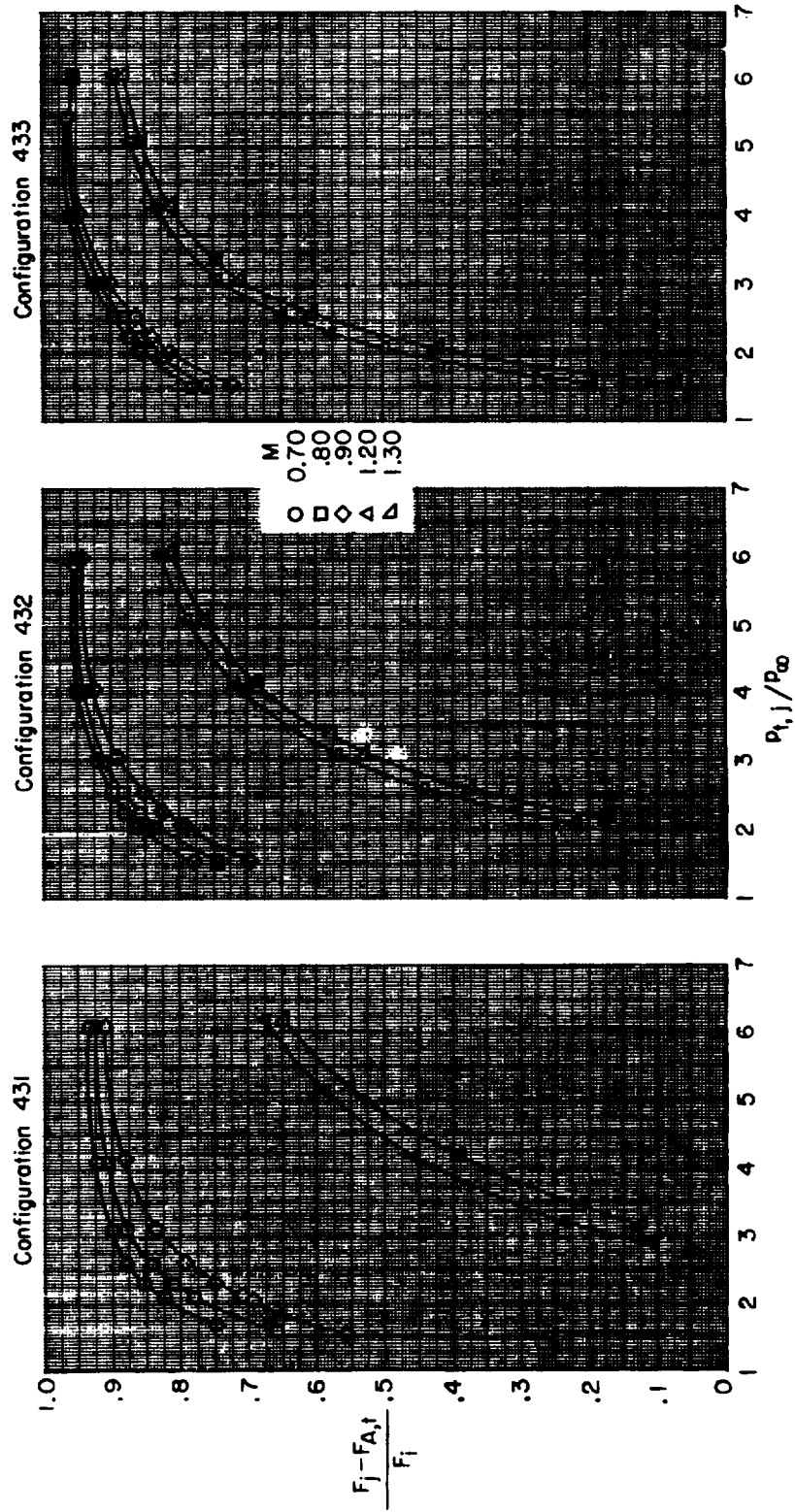
(a) Iris-convergent nozzles.

Figure 18.- Variation of gross thrust minus total afterbody axial force performance with primary total-pressure ratio for afterbody 4.



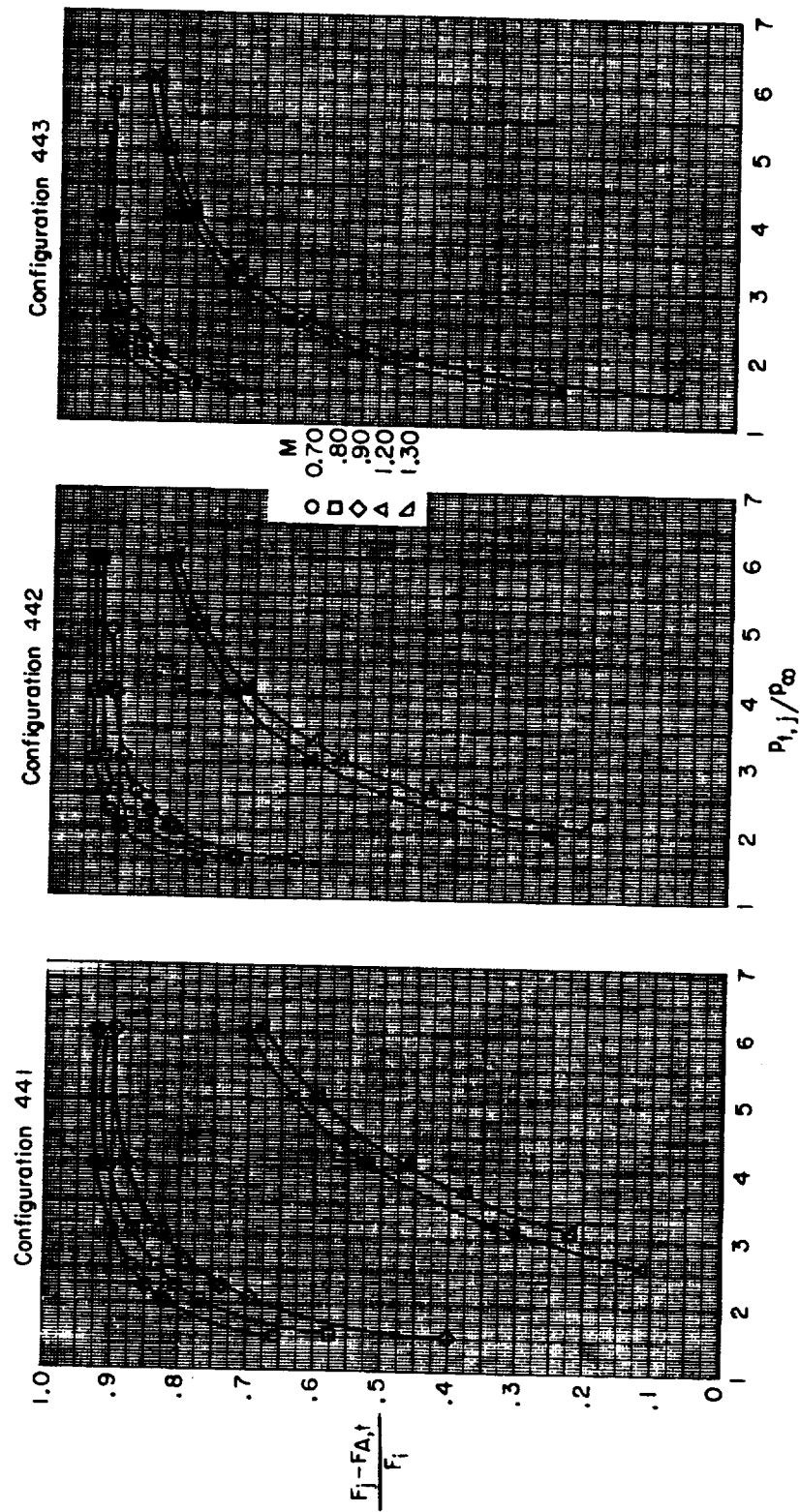
(b) Convergent-divergent nozzles.

Figure 18. - Continued.



(c) Plug nozzles with fixed tail flaps.

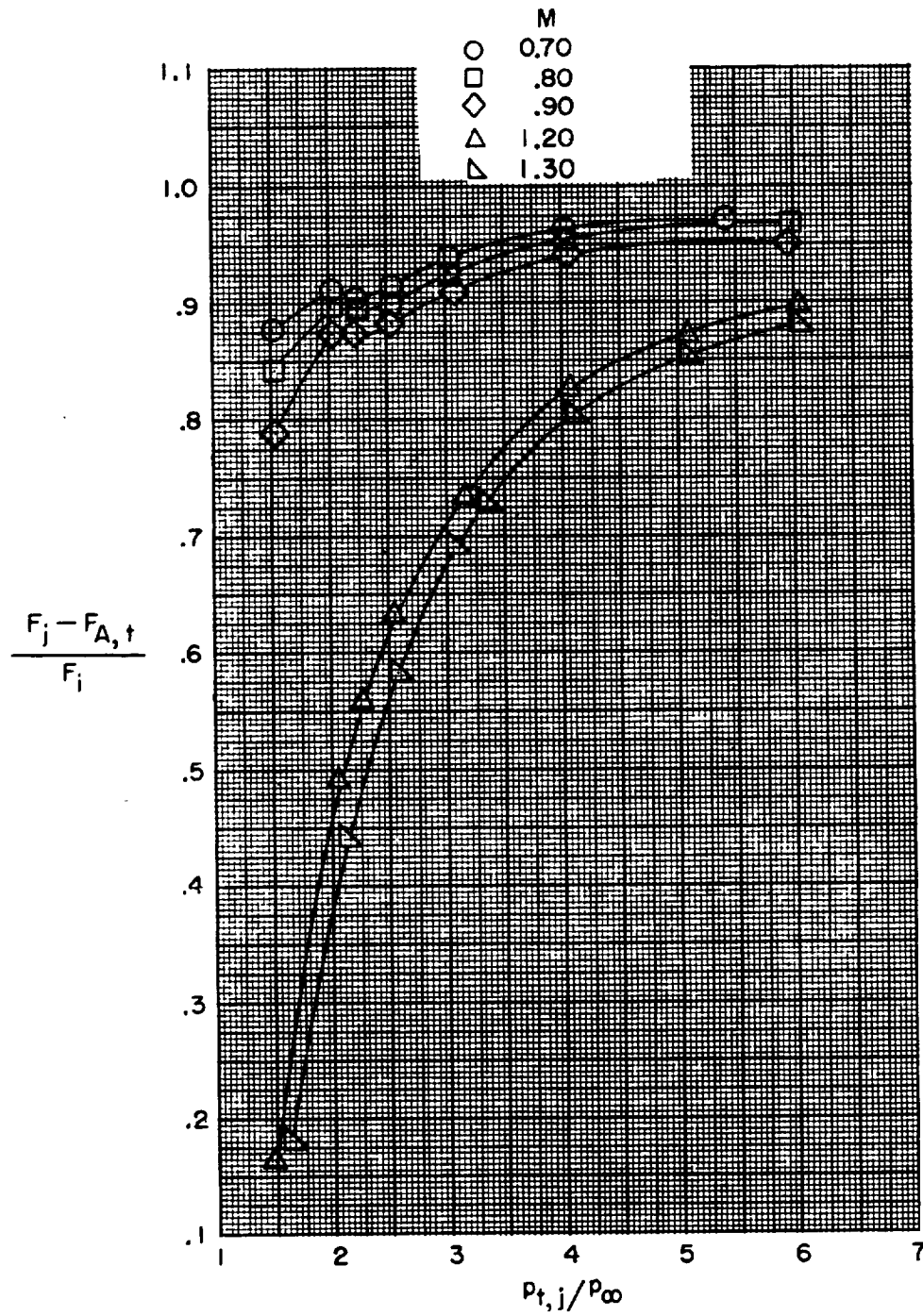
Figure 18.- Continued.



(d) Blow-in-door nozzles.

Figure 18.- Continued.

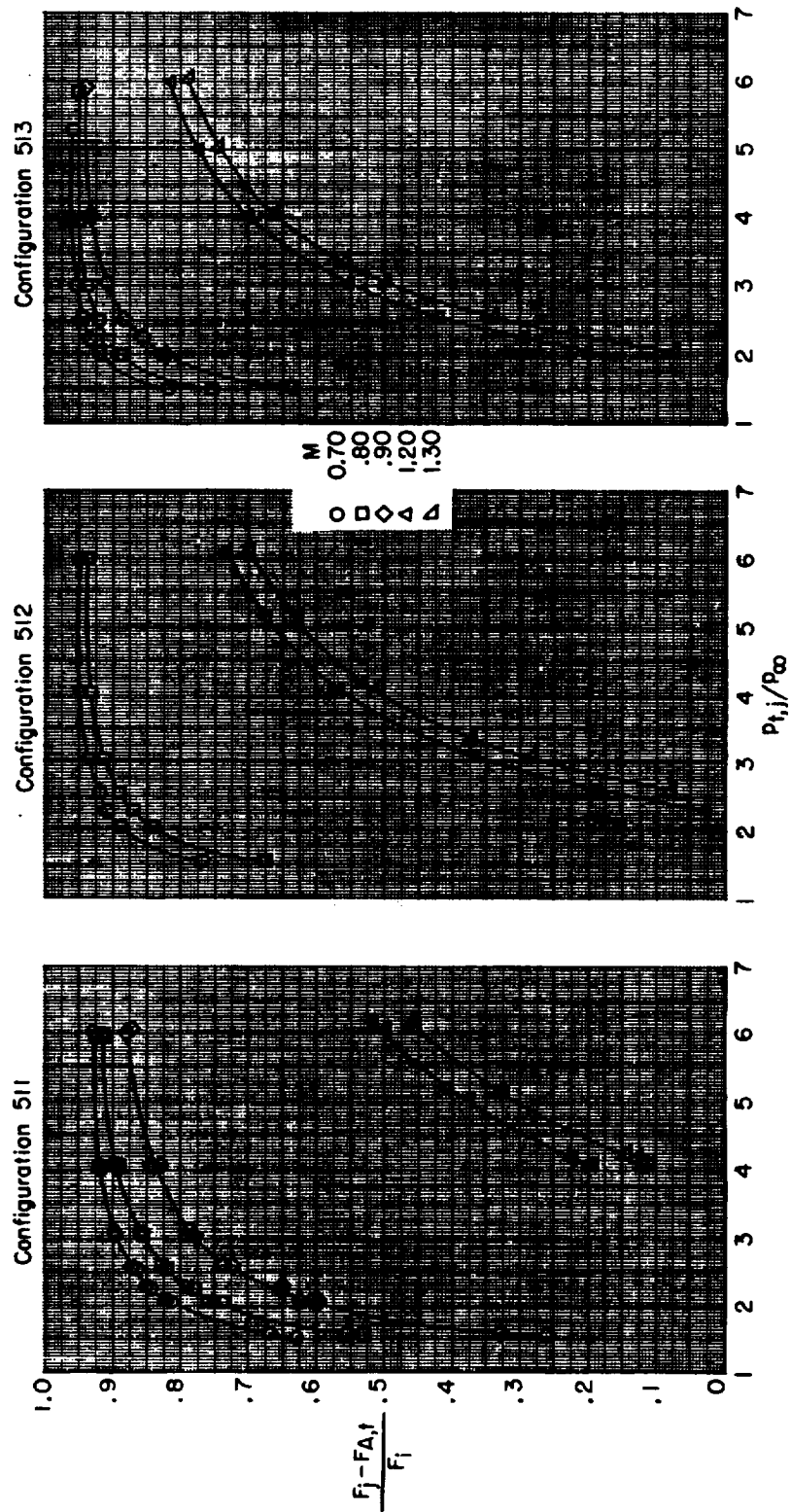
Configuration 453



(e) Convergent-divergent-iris nozzles.

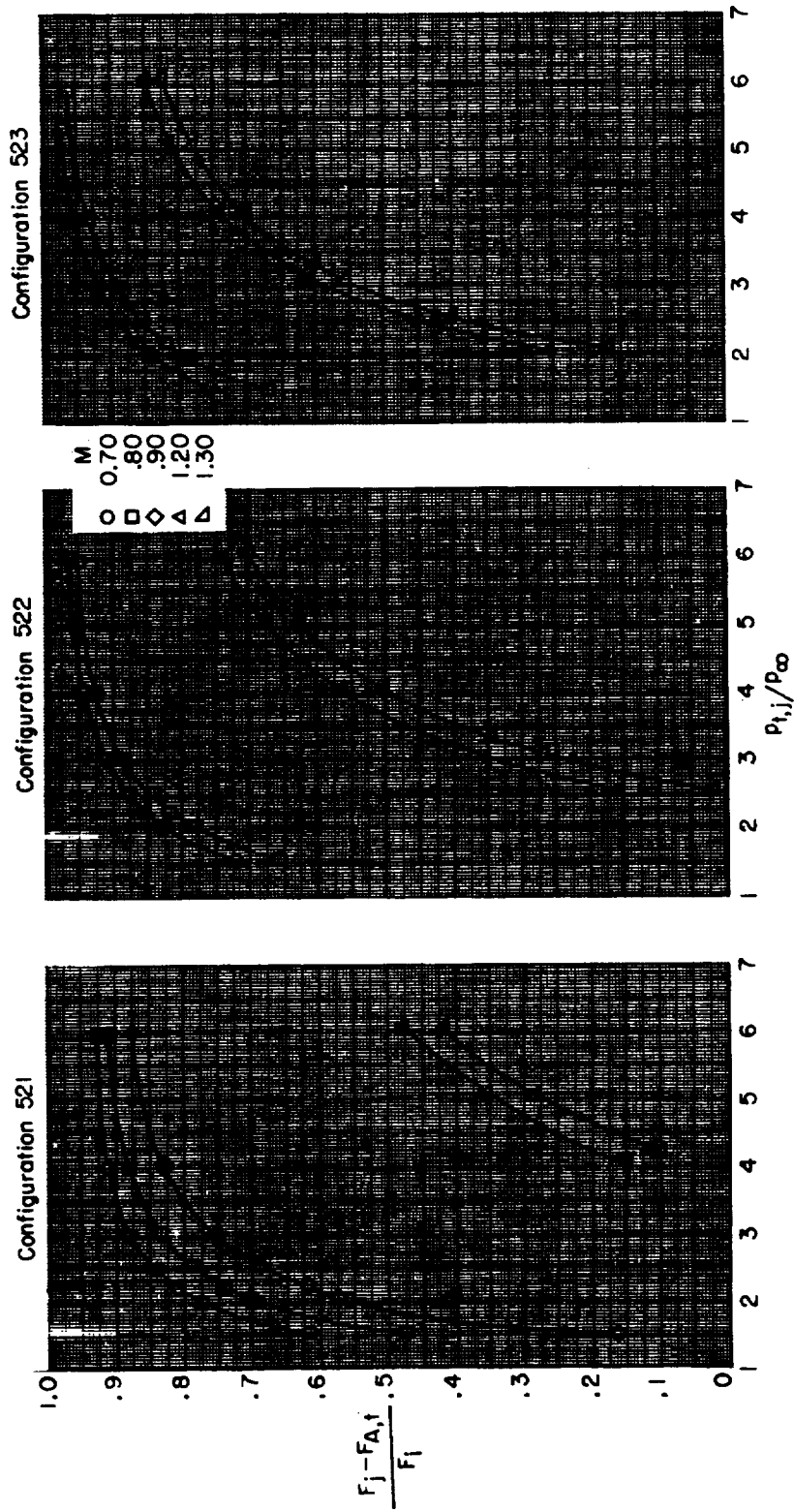
Figure 18.- Concluded.

CONFIDENTIAL



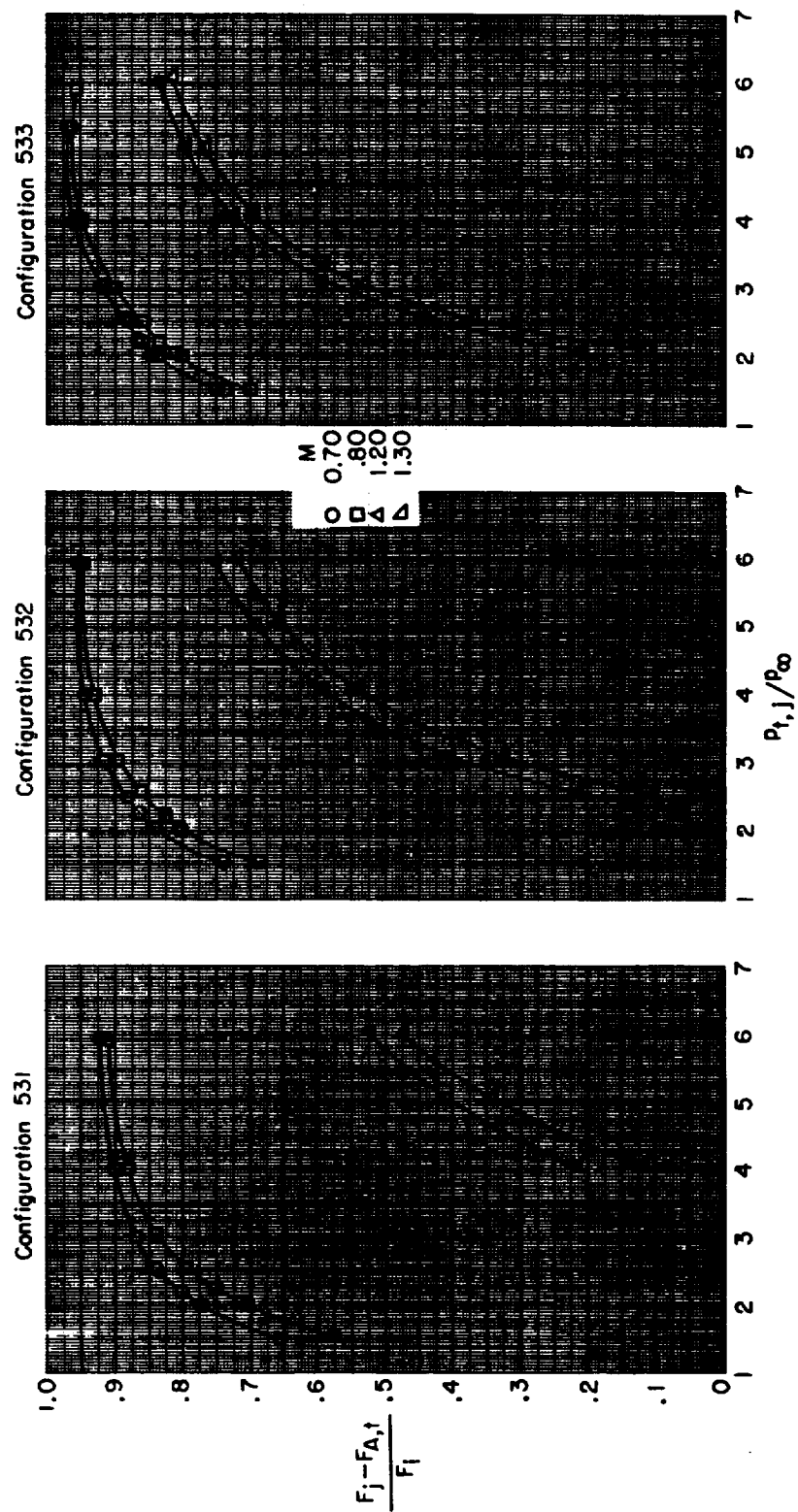
(a) Iris-convergent nozzles.

Figure 19.- Variation of gross thrust minus total afterbody axial-force performance with primary total-pressure ratio for afterbody 5.



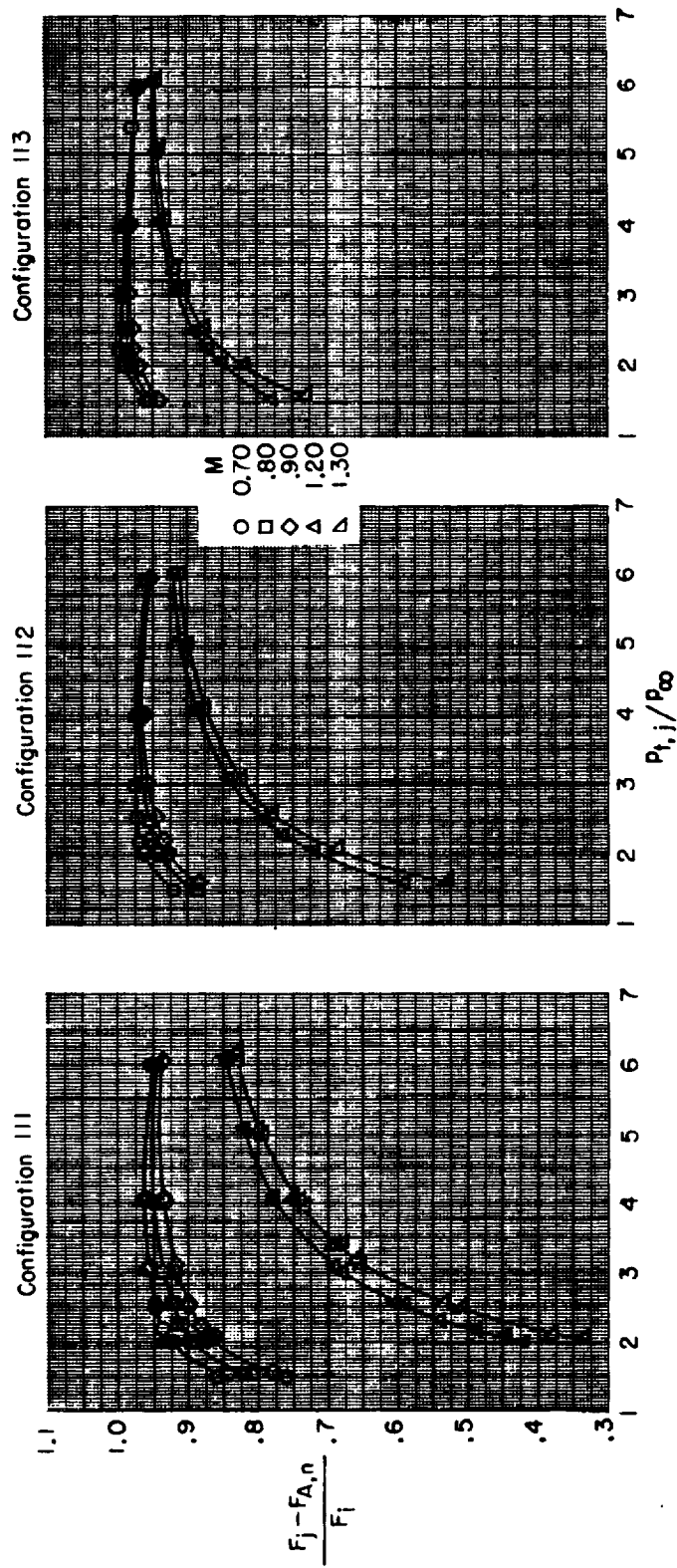
(b) Convergent-divergent nozzles.

Figure 19. - Continued.



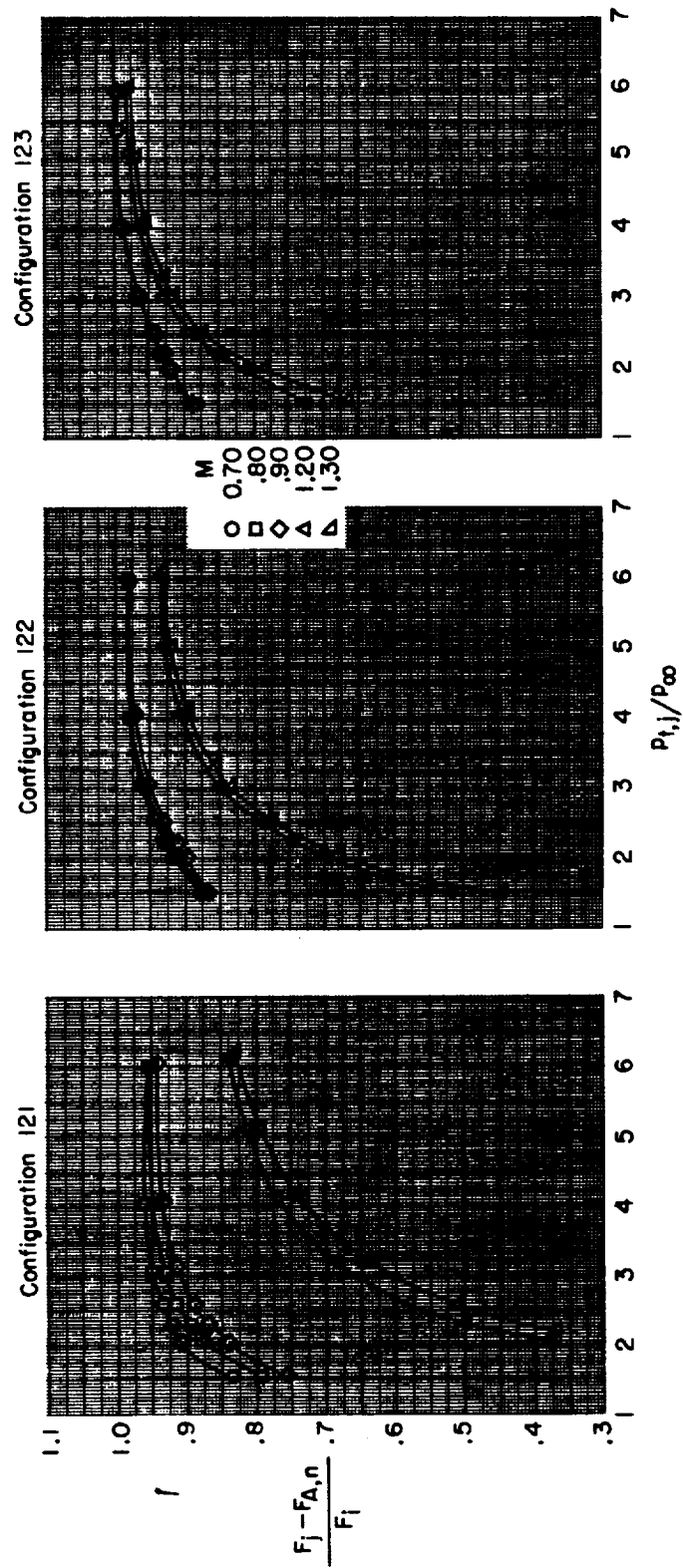
(c) Plug nozzles with fixed tail flaps.

Figure 19.- Concluded.



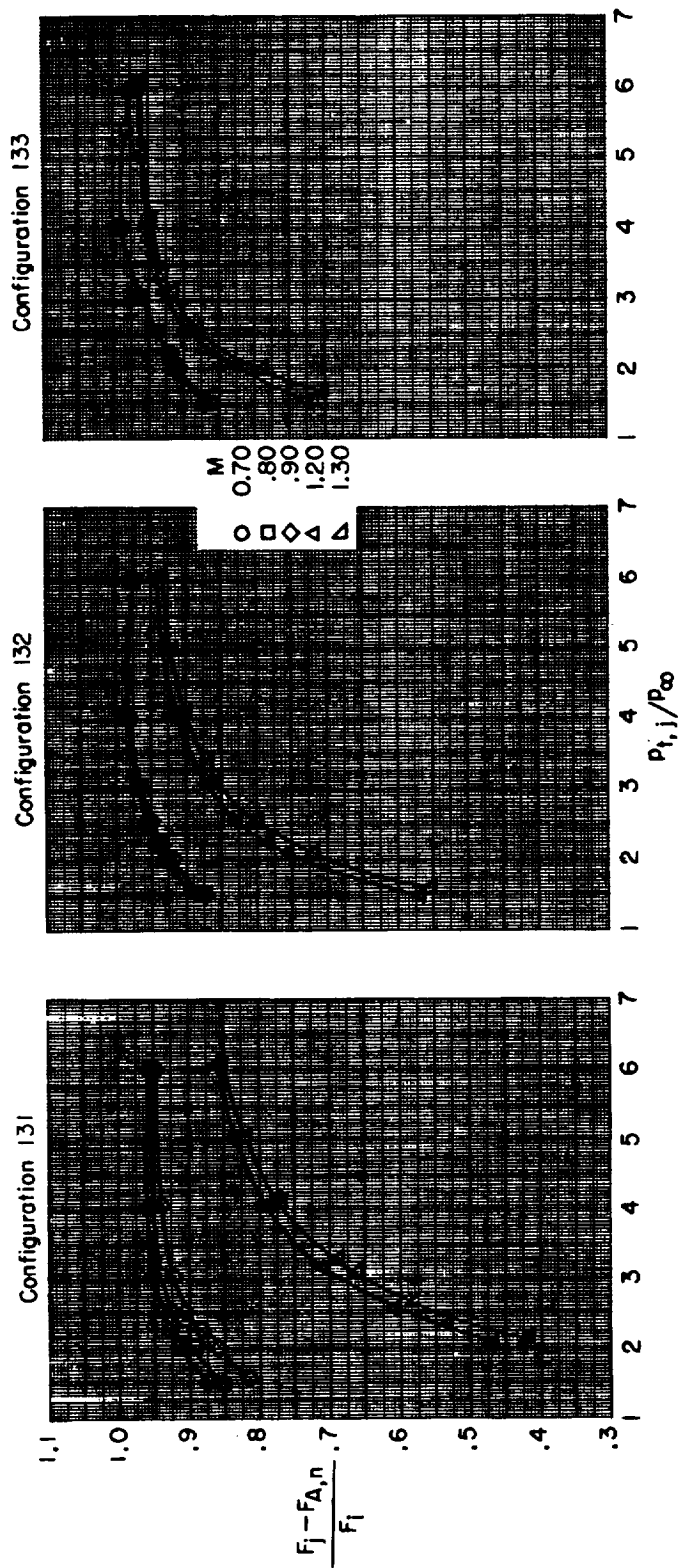
(a) Iris-convergent nozzles.

Figure 20.- Variation of gross thrust minus nozzle axial-force performance with primary total-pressure ratio for afterbody 1.



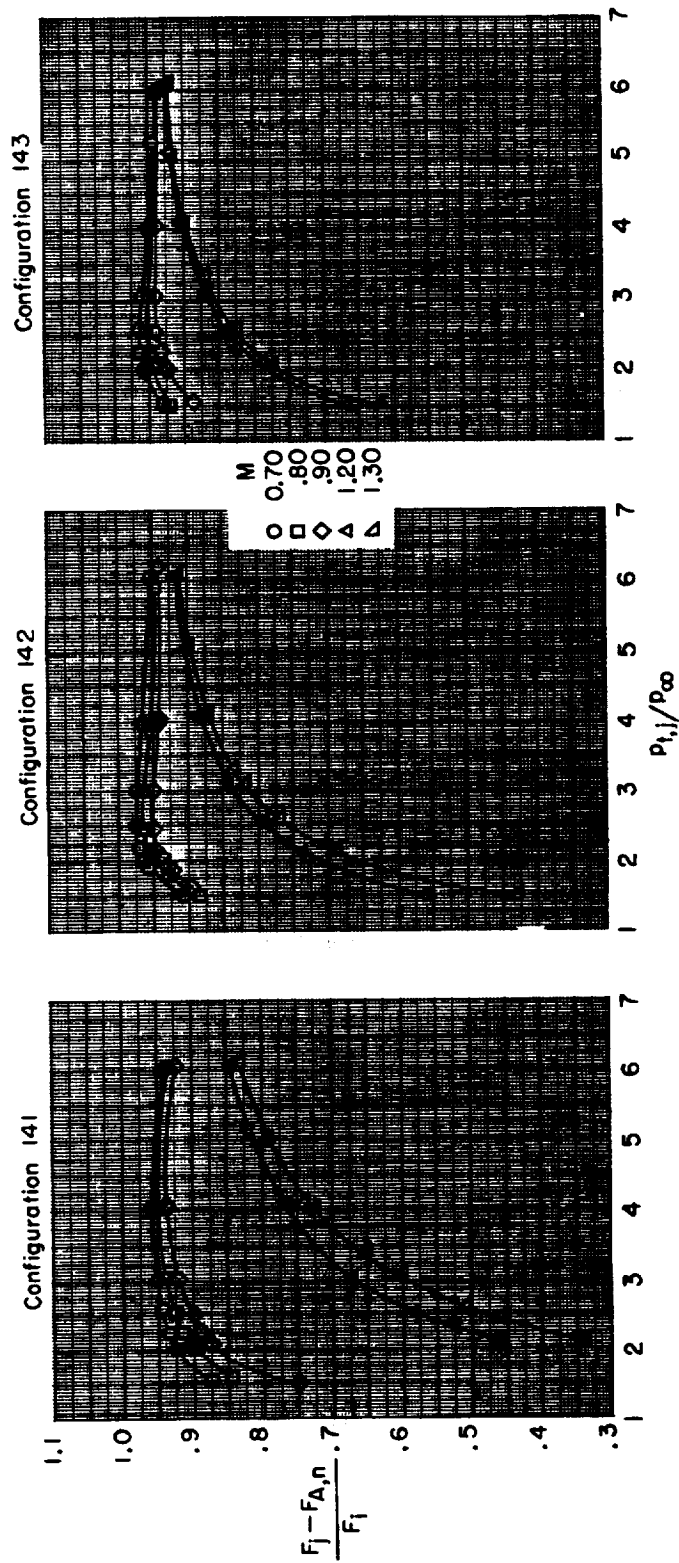
(b) Convergent-divergent nozzles.

Figure 20.- Continued.



(c) Plug nozzles with fixed tail flaps.

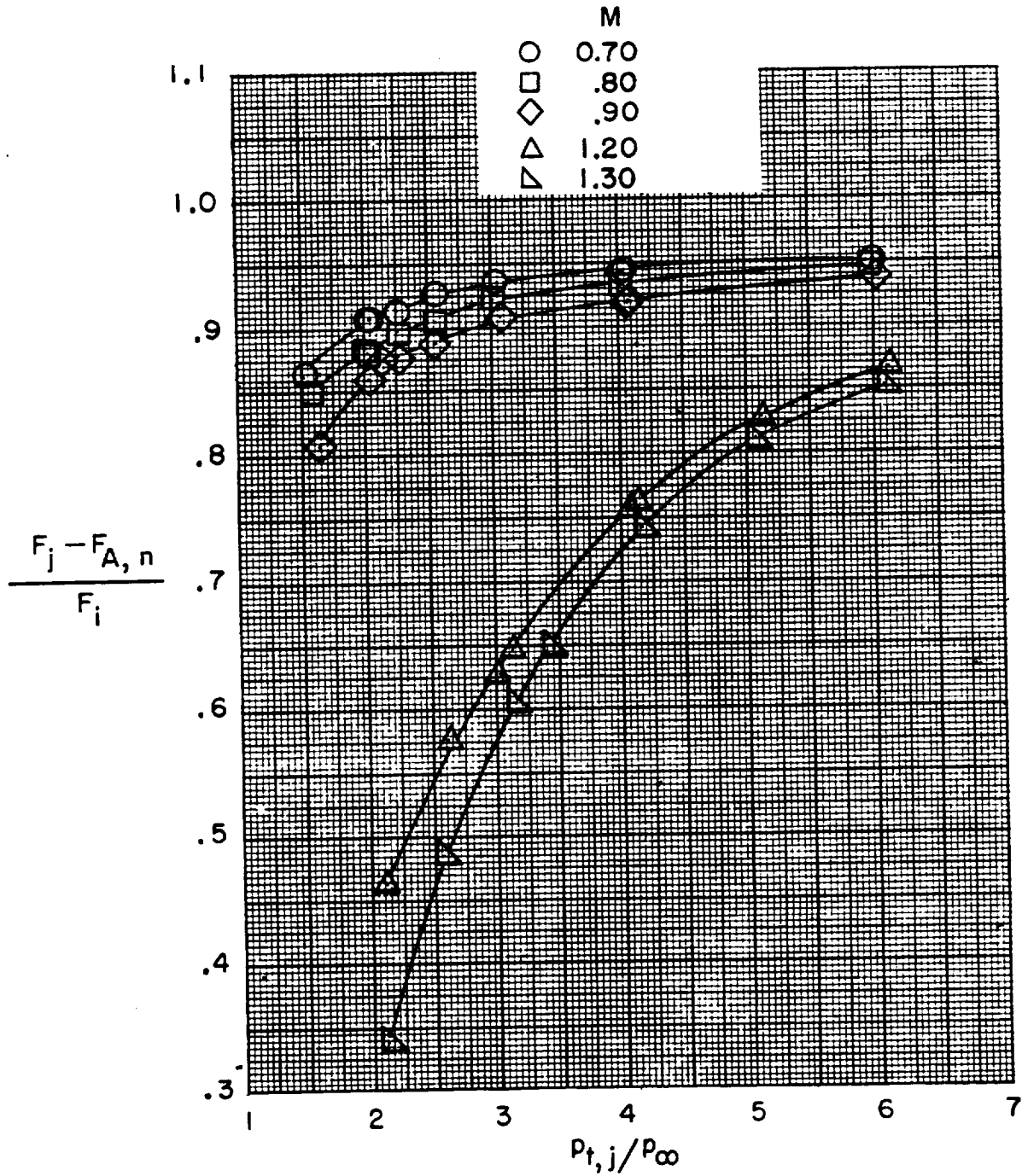
Figure 20.- Continued.



(d) Blow-in-door nozzles.

Figure 20.- Continued.

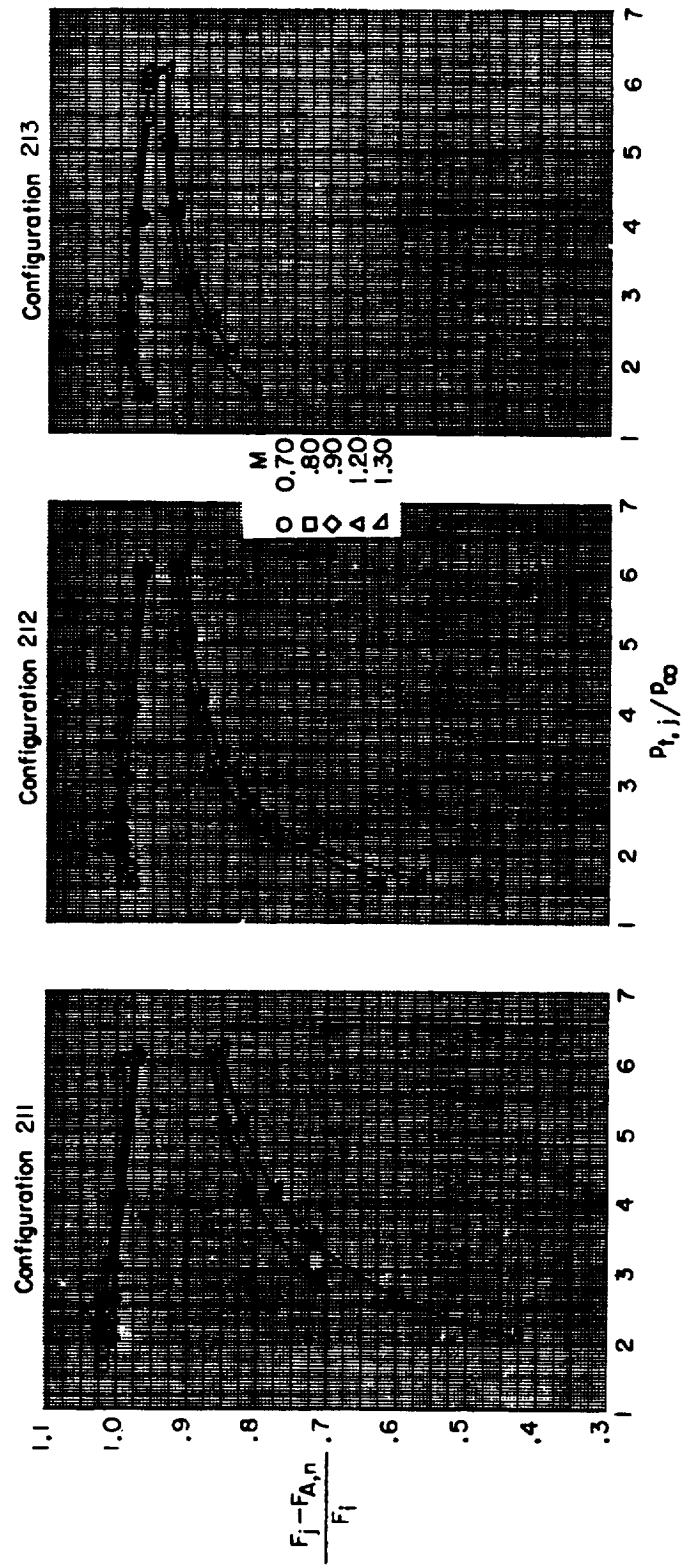
Configuration 101



(e) Reference blow-in-door nozzles.

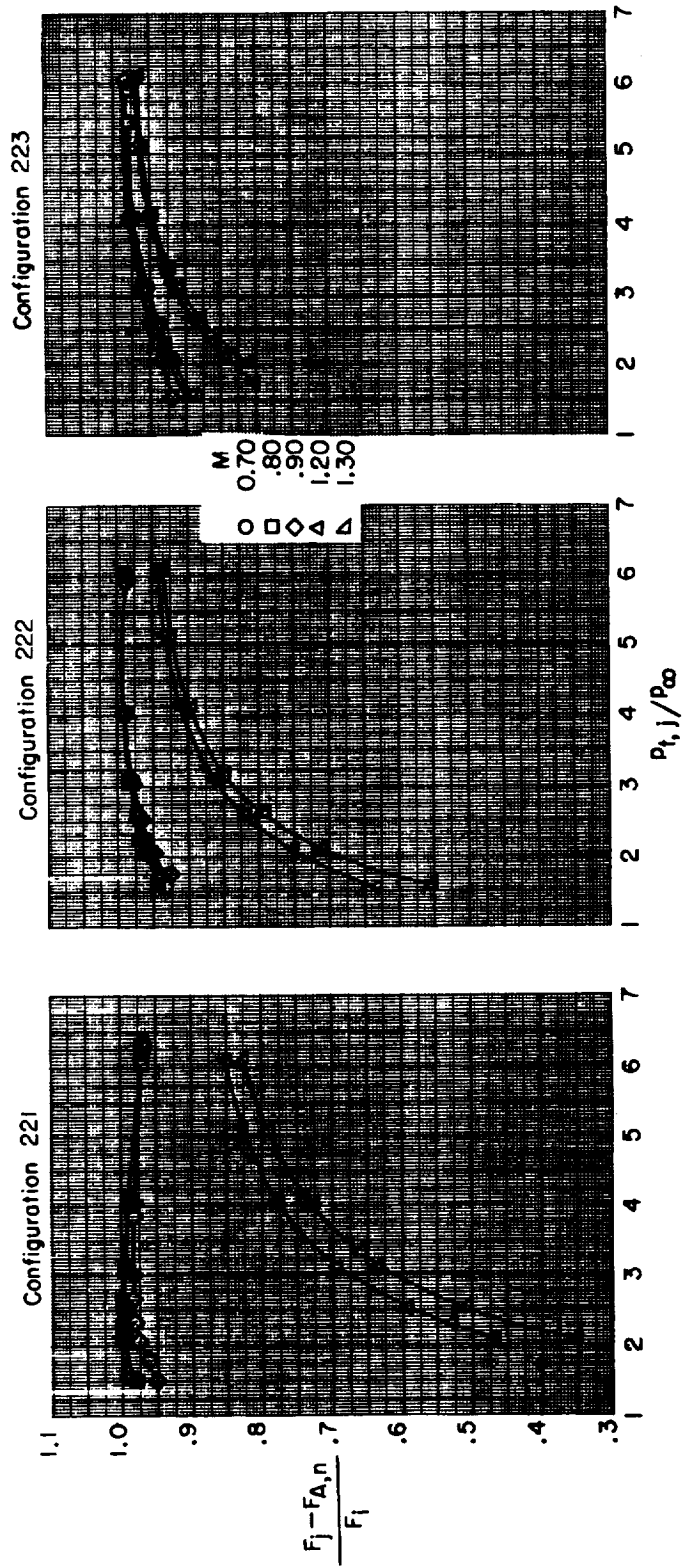
Figure 20.- Concluded.

EXPERIMENTAL



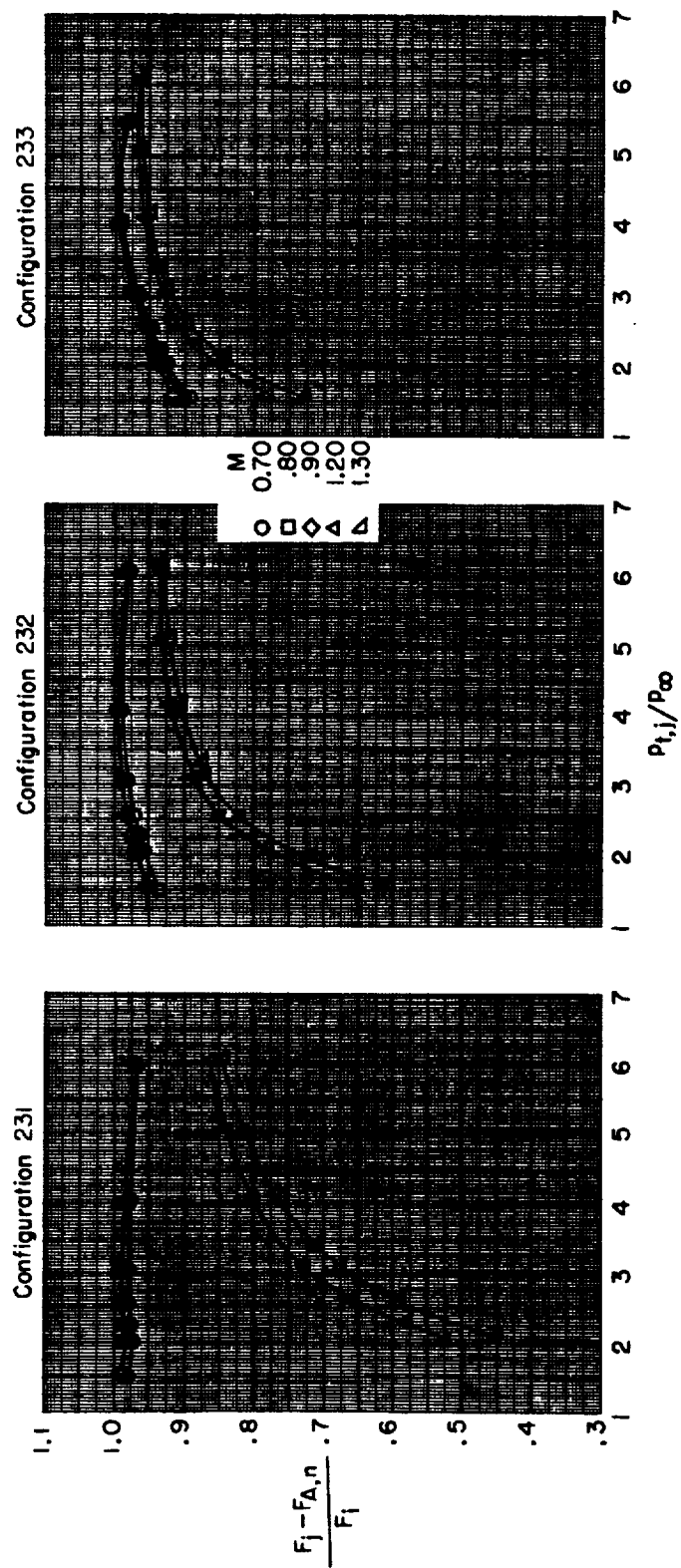
(a) Iris-convergent nozzles.

Figure 21.- Variation of gross thrust minus nozzle axial-force performance with primary total-pressure ratio for afterbody 2.



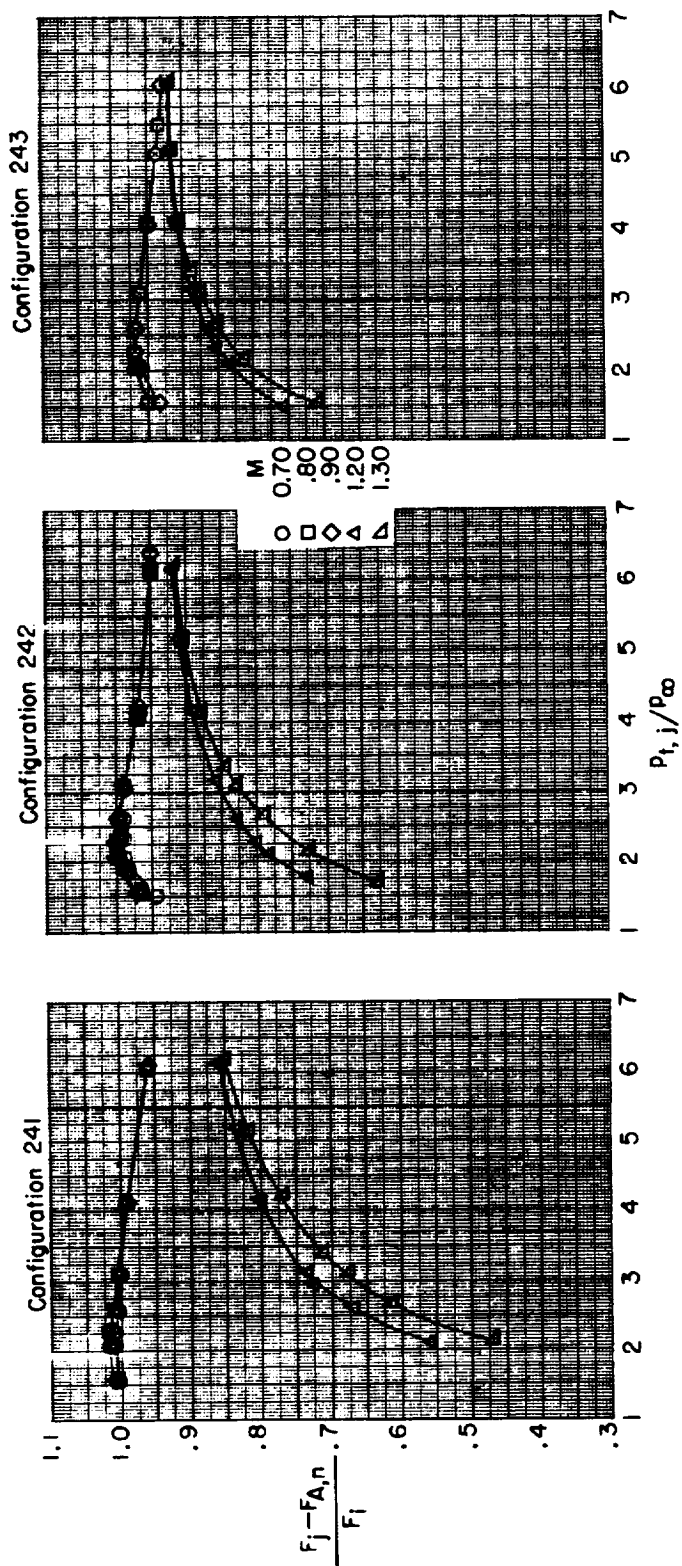
(b) Convergent-divergent nozzles.

Figure 21.- Continued.



(c) Plug nozzles with fixed tail flaps.

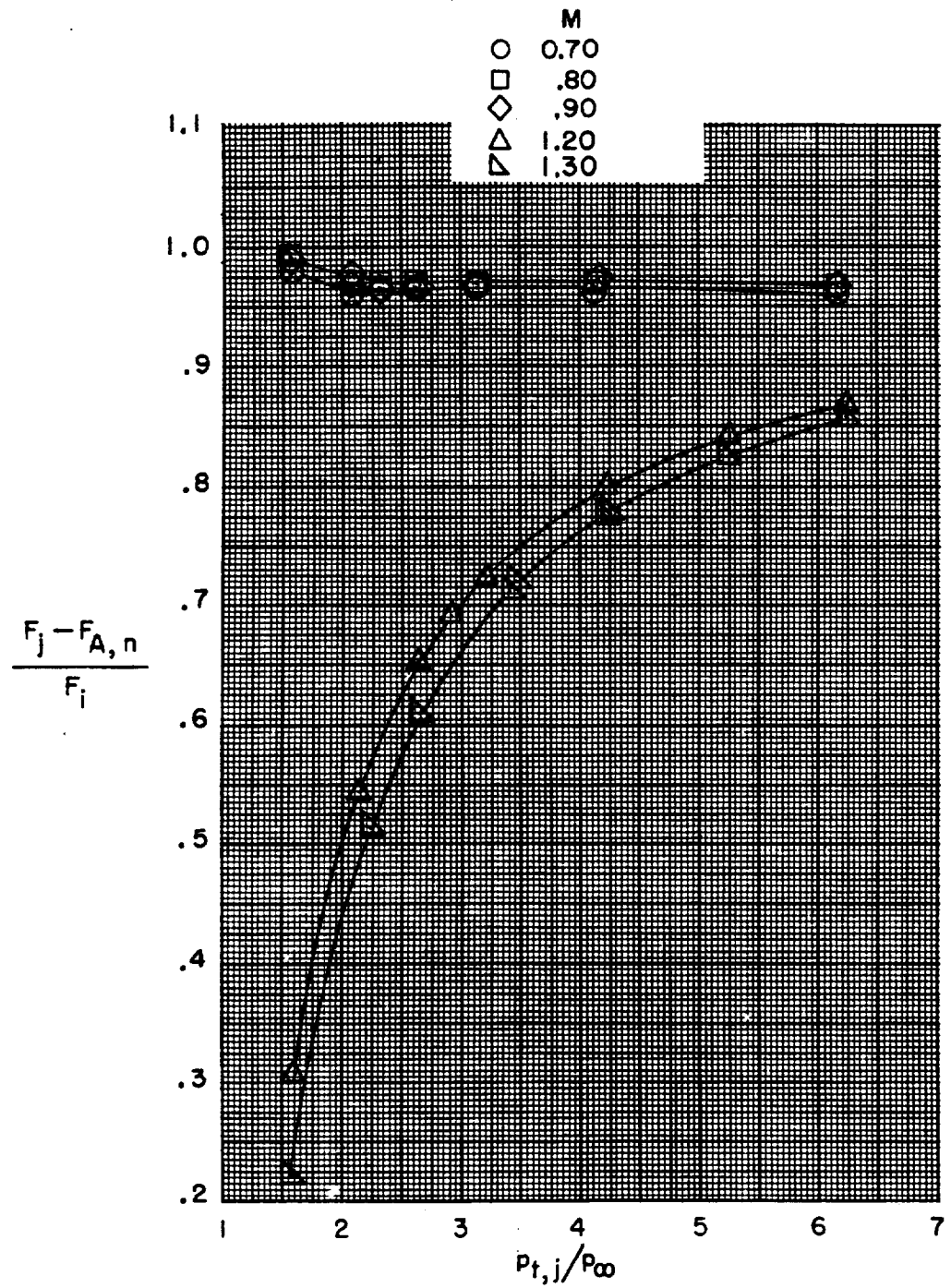
Figure 21.- Continued.



(d) Blow-in-door nozzles.

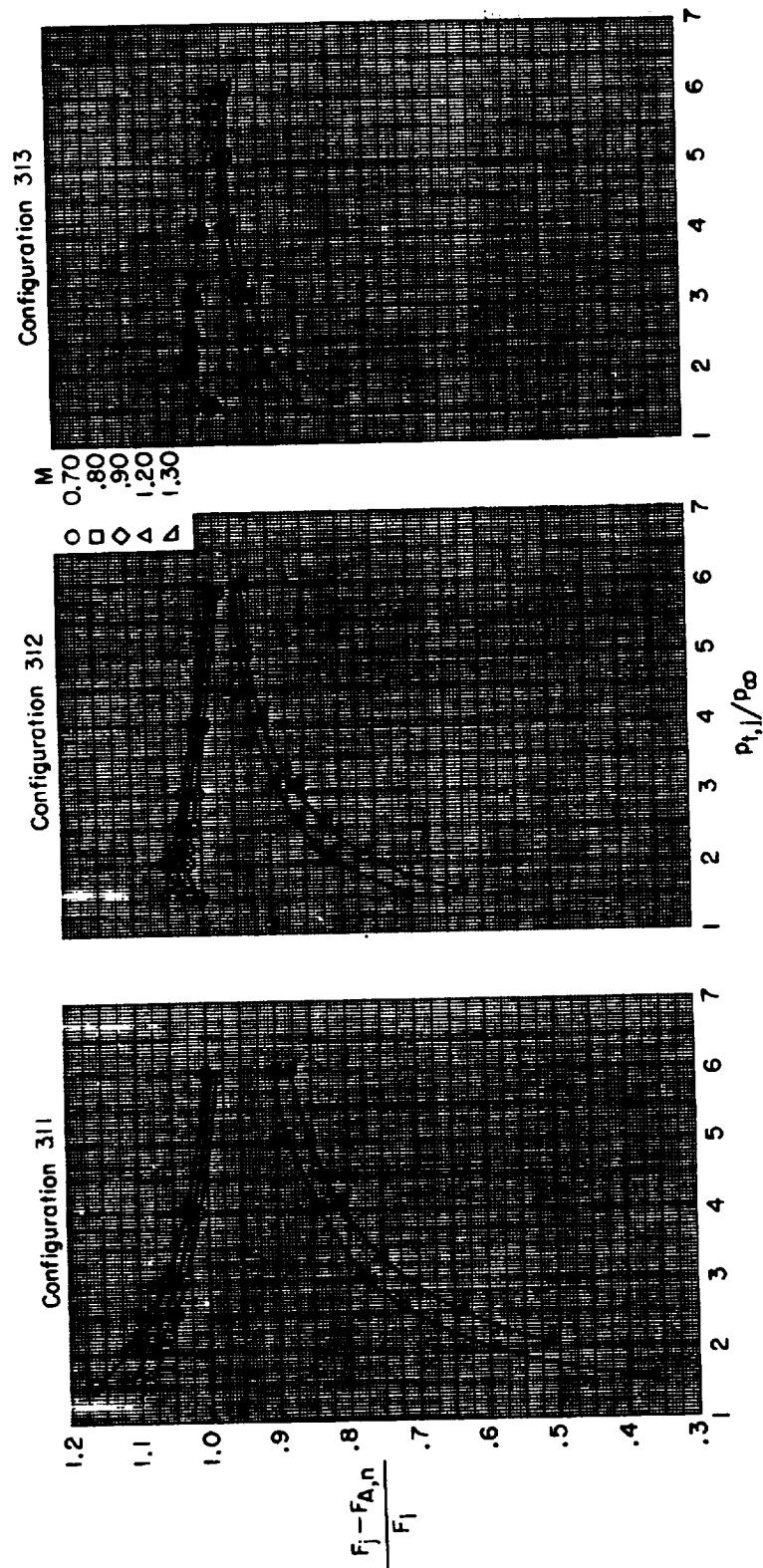
Figure 21.- Continued.

Configuration 261



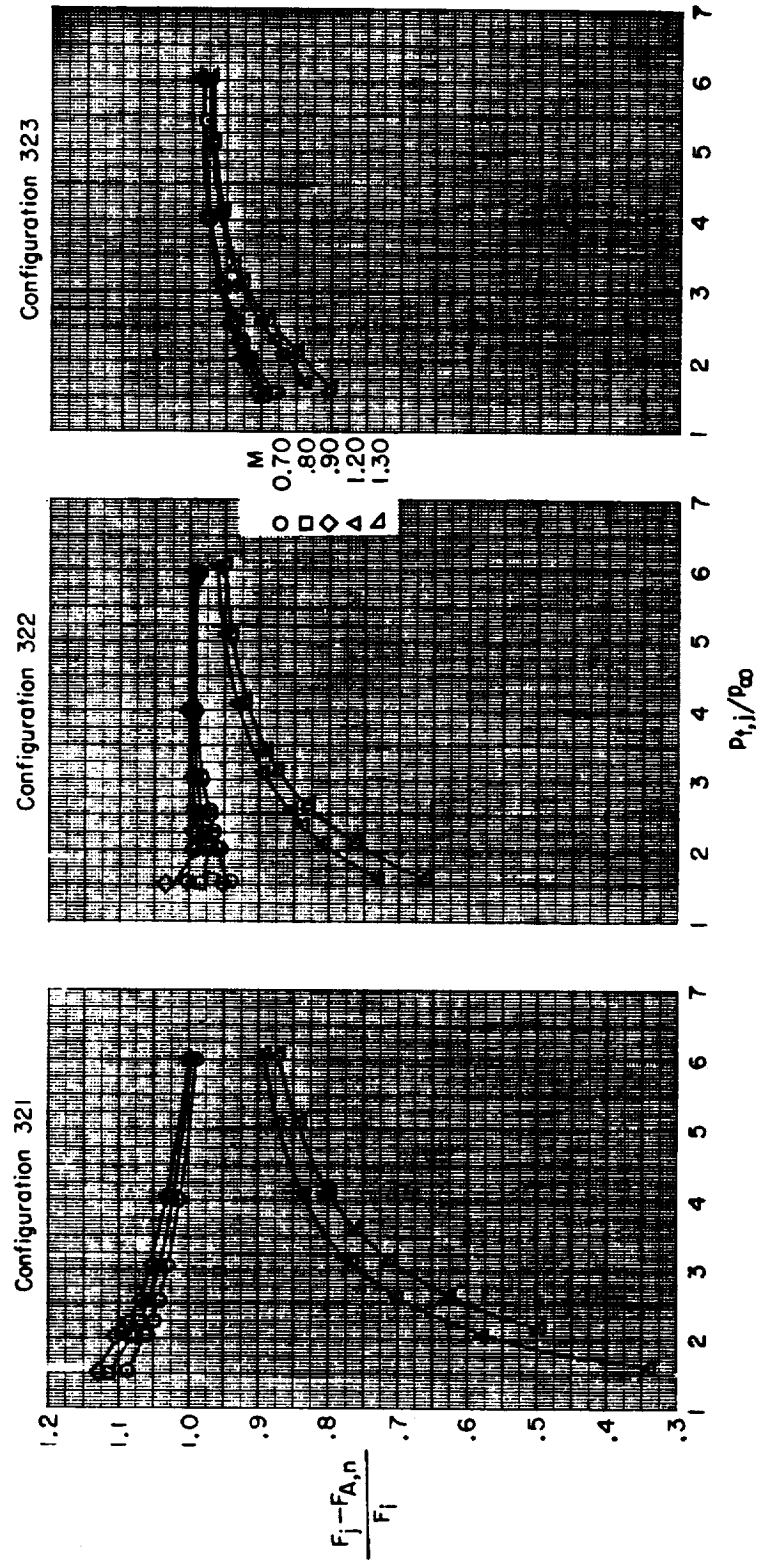
(e) Plug nozzles with floating tail flaps.

Figure 21.- Concluded.



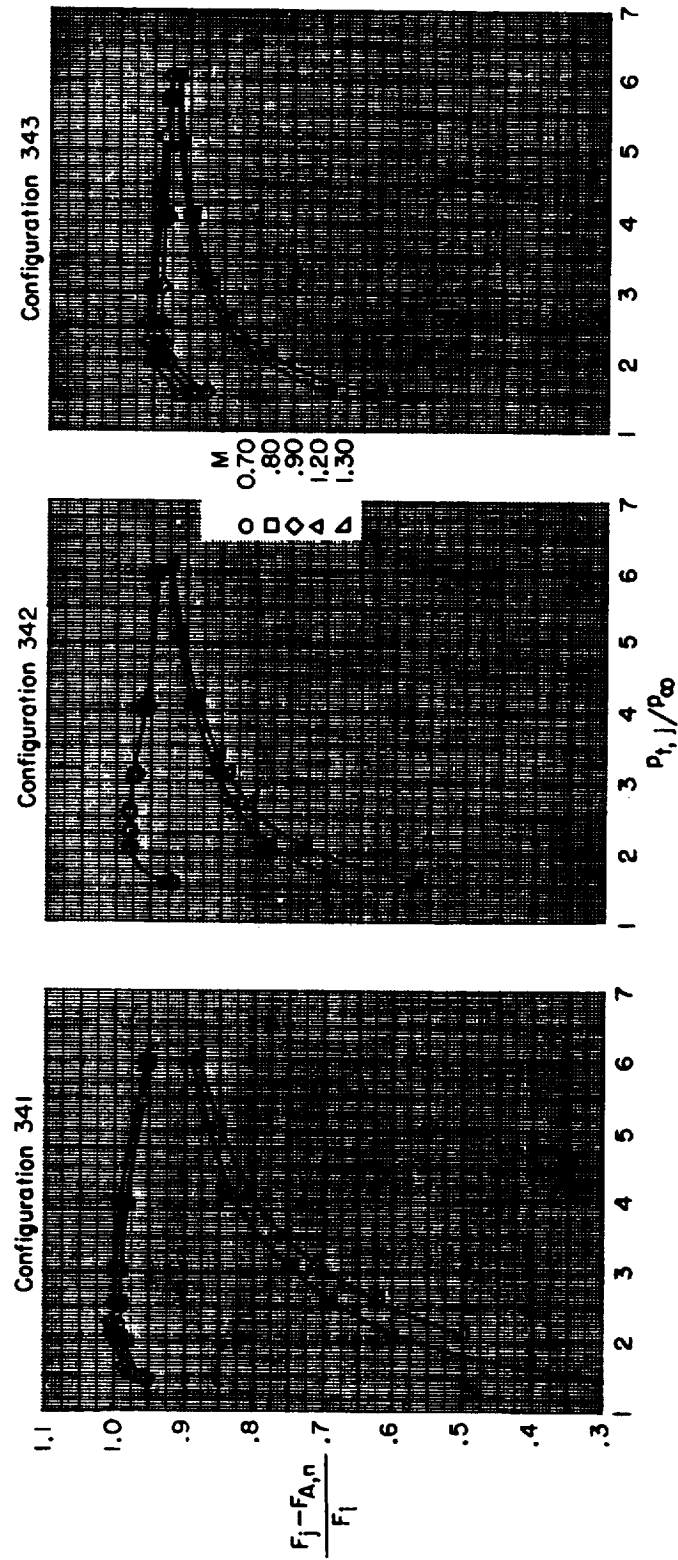
(a) Iris-convergent nozzles.

Figure 22.- Variation of gross thrust minus nozzle axial-force performance with primary total-pressure ratio for afterbody 3.



(b) Convergent-divergent nozzles.

Figure 22 - Continued.

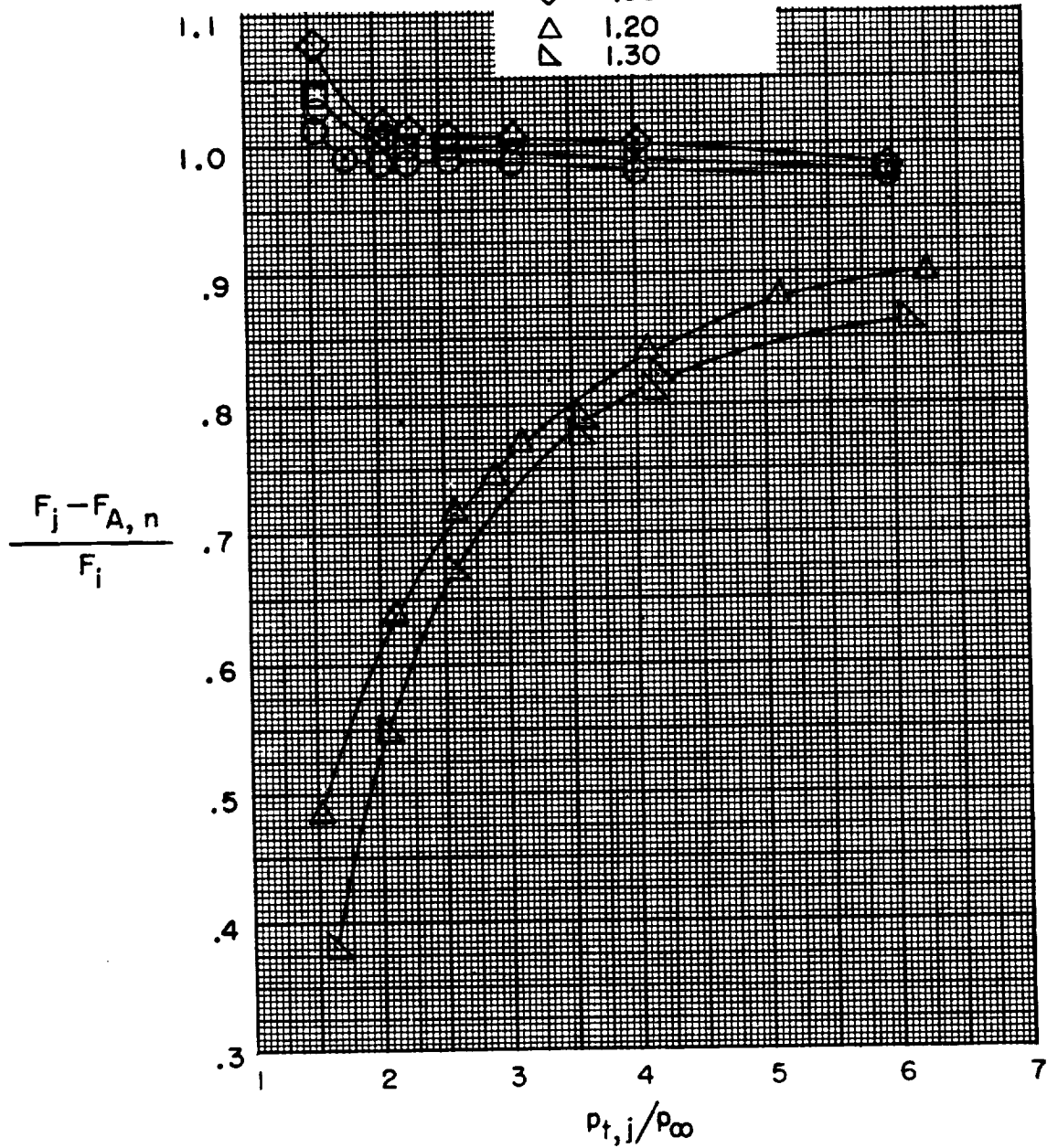


(d) Blow-in-door nozzles.

Figure 22.- Continued.

Configuration 361

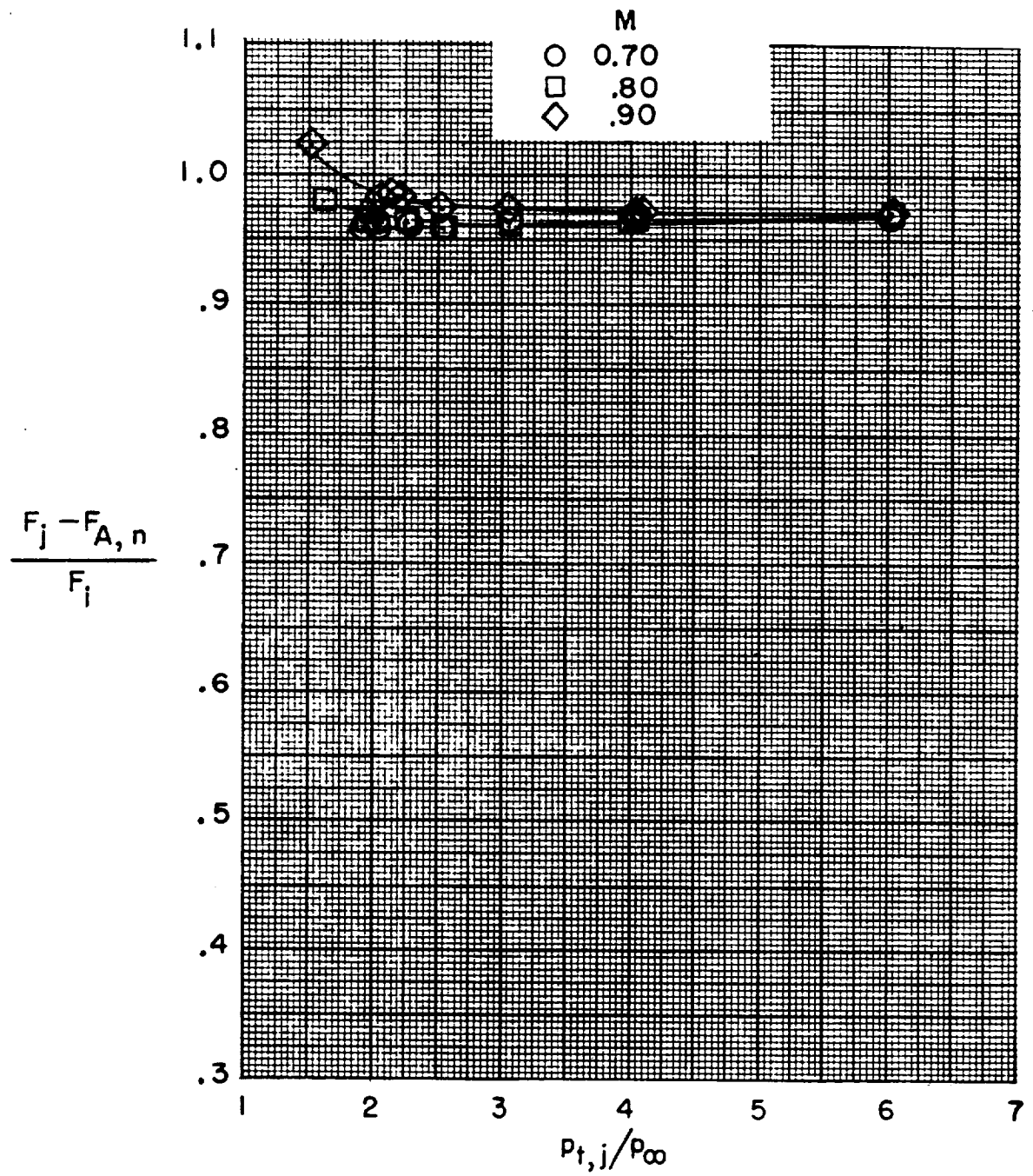
M
 ○ 0.70
 □ .80
 ◇ .90
 △ 1.20
 ▽ 1.30



(e) Plug nozzles with floating tail flaps.

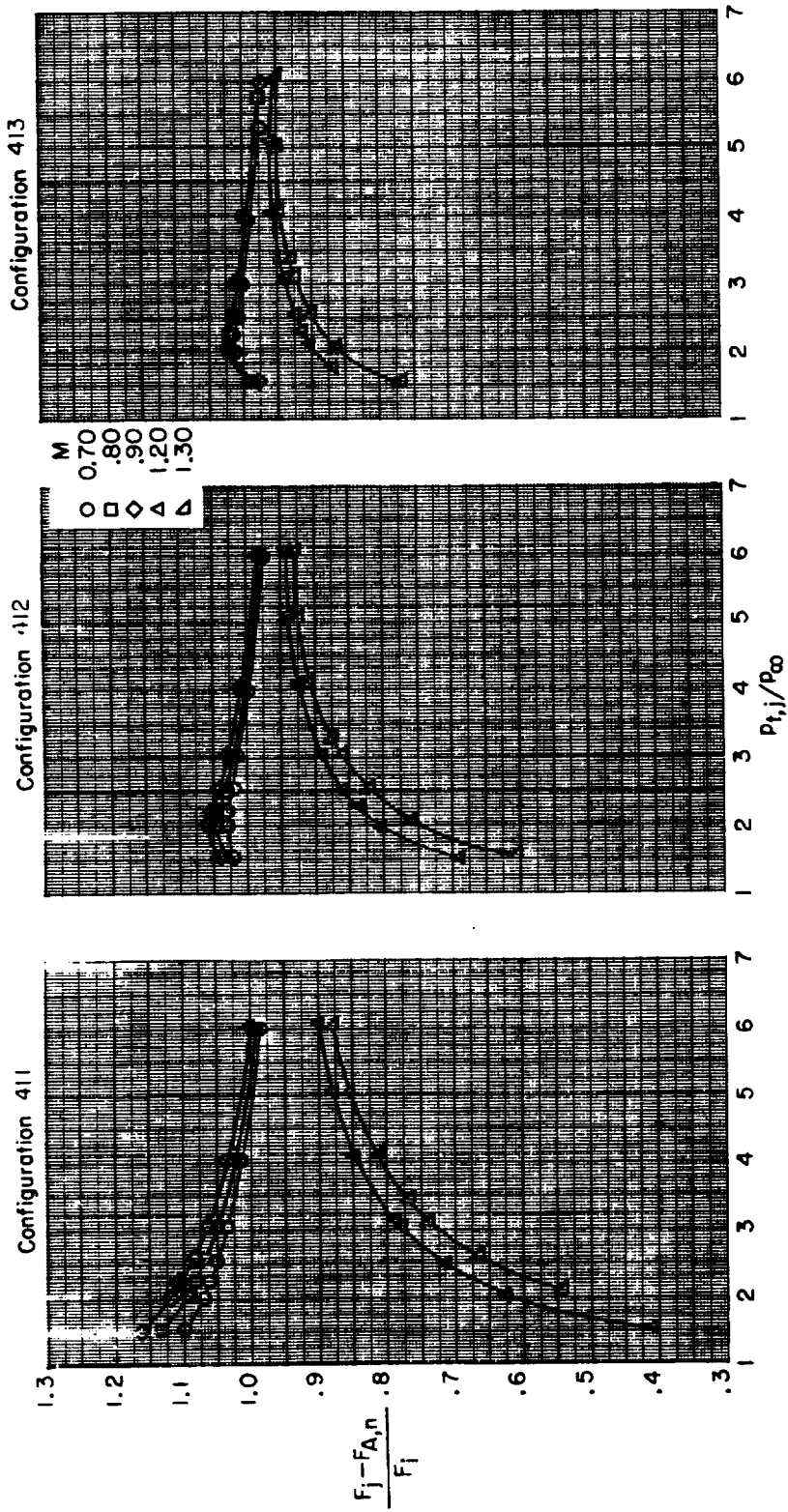
Figure 22.- Continued.

Configuration 301



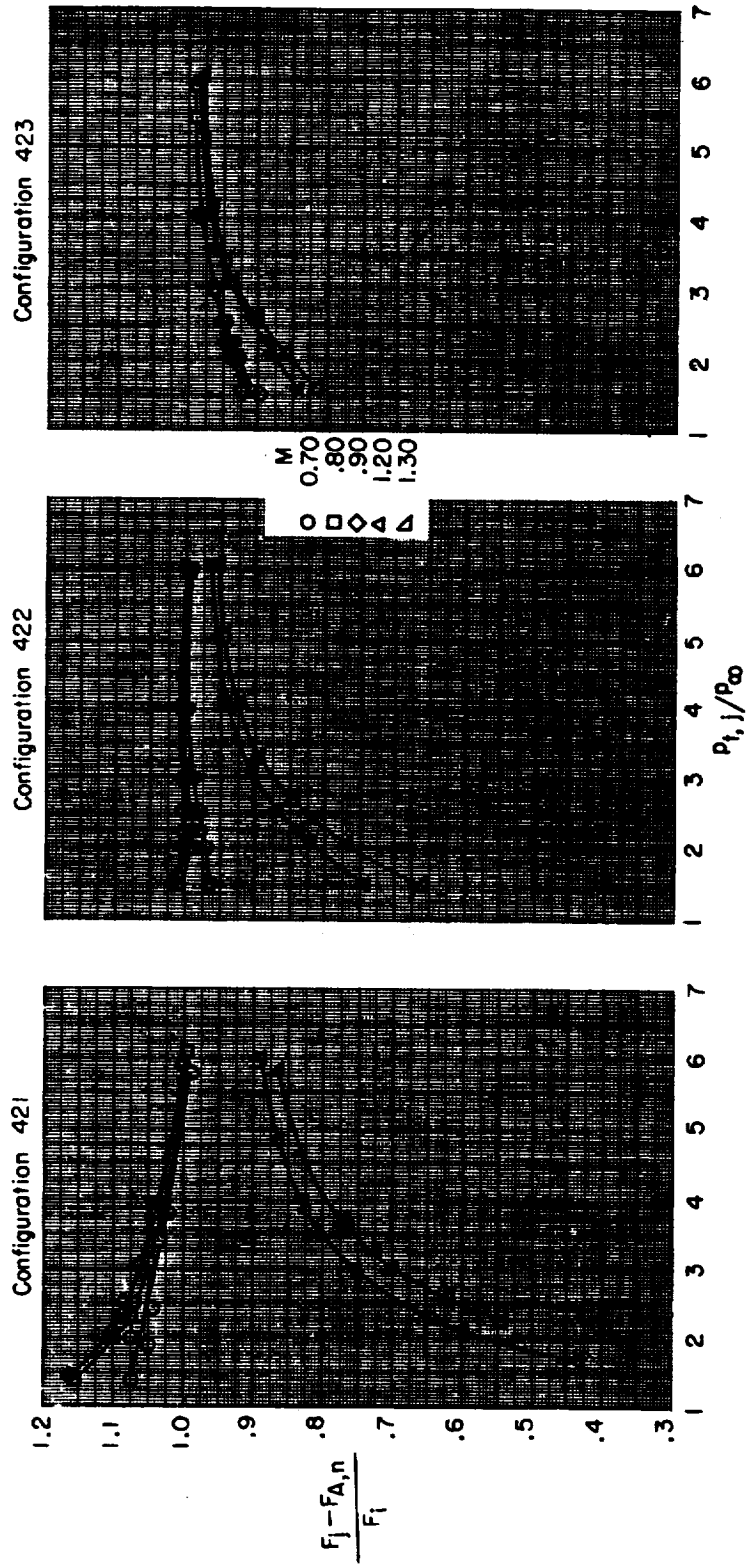
(f) Reference blow-in-door nozzles.

Figure 22.- Concluded.



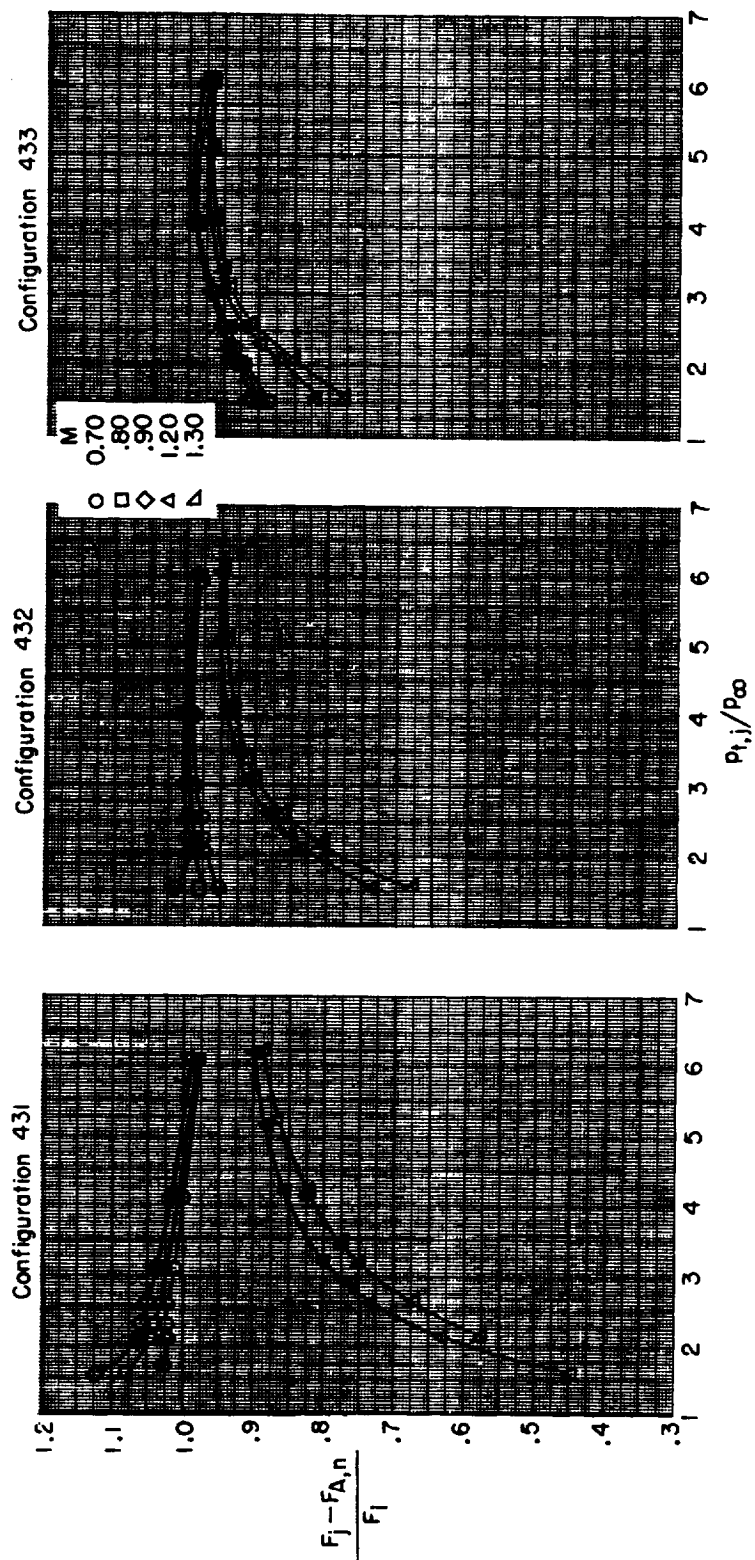
(a) Iris-convergent nozzles.

Figure 23.- Variation of gross thrust minus nozzle axial-force performance with primary total-pressure ratio for afterbody 4.



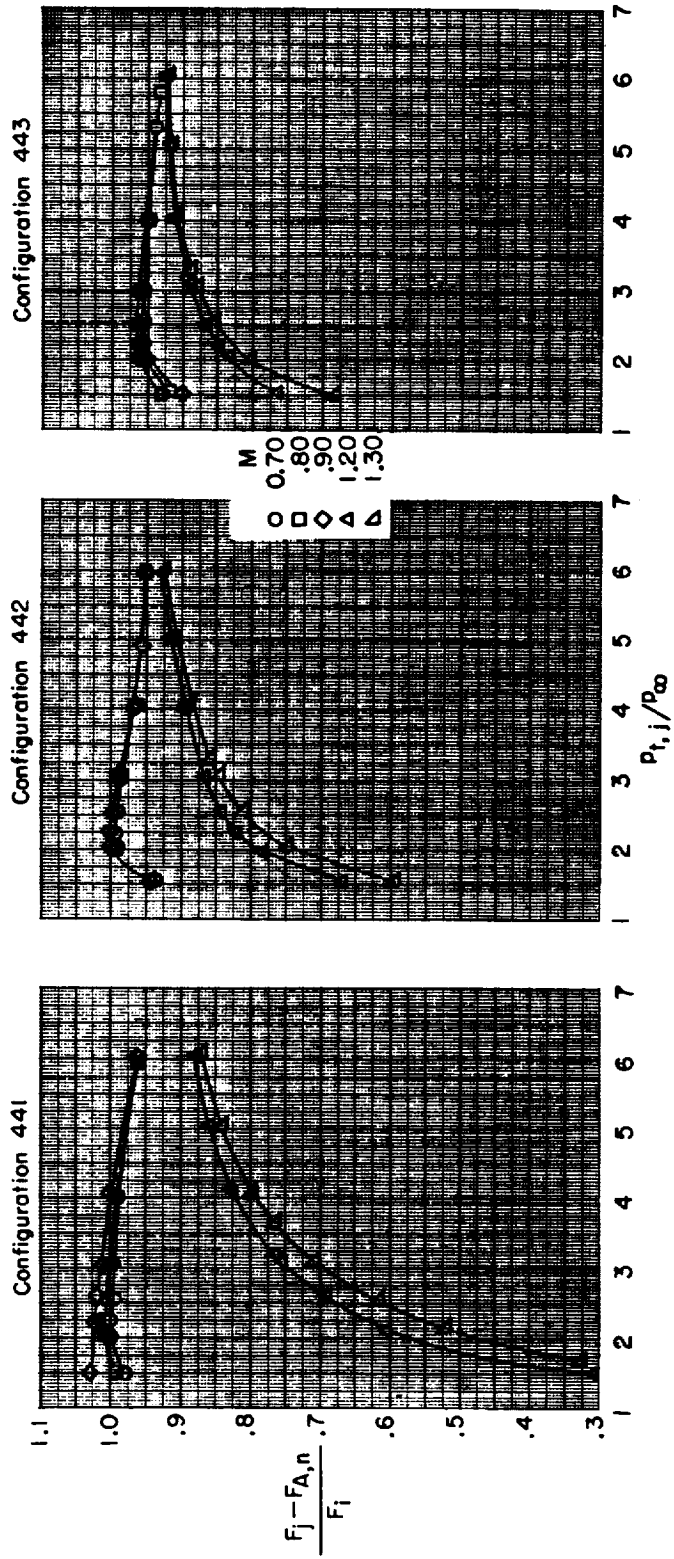
(b) Convergent-divergent nozzles.

Figure 23.- Continued.



(c) Plug nozzles with fixed tail flaps.

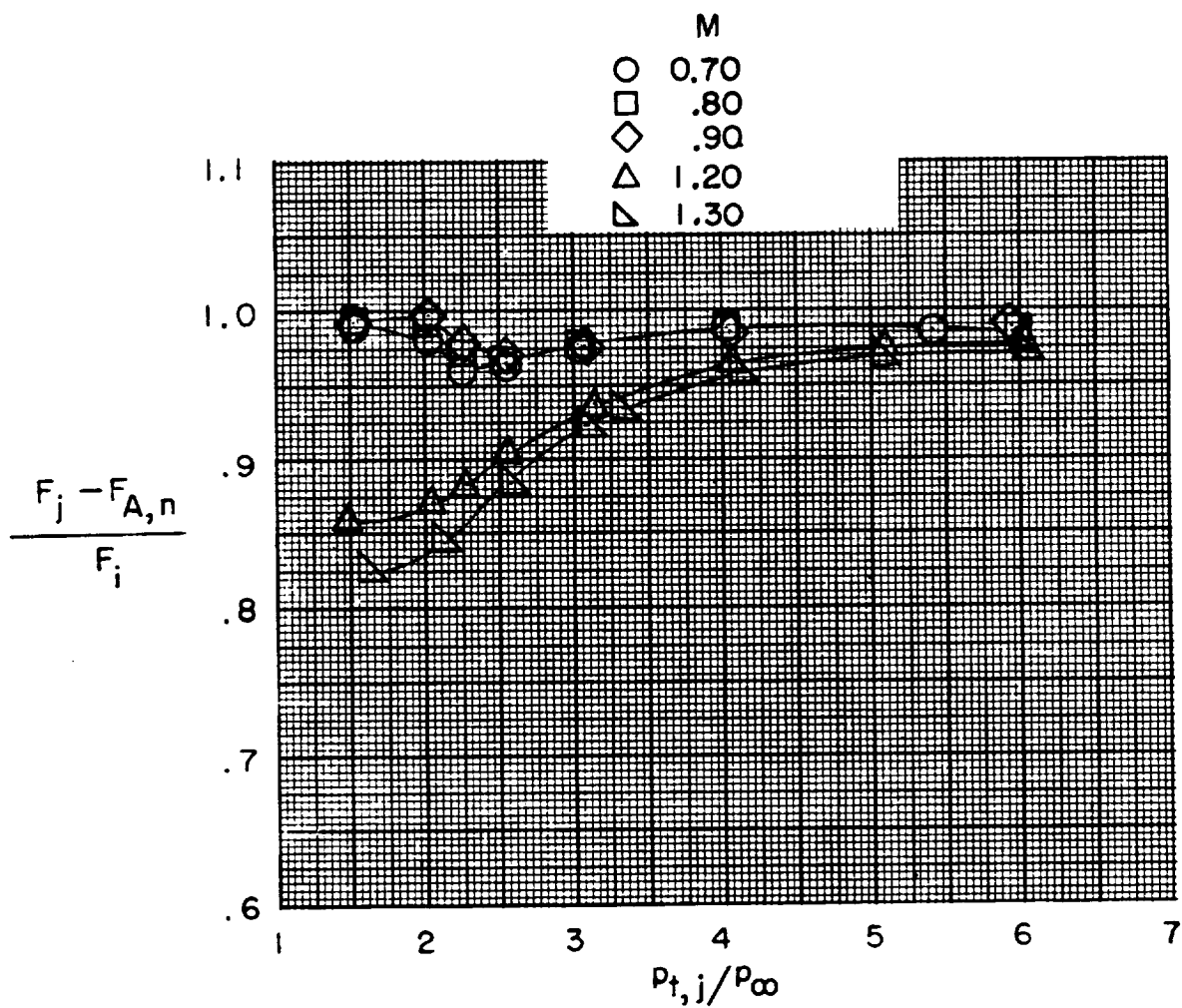
Figure 23.- Continued.



(d) Blow-in-door nozzles.

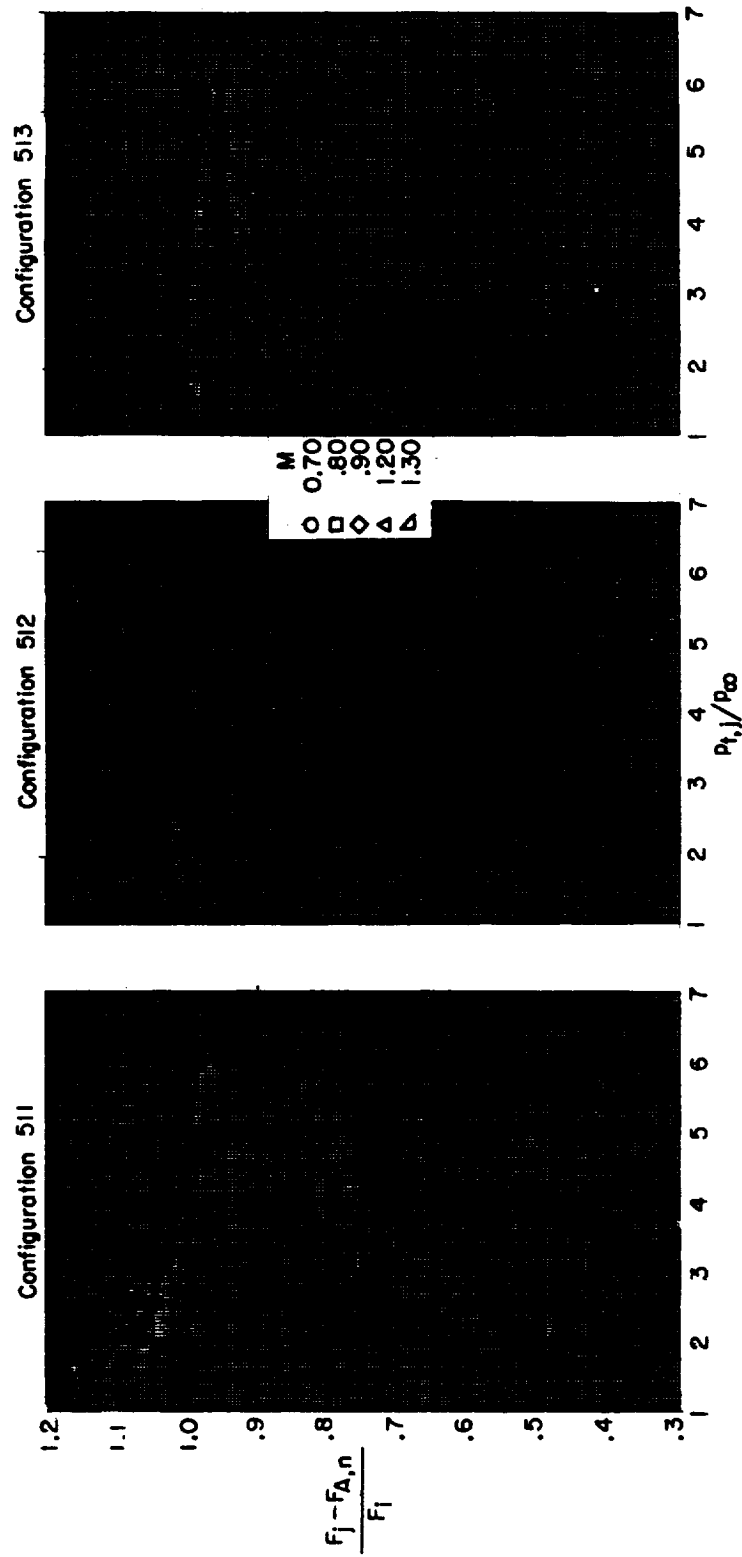
Figure 23.- Continued.

Configuration 453



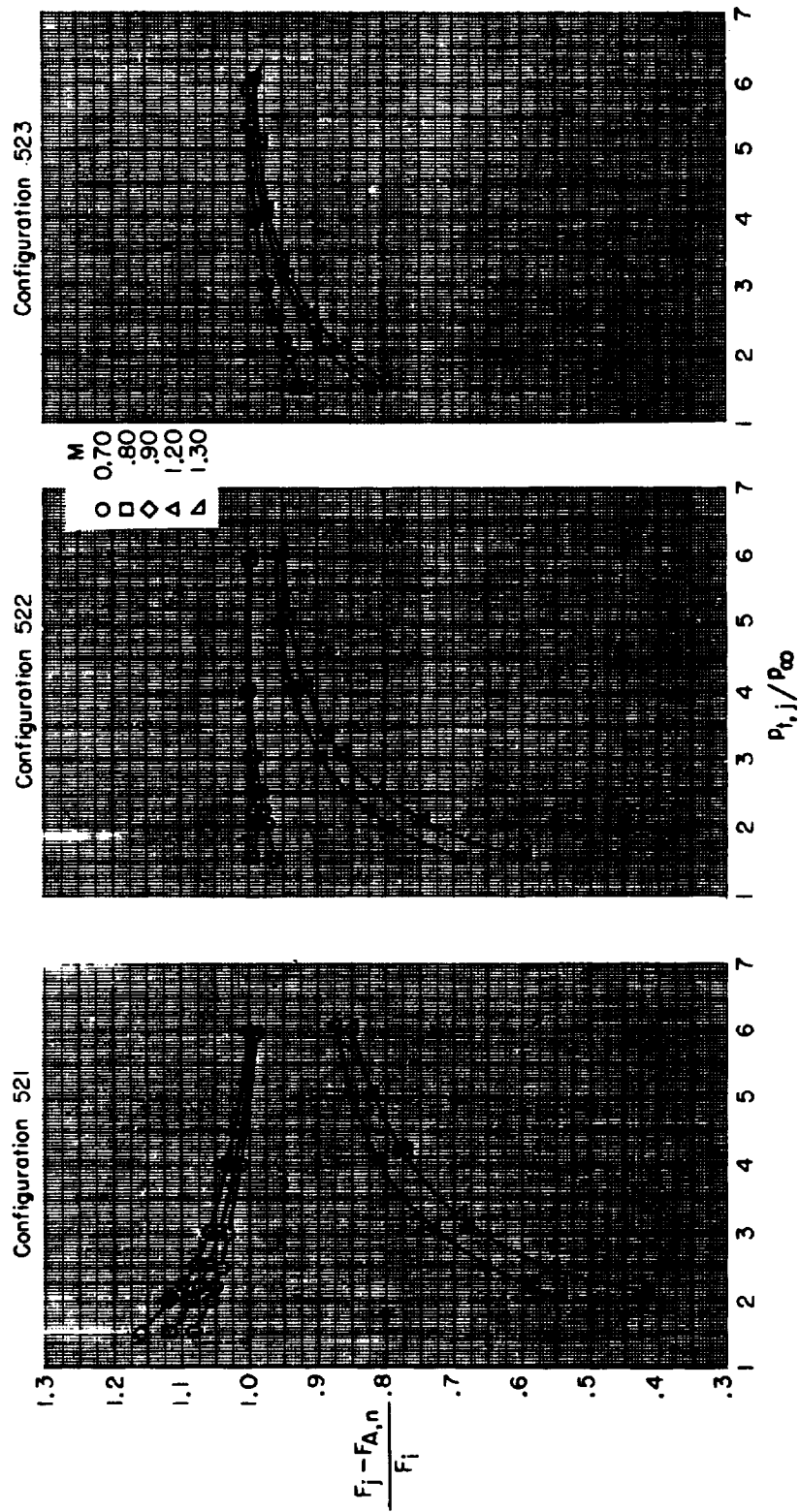
(e) Convergent-divergent-iris nozzles.

Figure 23.- Concluded.



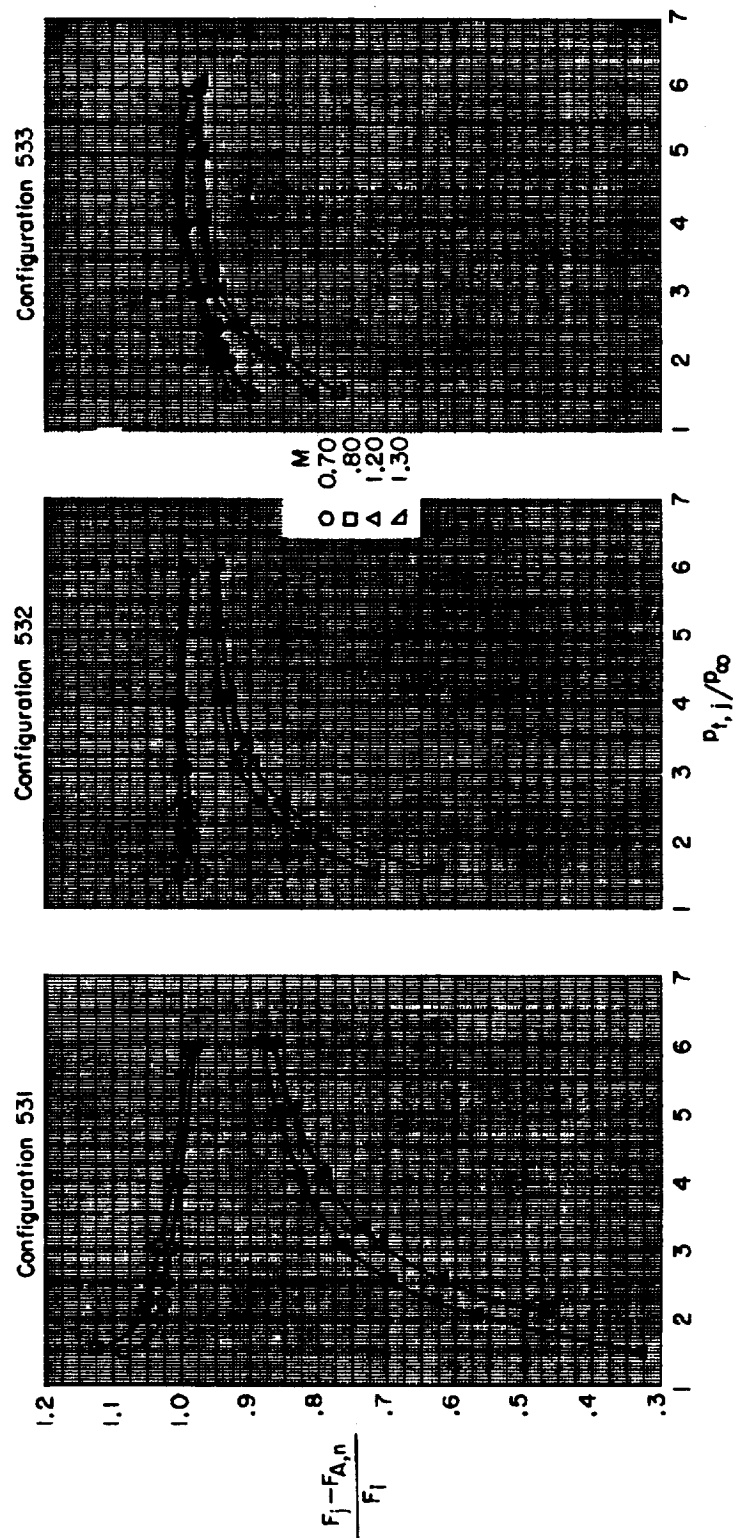
(a) Iris-convergent nozzles.

Figure 24.- Variation of gross thrust minus nozzle axial-force performance with primary total-pressure ratio for afterbody 5.



(b) Convergent-divergent nozzles.

Figure 24.- Continued.



(c) Plug nozzles with fixed tail flaps.

Figure 24.- Concluded.

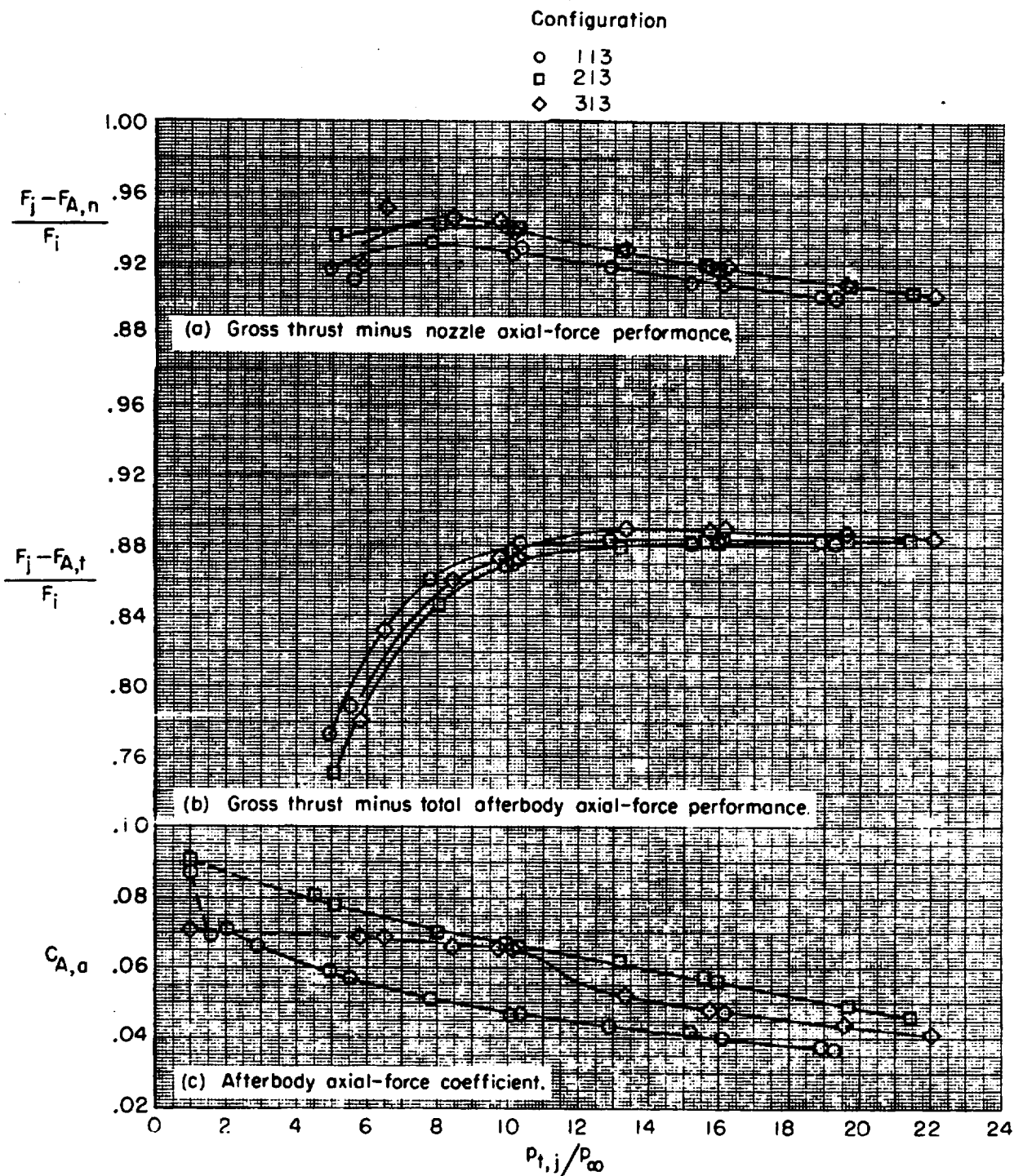


Figure 25.- Propulsive and aerodynamic performance of an iris-convergent nozzle installed on the various afterbodies. $M = 2.2$.

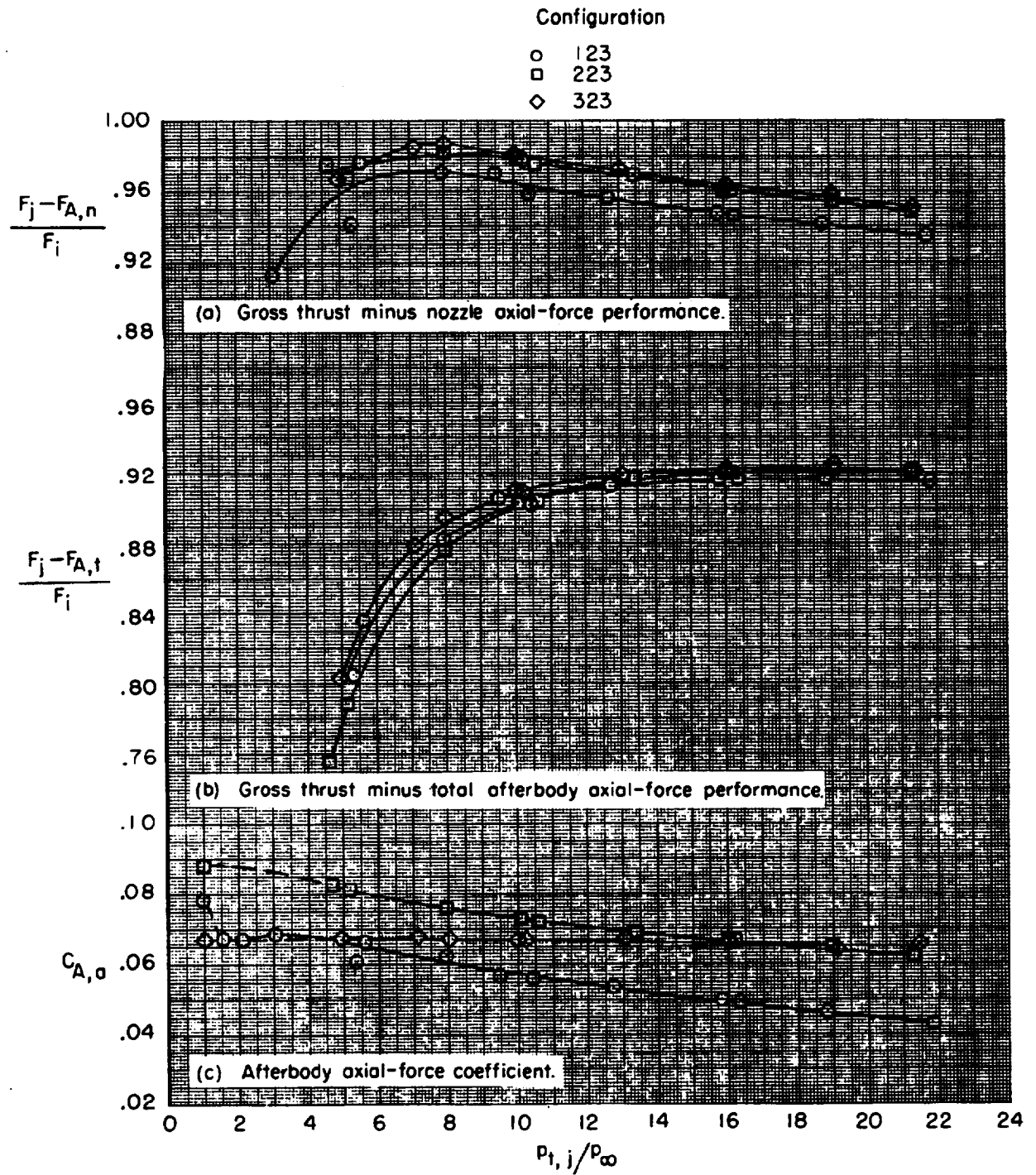


Figure 26.- Propulsive and aerodynamic performance of a convergent-divergent nozzle installed on the various afterbodies. $M = 2.2$.

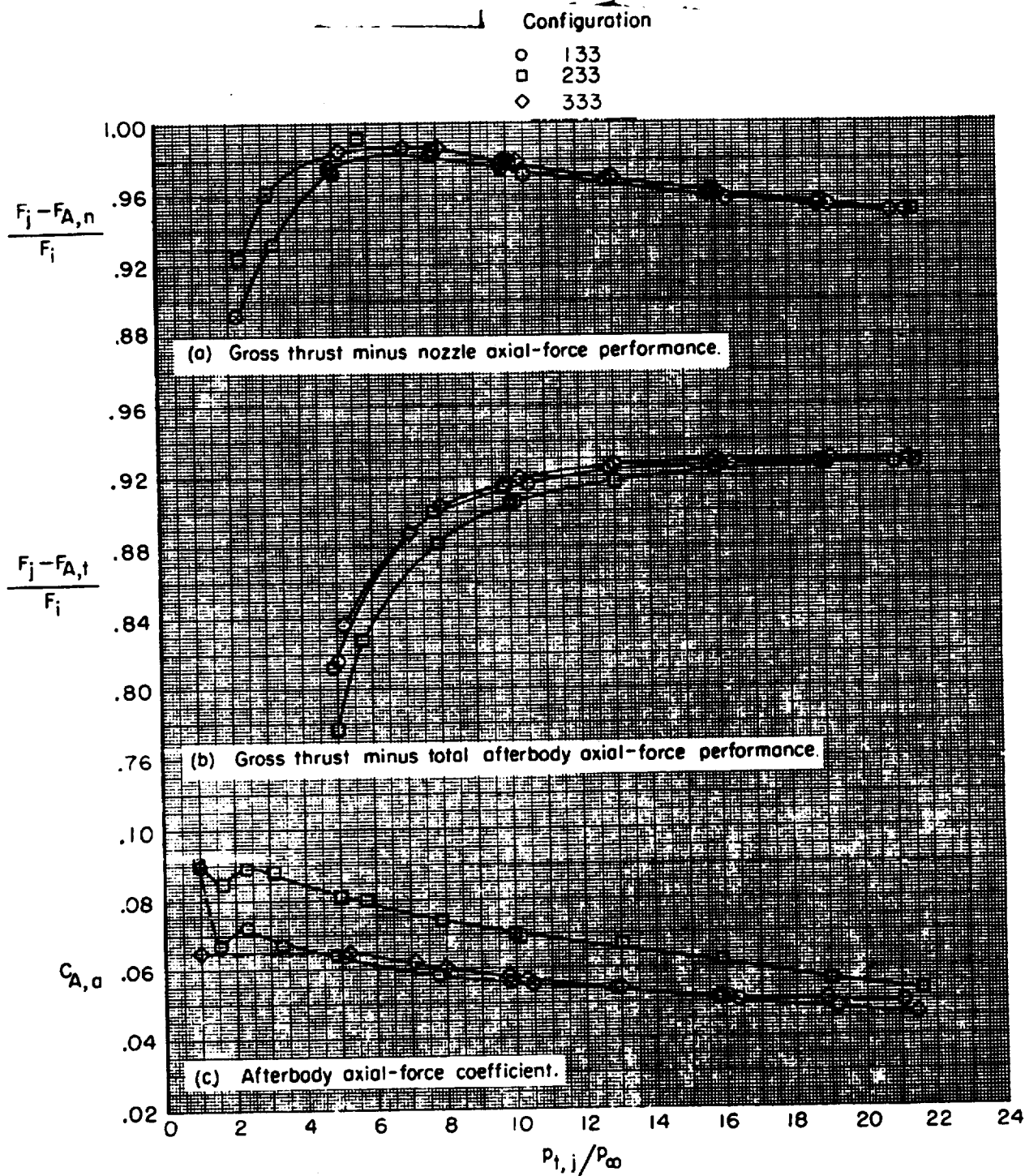


Figure 27.- Propulsive and aerodynamic performance of a plug nozzle installed on the various afterbodies. $M = 2.2$.

CONFIDENTIAL

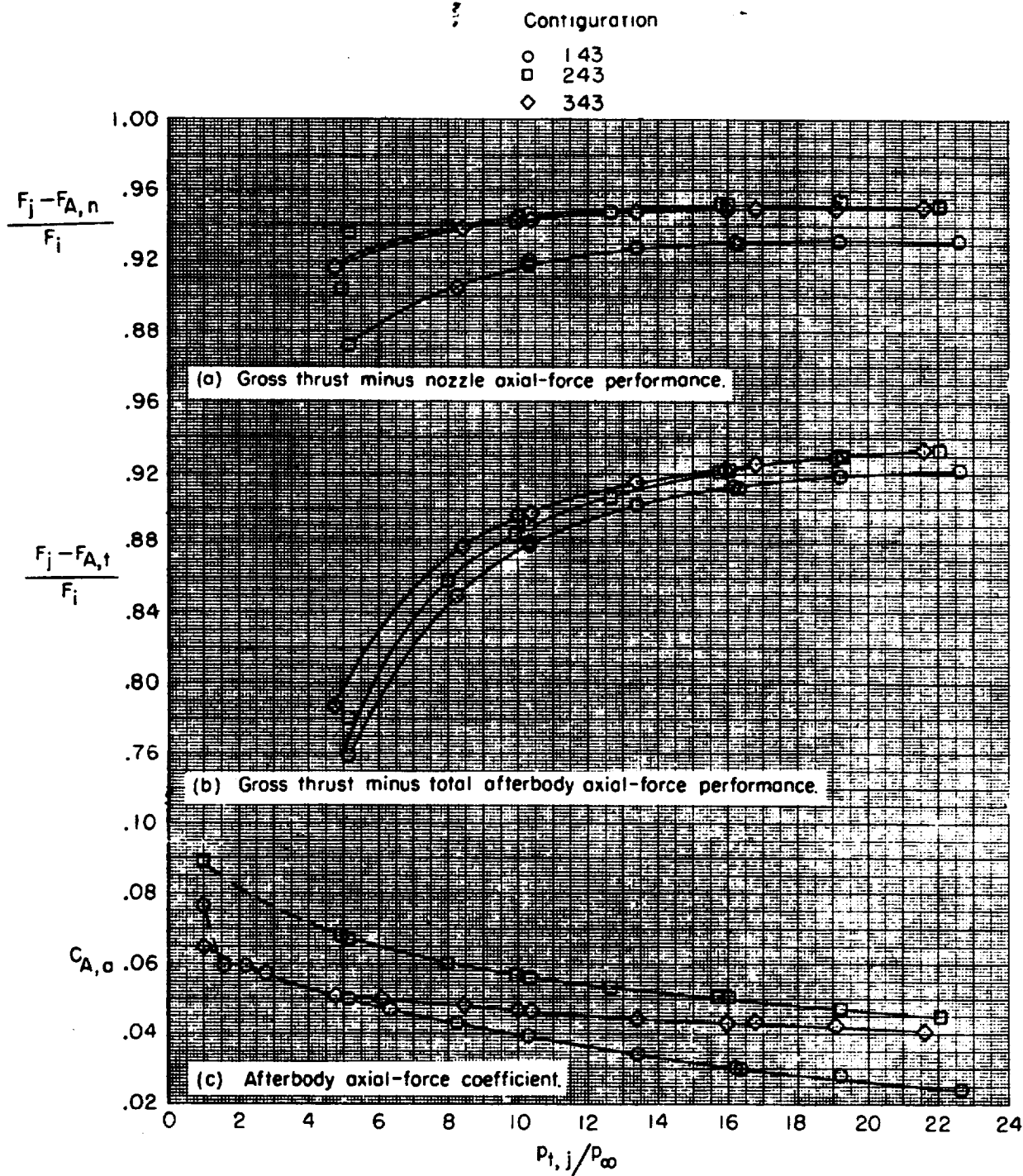


Figure 28.- Propulsive and aerodynamic performance of a blow-in-door nozzle installed on the various afterbodies. $M = 2.2$.

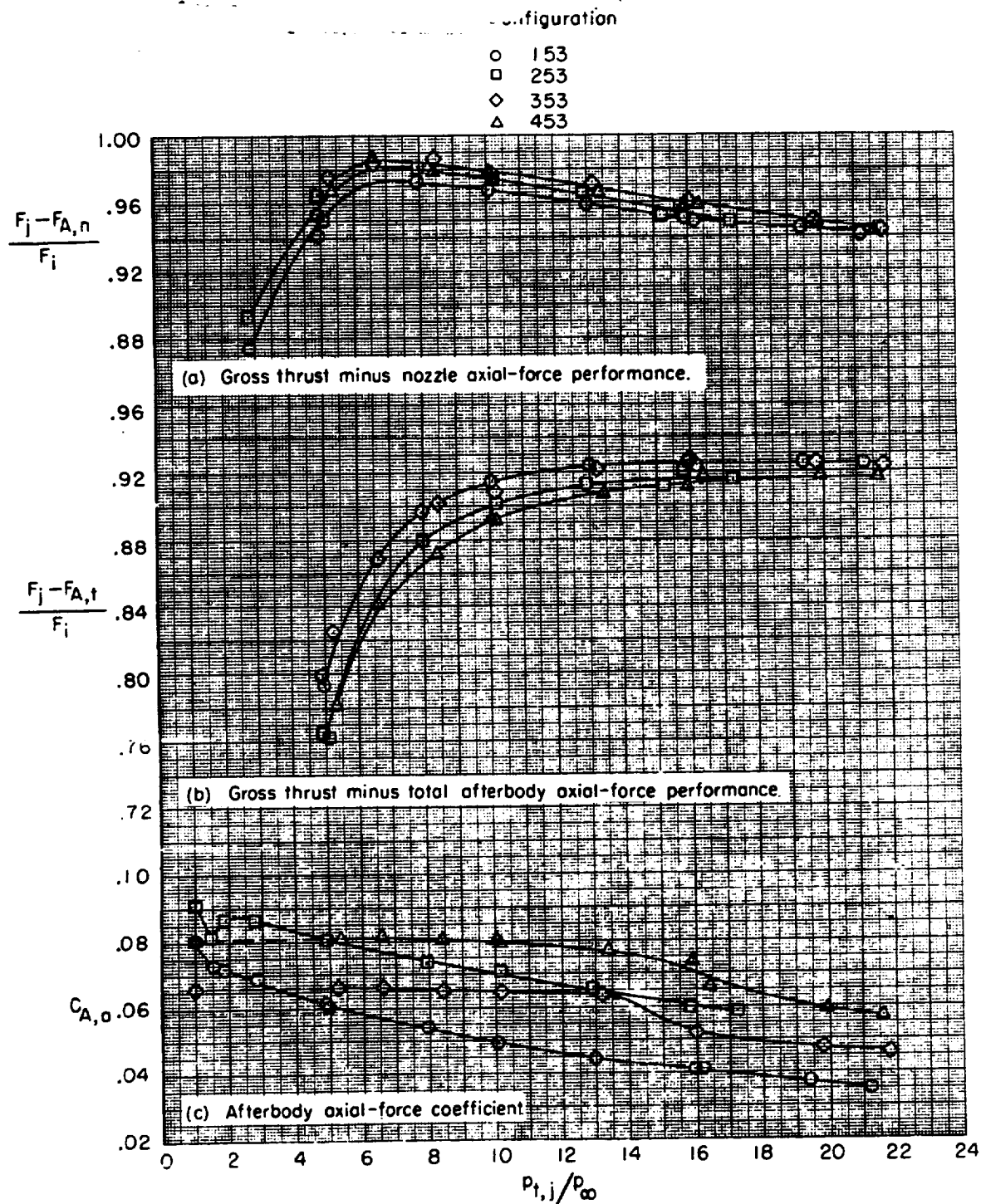


Figure 29.- Propulsive and aerodynamic performance of a convergent-divergent-iris nozzle installed on the various afterbodies. $M = 2.2$.

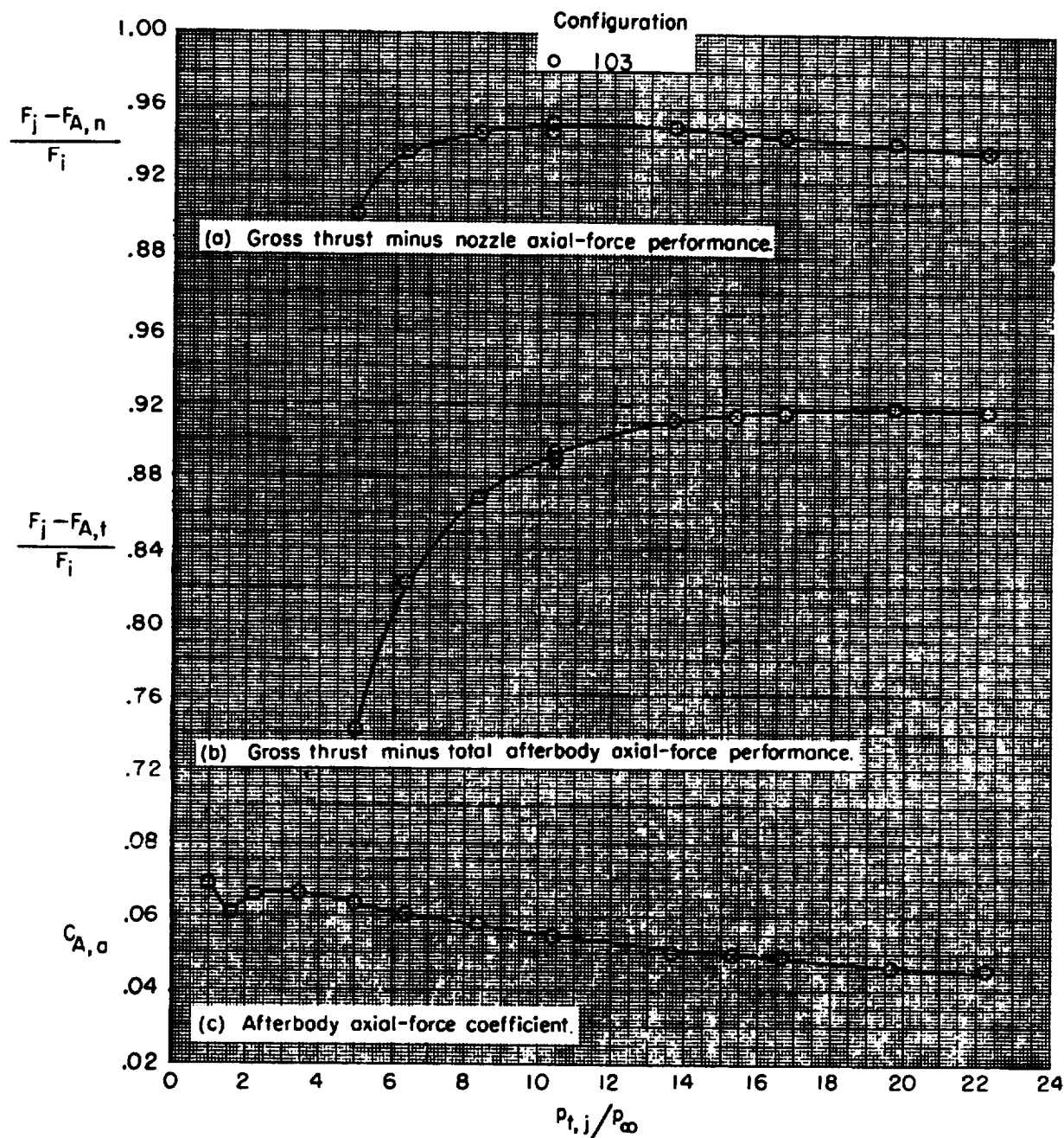


Figure 30.- Propulsive and aerodynamic performance of a reference blow-in-door nozzle installed on afterbody 1. $M = 2.2$.

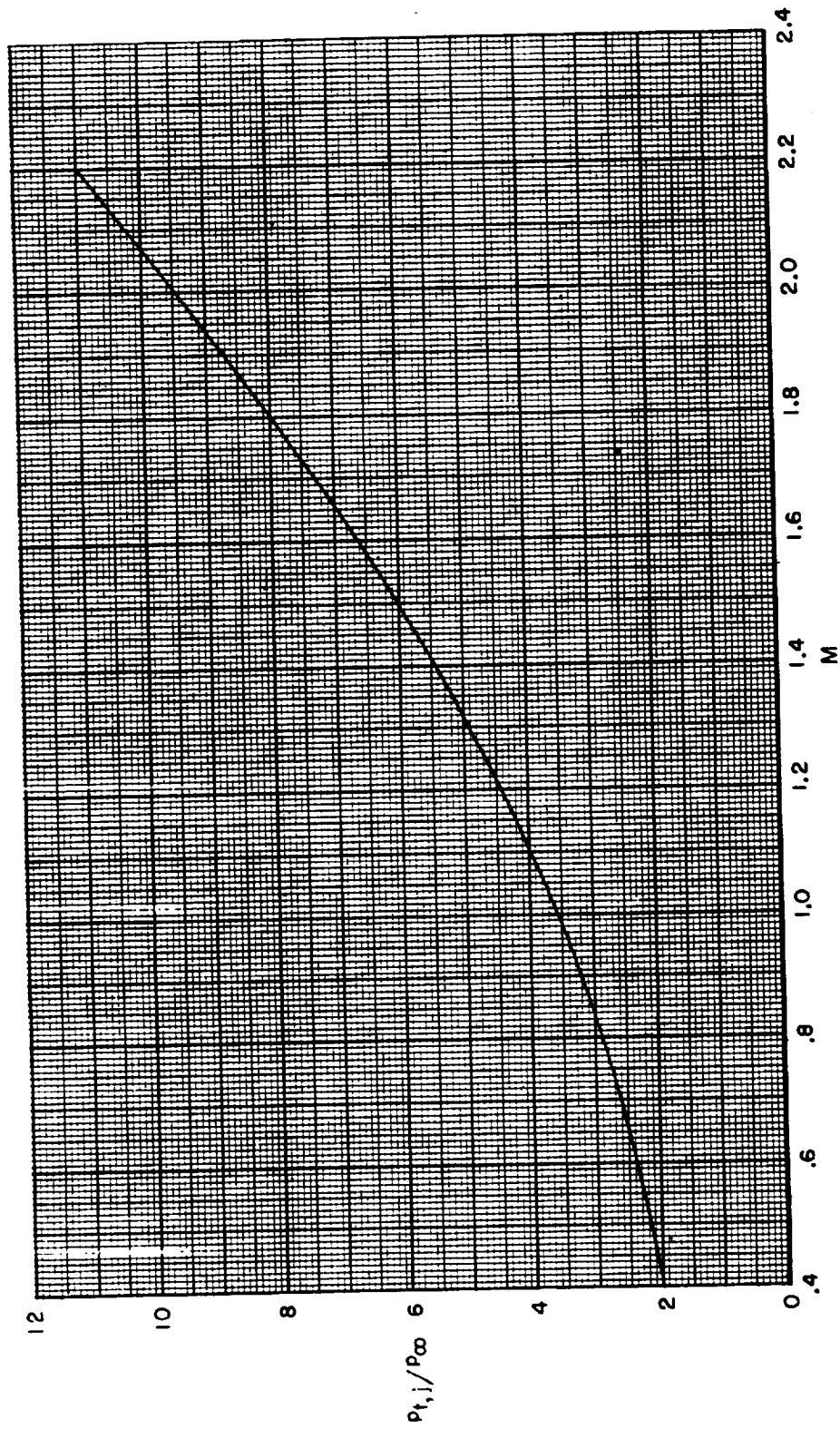
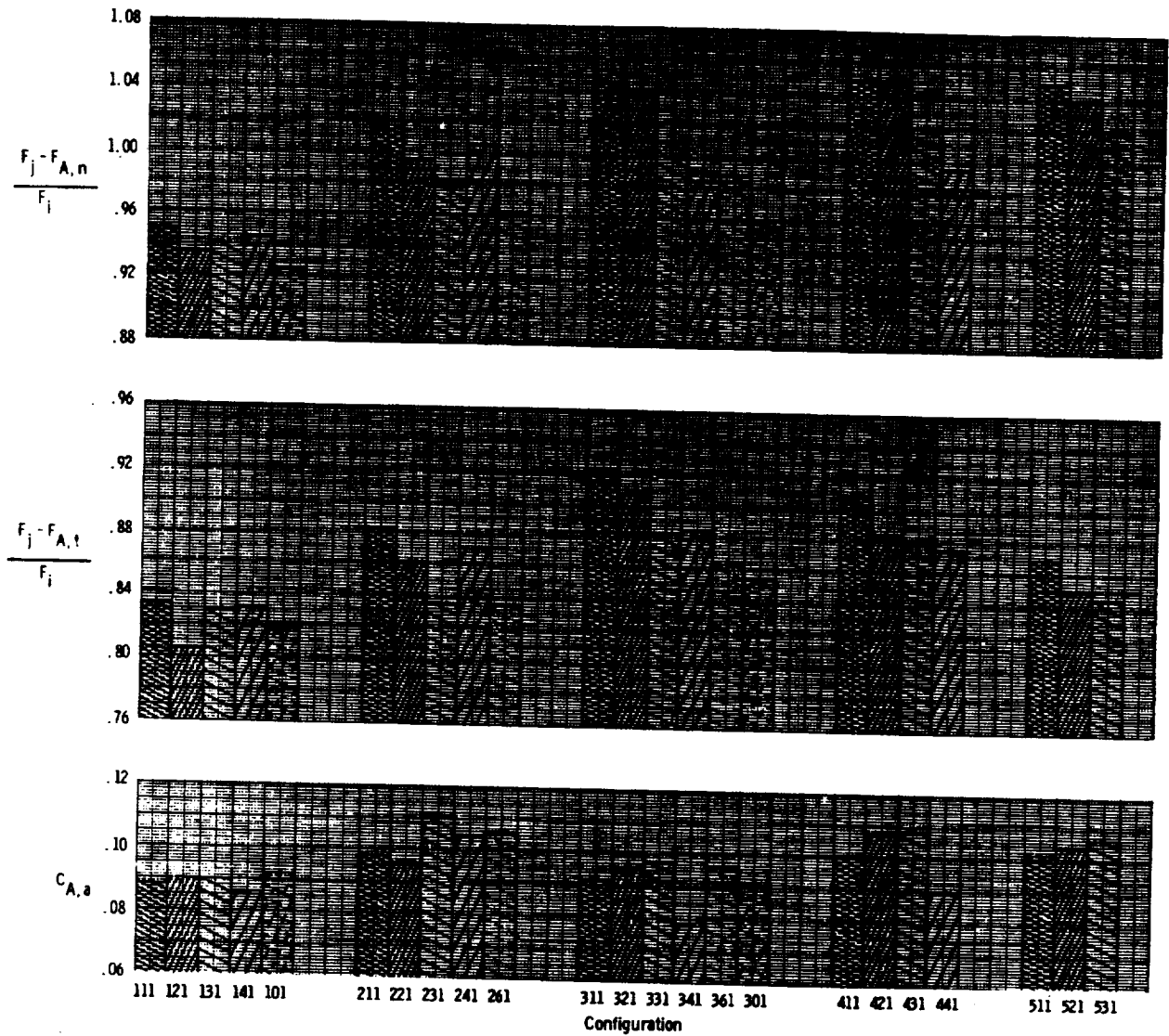
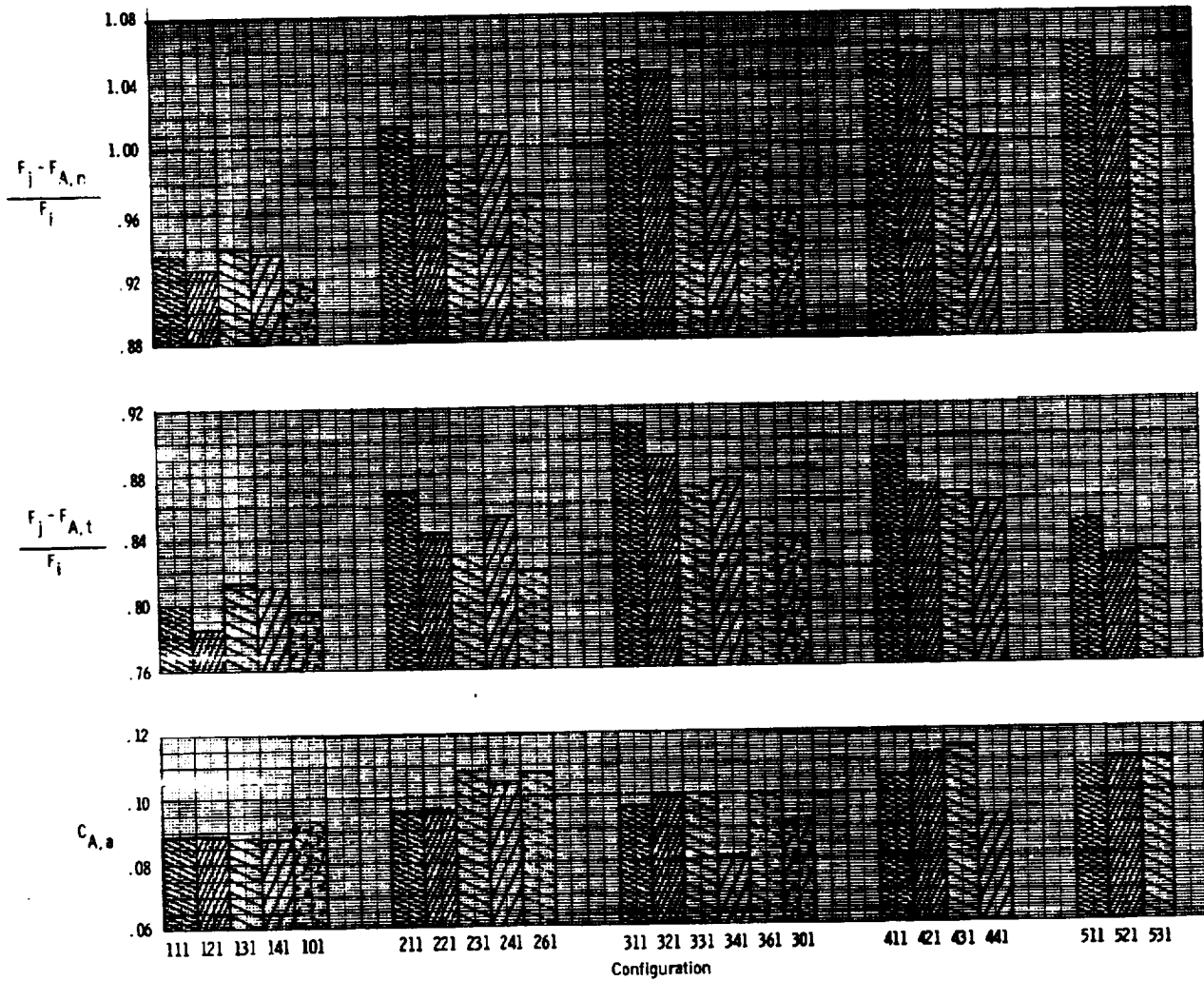


Figure 31.- Variation of jet pressure ratio with Mach number for a schedule typical of a turbfan-engine configuration.



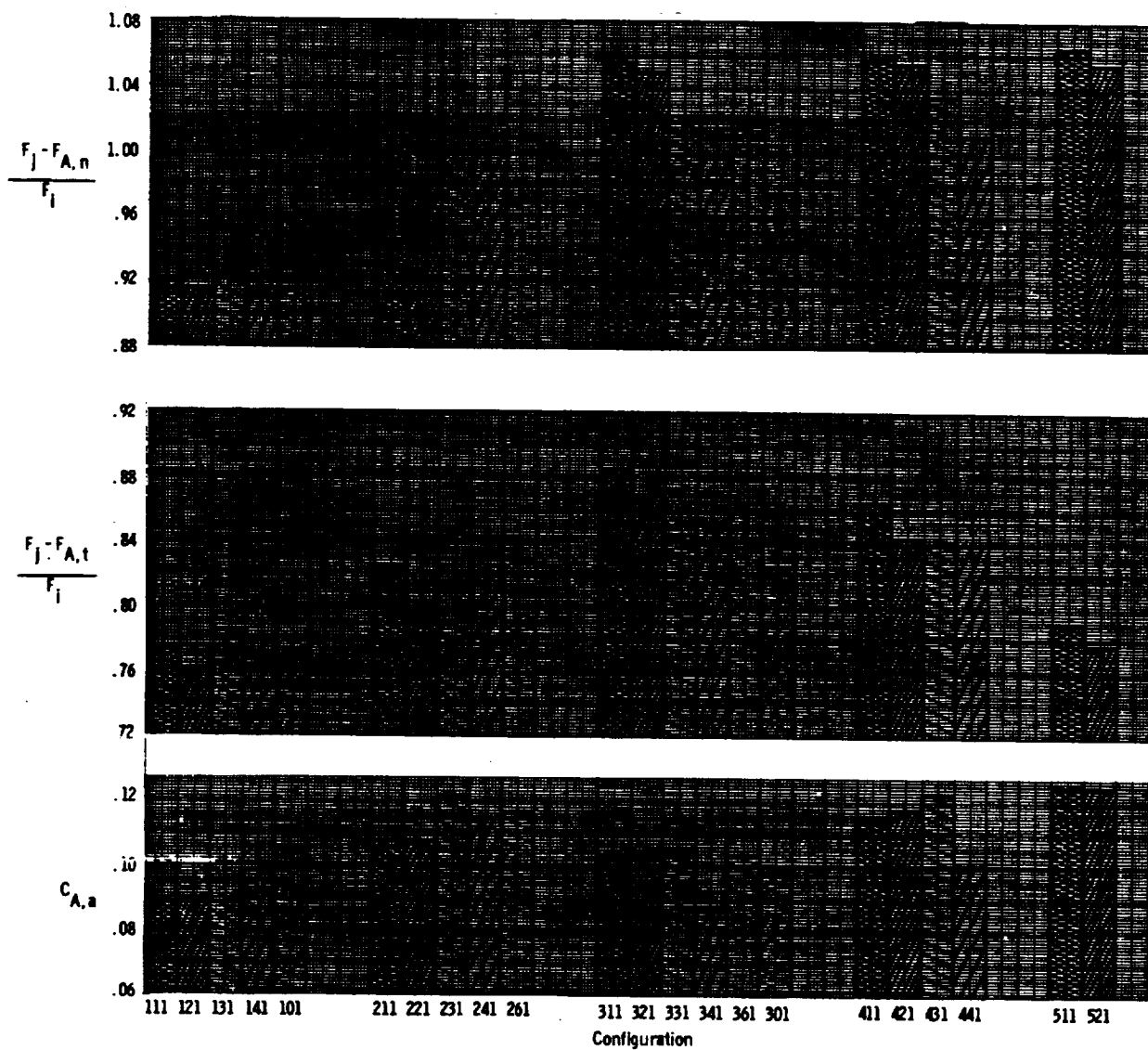
(a) $M = 0.70$; $\frac{P_{t,j}}{P_{\infty}} = 2.6$.

Figure 32.- Propulsive and aerodynamic performance for the various afterbody-nozzle combinations at military power setting.



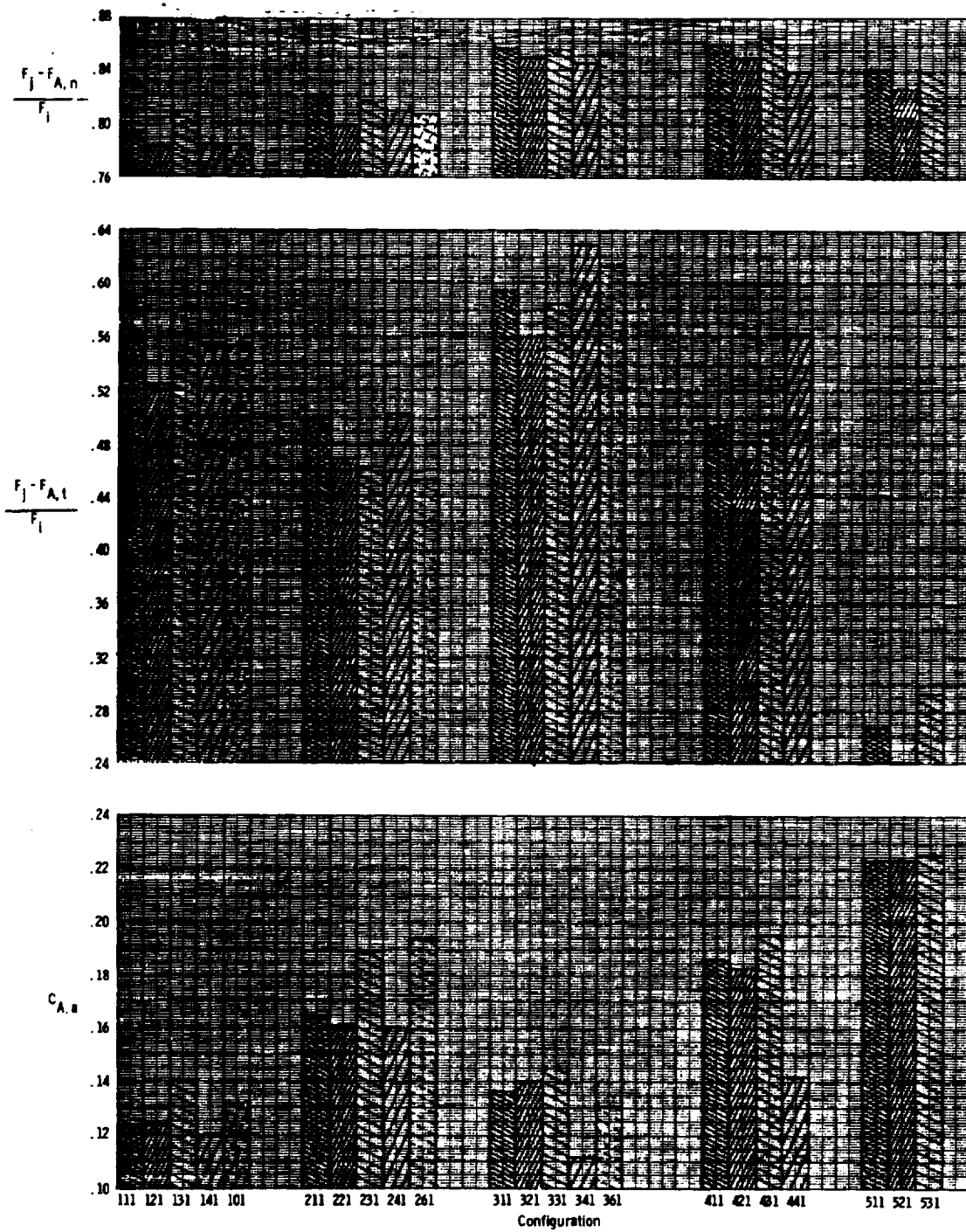
(b) $M = 0.80$; $\frac{p_{t,j}}{p_{\infty}} = 2.9$.

Figure 32.- Continued.



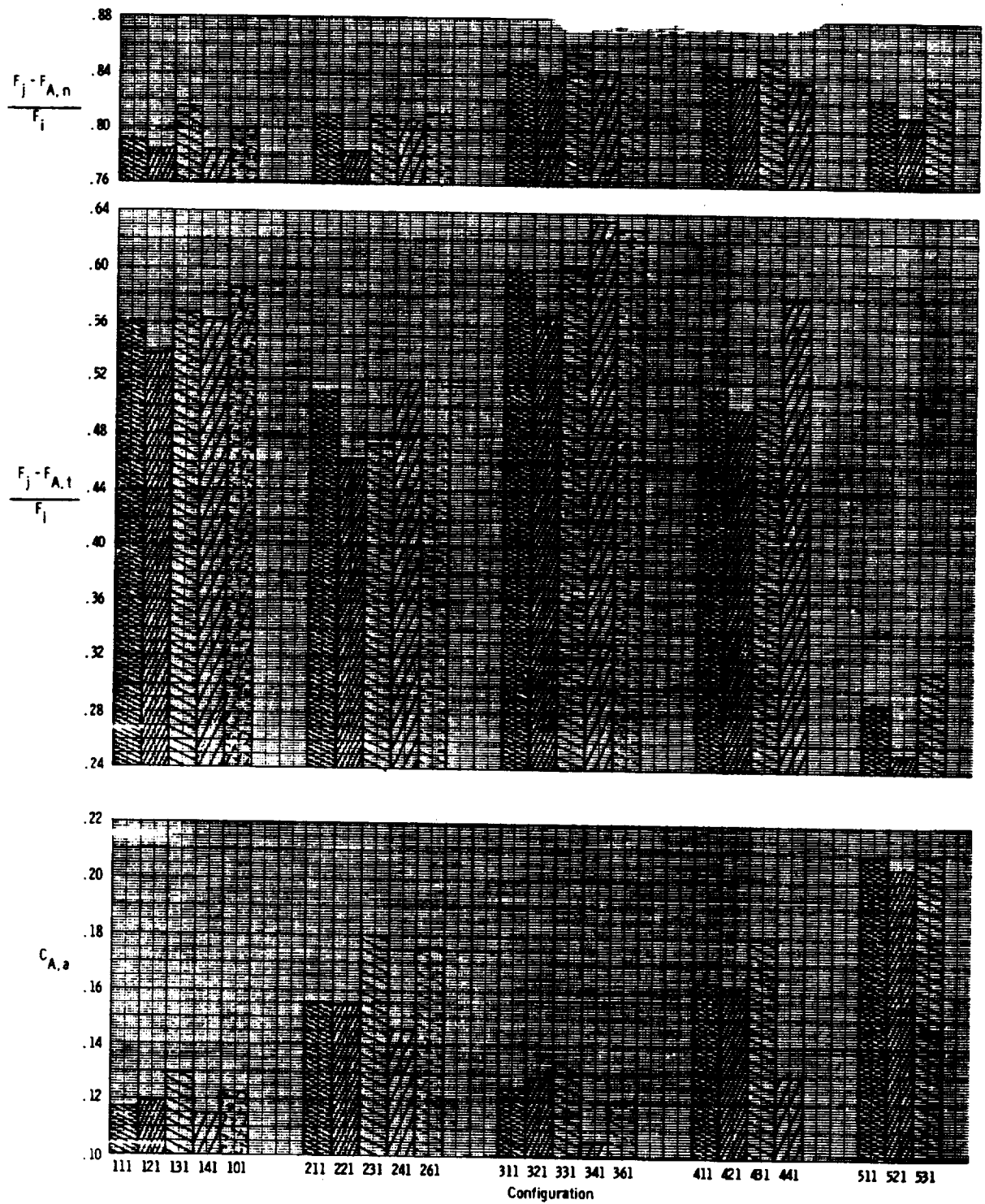
(c) $M = 0.90$; $\frac{p_{t,j}}{p_{\infty}} = 3.2$

Figure 32.- Continued.



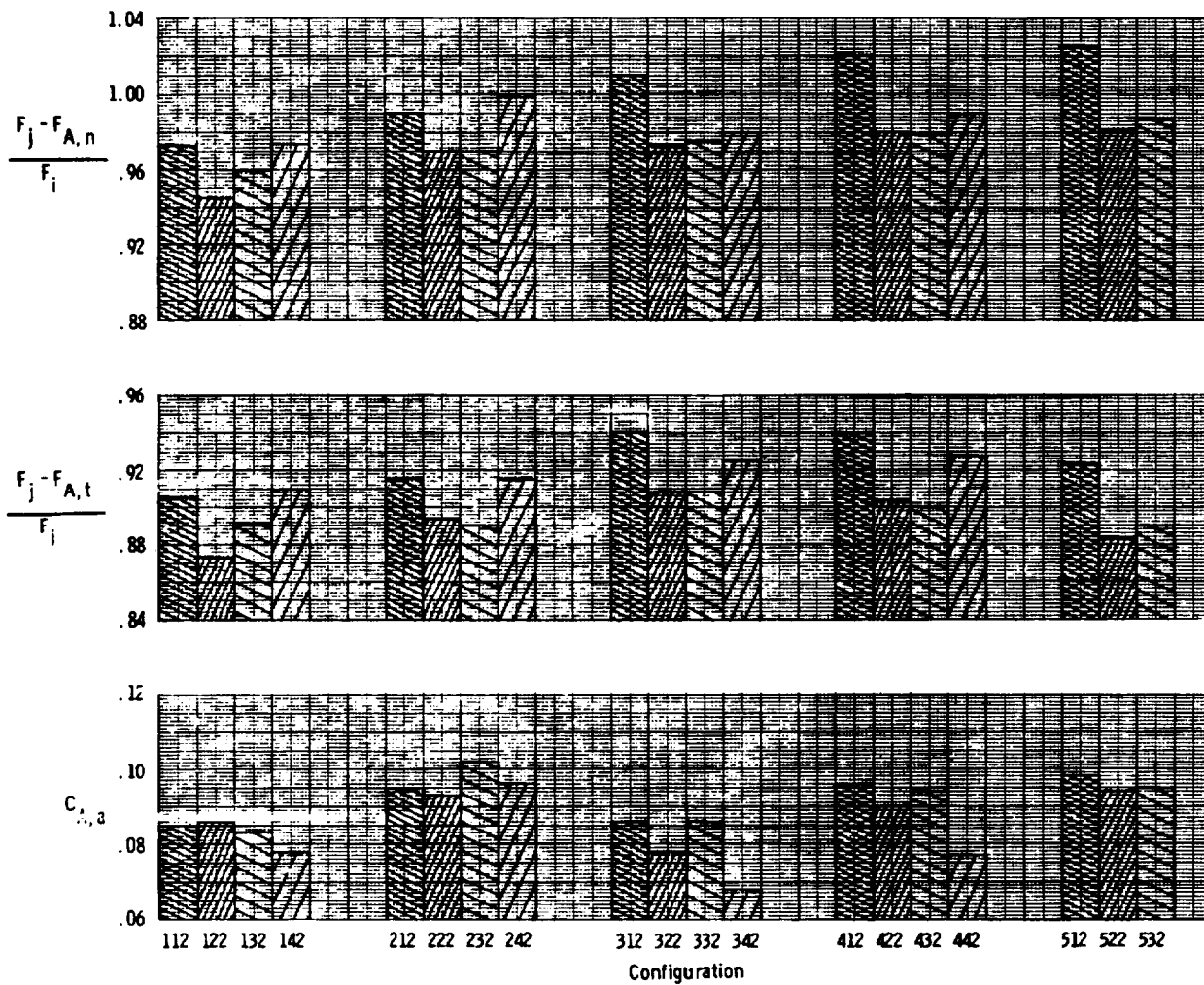
(d) $M = 1.20$; $\frac{p_{t,j}}{p_\infty} = 4.4$.

Figure 32.- Continued.



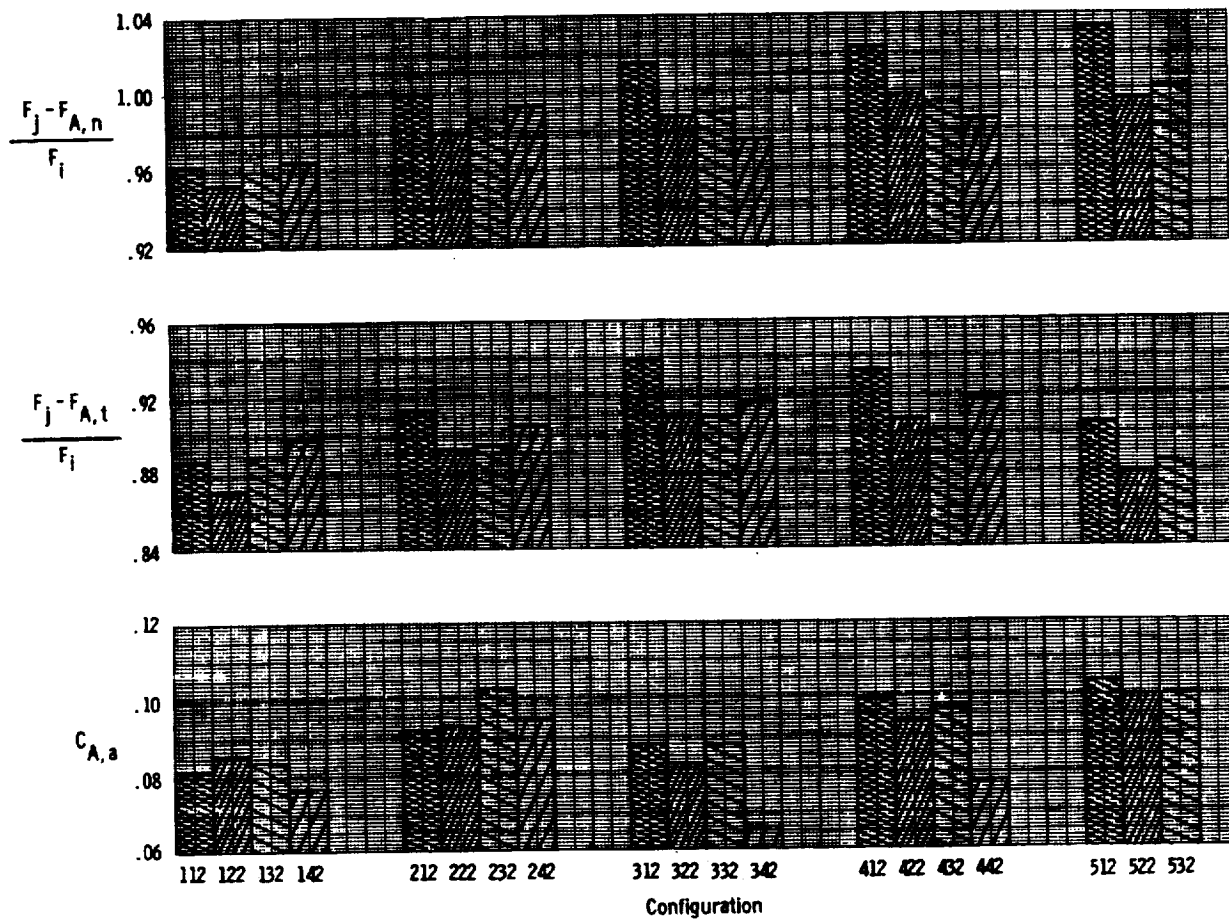
(e) $M = 1.30$; $\frac{p_{t,j}}{p_{\infty}} = 4.9$.

Figure 32.- Concluded.



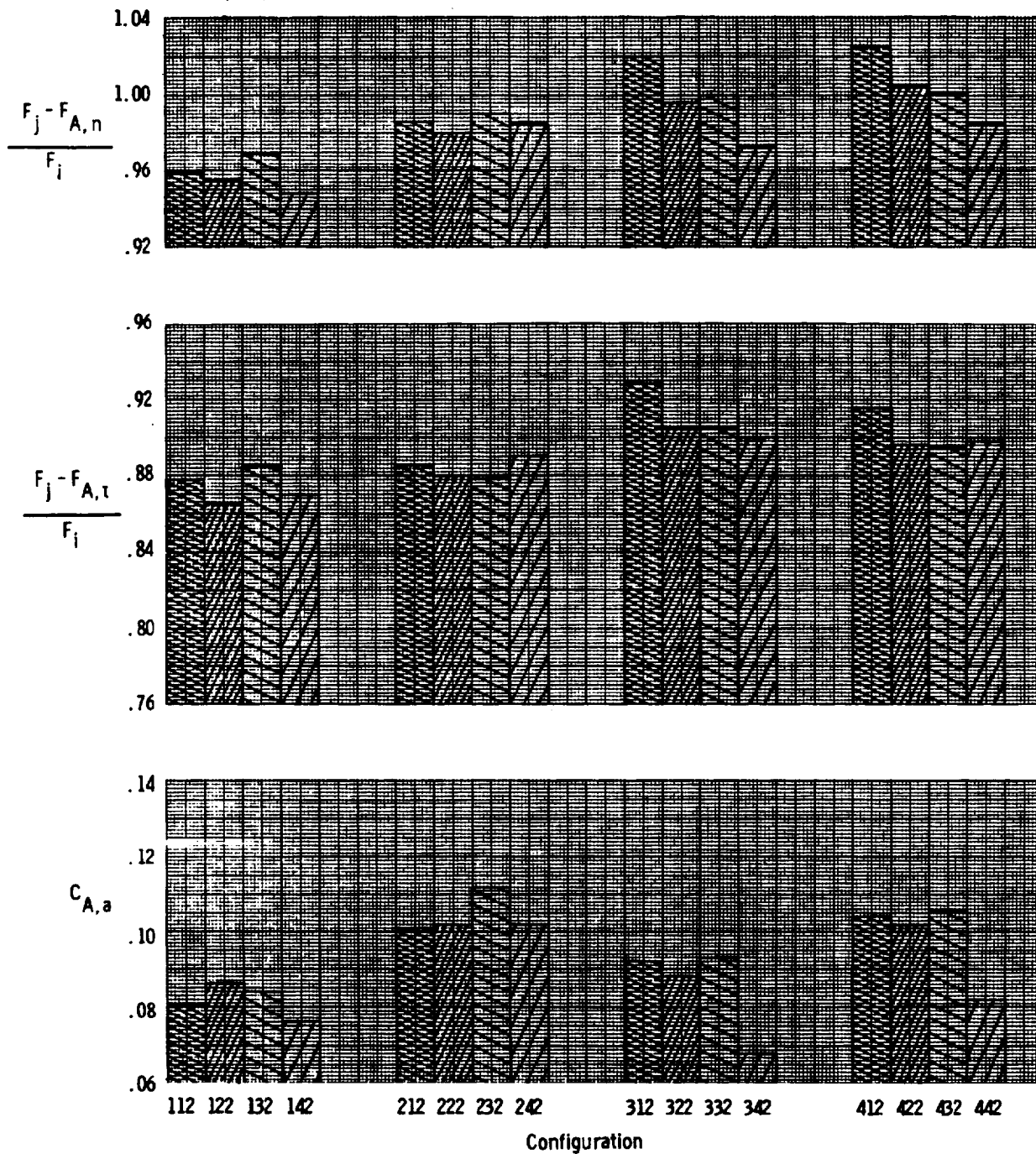
(a) $M = 0.70$; $\frac{P_{t,j}}{P_{\infty}} = 2.6$.

Figure 33.- Propulsive and aerodynamic performance for the various afterbody-nozzle combinations at partial afterburning power setting.



(b) $M = 0.80$; $\frac{p_{t,j}}{p_\infty} = 2.9$.

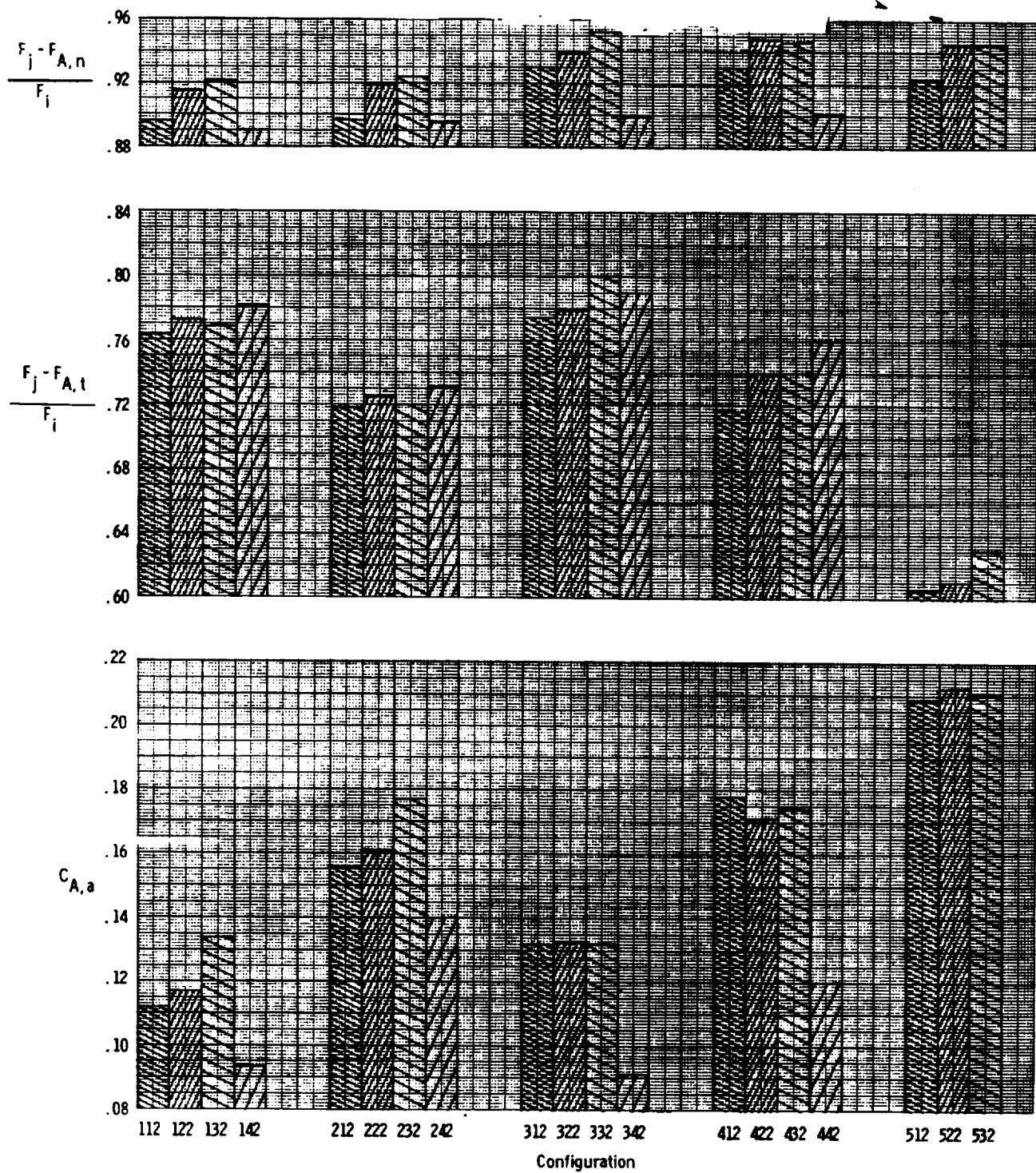
Figure 33.- Continued.



(c) $M = 0.90$; $\frac{p_{t,i}}{p_{\infty}} = 3.2$.

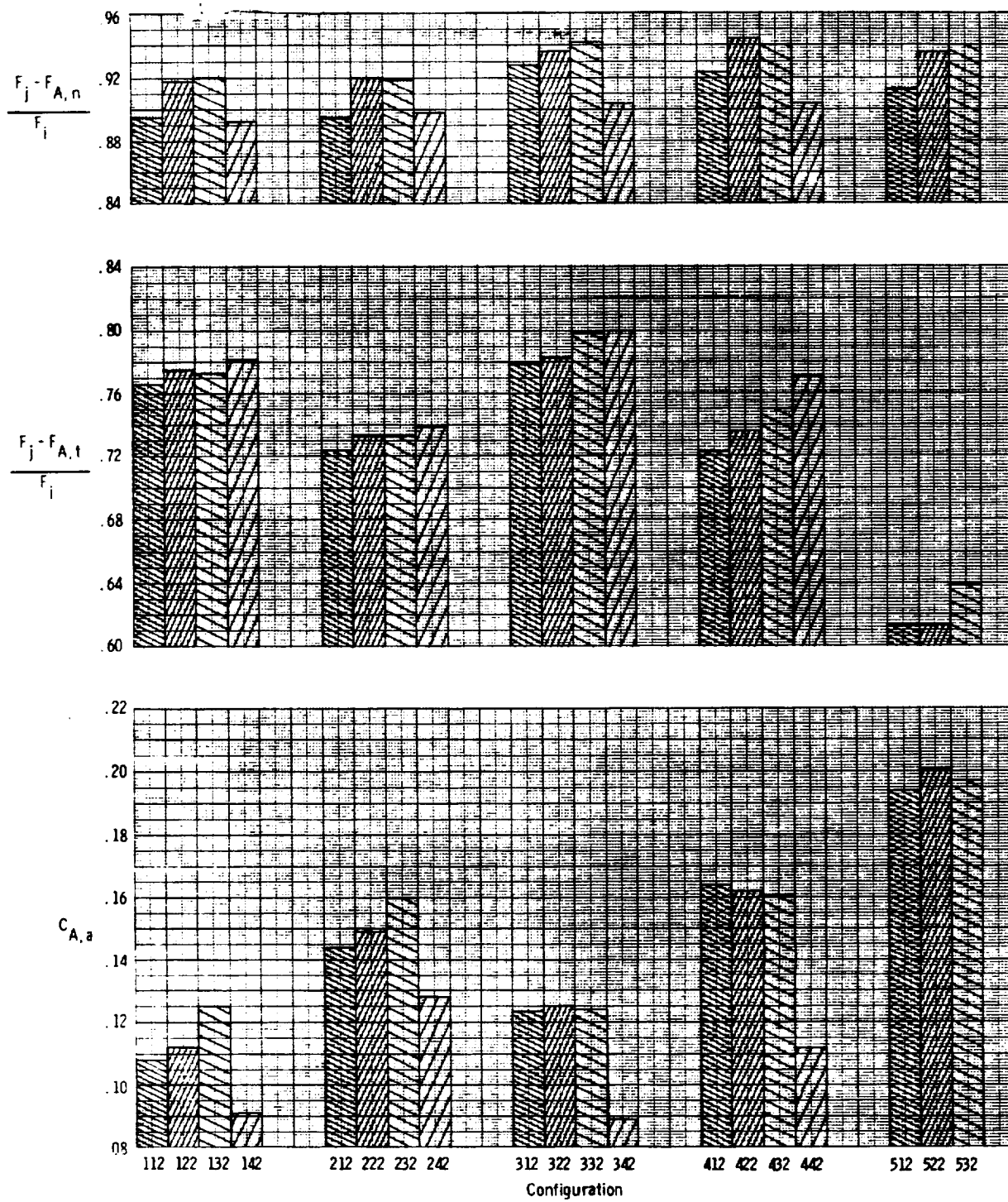
Figure 33.- Continued.

~~CONFIDENTIAL~~



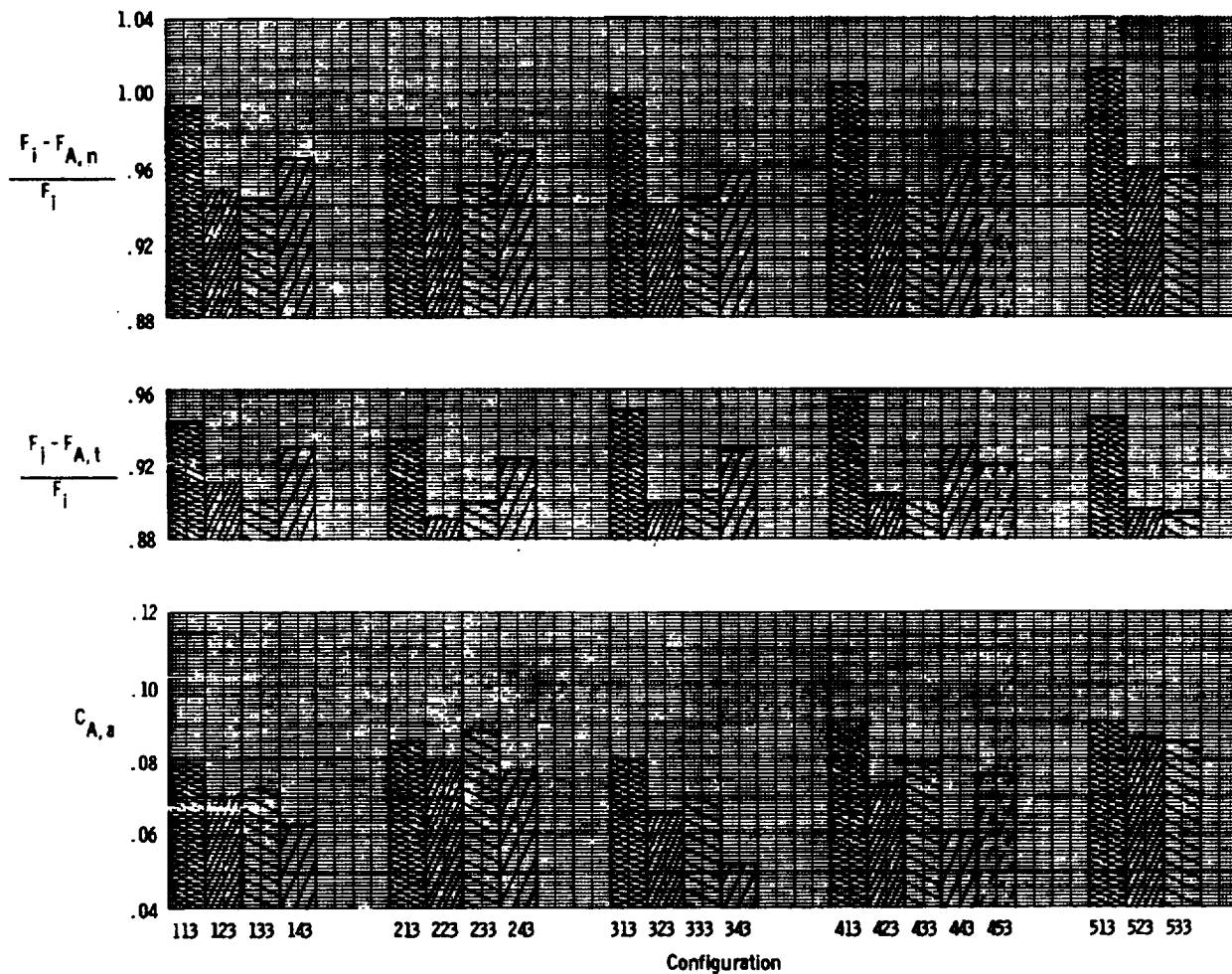
(d) $M = 1.20$; $\frac{p_{tj}}{p_{\infty}} = 4.4$.

Figure 33.- Continued.



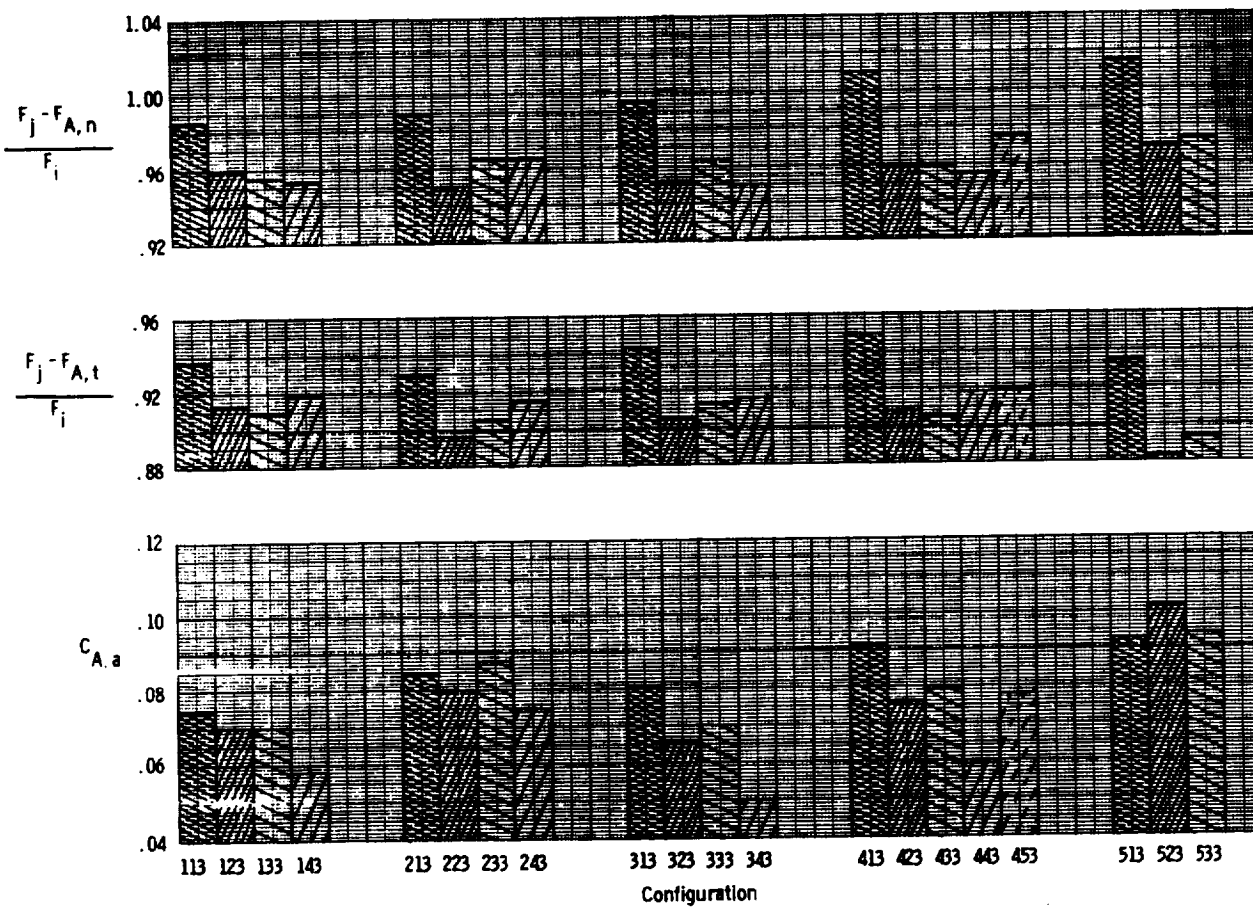
(e) $M = 1.30$; $\frac{p_{t,j}}{p_\infty} = 4.9$.

Figure 33.- Concluded.



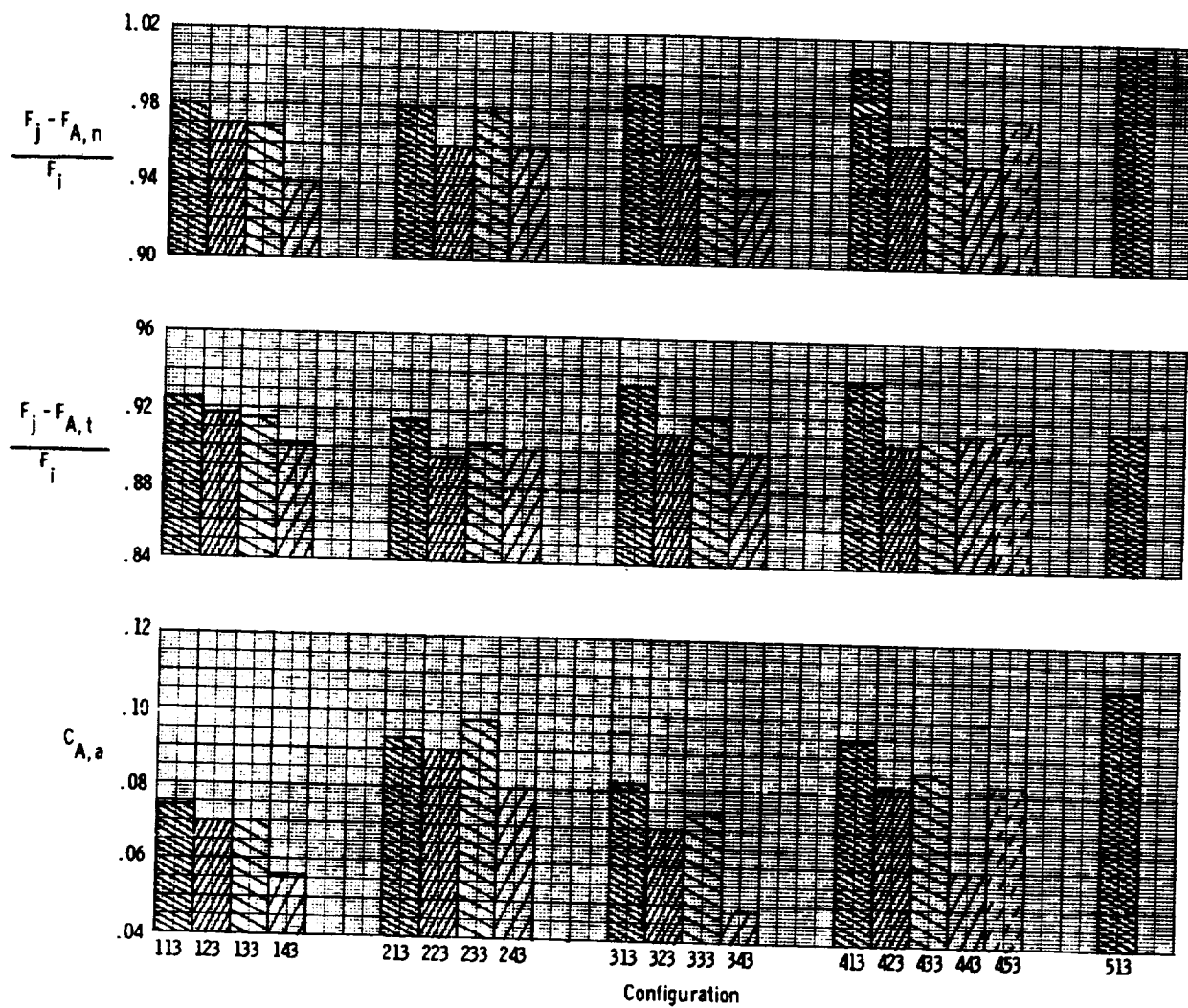
(a) $M = 0.70$; $\frac{P_{t,j}}{P_{\infty}} = 2.6$.

Figure 34.- Propulsive and aerodynamic performance for the various afterbody-nozzle combinations at maximum afterburning power setting.



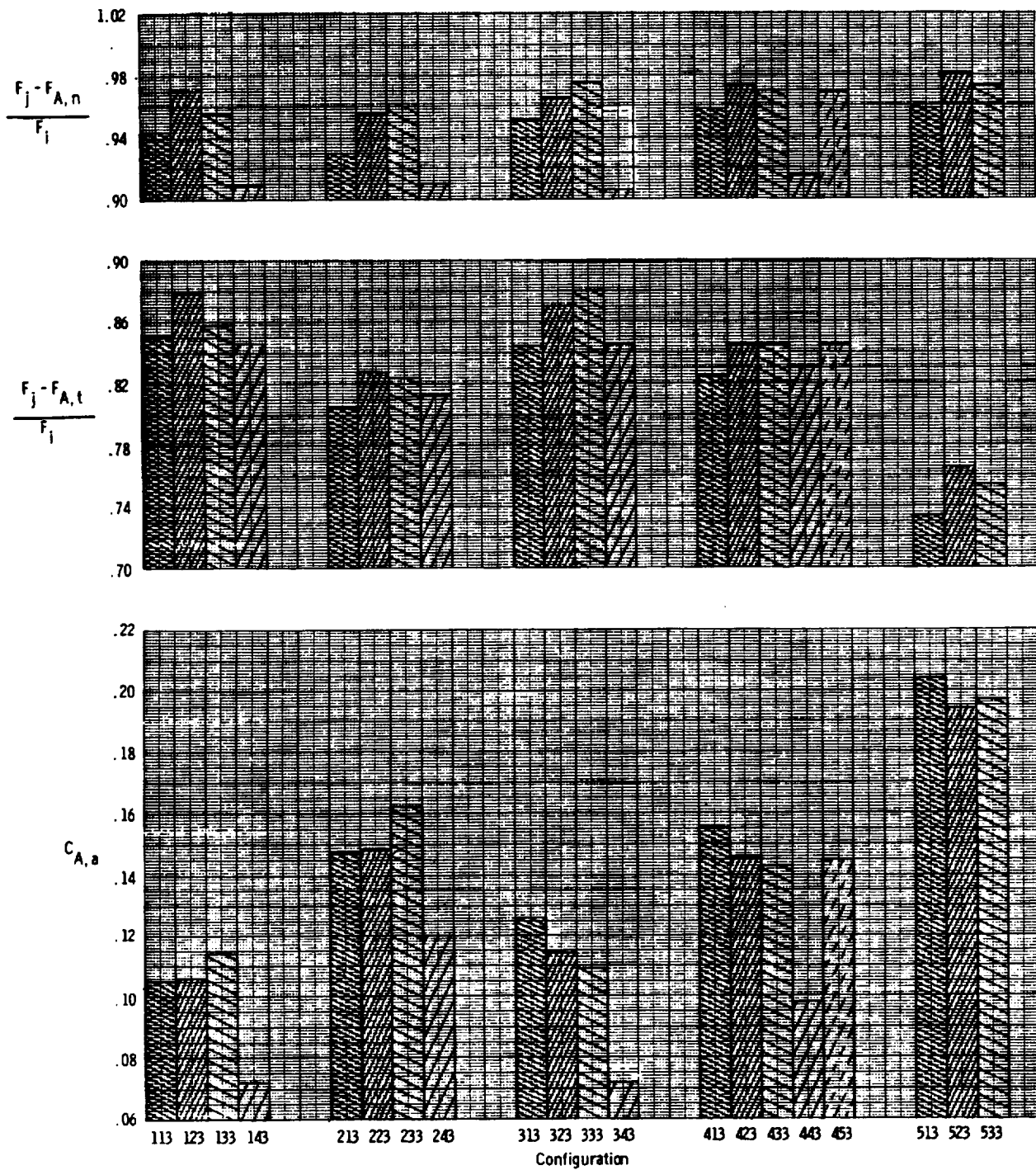
(b) $M = 0.80; \frac{p_{t,j}}{p_{\infty}} = 2.9.$

Figure 34.- Continued.



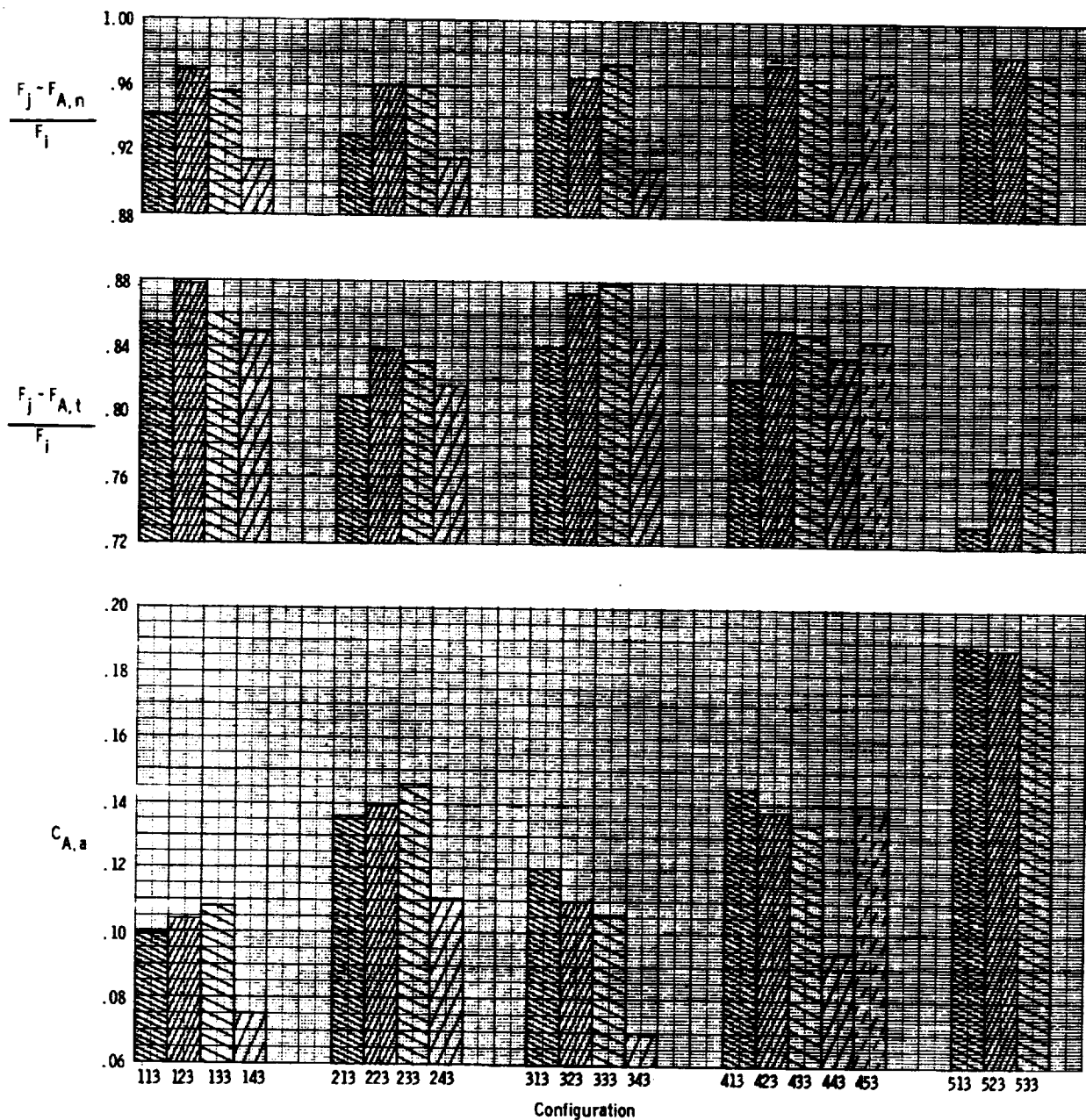
(c) $M = 0.90$; $\frac{P_{t,j}}{P_{\infty}} = 3.2$.

Figure 34.- Continued.



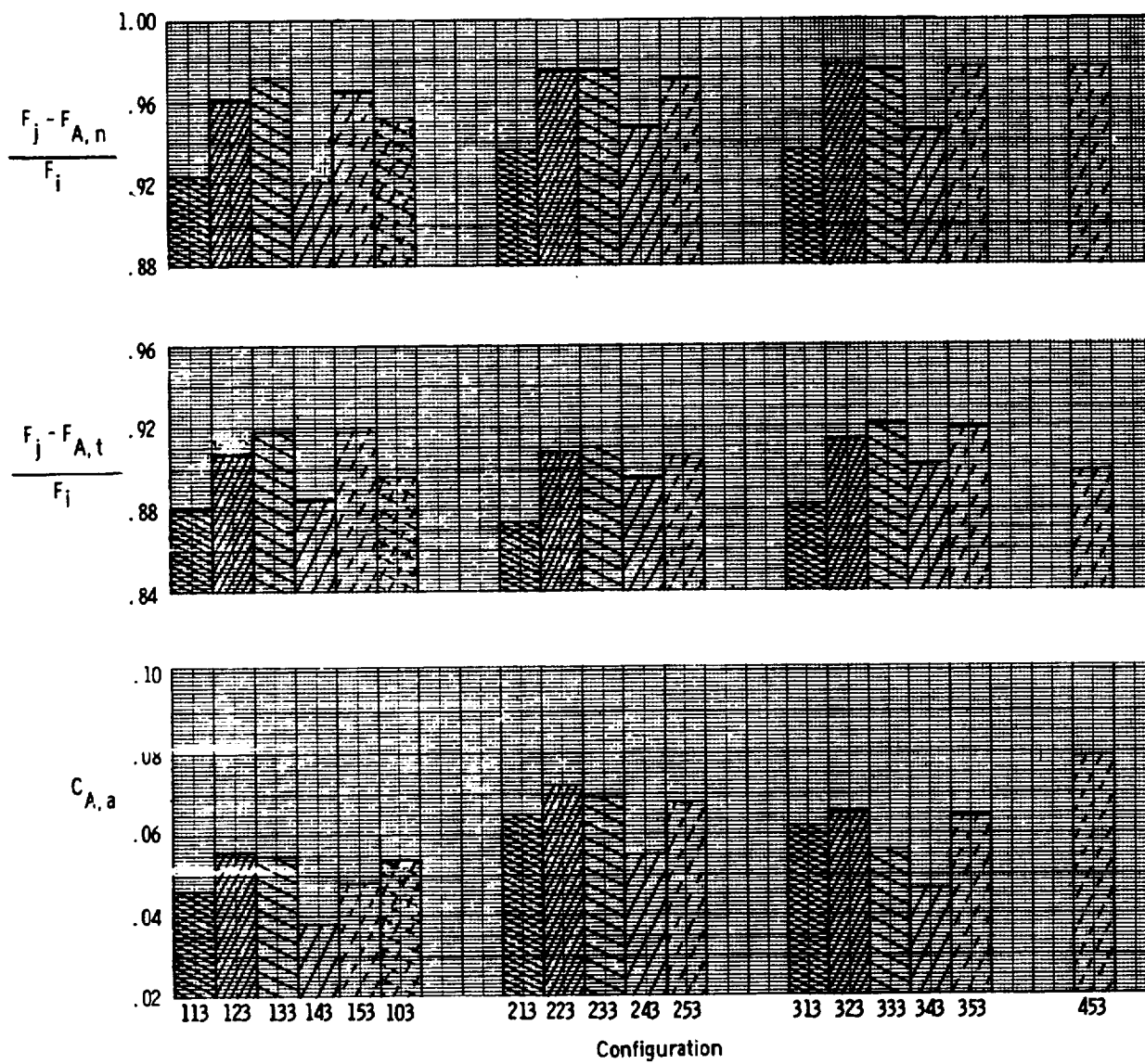
(d) $M = 1.20$; $\frac{p_{t,j}}{p_{\infty}} = 4.4$.

Figure 34.- Continued.



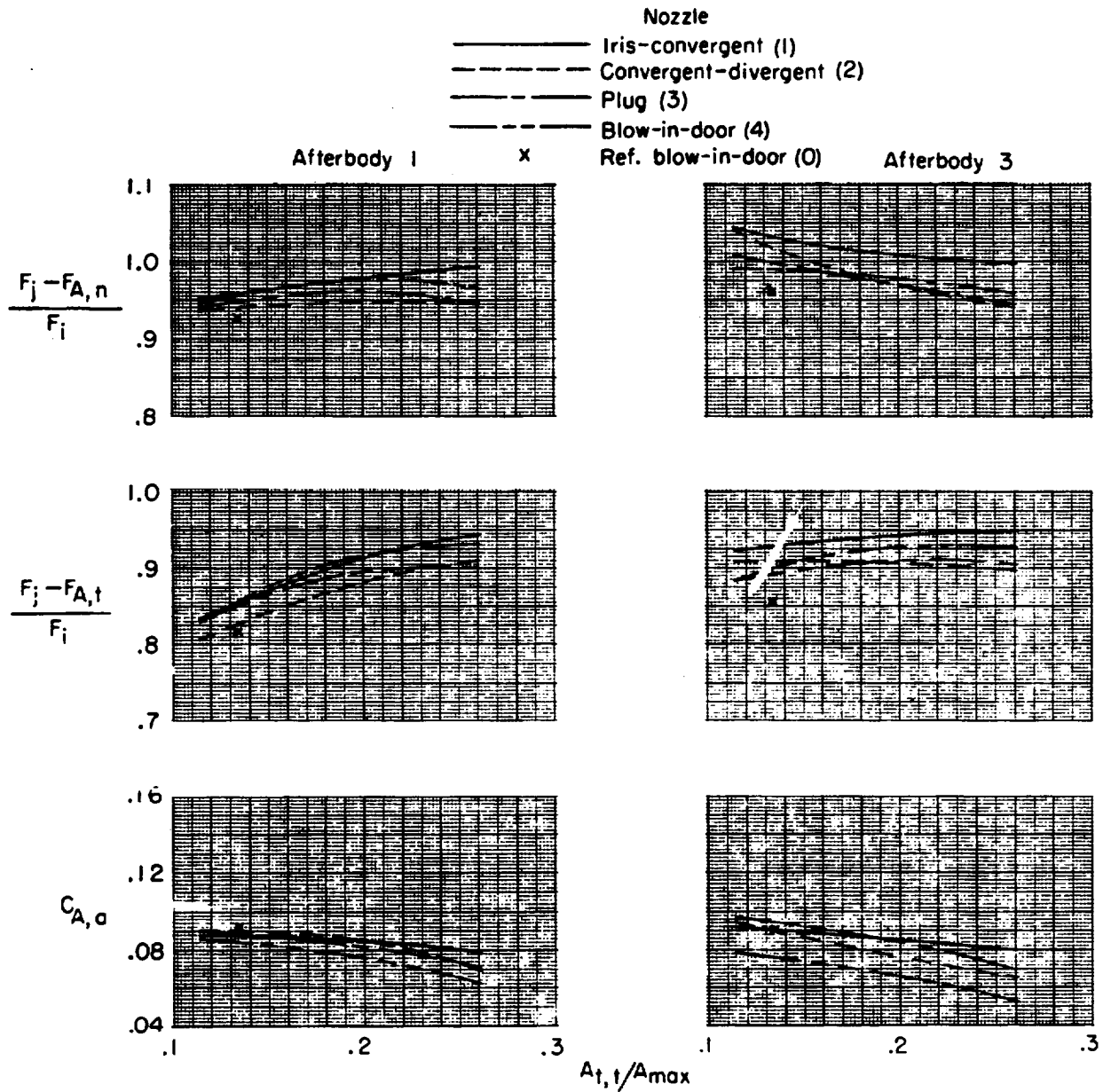
(e) $M = 1.30; \frac{p_{t,j}}{p_{\infty}} = 4.9.$

Figure 34.- Continued.



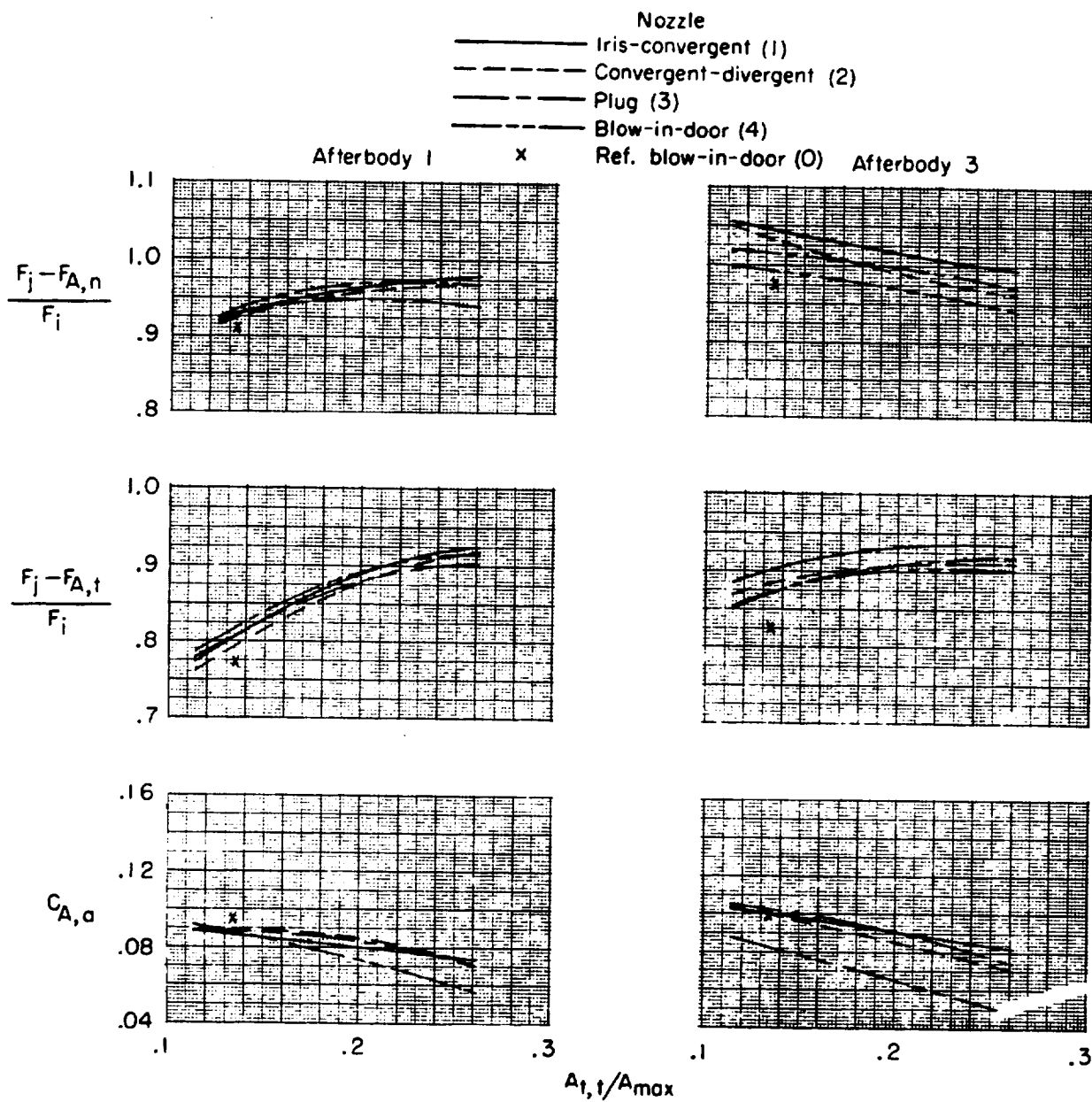
(f) $M = 2.2$; $\frac{p_{t,j}}{p_{\infty}} = 11.0$.

Figure 34.- Concluded.



(a) $M = 0.70; \frac{p_{t,j}}{p_{\infty}} = 2.6.$

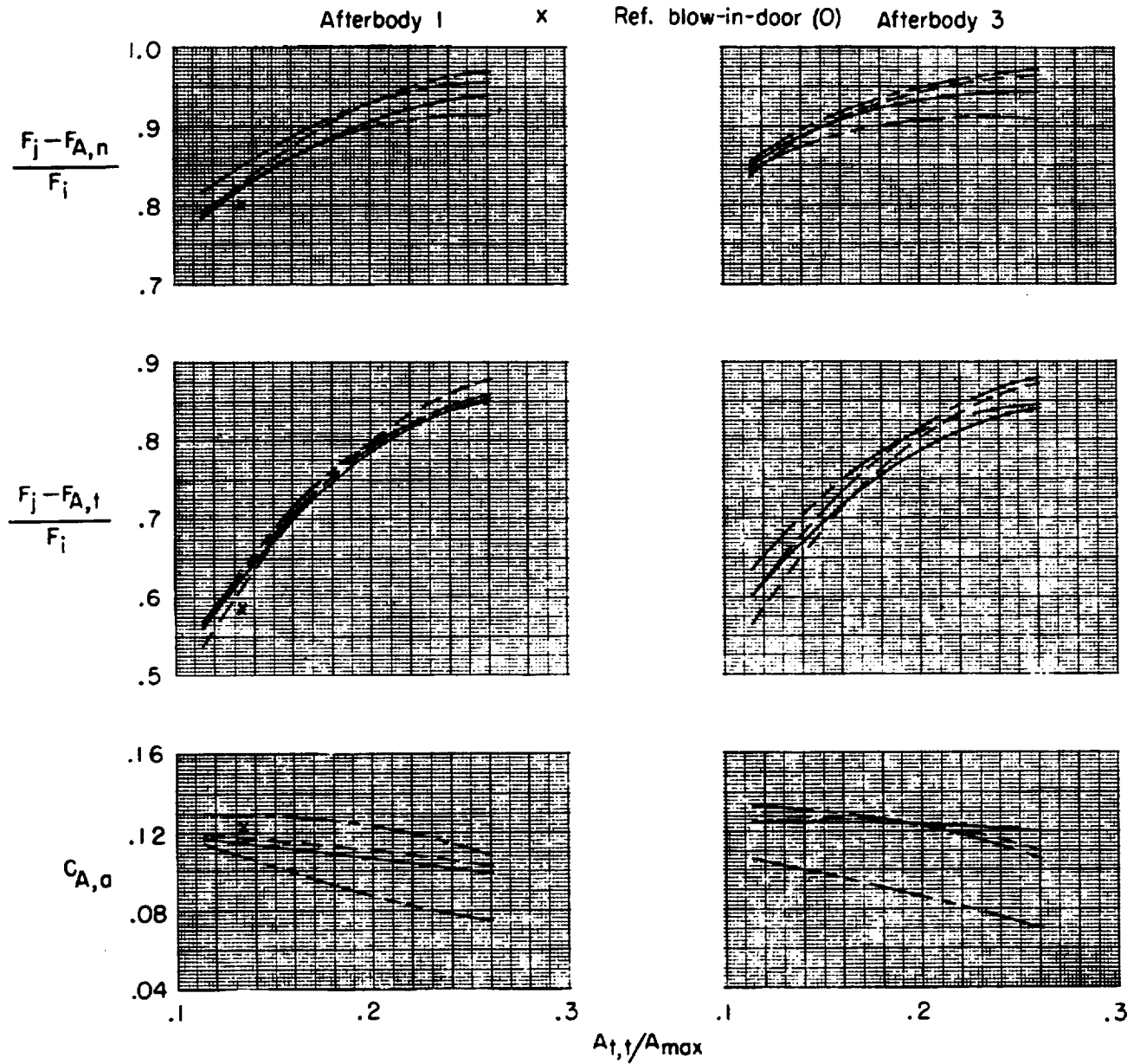
Figure 35.- Effect of power setting on the installed performance of the various nozzles in combination with two afterbody types for several Mach numbers.



(b) $M = 0.90; \frac{p_{t,j}}{p_{\infty}} = 3.2.$

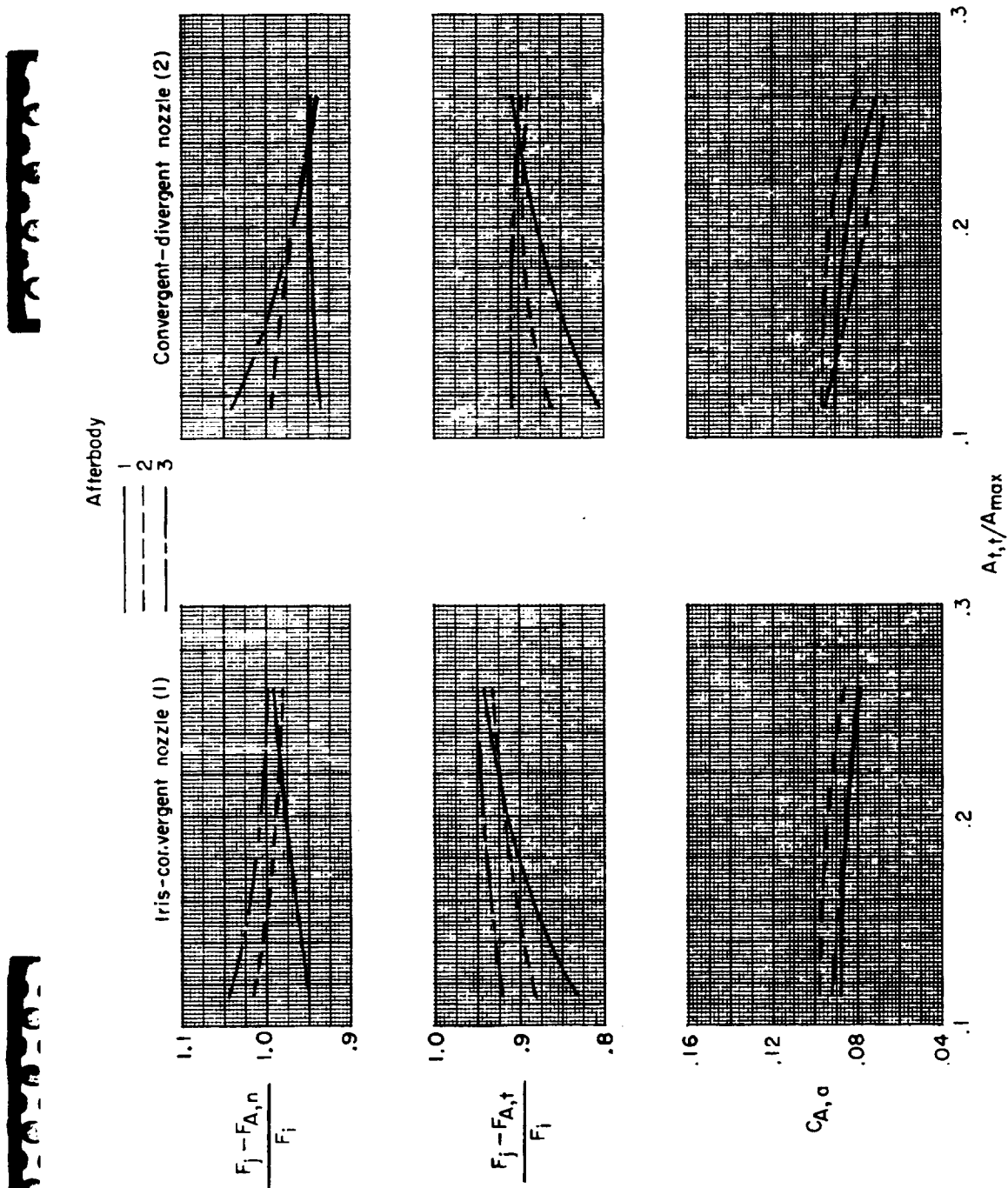
Figure 35.- Continued.

- Nozzle
- Iris-convergent (1)
 - - - Convergent-divergent (2)
 - Plug (3)
 - - - Blow-in-door (4)
 - Ref. blow-in-door (0)



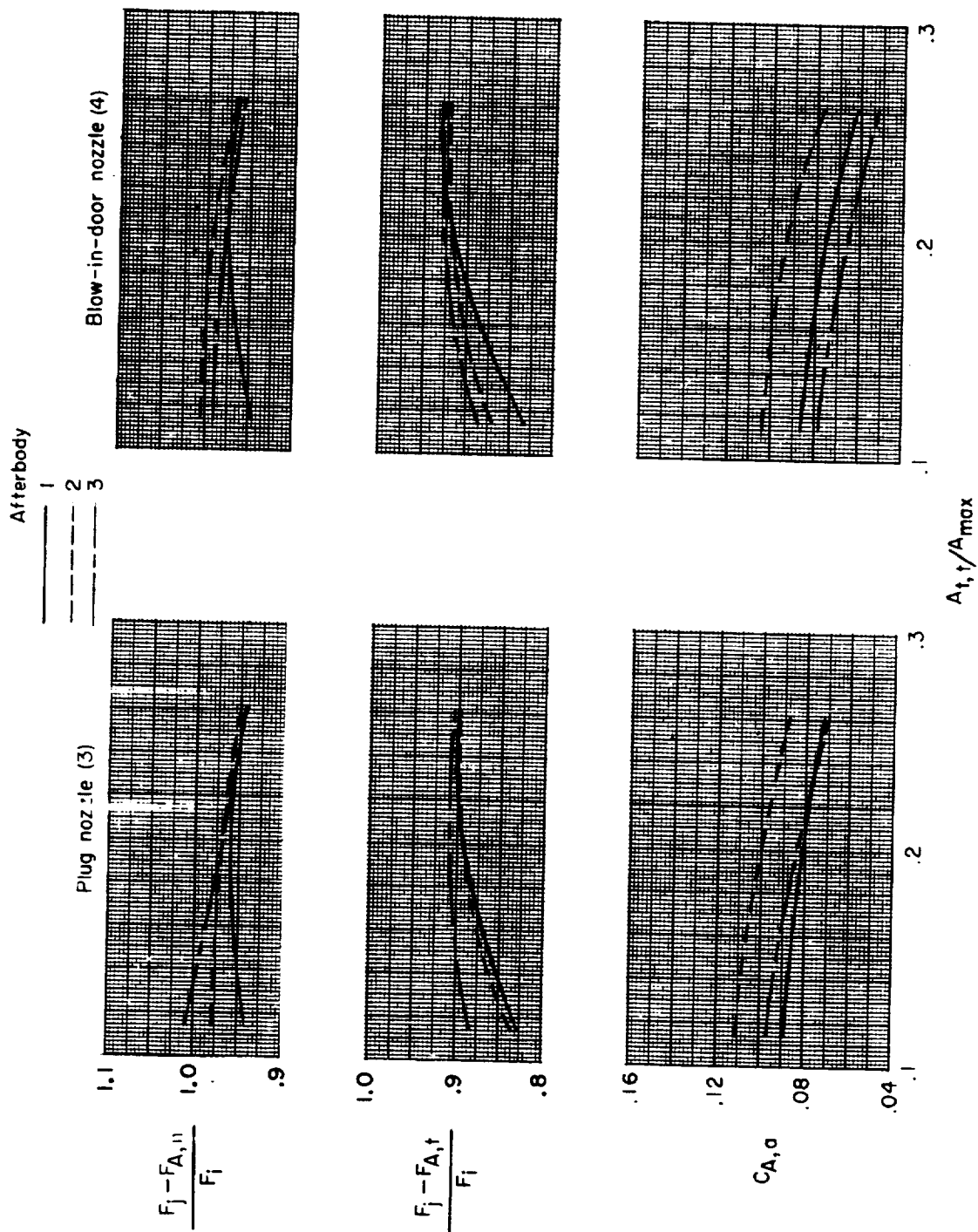
(c) $M = 1.30$; $\frac{p_{t,j}}{p_{\infty}} = 4.9$.

Figure 35.- Concluded.



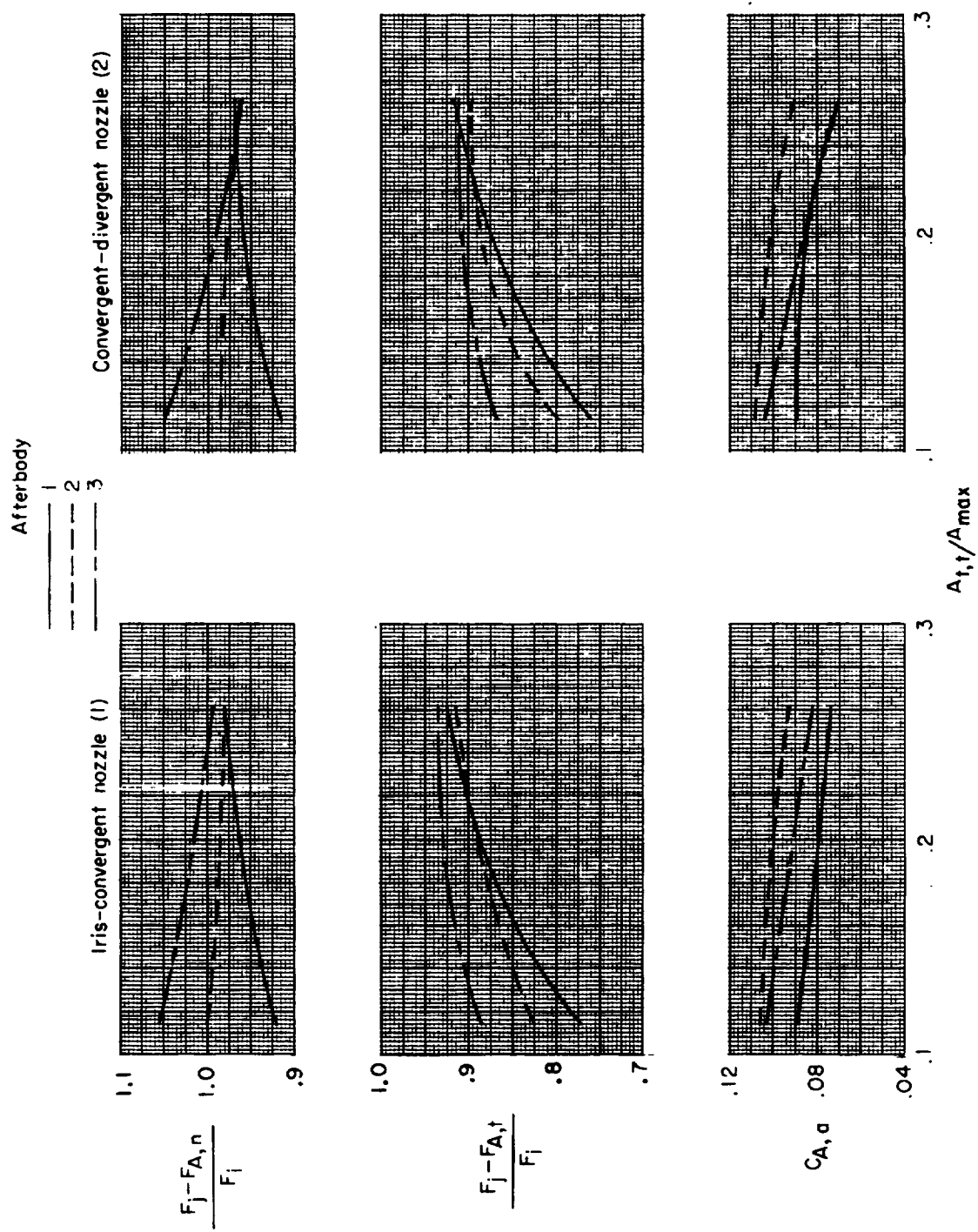
(a) $M = 0.70$; $\frac{p_{t,j}}{p_{\infty}} = 2.6$.

Figure 36.- Effect of power setting on the installed performance of the complex geometry afterbodies (afterbodies 1, 2, and 3) for the various nozzles at several Mach numbers for a typical jet total-pressure-ratio schedule.



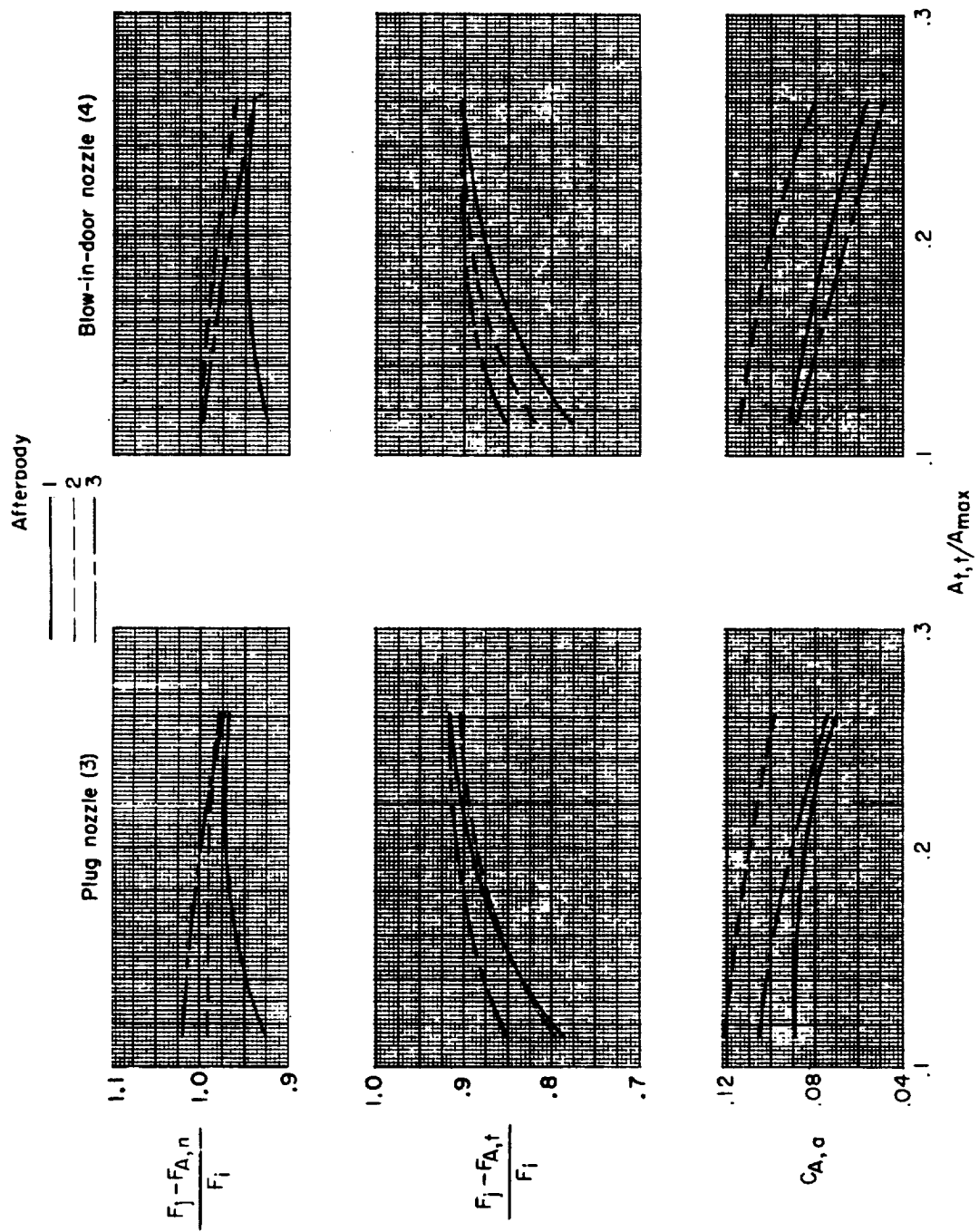
(a) Concluded.

Figure 36.- Continued.



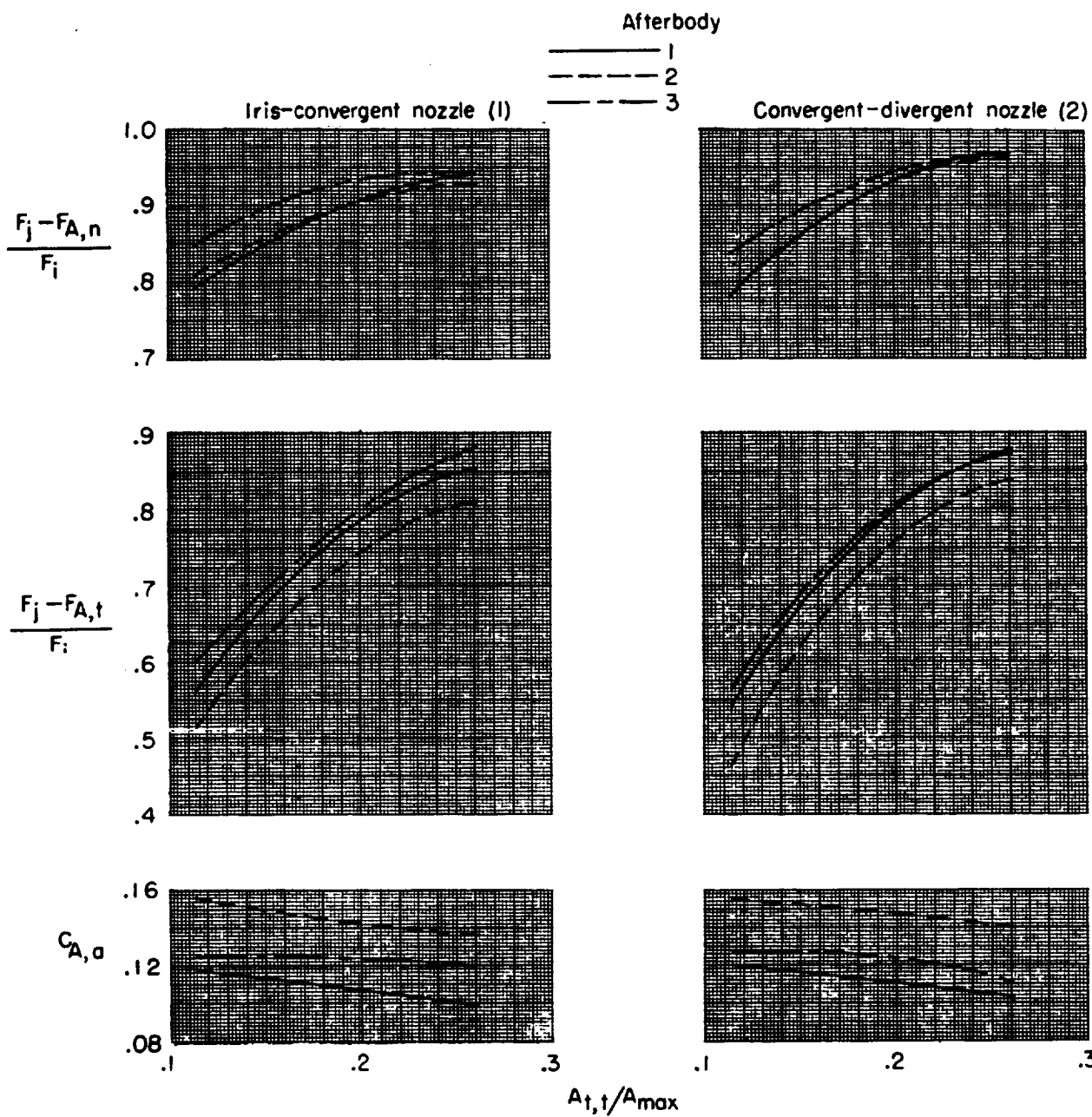
(b) $M = 0.90$; $\frac{p_{t,j}}{p_{\infty}} = 3.2$.

Figure 36.- Continued.



(b) Concluded.

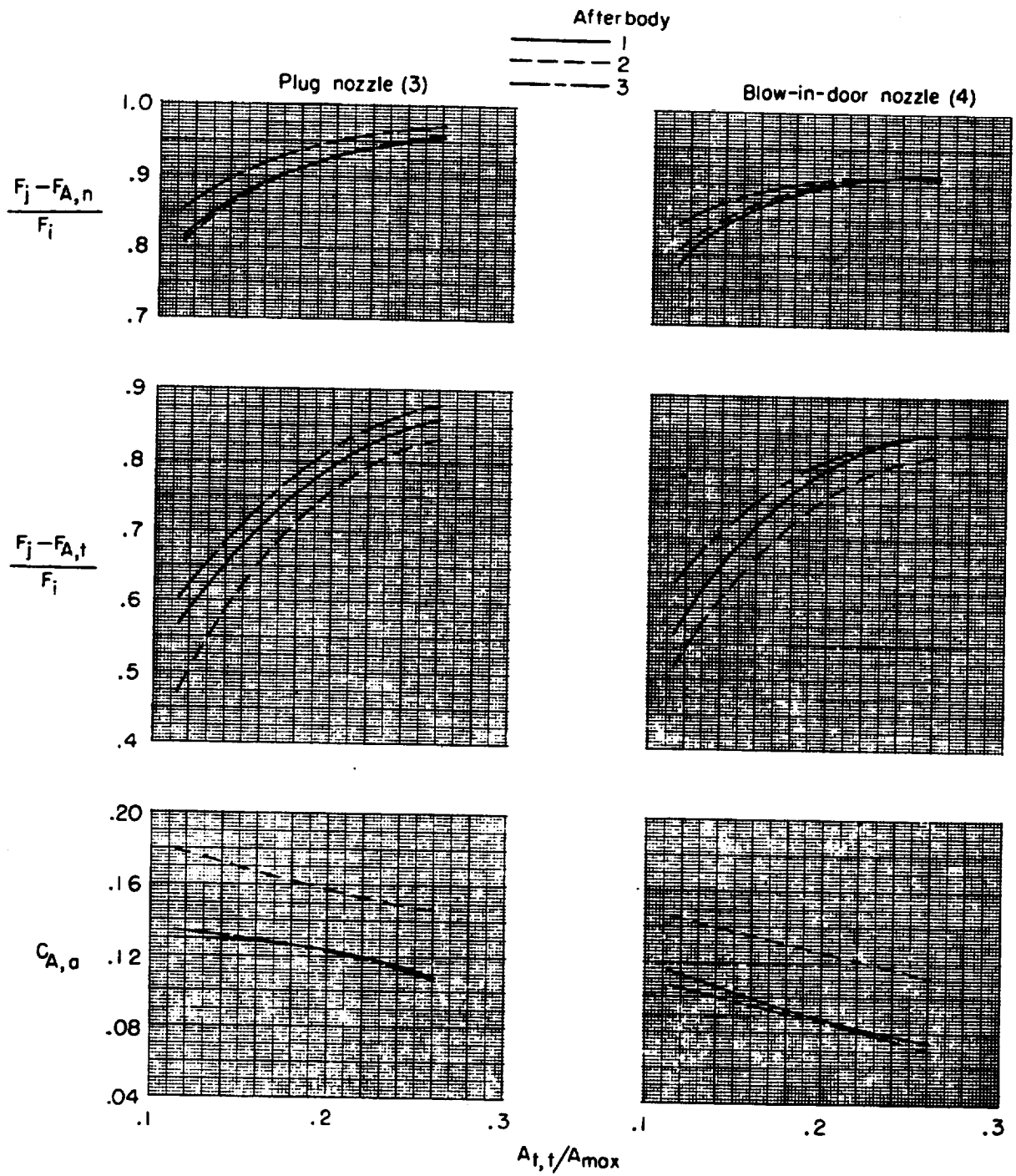
Figure 36.- Continued.



(c) $M = 1.30$; $\frac{p_{t,j}}{p_{\infty}} = 4.9$.

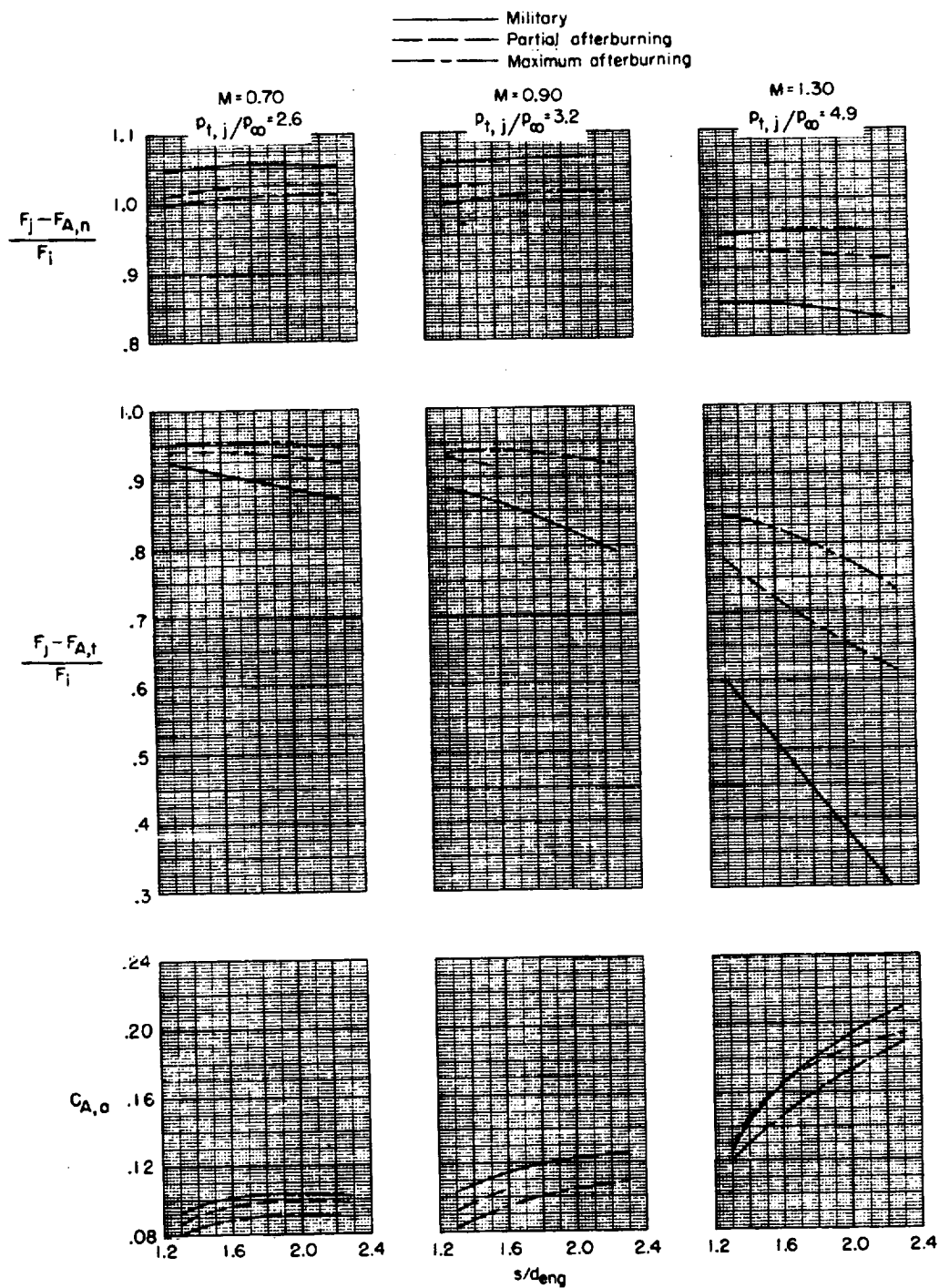
Figure 36.- Continued.

~~CONFIDENTIAL~~



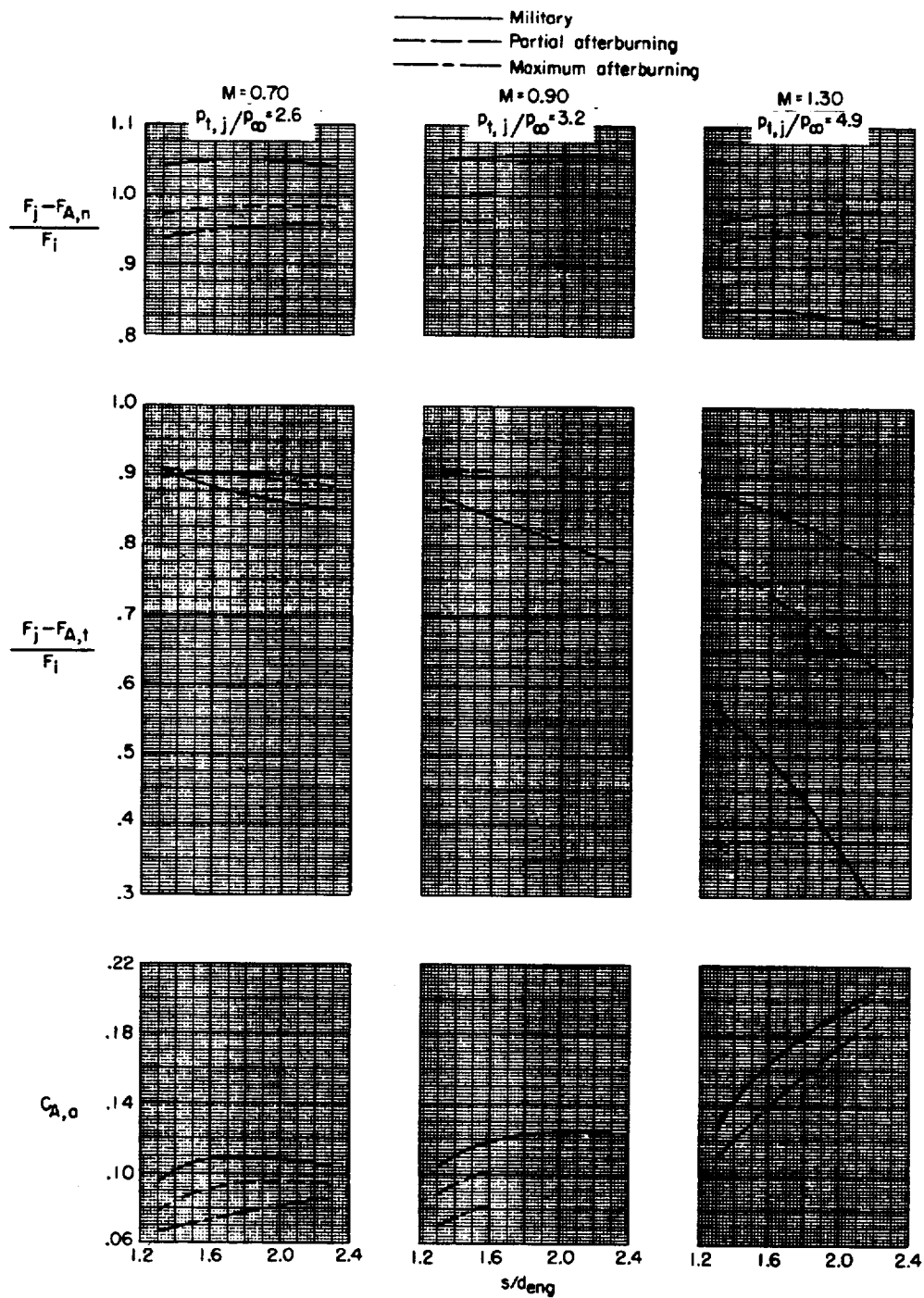
(c) Concluded.

Figure 36.- Concluded.



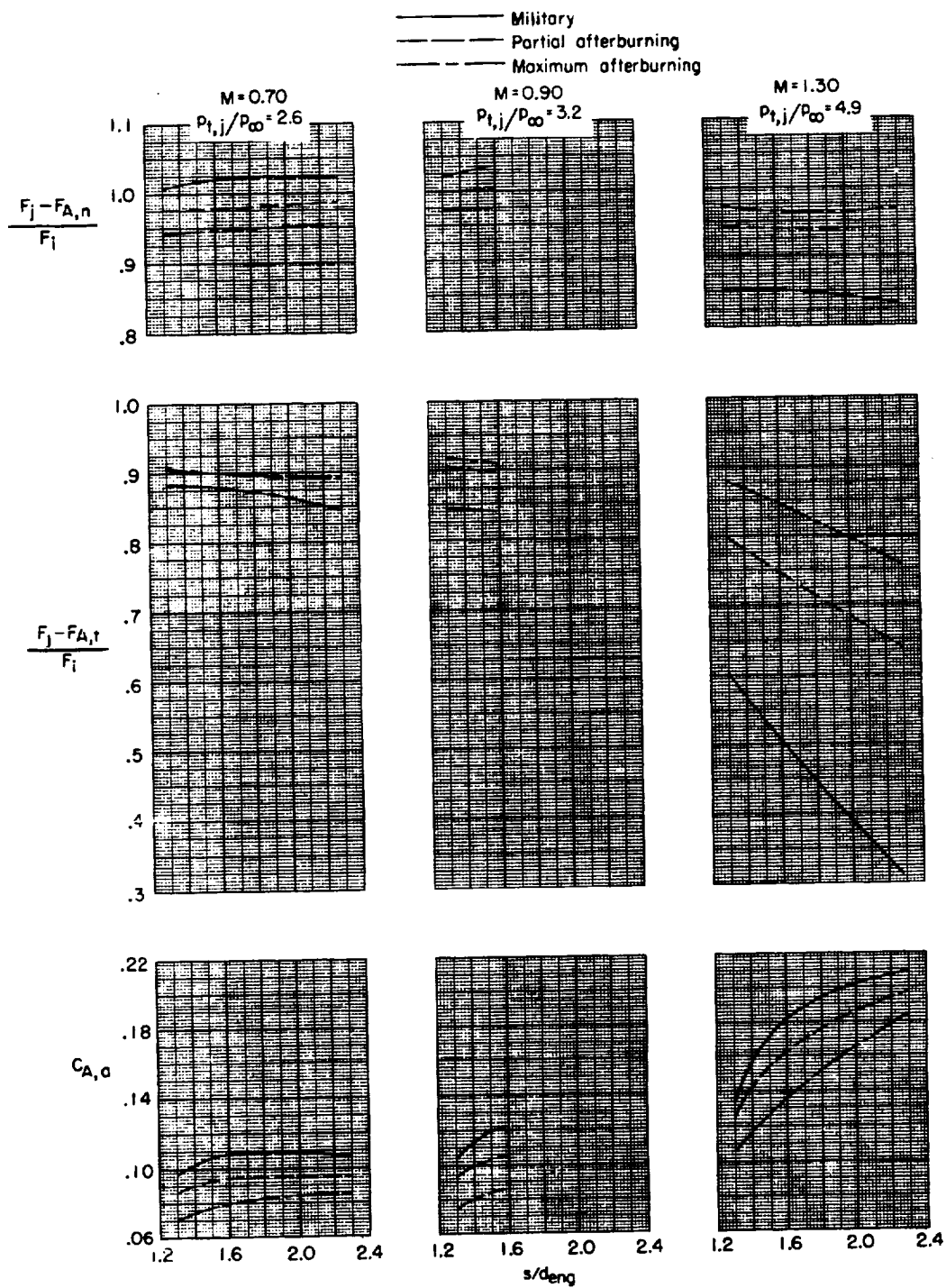
(a) Convergent nozzles. (Nozzle 1.)

Figure 37.- Effect of nozzle spacing ratio on nozzle and afterbody performance for several Mach numbers at a scheduled pressure ratio.



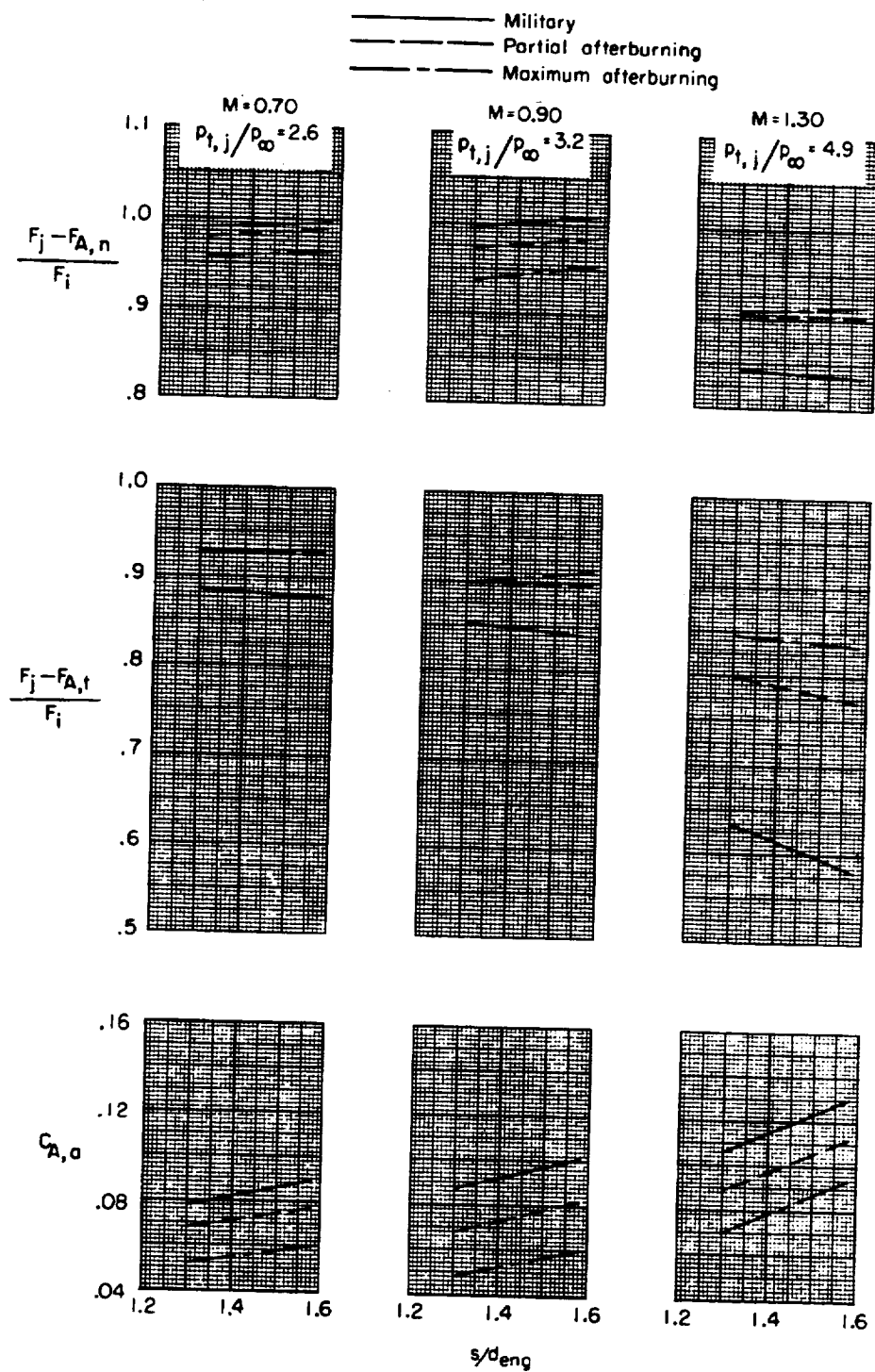
(b) Convergent-divergent nozzles. (Nozzle 2.)

Figure 37.- Continued.



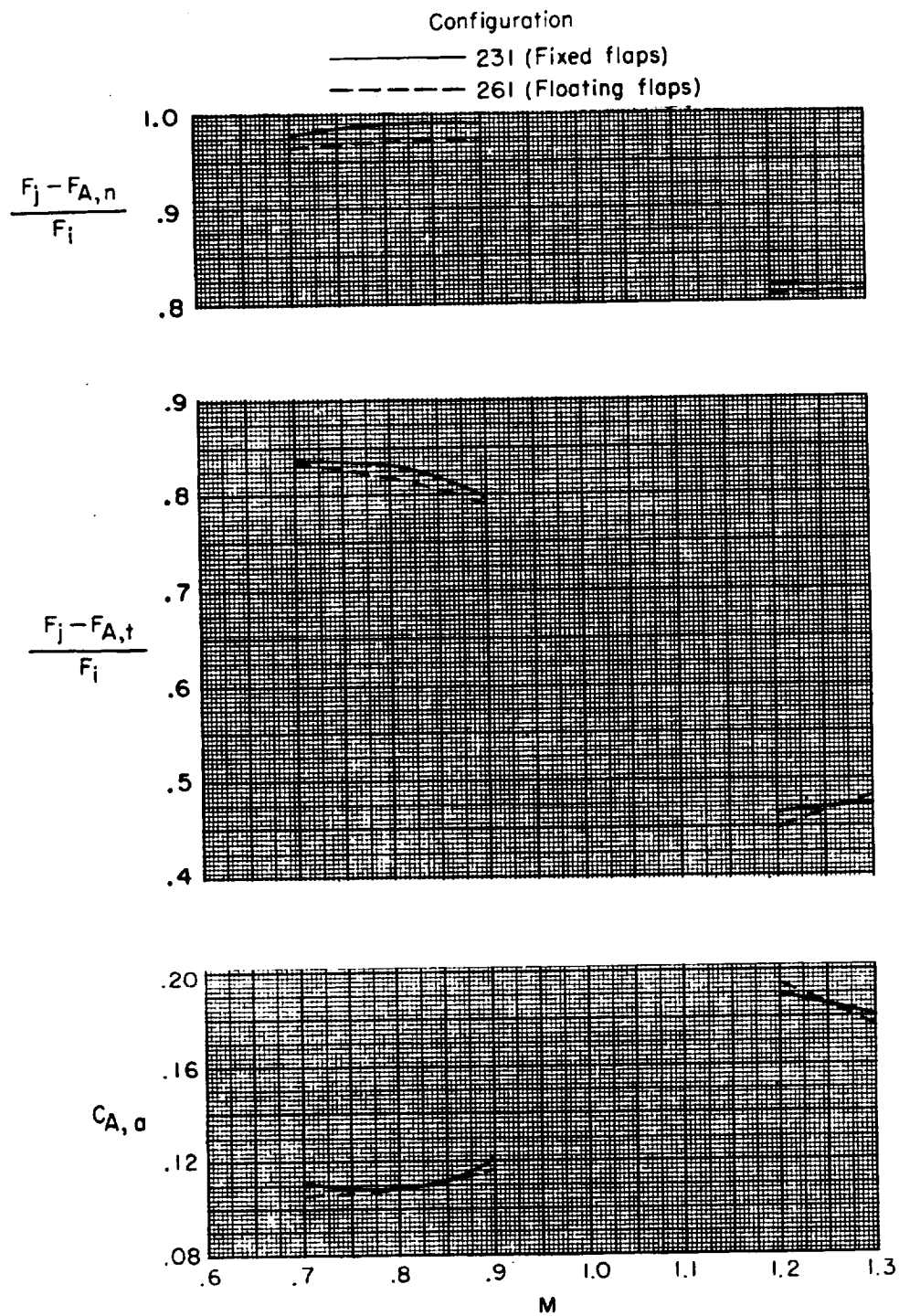
(c) Plug nozzles. (Nozzle 3.)

Figure 37.- Continued.



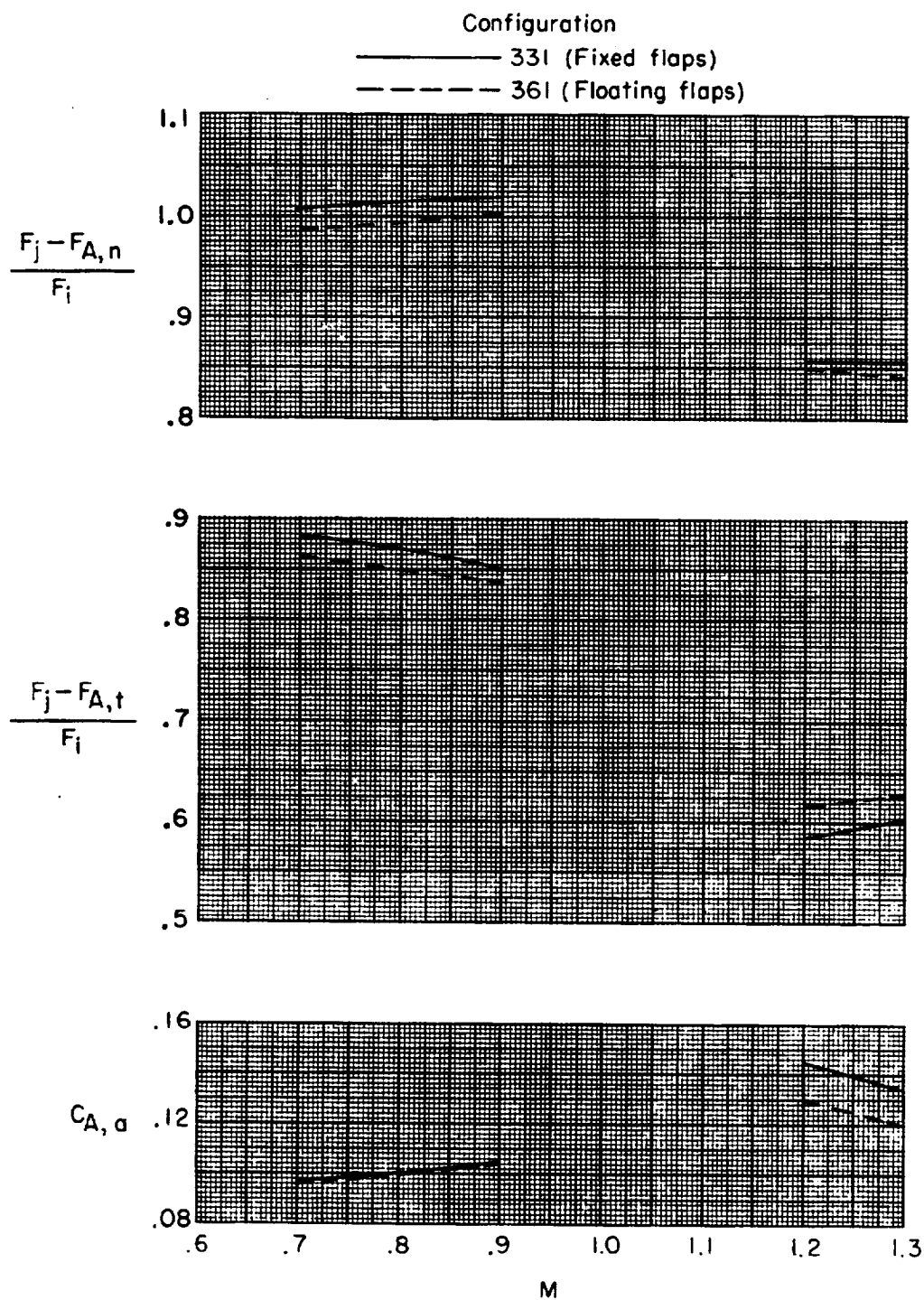
(d) Blow-in-door ejector nozzles. (Nozzle 4.)

Figure 37.- Concluded.



(a) Afterbody 2.

Figure 38.- Installed performance of a plug nozzle having fixed or floating tail flaps for the Mach number range at scheduled jet total-pressure ratios.



(b) Afterbody 3.

Figure 38.- Concluded.